



Durham E-Theses

A Study of Light-Emitting Diodes and Transistors based on Ambipolar Organic Materials

FISHER, ALISON,LAUREN

How to cite:

FISHER, ALISON,LAUREN (2014) *A Study of Light-Emitting Diodes and Transistors based on Ambipolar Organic Materials*, Durham theses, Durham University. Available at Durham E-Theses Online:
<http://etheses.dur.ac.uk/10626/>

Use policy

The full-text may be used and/or reproduced, and given to third parties in any format or medium, without prior permission or charge, for personal research or study, educational, or not-for-profit purposes provided that:

- a full bibliographic reference is made to the original source
- a [link](#) is made to the metadata record in Durham E-Theses
- the full-text is not changed in any way

The full-text must not be sold in any format or medium without the formal permission of the copyright holders.

Please consult the [full Durham E-Theses policy](#) for further details.

Academic Support Office, Durham University, University Office, Old Elvet, Durham DH1 3HP
e-mail: e-theses.admin@dur.ac.uk Tel: +44 0191 334 6107
<http://etheses.dur.ac.uk>

**A Study of Light-Emitting Diodes and Transistors
based on Ambipolar Organic Materials**

by

Alison L. Fisher

Ustinov College

A thesis submitted in partial fulfilment
of the requirements for the degree of Ph.D.



Centre for Molecular and Nanoscale Electronics
School of Engineering and Computing Sciences

Durham University

May 2014

Copyright © 2014 by Alison L. Fisher

The copyright of this thesis rests with the author. No quotation from it should be published without the prior written consent and information derived from it should be acknowledged.

Declaration

I hereby declare that the work carried out in this thesis has not been previously submitted for any degree and is not currently being submitted in candidature for any other degree.

Signed.....

Candidate

The work of this thesis was carried out by the candidate.

Signed.....

Director of Studies

Signed.....

Director of Studies

Signed.....

Candidate

Several of the chapters in this thesis are based on papers that are published. A list of papers is provided in the **Publications**.

Acknowledgements

I will start with the man himself, Professor Michael C. Petty, who, along with Dr. Christopher Pearson, endured weekly meetings with me for all those years. Thank you both for your guidance, patience and brilliance. It has been a privilege to work with you and your research group.

Thanks to Chris for the good times on the AFM. I'll always remember you singing Scooby Dooby Doo to the tune of Sinatra's "Strangers in the Night" and our in-depth conversations about what was on television last night. Thank you for your help in teaching me many of the laboratory techniques I have learned at Durham and for putting up with my plethora of ridiculous questions. I would like to add that I am also very grateful for your assistance with collecting a number of images for this thesis.

Thanks to everybody else for your words of wisdom over the years. There are far too many people to name – colleagues at university and at my workplace – and to those people that became my friends. To those that were already my friends, thank you for sticking by me!

To my family, thank you for your continued words of confidence and encouragement and to Paul for your unwavering help and for keeping me sane. I should also mention our cats, who coped well with my temperamental behaviour and always managed to cheer me up. I love you all.

To anybody else I have missed, (I will no doubt remember you when this has been submitted) thank you!

We got there in the end.

Abstract

This thesis is concerned with the incorporation of a range of fluorescent ambipolar materials into Organic Light-Emitting Diodes (OLEDs) and transistors and the characterisation of their optoelectronic properties.

Initial studies focused on the incorporation of donor-acceptor compounds based on carbazole-fluorene-oxadiazole in OLEDs. Using this approach, a simple, efficient, deep-blue device was realised, with Commission Internationale de l'Eclairage, CIE (x , y) coordinates (0.16, 0.08), very close to the blue standard of (0.14, 0.08) defined by the National Television System Committee. The devices also exhibited one of the highest efficiencies reported for simple deep-blue OLEDs at 4.71%. Further experiments revealed that the efficiency was dependent on the thin film processing technique used in the device fabrication, with thermally evaporated layers of active materials showing enhanced properties, compared to spin-coated films.

The development of OLEDs incorporating structural analogues of the deep-blue emitting carbazole molecule revealed how molecular modification can be used to tune the emission colour of OLEDs, and was found to fit well with the calculated band gap for each molecule. Removing fluorene from the fluorescent materials resulted in a very deep-blue emission, with CIE (x , y) coordinates of (0.16, 0.05), but a simultaneous drop in efficiency. Therefore it was shown that carbazole, not fluorene, was responsible for the deep-blue colour observed during light emission. These experiments revealed that the combination of carbazole separated from oxadiazole (OXD) by the fluorene group is required to achieve high efficiency.

Improvement of efficiency through the chemical addition of OXD groups was also explored as an alternative approach to adding an electron transporting OXD7 layer in the

device structure. Addition of two OXD groups was found to result in a complex and more white emission.

Blending of the deep-blue emitting carbazole compound with a yellow-emitting phosphorescent iridium dye produced a single-active-layer white-emitting OLED with CIE (x , y) coordinates (0.30, 0.31), very close to the pure white point of (0.33, 0.33). The efficiency of the device was shown to improve with addition of an OXD7 layer, resulting in simple, white-emitting OLEDs, with an external quantum efficiency of 2.5%. White OLEDs were also tested based on the blending of yellow dye with a carbazole analogue consisting of chemically attached OXD groups, but the efficiency was lower at 0.42%.

Incorporation of the ambipolar donor-acceptor compounds into organic field-effect transistors (OFETs) generally resulted in electrical behaviour that was atypical of a classical transistor, and apparent ambipolar conduction was identified as an artefact due to current from the gate contact leaking to the drain. Further experiments utilised pentacene as a hole transporter to favour ambipolar conduction, but measurements confirmed that the properties of the resulting devices resembled pentacene-only OFETs.

Further study concentrated on devices based on the ambipolar polymer F8BT. The development of in-plane OLEDs was used to characterise the electroluminescent properties of the material. Several contradictions with literature reports were identified during the study of F8BT, including the correct solvent for spin-coating and the effect of annealing temperature. Notably, high temperature annealing was linked to a reduction in F8BT film crystallinity, as identified by Atomic Force Microscopy (AFM) and a resulting instability in electrical characteristics.

Blending of F8BT with an ionic liquid (IL) in a transistor structure produced a device that emitted light, although further study suggested the device in fact behaved as an OLED.

However, IL blended with F8BT was successfully used in place of calcium and PEDOT:PSS to produce functioning F8BT OLEDs.

Contents

Copyright © 2014 by Alison L. Fisher	i
Declaration	ii
Acknowledgements	iii
Abstract	iv
Contents	vii
List of Figures	xi
List of Tables.....	xxi
Symbols and Abbreviations	xxiii
1 Introduction.....	1
1.1 Aims	2
1.2 Chapter Summary	2
2 A Review of Organic Electronics	5
2.1 In this Chapter... ..	5
2.2 Introduction to Organic Electronics	5
2.3 Organic Light-Emitting Devices (OLEDs)	6
2.3.1 Theory of Operation	8
2.3.2 Colour and the CIE Diagram.....	12
2.3.3 Characterisation of Brightness and Efficiency.....	13
2.3.4 Examples of OLEDs in Literature.....	17
2.3.5 Blue OLEDs	19
2.3.6 White OLEDs.....	26
2.4 Organic Field-Effect Transistors (OFETs).....	28
2.5 Organic Light-Emitting Field-Effect Transistors (OLEFETs)	36
2.6 Conclusions	42
2.7 References	42
3 Experimental.....	53
3.1 In this Chapter... ..	53
3.2 Materials	53
3.2.1 Commercial Materials.....	53
3.2.2 Synthesised Compounds	59
3.3 Equipment and Techniques	62
3.3.1 Spin-Coating	62

3.3.2	Thermal Evaporation.....	64
3.4	Device Characterisation	66
3.4.1	Atomic Force Microscope (AFM)	66
3.4.2	Electrical Characterisation of OLEDs.....	69
3.4.3	Electrical Characterisation of OFETs	71
3.5	Device Fabrication	71
3.5.1	Standard OLEDs	71
3.5.2	F8BT:IL OLEDs	74
3.5.3	Production of Dissimilar Electrodes	75
3.5.4	F8BT:IL In-Plane OLED with Dissimilar Electrodes.....	77
3.5.5	Standard OFETs	77
3.5.6	F8BT Transistors with Top Gate (Chapter 8)	80
3.5.7	OFETs with Dissimilar Electrodes	81
3.5.8	Progression Towards Multilayer OFET Structure	82
3.5.9	Nanogap Devices	83
3.6	Conclusions	84
3.7	References	84
4	Simple OLEDs Incorporating Triad Molecules.....	86
4.1	In this Chapter... ..	86
4.2	Improvement of Device Characteristics with Carbazole.....	86
4.3	Effect of Processing Technique on Device Characteristics.....	93
4.4	Colour Tuning Study	101
4.5	Conclusions	114
4.6	References	115
5	Devices Based on Novel D-A Compounds.....	117
5.1	In this Chapter... ..	117
5.2	Compound 1A	117
5.3	Further Manipulations to Carbazole Compound 2	122
5.3.1	Compound 9	122
5.3.2	Compound 10.....	127
5.4	Conclusions	133
5.5	References	134
6	White OLEDs based on Spin-Coated Blends	135
6.1	In this Chapter... ..	135

6.2	Super Yellow	136
6.2.1	Devices Incorporating Super Yellow	136
6.2.2	OXD7 Blend with Super Yellow	140
6.2.3	Conclusions to Super Yellow	142
6.3	PO-01	143
6.3.1	Devices Incorporating the Yellow Phosphorescent Dye, PO-01	143
6.3.2	OXD7 Blend with PO-01	146
6.3.3	Conclusions to PO-01	150
6.4	Blended-layer Devices Incorporating Compound 9	151
6.4.1	Conclusions to Compound 9	154
6.5	Conclusions	154
6.6	References	155
7	Transistor Development	157
7.1	In this Chapter	157
7.2	Pentacene	157
7.3	Compound 8	161
7.4	Compound 1	162
7.5	Compound 2	165
7.6	Conclusions	176
7.7	References	178
8	F8BT OLEDs and Transistors	180
8.1	In this Chapter	180
8.2	Initial Experiments into Thin Film Processing	180
8.3	F8BT Standard OLEDs (Out-of-Plane Structure)	184
8.4	F8BT Transistors	187
8.4.1	Nanogap Contacts	192
8.5	Study into Ionic Liquid blends as a Replacement for PEDOT:PSS	195
8.5.1	Out-of-plane OLED Optimisation Study	195
8.5.2	In-plane OLED and Transistor	208
8.6	Conclusions	213
8.7	References	214
9	Conclusions & Suggestions for Further Work	217
9.1	In this Chapter	217
9.2	Summary	217

9.3	Conclusions	218
9.4	Suggestions for Further Work	222
9.5	References	223
10	Publications	225
	Appendix A Computational Study of the Triad Molecules	227
	Appendix B Photoluminescence Measurements	230
	Appendix C Pentacene OLEDs	232
	Appendix D 25 Wt% F8BT:IL Devices (Batch 3) and Annealing Temperature Study.....	237

List of Figures

2.1	Commercially available OLEDs.	7
2.2	Bonding and delocalisation in polyacetylene.	8
2.3	Simplified bonding diagram for two carbon atoms forming a π -bond.	9
2.4	Electroluminescence in a single layer OLED.	10
2.5	IV characteristics of one of the first OLEDs.	11
2.6	A CIE 1931 chromaticity diagram.	13
2.7	Schematic of possible routes of emitted light in an OLED.	17
2.8	Schematic of an OLED containing three organic layers.	18
2.9	Schematic for the various structures of an OFET.	29
2.10	Output characteristics for an OFET based on pentacene.	30
2.11	Schematic showing pinch-off and saturation in an OFET.	32
2.12	Plot of $\sqrt{ I_{DS} }$ against V_G for a pentacene OFET.	33
2.13	Transfer characteristics obtained for a pentacene OFET.	34
2.14	Schematic of an ambipolar OLEFET.	37
2.15	Structures of P13 and T5.	38
2.16	Schematic of an OLEFET based on a bilayer structure.	38
2.17	Transfer characteristics for an ambipolar OLEFET.	40

3.1	Structure of F8BT.	54
3.2	Structure of Ionic Liquid.	55
3.3	Structure of OXD7.	56
3.4	Structure of PEDOT:PSS.	56
3.5	Structure of Pentacene.	57
3.6	Structure of PO-01.	57
3.7	Structure of PMMA.	58
3.8	Structure of Super Yellow.	58
3.9	Labelled photograph of a spin-coater.	63
3.10	Schematic showing the four steps in the spin-coating process.	63
3.11	Diagram of a thermal evaporator.	65
3.12	Schematic of an AFM.	67
3.13	Photograph of the setup for electrical and photocurrent measurements of OLEDs.	69
3.14	Photodiode responsivity curve used to calculate photodiode conversion ratio.	70
3.15	Photograph of six OLEDs, one connected to a circuit.	74
3.16	Schematic of the Standard OLED structure.	74
3.17	Schematic showing the set up and evaporation path of the gold and aluminium inside the evaporator, for the production of dissimilar	76

electrodes.		
3.18	Microscope images and schematic of dissimilar electrodes on glass.	76
3.19	Schematic structure of F8BT:IL in-plane OLEDs with dissimilar electrodes.	77
3.20	Schematic of the Standard OFET structure.	77
3.21	Photograph of gate mask and source-drain mask.	79
3.22	Plan view of source and drain electrodes showing the channel dimensions.	79
3.23	Schematic of F8BT transistors with top gate structure.	80
3.24	Schematic of dissimilar electrode Compound 2 device.	81
3.25	Device schematic: Al / PMMA / Pentacene / Compound 2 / Al/Au.	82
3.26	Alternative structure with Compound 2 as top layer above dissimilar electrodes.	82
3.27	Device schematic: Al / PMMA / Pentacene / Compound 2 / OXD7 / Al/Au.	83
3.28	Schematic of the Nanogap structure.	83
4.1	Structures of compounds 1 and 2 .	87
4.2	Orbital energy level diagrams for the compounds 1a and 2a .	88
4.3	Optoelectronic properties of spin-coated devices based on 1 and 2 .	89
4.4	External quantum efficiencies of OLED devices based on spin-coated	90

compounds 1 and 2 .	
4.5 Electroluminescence spectra and CIE of devices based on spin-coated layers of 1 and 2 .	92
4.6 AFM images of spin-coated and evaporated films of 1 and 2 .	95
4.7 Comparison of the current and photocurrent versus electric field for spin-coated and evaporated devices of Compound 2 .	97
4.8 External quantum efficiencies of OLED devices based on spin-coated and evaporated layers of 1 and 2 .	98
4.9 Comparison of CIE coordinates of devices based on spin-coated and evaporated layers of 1 and 2 .	99
4.10 Stability data of OLEDs containing evaporated layers of Compound 1 and Compound 2 .	100
4.11 Molecular orbital energy diagram of HOMO and LUMO levels for compounds 2a-8 .	104
4.12 Current-voltage and photocurrent-voltage characteristics of the devices incorporating the new materials.	105
4.13 External quantum efficiency of devices incorporating materials 2-8 .	106
4.14 Electroluminescence spectra of devices incorporating materials 2-8 .	106
4.15 CIE diagram indicating the colour emission of devices 2-8 compared to standard white light.	107
4.16 Relationship between band gap, E_g and $1/CIE_y$ for OLEDs based on molecules 2-8 .	110

5.1	Molecular structure of Compound 1A and AFM image of Compound 1A evaporated film.	118
5.2	Current and photocurrent vs bias graph of a typical device with structure ITO / PEDOT:PSS / Compound 1A / Ca / Al.	119
5.3	Best efficiency graph of OLED incorporating Compound 1A .	119
5.4	Electroluminescence spectrum for a device with structure ITO / PEDOT:PSS / Compound 1A / Ca / Al.	120
5.5	CIE diagram for a device with structure ITO / PEDOT:PSS / Compound 1A / Ca / Al.	121
5.6	Molecular structure of Compound 9 and AFM scan of evaporated Compound 9 film.	123
5.7	Current and photocurrent vs bias graph of a device with structure ITO / PEDOT:PSS / Compound 9 / Ca / Al.	124
5.8	External quantum efficiency graph of a device with structure ITO / PEDOT:PSS / Compound 9 / Ca / Al.	125
5.9	Electroluminescence spectrum of a device with structure ITO / PEDOT:PSS / Compound 9 / Ca / Al.	125
5.10	CIE diagram of a device with structure ITO / PEDOT:PSS / Compound 9 / Ca / Al.	126
5.11	Structure of Compound 10 and topography of a spin-coated film of Compound 10 .	128

5.12	Current and photocurrent vs bias graph of a device with structure ITO / PEDOT:PSS / Compound 10 / Ca / Al.	129
5.13	External quantum efficiency graph of a device with structure ITO / PEDOT:PSS / Compound 10 / Ca / Al.	130
5.14	Electroluminescence spectrum of a device with structure ITO / PEDOT:PSS / Compound 10 / Ca / Al.	131
5.15	CIE diagram of a device with structure ITO / PEDOT:PSS / Compound 10 / Ca / Al.	131
6.1	Structures of Compound 2 , OXD7, Super Yellow, PO-01 and Compound 9 .	136
6.2	Normalised electroluminescence spectra for the Compound 2 devices, blended with different percentages of Super Yellow, expressed in weight ratios.	137
6.3	CIE coordinates for spin-coated devices prepared with different amounts of Compound 2 and Super Yellow.	138
6.4	Potential energy diagram indicating the HOMO and LUMO levels for the different molecules used in this work.	141
6.5	Electroluminescence spectra (not normalised) for blended-layer devices incorporating Compound 2 , Super Yellow and OXD7.	142
6.6	Normalised electroluminescence spectra for the devices prepared with different amounts of compounds 2 and PO-01.	144

6.7	CIE and electroluminescence spectra for devices prepared with different amounts of compounds 2 and PO-01.	145
6.8	Current versus bias data for PO-01: 2 OLEDs with different percentages of OXD7 in the blended film. The inset shows the external quantum efficiency variation with the weight concentration of OXD7.	146
6.9	CIE diagram showing coordinates for WOLED 2 before and after applying higher current intensities. The inset shows the normalised spectra for the devices.	148
6.10	Photographs of the light output of the reference blue and yellow devices and WOLED 2.	150
6.11	CIE coordinates for devices prepared with different amounts of Compound 9 and Super Yellow and Compound 9 and PO-01.	151
7.1	Output characteristics for a pentacene OFET with channel dimensions $L = 200 \mu\text{m}$ and $W = 4000 \mu\text{m}$.	158
7.2	Transfer characteristics for a pentacene OFET with channel dimensions $L = 200 \mu\text{m}$ and $W = 4000 \mu\text{m}$.	159
7.3	Graph of $\sqrt{ I_{\text{DS}} }$ vs V_{G} for a pentacene OFET with channel dimensions $L = 200 \mu\text{m}$ and $W = 4000 \mu\text{m}$.	160
7.4	Output characteristics measured for OFETs based on Compound 8 .	161
7.5	Output characteristics obtained from a $L = 50 \mu\text{m}$ and $W = 4000 \mu\text{m}$ Compound 1 device.	163

7.6	Transfer characteristics of transistor from Batch 2 with channel dimensions $L = 50 \mu\text{m}$ and $W = 4000 \mu\text{m}$.	163
7.7	AFM image of Compound 1 film.	164
7.8	Microscope images, AFM line scan and schematic of gold and aluminium dissimilar electrodes.	166
7.9	Output and transfer characteristics of a device with structure Al / PMMA / Compound 2 / Al/Au.	167
7.10	Schematic structure of a multilayer OLET.	168
7.11	Device configuration incorporating pentacene as hole transport layer.	169
7.12	Output and transfer characteristics from a repeated set of devices with Compound 2 and without Compound 2 .	170
7.13	Structure of Compound 2 device with Compound 2 as the top layer.	171
7.14	Output and transfer characteristics of a device with Compound 2 deposited on top, and of a pentacene-only device.	172
7.15	Stack including both hole and electron transporting materials.	174
7.16	Output and transfer characteristics of a device incorporating both pentacene and OXD7, and of a pentacene-only device.	176
8.1	Molecular structure of F8BT.	181
8.2	F8BT device surface appearance under microscope with electrode for scale.	183

8.3	Electrical characteristics of standard F8BT OLEDs.	185
8.4	External quantum efficiency data of standard F8BT OLEDs.	186
8.5	Electroluminescence spectra of standard F8BT OLEDs.	186
8.6	CIE coordinates of standard F8BT OLEDs.	187
8.7	Output and transfer characteristics for an F8BT device with channel dimensions $L = 200 \mu\text{m}$ and $W = 4000 \mu\text{m}$.	188
8.8	Plot of $\sqrt{ I_{\text{DS}} }$ vs V_{G} for the F8BT device with channel dimensions $L = 200 \mu\text{m}$ and $W = 4000 \mu\text{m}$.	189
8.9	Photographs taken through a microscope of an F8BT device switched on and then off.	190
8.10	Output graph from an F8BT device showing leakage and no field-effect.	190
8.11	Electroluminescence spectra and CIE diagram of the light emitted by the F8BT transistor devices.	191
8.12	Nanogap contacts as imaged by AFM and averaged cross section.	193
8.13	AFM image and averaged cross section confirming that F8BT was present in the nanogap.	194
8.14	Current and photocurrent vs bias graph of best devices from Batch 1.	197
8.15	External quantum efficiency graph of Batch 1 Substrates 3 and 4.	198
8.16	Electroluminescence data of Batch 1 Substrates 3 and 4.	199
8.17	CIE coordinates of Batch 1 Substrates 3 and 4.	200
8.18	Electrical characteristics of the best devices on Substrates 1-3 and	203

Substrates 4-6.		
8.19	Electroluminescence graphs of Substrate 4 and Substrate 5, both at 20 mA.	204
8.20	CIE diagram of Substrate 4 and Substrate 5 showing coordinates with current of 20 mA.	205
8.21	Current and photocurrent vs bias data for in-plane OLED containing F8BT:IL (5 wt%).	209
8.22	Photograph of an F8BT:IL transistor device emitting light.	210
8.23	Output and transfer characteristics for a device with dimensions $L = 50 \mu\text{m}$ and $W = 2000 \mu\text{m}$.	212

List of Tables

2.1	CIE coordinates for the NTSC standard.	19
2.2	Device structures and electroluminescent performances based on non-doped blue fluorescent emitters.	22
2.3	Advantageous properties of the proposed molecular units incorporated into various OLED molecules.	26
3.1	List to identify synthesised compounds used throughout this study.	60
3.2	Evaporation conditions for each synthesised compound.	72
3.3	Channel dimensions of the 16 devices that can be produced using the shadow masks.	80
4.1	Comparison of results for 1 and 2 with spin-coated and evaporated layers.	94
4.2	Structures of compounds 3-8 .	102
4.3	Electroluminescence data for OLEDs based on compounds 2-8 .	107
4.4	AFM images for films of each compound in the series of compounds 2-8 .	111
5.1	Comparison of key optical and electrical properties for pure Compound 2 devices with OXD7 blended devices and chemical attachment of OXD groups.	133

6.1	Optoelectronic properties of ITO / PEDOT:PSS / 2 :Super Yellow / Ca / Al devices with different concentrations of Super Yellow.	139
6.2	Optoelectronic properties of ITO / PEDOT:PSS / 2 :PO-01:OXD7 / Ca / Al OLEDs for different concentrations of PO-01 and OXD7 molecules. WOLED 3 is prepared using a cathode of CsF/Al.	149
6.3	Optoelectronic properties of ITO / PEDOT:PSS / Compound 9 :Super Yellow / Ca / Al devices with different concentrations of Super Yellow.	152
6.4	Optoelectronic properties of ITO / PEDOT:PSS / Compound 9 :PO-01 / Ca / Al devices with different concentrations of PO-01.	152
8.1	Summary of F8BT solutions, film qualities and film thicknesses.	181
8.2	Device configurations for substrates in Batch 1.	196
8.3	AFM images and thicknesses of films of F8BT:IL (5 wt%) and F8BT.	201
8.4	Summary of the substrates in Batch 2 with device configuration and annealing temperatures.	202
8.5	AFM images of each substrate in Batch 2.	207
8.6	Microscope images and descriptions of light from a device with dissimilar electrodes. Channel dimensions $L = 200 \mu\text{m}$ and $W = 4000 \mu\text{m}$.	211

Symbols and Abbreviations

A	Amp or Active area
AFM	Atomic Force Microscope
c	Speed of light in a vacuum ($299\,792\,458\text{ m s}^{-1}$)
cd	Candela
C_i	Capacitance per unit area of insulator
CIE	Commission Internationale de l'Eclairage
d	Thickness of the spun film
e	Charge on an electron (1.602×10^{-19} Coulombs)
E	Energy
E_g	Band gap
EL	Electroluminescence
EML	Emissive Layer
EQE	External quantum efficiency
ETL	Electron Transport Layer
eV	Electron volt
FET	Field-Effect Transistor
h	Planck's Constant ($6.62606957 \times 10^{-34}$ J s)
HOMO	Highest Occupied Molecular Orbital

HTL	Hole Transport Layer
Hz	Hertz
I	Current
I_{DS}	Drain-source current
J	Current Density
J_{ph}	Photocurrent per unit area
L	Channel length or Luminance
LCD	Liquid Crystal Display
LED	Light-Emitting Diode
lm	Lumen
LUMO	Lowest Unoccupied Molecular Orbital
m	Metre
mm	Millimetre
mA	Milliamp
mV	Millivolt
MW	Molecular Weight
n_e	Number of electrons injected per second
n_p	Number of photons emitted per second
nm	Nanometre

OLED	Organic Light-Emitting Device
OLEFET	Organic Light-Emitting Field-Effect Transistor
OFET	Organic Field-Effect Transistor
OPVs	Organic Photovoltaics
PL	Photoluminescence
R_a	Arithmetic mean roughness
rpm	Revolutions per minute
s	Seconds
sr	Stearadian
t	Spinning time
TFT	Thin Film Transistor
UV	Ultraviolet
V	Volts / Voltage
V_{DS}	Drain-source Voltage
V_G	Gate Voltage
V_T	Threshold Voltage
W	Channel width or Watts
WOLED	White Organic Light-Emitting Device
$^{\circ}\text{C}$	Degrees Celsius

η	Viscosity coefficient of the solution
η_l	Luminous efficiency
η_p	Luminous power efficiency (luminosity)
λ	Wavelength
μ	Charge carrier mobility
μl	Microlitre
μm	Micrometre
ν	Frequency
ρ	Density of the spinning solution
ω	Angular velocity of the spinning
$\Omega \text{ sq}^{-1}$	Ohms per square

1 Introduction

In recent years display technology based on organic electronics has continued to receive increasing research interest. Now, the field has moved on to a recognised, marketable technology, seeing use in consumer products such as mobile phones, MP3 players and portable game consoles. Organic materials are attractive as rivals to existing Liquid Crystal Display (LCD) and plasma display technology in the form of Organic Light-Emitting Devices (OLEDs) and Organic Field-Effect Transistors (OFETs). Due to their unique properties, organic materials are also predicted to be applied to niche areas and therefore to complement existing technology.

In spite of the significant leaps in the use of organic electronic materials, important areas still require development. Efficient, blue-emitting OLEDs remain an area of active research, especially in terms of application to television displays. White-emitting OLEDs are also receiving extensive interest as candidates in lighting applications as they offer a 'true' white light compared to the 'cold' white produced by existing fluorescent lighting. Interest in ambipolar organic materials (i.e. molecules capable of conducting both holes and electrons) also promises to improve further important device properties of OLEDs, including brightness and efficiency.

Further improvements to OFETs are also required to move on from prototype flexible displays to the realisation of mass market versions. In addition, research into ambipolar materials has fuelled the development of the organic light-emitting field-effect transistor (OLEFET), an entirely new electronic device incorporating the electronic properties of an OFET with the light emission of an OLED. Improvements in this area offer the exciting possibility of a complete display based on only one type of component.

1.1 Aims

The purpose of this thesis is to explore a novel set of organic electroluminescent compounds and their incorporation into OLEDs and OFETs.

Highly efficient deep blue OLEDs are developed and their properties optimised by considering two different processing techniques. The emission colour is tuned from deep blue to white by chemically altering the structure of the compounds used and by blending the compounds with other materials.

A number of these materials are incorporated into OFETs along with pentacene and the well-known polymer poly(9,9-di-*n*-octylfluorene-*alt*-benzothiadiazole) (F8BT) to investigate their potential as light-emitting transistors.

1.2 Chapter Summary

2. *A Review of Organic Electronics*: This chapter covers literature, device theory and progression, as well as the latest technological advances in the field of organic electronics.

3. *Experimental*: This chapter begins with a description of the materials used to fabricate devices in this project. As well as standard commercial materials, Katharine Linton, a PhD student in the Bryce group at the Department of Chemistry, Durham University synthesised some compounds specifically for use in this project. From here, the chapter moves on to discuss laboratory methods of depositing these materials and why certain methods were chosen over other options. Finally, details of how each type of device mentioned in this thesis was fabricated are listed clearly in their own separate sections with detailed instructions for each step in the process.

4. *Simple OLEDs Incorporating Triad Molecules*: The effect of introducing a carbazole moiety into a previously reported ambipolar triad molecule was investigated and the new

molecular structure incorporated into a simple OLED device architecture. The influence of the molecular change was studied by measuring fundamental properties of the OLED – emission colour, brightness, power efficiency, current efficiency and external quantum efficiency. In addition, a series of analogous carbazole-containing triad molecules was studied to show how chemical changes could enable tuning of the emission colour in OLEDs.

5. Devices Based on Novel D-A Compounds: This short chapter contains a number of proof of concept experiments involving the incorporation of new molecules into OLEDs, focusing on analogues of the triad molecules reported in Chapter 4. One analogue was prepared via a simpler and faster synthetic route and was therefore studied with a view to using it as a replacement for the original compound. Two further analogues experimented with the addition of oxadiazole (OXD) groups to the structure, with an aim to improve the efficiency of the OLED without the need for additional layers within the device structure. These experiments have their own conclusions and do not need any further investigation at present or for this thesis.

6. White OLEDs Based on Spin-Coated Blends: The majority of this work was carried out in collaboration with a visiting student on a summer placement, Cristina Roldan-Carmona, over who I had a supervisory role. With a triad molecule in Chapter 4 producing efficient deep blue OLEDs, a further study was undertaken to assess whether this material could be combined with a yellow emitter, and create white light. The idea was that if the yellow emitters, Super Yellow and the dye Iridium(III)bis(4-phenylthieno[3,2-c]pyridinato-N,C2')acetylacetonate (PO-01), were combined with the triad molecule in the correct proportions, white light emission in a simple device architecture would be possible. A further part of the study looked at improving the efficiency of the fabricated white OLEDs (WOLEDs) by blending with the electron transport compound OXD7. Finally, the effect of

the chemical attachment of OXD7 (Compound **9**, as seen in Chapter 5) was considered as an alternative for improving the efficiency of WOLEDs.

7. Transistor Development: Initial studies were carried out on a simple pentacene transistor to provide a proof of concept for the further development of transistors based on three novel materials, synthesised by the Bryce group in the Department of Chemistry at Durham University.

8. F8BT OLEDs and Transistors: This chapter begins with the description of some initial experimentation on the light-emitting polymer F8BT, which has been previously incorporated in OLEFETs. The testing of different solvents and electrical measurements on OLED and OLEFET devices is included and some success with light output from the OLEFETs is reported. The chapter then moves on to discuss alternative device configurations, using nanogap contacts as well as experimenting with ionic liquid blends as a replacement for the hole injector, PEDOT:PSS.

9. Conclusions and Suggestions for Further Work: This chapter gives a summary and findings of the thesis as well as ideas for further work to develop the research in the future.

2 A Review of Organic Electronics

2.1 In this Chapter...

This chapter covers literature, device theory and progression, as well as the latest technological advances in the field of organic electronics.

2.2 Introduction to Organic Electronics

Organic Electronics is a broad field ranging from molecular scale electronics incorporating individual molecules to large-area devices where the active component is an organic material. Large-area organic electronic devices are receiving increasing interest and are already beginning to emerge as rivals to traditional inorganic materials. Their key advantage is in the cost of manufacture – high quality thin films of an organic material can be deposited from dilute solutions by spin-coating. This is significantly cheaper than the methods used to obtain inorganic devices, which usually involve high temperature processing. Owing to their inexpensive construction, organic electronic devices are very attractive for large-area applications.¹ Furthermore, the mechanical flexibility observed in organic devices offers an entirely new range of thin film technologies including e-paper and flexible/foldable displays.

Research into large-area organic electronics covers a broad range of devices such as organic photovoltaics (OPVs), organic field-effect transistors (OFETs) and organic light-emitting devices (OLEDs), which also include organic light-emitting field-effect transistors (OLEFETs). One of the greatest areas of growth for organic electronics is in display and lighting applications, and as such the main focus of this study is OLEDs, OFETs and OLEFETs.

2.3 Organic Light-Emitting Devices (OLEDs)

OLEDs are becoming well established in the display and lighting industries and at present there is much ongoing research and development into the technologies.²⁻⁷ OLEDs can be produced on a diverse range of substrates, such as glass, plastics and metals. Commercial examples of OLEDs in display technology are prominent in certain mobile phones, MP3 players, car audio systems, laptop displays, portable games consoles, such as the Sony PS Vita, televisions and there are even prototype car dashboard displays. Displays based on OLEDs are sometimes combined with FETs in active matrix OLEDs (AMOLEDs). Some devices have been implemented incorporating OFETs in the design, allowing for the realisation of mechanically flexible display components based wholly on organic electronics. Flexible display technology has developed from the early device demonstrated by Sony in 2003 (Figure 2.1 (a)) to incorporate more colours (Toshiba 2007, Figure 2.1 (b)) to the most recent application in curved mobile phones by Samsung (Figure 2.1 (c)).

Competing display technologies include liquid crystal displays (LCDs) and plasma flat panel displays. LCDs use a white light source, polarising filters and colour filters to generate an image. As such, LCDs always require a backlight and never reproduce a true black colour. Another well-known problem with this technology is the relatively narrow viewing angle. OLEDs, in contrast, are self-emissive devices, removing the need for a backlight⁸ and are known to give high quality images, coupled with a wide viewing angle. In plasma displays, each pixel is an individual plasma cell that emits light. The quality of the picture is similar to that of an OLED display, but they are inefficient in comparison and are usually bulkier due to the gas chambers inside the unit. Due to their light weight, low operating voltages and power consumption, OLEDs are inherently more portable, with the added advantage of being more durable and easier to make flexible and transparent. Furthermore, OLEDs can switch on in less than 1 μs , allowing for the design of high resolution displays with super-fast pixel changes.

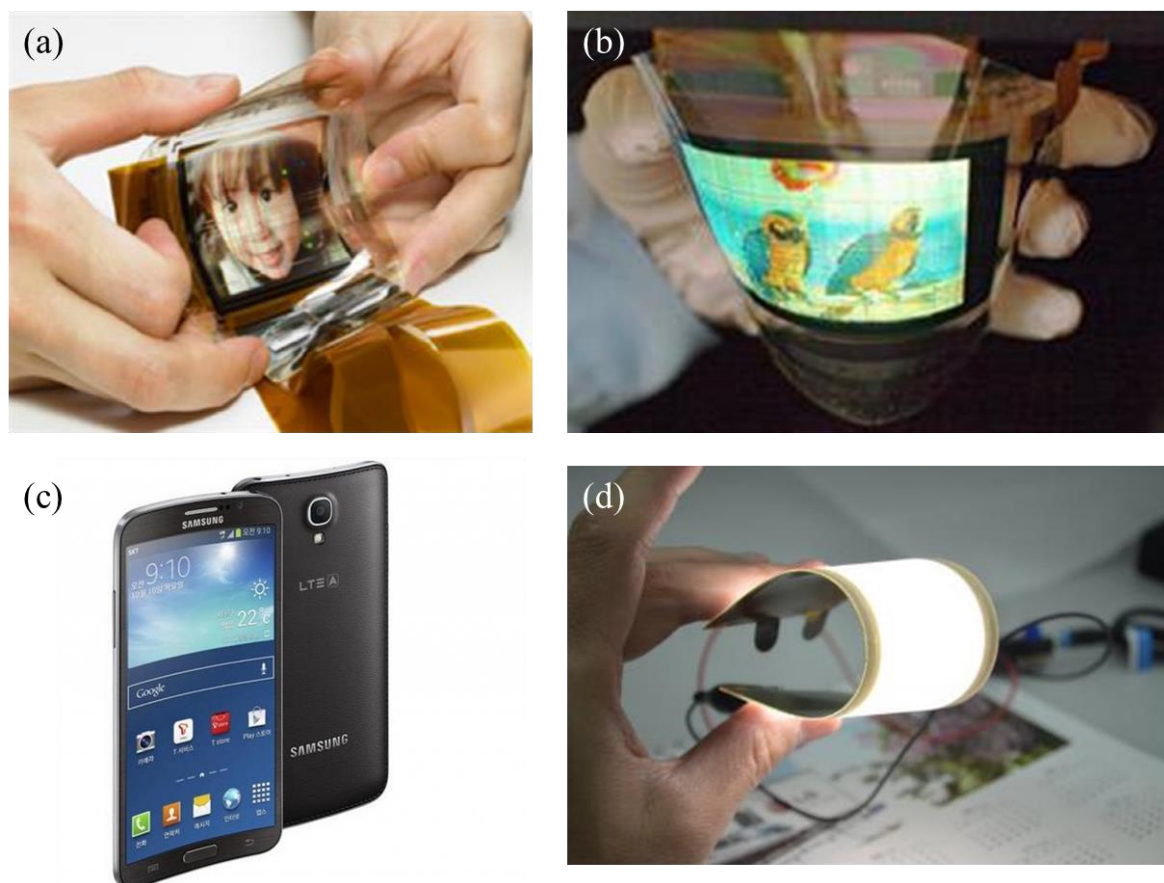


Figure 2.1: (a) A thin, flexible 2.5" display constructed from OLEDs and OFETs manufactured by Sony in 2007.⁹ (b) Toshiba's ultra-thin (0.1 mm), flexible 3" OLED display prototype from 2011.¹⁰ (c) World's first curved display smartphone, the Samsung Galaxy Round with a 5.7" screen¹¹ available 10th October 2013. (d) LG Chem's flexible 210 x 50 mm lighting panel with a power efficiency of 55 lm W⁻¹ available end of 2013.¹²

OLEDs are also being explored as alternatives to incandescent light sources as well as fluorescent tubes (which require toxic materials) due to their improving power efficiency and brightness. For example, white OLEDs with 90 lm W⁻¹ efficiency have recently been developed,^{13, 14} which outperform incandescent (20 lm W⁻¹) and fluorescent (70 lm W⁻¹) light sources,¹⁵ and approach the 150 lm W⁻¹ efficiency typically reported for inorganic LEDs.⁷ OLED lighting is already on the market, although still relatively expensive due to its status as an emerging technology. Available at companies such as Philips, Novaled, Blackbody and LG Chem (Figure 2.1(d)), these OLEDs offer a diffuse light source that is complementary to the LED point sources that are currently available.⁸

There are many good reasons for further development of OLEDs as a technology, some of which have already been described. In addition to these, OLEDs are novel due to the potential to create devices with chemically and electrically tuned colour properties.

2.3.1 Theory of Operation

OLEDs are in principle a Light-Emitting Diode (LED) based on an organic material, and, in the same sense, are two-terminal devices. The emission of light observed in OLEDs is due to electroluminescence in the organic layer(s), which occurs when an electric current passes through the material. The process is best explained by first considering the structure of the organic material in terms of its energy levels.

OLEDs contain conjugated organic molecules, varying from small molecules through oligomers to polymers, that consist of alternating single and double bonds. An example of this type of molecule is shown below in Figure 2.2.

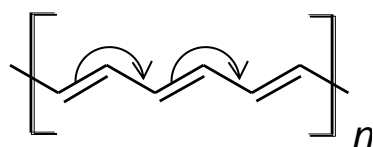


Figure 2.2: Polyacetylene – an example of a molecule with alternating single and double bonds. Arrows show delocalisation of electrons.

When two atoms form a double bond (π -bond) their atomic orbitals combine to form σ and π -molecular orbitals. In terms of the semiconducting phenomena and electroluminescence observed in some organic molecules, the π -molecular orbitals are the most important. As shown in Figure 2.3, two sets of π -molecular orbitals contribute to a double bond: a bonding orbital (π) and anti-bonding orbital (π^*). The orbitals represent the different energy states available to electrons in the double bond, where the bonding orbital is lower

in energy than the anti-bonding orbital. At the ground state of a molecule, electrons only occupy the π -orbital and hence it is referred to as the Highest Occupied Molecular Orbital (HOMO). The π^* -orbital is referred to as the Lowest Unoccupied Molecular Orbital (LUMO). As these organic molecules are conjugated, the electron density of each double bond is delocalised throughout and so this description of bonding can be considered to represent the available energy levels over the entire structure. For this reason, the HOMO can be referred to as the valence band and the LUMO as the conduction band, analogous to the naming of bands in solid state semiconductors. The energy difference between these bands is known as the band gap (E_g).

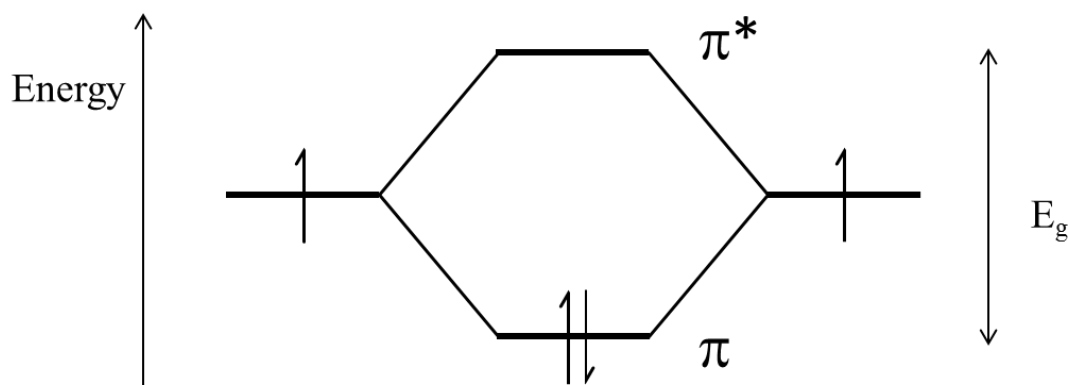


Figure 2.3: Simplified bonding diagram for two carbon atoms forming a π -bond.

Most OLEDs are based on at least one layer of organic material sandwiched between two electrodes possessing different work functions. The cathode is typically a low work function metal such as aluminium and the anode a transparent, high work function material such as indium tin oxide (ITO).¹ Under forward bias, electrons are injected into the LUMO of the organic layer(s) from the low work function cathode and positive holes into the HOMO from the high work function anode. The two charge carriers move across the organic material towards the electrode of opposite polarity due to the presence of the electric field. As the electrons and holes travel in opposite directions across the organic material there is a possibility that they will collide, resulting in an exciton, which is an

electron-hole pair. If hole and electron injection is not balanced, the minority carrier limits the overall performance of the device. The exciton may move through the organic layer as a single ‘particle’ before finally relaxing. Relaxation of the exciton occurs when the electron in the LUMO loses energy so that it combines with the hole in the HOMO. For the electron to lose sufficient energy it emits a photon of light. The energy, and thus colour, of the emitted photon depends upon the band gap between the HOMO and LUMO and so different materials can emit light of different colour. Red emission requires a relatively small energy gap compared to the large gap required for blue devices.

A diagram of electroluminescence in a simple OLED containing one layer of organic material is depicted in Figure 2.4. In this example the organic (active) layer both conducts electrical current and emits light.

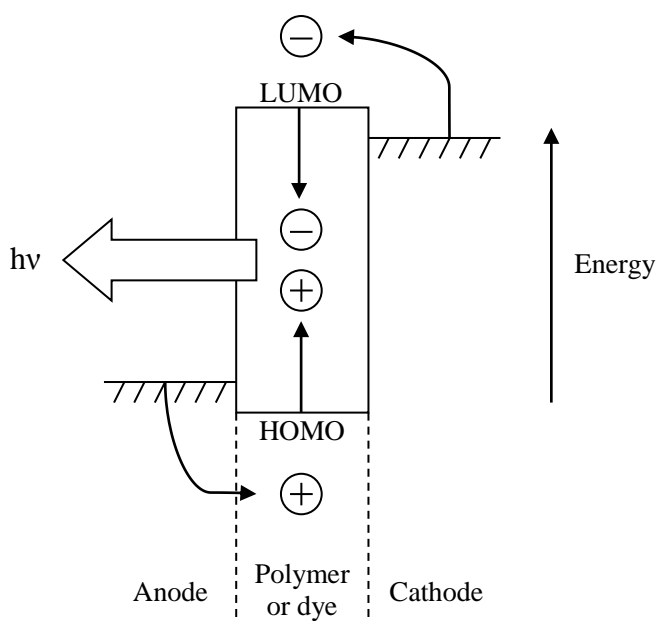


Figure 2.4: Electroluminescence in a single layer OLED. The negative electron and positive hole recombine to emit light of energy $h\nu$. (Reproduced from ¹⁶.)

An alternative configuration is the dye-host system where the active layer is a host matrix doped with luminescent or phosphorescent dye molecules. The host serves to conduct the

electrical current and is where excitons are generated. These excitons then transfer to the dye where they recombine, emitting light.

It is worth pointing out that OLEDs only readily conduct under forward bias. If the polarity of the electrodes is reversed, much higher voltages must be applied to achieve current flow and the device undergoes limited electroluminescence. OLEDs therefore behave as rectifiers and exhibit diode-like current-voltage (IV) characteristics (Figure 2.5).

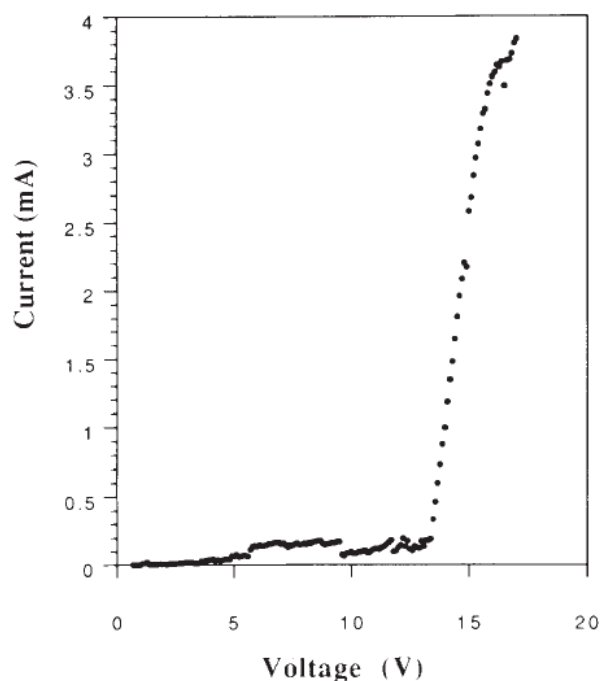


Figure 2.5: Forward bias IV characteristics of a PPV OLED reported by Burroughes et al.¹⁷ This was one of the first OLEDs to attract major attention and subsequent OLEDs show similar diode-like properties.

The turn-on voltage occurs at the sharp change in gradient of the IV curve. This is the voltage applied that causes a rapid increase in current and the point above which EL occurs. Further increases in voltage generate a rapid increase in both current and the intensity of light emitted. The small increase in current prior to the turn-on voltage is due to insufficient electric field strength to overcome the barriers to charge injection into the HOMO and LUMO.

2.3.2 Colour and the CIE Diagram

The usual method for representing the colour output of an OLED is to compare it to a Commission Internationale de l'Eclairage (CIE) 1931 chromaticity diagram.¹⁸ A CIE diagram (Figure 2.6) accounts for the properties of colour perceivable by humans: hue, saturation and brightness. Whilst individual wavelengths in the visible spectrum are related to individual colours, combinations of different wavelengths can lead to the same perception of colour. The outer edges of the CIE diagram represent the limit of human colour perception, and the fully saturated spectral colours (i.e. containing no white light) make up the horseshoe shaped boundary. The straight line boundary between blue and red are colours that cannot be produced by individual wavelengths of light. Any point within the diagram shows a unique and perceivable colour hue, but equally any hue may be produced by a combination of different colours.

The colour of light is plotted on the CIE diagram as a function of the two colour coordinates x and y , which map the colour in relation to hue and saturation. The value of the x and y coordinates are determined from the spectral power density of light measured with a spectrophotometer after factoring with sensitivity curves determined for the average human eye. In this way, the emission of light from an OLED consisting of a range of different wavelengths at different intensities is simplified into two coordinates relevant to the perception of colour, allowing for effective and quantitative comparisons of colour emission. OLEDs of different colours have been designed although many show the common problem of broad emission, so the colours produced possess low colour purity.¹⁶

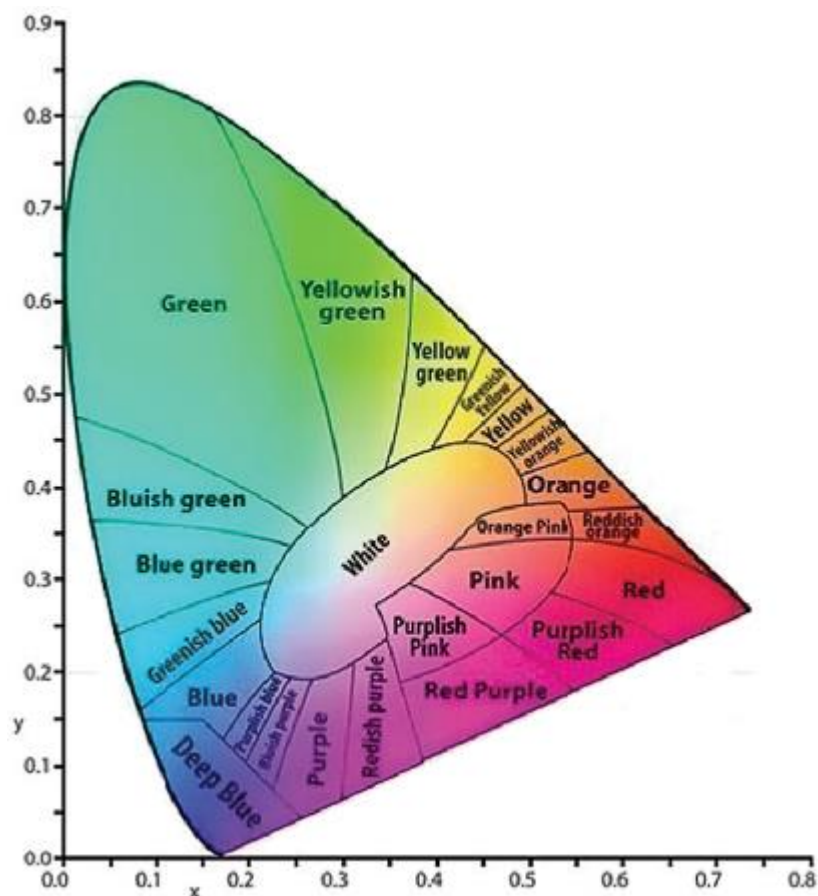


Figure 2.6: A CIE 1931 chromaticity diagram.¹⁹

2.3.3 Characterisation of Brightness and Efficiency

A variety of units characterise the light emission of OLEDs, broadly grouped under radiometry and photometry. Radiometry is the measure of optical radiation, which encompasses the ultraviolet, visible and infrared regions of the electromagnetic spectrum, i.e. light ranging in wavelength from 0.01 to 1000 μm and frequency 3×10^{11} - 3×10^{16} Hz. The power of light emission, i.e. rate of energy emission (radiant flux), is measured in watts. Photometry is effectively radiometry limited to wavelengths of light visible to humans, covering the range 380-780 nm. Photometric units are therefore more often used to characterise the efficiency of OLEDs. In photometry the rate of energy emission is the luminous flux emitted from a point source, expressed in lumens (lm). The luminous flux

emitted into a unit solid angle in space (known as a steradian, sr) is the luminous intensity, (lm sr^{-1}), which is measured in candelas (cd). As there are 4π sr in a sphere, a point source emitting 1 cd in all directions produces a luminous flux of 4π lm. It is common to consider the luminance, or brightness, of an OLED, which is the amount of light emitted per unit area of the surface, expressed in cd m^{-2} .

OLEDs emit light in all directions. However, as a display device, only the light emitted from the outer surface in the viewing direction is of use and several methods are used to characterise the efficiency. Luminous efficiency, η_l measured in cd A^{-1} , shows the amount of visible light output per amp applied to a device and is calculated by considering the luminance, L and active area, A of the device at a sample current, I_s , as in Equation 2.1:

$$\eta_l = \frac{AL}{I_s} \quad (2.1)$$

Luminous power efficiency, or luminosity, η_p compares the luminous power emitted (in lm) to the electrical power required to drive the OLED at a particular voltage, V . Luminous power efficiency is therefore expressed in lm W^{-1} and is calculated from the luminance using Equation 2.2:

$$\eta_p = \frac{AL\pi}{I_s V} \quad (2.2)$$

External quantum efficiency, EQE, is commonly used to compare the efficiencies of different OLEDs by measuring the ratio between the total number of photons emitted per second, n_p out of the device in the viewing direction to the number of electrons injected per second, n_e , as shown in Equation 2.3:

$$\text{EQE} = \frac{n_p}{n_e} \quad (2.3)$$

n_e is calculated using the current applied to a functioning OLED and the charge on an electron, e , (Equation 2.4) and n_p is the ratio of radiant power to photon energy, E (Equation 2.5).

$$n_e = \frac{I_s}{e} \quad (2.4)$$

$$n_p = \frac{\text{Radiant Power}}{E} \quad (2.5)$$

where the energy of the photon, E , is determined using Planck's constant, h , the speed of light in a vacuum, c and wavelength, λ :

$$E = \frac{hc}{\lambda} \quad (2.6)$$

Radiant power is determined experimentally by measuring the light output in the viewing direction as a photocurrent, I_p , using a photodiode, and correcting for the photodiode conversion ratio, R , as in Equation 2.7. The ratio is determined by considering typical performance curves for the photodiode to obtain a value of its responsivity to different wavelengths in A W^{-1} .²⁰

$$\text{Radiant Power} = \frac{I_p}{R} \quad (2.7)$$

Combining Equations 2.6 and 2.7 into Equation 2.5 gives:

$$n_p = \frac{I_p \lambda}{Rhc} \quad (2.8)$$

allowing the external quantum efficiency (Equation 2.3) to be written as:

$$\text{EQE} = \frac{I_p \lambda e}{I_s R h c} \quad (2.9)$$

The external quantum efficiency of OLEDs depends on a number of factors, including the relative energy levels of different compounds within the structure, which determines the efficiency of electron and hole injection and subsequent recombination. In addition, as external quantum efficiency considers light output only in the viewing direction, it can be improved by increasing the outcoupling of light from the OLED. The internal quantum efficiency accounts for the number of photons emitted in all directions from an OLED and is therefore larger than the external quantum efficiency as only a fraction of the light produced emits in the viewing direction.

Outcoupling refers to light produced by an OLED that passes through each of the layers comprising the device to emit in the viewing direction. In a standard OLED structure, the individual layers all possess different refractive indices and a significant proportion of the generated light is lost due to total internal reflection as a result of light arriving at each layer with an angle greater than the critical angle, as shown schematically in Figure 2.7. This leads to reabsorption in either the organic layer or by the electrode due to plasmonic effects. Alternatively, the reflected light may be waveguided at the interfaces of the different layers and emerge out of the edges of the device, not in the viewing direction.

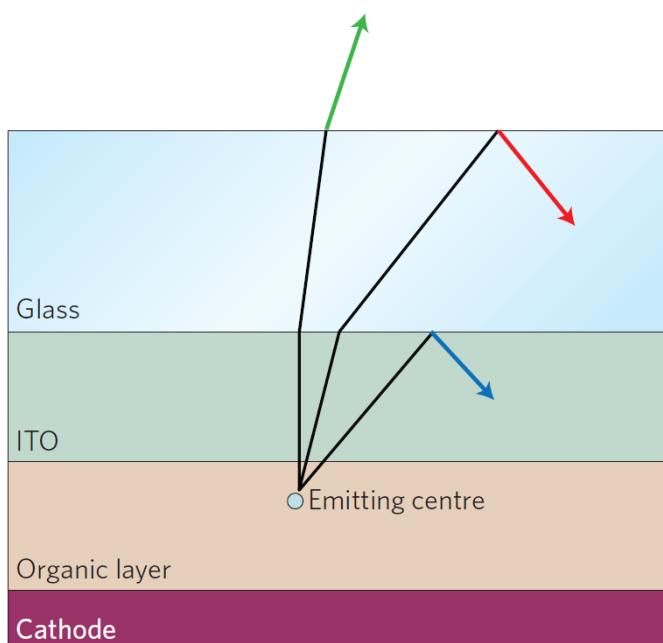


Figure 2.7: Schematic of possible routes of light in an OLED. The green arrow shows outcoupled light, the red arrow shows total internal reflection in the substrate and the blue arrow shows reflection in the anode.²¹

Outcoupling and, therefore, external quantum efficiency in OLEDs has been improved by adding microlenses to the substrate²² and embedding grids in the organic layer.²³

2.3.4 Examples of OLEDs in Literature

Early OLEDs as described in Figure 2.4 consisted of a single organic layer between two electrodes, but showed very poor efficiencies and required relatively large voltages to operate. Several early examples were in fact virtually ignored until Burroughes et al¹⁷ reported an OLED based on poly(*p*-phenylenevinylene) (PPV) with efficiencies up to 0.05%. The key problem with single layer OLEDs was selecting an organic material with both HOMO and LUMO energy levels similar to the work functions of the anode and cathode, respectively. Thus, the injection of holes and electrons was limited by the energy difference between each electrode and the corresponding molecular orbital. Later bilayer devices^{24, 25} did much to solve this problem by incorporating an electron transport layer

(ETL) with a LUMO of similar energy to the work function of the cathode or a hole transport layer (HTL) with a HOMO matched to the work function of the anode. This modification allowed for a more balanced injection of holes and electrons, and for the device to function at lower operating voltages (the turn-on voltage was effectively reduced). A further advantage of the new design was that recombination and light emission occurred at the interface of the two layers, away from the electrodes where quenching occurred. The bilayer devices show much higher efficiency when compared to single layer OLEDs. Further improvements in efficiency were observed for OLEDs consisting of three layers,^{26, 27} the central layer serving as a recombination zone. A schematic of a three layer OLED is included in Figure 2.8.

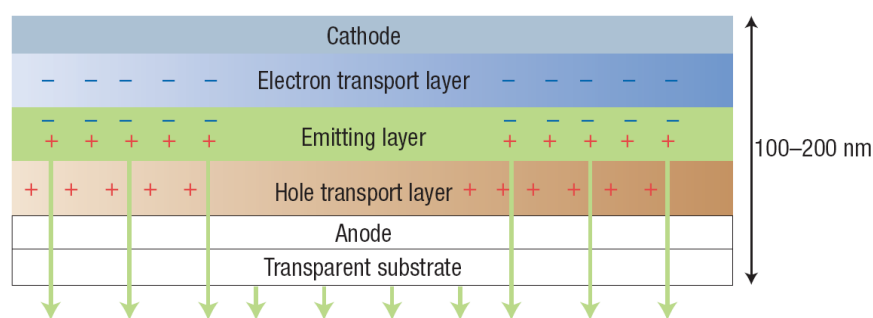


Figure 2.8: An OLED containing three organic layers. The blue ‘negatives’ represent electrons and the red ‘positives’ holes.²⁸

In 1987, Tang and Van Slyke at Kodak reported a working two-layer OLED fabricated by vapour deposition, with efficient (EQE of 1%) green, low-voltage electroluminescence, with only 5.5 V required to drive the device. The best at the time required near 30 V to drive the device and gave an EQE of 0.05%. Others required high voltages of around 100 V.²⁹ From this point onwards, interest in the field has grown year on year and improvements to devices are still continuing. Additional improvements in device performance have been achieved through the addition of hole injection layers such as PEDOT:PSS,³⁰ and electron injection layers such as CsF³¹ to the anode and cathode, respectively.

2.3.5 Blue OLEDs

An area of particularly intense research is blue OLEDs. For realisable OLED displays, devices must be produced that meet the National Television System Committee (NTSC) standard for blue light, i.e. the CIE coordinates of any OLED emission must be (0.14, 0.08). Highly efficient red and green devices that match the NTSC standards set out in Table 2.1 are already available but blue,^{19, 32} specifically deep blue, OLEDs remain a challenge, as blue light is inherently higher energy.

Table 2.1: CIE (x , y) coordinates for the NTSC standard.³³

Colour	Coordinates
Red	(0.67, 0.33)
Green	(0.21, 0.71)
Blue	(0.14, 0.08)

To achieve blue emission, molecules require a wide band gap, which in turn makes it difficult to match the HOMO and LUMO levels to either the electrode work functions or the energy levels in ETLs and HTLs. This energy mismatch causes an imbalance between the injection of holes and electrons in the structure, creating problems with device stability and efficiency. As a result, there are few deep blue devices that give external quantum efficiencies of greater than 1%,^{34, 35} so there is still much scope for improvement in blue OLEDs.

There are a number of potential blue OLED materials in the literature that exhibit higher efficiency, though these are often organometallic complexes. For example Sasabe et al reported a blue OLED with an EQE of 18.6% based on an iridium carbene complex.³⁶ These complexes have the advantage of potentially exploiting phosphorescence with the desired narrow emission spectrum but there is still an incentive to work with fluorescent

small molecules and polymers due to their ability to be incorporated into simple device structures. Organometallic complexes are difficult to modify structurally compared to fluorescent molecules and typically must be blended with an additional host material to prevent concentration quenching of the phosphorescence. The host material adds a further complexity to the OLED structure and if the triplet energy of the host is lower than that of the emitter, phosphorescence is reduced due to energy transfer from the excited emitter to the host, which is a particular challenge in blue OLEDs.³⁷ In addition, it has been suggested that the efficiency limits given previously for fluorescent devices may be exceeded due to the possibility that the percentage of singlet excitons may be greater than the originally predicted 25%.

It should be noted that a blue OLED with 30% external quantum efficiency has recently reported to have been produced at Dankook University. This device used the organometallic, phosphorescent emitter FIrpic with a new high triplet energy host material based on a pyridoindole derivative.³⁸ The device structure was also complex, consisting of eight individual layers, including additional hole and electron injecting materials.

There are a number of different moieties that are known to give blue fluorescent OLEDs when included in the molecular structure, such as carbazole,³⁹ arylamine, anthracene⁴⁰ and fluorene.⁴¹ Interest in fluorene polymers for blue OLEDs goes back as far as 1998.⁴²

Table 2.2 summarises the characteristics of a variety of blue fluorescent OLEDs along with their device architecture, as reported in the literature. Further details regarding the molecular structure of the emissive layer can be found in each reference.

It can be seen from Table 2.2 that the best fluorescent deep blue emitter available in the literature is reported by Kim et al⁶³ and based on an anthracene derivative that produced an OLED with CIE coordinates (0.16, 0.09), power efficiency of 1.9 lm W⁻¹, current efficiency of 3.6 cd A⁻¹ and external quantum efficiency (EQE) of 7.2%. Although an

impressive set of values, the structure of the OLED was a very complex seven-layer stack. Similarly, all of the blue OLEDs with EQE greater than 5% are based on multilayer structures, making them ultimately difficult to implement in a working display.

A simpler, quicker to manufacture and thus cheaper device structure is desirable. Therefore a key aim of OLED research should be to combine the properties of the individual layers into one molecular structure, whilst retaining the deep blue emission and high efficiency. It can be seen from Table 2.2 that simple deep-blue OLEDs are relatively rare and most show an EQE of less than 4%. The OLEDs reported in this thesis (shown in bold) have the highest EQE of any simple deep-blue fluorescent OLED in the literature.

Table 2.2: Device structures and electroluminescent performances based on non-doped blue fluorescent emitters. Adapted from a review paper by M. Zhu and C. Yang.¹⁹

Active layers in device structure	Peak EL (nm)	Turn-on Voltage (V)	Luminance (cd m ⁻²)	Current Efficiency (cd A ⁻¹)	Luminous Efficiency (lm W ⁻¹)	EQE (%)	CIE (x, y)	Reference
NPB/EML	456	2.7	21663	2.8	2.3	3.0	0.14, 0.11	43
TFTPA/EML/TPBI	456	4.9	-	5.3	2.8	5.3	0.14, 0.12	44
EML/TPBI	432	-	2838	1.9	-	2.7	0.15, 0.07	45
BPAF/EML	444	3.0	-	2.9	2.9	4.3	0.15, 0.07	46
NPB/TCTA/EML	444	4.0	2204	1.3	-	3.2	0.15, 0.07	47
BPAF/EML/TPBI	445	3.0	-	3.2	3.3	4.7	0.15, 0.07	46
2-TNATA/NPB/EML/Alq ₃	452	-	-	2.0 ^a	0.9 ^a	4.6 ^a	0.15, 0.08	48
EML	-	-	754	0.8	-	-	0.15, 0.09	49
CuPc/ α -NPD/EML/Alq ₃	436	-	5400	1.3 ^a	0.6 ^a	-	0.15, 0.09	50
NPB/EML/TPBI	438	4.0	10243	-	-	4.2	0.15, 0.09	51

Active layers in device structure	Peak EL (nm)	Turn-on Voltage (V)	Luminance (cd m ⁻²)	Current Efficiency (cd A ⁻¹)	Luminous Efficiency (lm W ⁻¹)	EQE (%)	CIE (x, y)	Reference
NPB/EML/TPBI	443	6.5	5350	3.3	1.3	4.3	0.15, 0.09	52
NPB/EML/TPBI	448	2.8	-	2.6	2.5	3.1	0.15, 0.09	53
EML/TPBI	-	3.8	3400	1.8	1.4	-	0.15, 0.10	54
EML/TPBI	-	3.9	5650	2.4	1.9	2.1	0.15, 0.11	55
CuPc/ α -NPD/EML/Alq ₃	457	-	-	3.0 ^b	1.2 ^b	-	0.15, 0.11	56
EML/TPBI	446	5.0	5713	2.2	0.7	2.0	0.15, 0.12	43
NPB/TCTA/EML/BIA _n	450	2.5	4382 ^a	5.6	5.7	5.1	0.15, 0.12	57
EML	452	2.9	16178	2.5	2.0	2.5	0.15, 0.12	43
TCTA/EML/BCP/Alq ₃	462	3.0	18240	7.5	7.3	6.3	0.15, 0.14	58
EML/TPBI	446	2.9	19416	-	-	4.5	0.15, 0.15	55
NPB/EML/TPBI	458	3.5	7332	4.4	3.1	-	0.15, 0.15	59

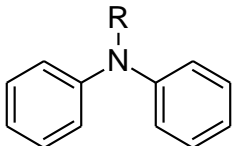
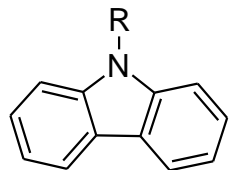
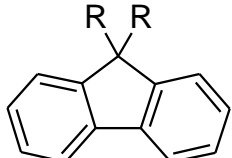
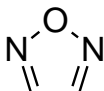
Active layers in device structure	Peak EL (nm)	Turn-on Voltage (V)	Luminance (cd m ⁻²)	Current Efficiency (cd A ⁻¹)	Luminous Efficiency (lm W ⁻¹)	EQE (%)	CIE (x, y)	Reference
DTAF/EML/TPBI	-	2.5	4600	1.6	1.07	3.0	0.16, 0.05	60
EML (spin-coated)	431	4.2	483^c	0.5^c	0.2^c	1.3^d	0.16, 0.07	61
EML (evaporated)	431	3.2	1520^c	1.5^c	0.5^c	4.7^d	0.16, 0.08	61
α -NPD/TCTA/EML/TPBI	-	3.0	8000	0.9	0.8	1.3	0.16, 0.08	35
PEDOT:PSS/EML/TPBI	-	3.4	732	3.8	3.2	4.2	0.16, 0.09	62
2-TNATA/NPB/EML/Alq ₃	444	-	363 ^a	3.6 ^a	1.9 ^a	7.2 ^a	0.16, 0.09	63
2-TNATA/NPB/EML/Bphen	-	-	-	2.1	1.8	2.5	0.16, 0.09	64
EML/TPBI	444	2.7	3933	1.7	2.0	-	0.16, 0.10	65
EML	456	2.6	8472	3.3	2.83	2.7	0.16, 0.16	66
NPB/EML/TPBI	428	3.5	4448	2.2	1.6	2.9	0.17, 0.07	67

^aData at 10 mA cm⁻². ^bData at 300 cd m⁻². ^cData under an applied current of 20 mA. ^dData at 100 cd m⁻². CuPc = copper phthalocyanine; α -NPD, NPB = *N,N'*-di(1-naphthyl)-*N,N'*-diphenylbenzidine; TPBI = 1,3,5-tris(*N*-phenylbenzimidazol-2-yl)benzene; BIAN = 2-*tert*-butyl-9,10-bis[4'-(1-phenylbenzimidazolyl)biphenyl-4-yl]anthracene; TFTP A = tris[4-(9-phenylfluoren-9-yl)phenyl]amine; 2-TNATA = 4,4',4''-tris(*N*-(2-naphthyl)-*N*-phenylamino)triphenyl amine; Bphen = 4,7-diphenyl-1,10-phenanthroline; EML = emissive layer.

A fundamental requirement for an efficient electroluminescent device is balanced hole and electron transport.⁶⁸⁻⁷¹ Therefore, ambipolar molecules that transport both holes and electrons are attractive candidates for simple OLEDs.⁷²⁻⁷⁶ Donor-acceptor (D-A) systems fulfil this requirement and offer the ability to manipulate the HOMO-LUMO levels and emission colour of a single molecule. A variety of D-A systems have been studied including triarylamine-quinoline,⁷⁷ phenoxazine-quinoline,^{78, 79} diphenylamine-diazaspirobifluorene,⁸⁰ triarylamine-1,3,4-diaryloxadiazole,^{81,82} and carbazole-1,3,4-diaryloxadiazole.⁸³ Alternative acceptor units in D-A systems include diarylboron,^{52, 84, 85} benzothiadiazole,⁸⁶ dibenzothiophene-S,S-dioxide,⁸⁷ and benzimidazole.⁴³

D-A systems as a basis for efficient blue OLEDs are promising. Kamtekar et al⁸² reported a selection of simple OLEDs based on triphenylamine-oxadiazole D-A molecules that showed green-blue emission, with one structure possessing an external quantum efficiency of 0.26%, although the colour did not meet the NTSC standard. The molecules also contained fluorene, which was thought to assist in the blue emission. This study uses the Kamtekar molecule as a basis for further structural manipulation towards producing a blue-emitting OLED. Several key moieties were incorporated into the molecules studied: arylamine, carbazole, fluorene and oxadiazole, and their properties are outlined in Table 2.3. Carbazole has been previously incorporated into polyfluorene molecules to achieve blue emission, although values for EQE or CIE coordinates were not reported.^{89, 90}

Table 2.3: Advantageous properties of the proposed molecular units incorporated into various OLED molecules.

Unit	Structure	Properties
Arylamine		<ul style="list-style-type: none"> ➤ e.g. Diphenylamine. Possesses a low electron affinity and therefore helps to prevent negative charge carriers reaching the anode in OLEDs. ➤ Hole-transporting ➤ Improve charge injection⁶³
Carbazole		<ul style="list-style-type: none"> ➤ Popular electron donor component ➤ Easy to functionalise ➤ Thermally and chemically very stable ➤ Good hole-transporting ability^{90, 91}
Fluorene		<ul style="list-style-type: none"> ➤ Thermally and kinetically stable ➤ Deep blue emission ➤ Well established strategies for functionalisation
Oxadiazole		<ul style="list-style-type: none"> ➤ Derivatives are widely used as versatile electron-transporting materials^{68, 69, 92, 93} ➤ Thermally and chemically very stable

2.3.6 White OLEDs

White devices (WOLEDs) are another area of intense research in the OLED industry. There is a strong drive to produce WOLEDs both for display and lighting applications. For lighting, WOLEDs have already been shown to reproduce the natural colours of objects under illumination better than rival technologies, and with a device efficiency comparable to fluorescent tubes. By combining phosphorescent red, green and blue emitters with a lens

based outcoupling technique, Reineke et al produced WOLEDs with 81 lm W^{-1} efficiency at 1000 cd m^{-2} .⁹⁵ This is far more efficient than the 20 lm W^{-1} associated with incandescent light bulbs and above the 70 lm W^{-1} reported for fluorescent tubes. More recently, Sasabe et al¹⁵ have reported a WOLED with a power efficiency of 90 lm W^{-1} . Compared to incandescent and fluorescent lighting, WOLEDs also have the advantage of remaining cool during operation and are mercury-free. The ability to produce white light is also significant for display technology, as white light can be converted to any colour in a number of ways. If a bright, stable, efficient white OLED could be produced, both lighting and display markets would flourish.

A number of options have been employed in the literature to produce WOLEDs. The first example of a WOLED was produced by Kido et al by mixing different coloured emitters in a single layer.⁹⁵ Single emissive layer devices sandwiched between ETL and HTL layers have been explored, where the emissive layer contains red, green and blue phosphorescent emitters doped into a host material. Such OLEDs have been reported to have an external quantum efficiency of 6.7% and power efficiency of 11.1 lm W^{-1} .⁹⁶ Another approach is the blending of two complementary colours in a single host layer. If properly chosen, it is easier to adjust the composition of a two-component system.^{6, 97} A convenient way to obtain white emission is to use blue and yellow emitters.¹⁵ A major problem that limits the use of such devices is the relatively short lifetime of the blue phosphorescent material. Mixing of red and green phosphorescent molecules with a blue emitting fluorescent material has shown promise, removing the need for the blue phosphor. However, the device structure is complicated by the need for spacer layers of undoped host material to prevent energy transfer from the blue emitter to the phosphorescent layers. Also, the low external quantum efficiencies encountered for blue fluorophores, typically $\sim 2.6\%$, have remained a problem, limiting both the overall device efficiency and brightness.⁹⁶ To improve the characteristics Kanno et al⁹⁸ have experimented with tandem stacked WOLED

units sandwiched between electrodes, achieving EQE values of 11%. However, the number of layers required makes device fabrication slow and complex. In addition, the relatively large thickness of the overall stacked structure requires high driving voltages and thus power efficiency suffers as more WOLEDs are incorporated, dropping to 11 lm W⁻¹ for a three-stack unit.

An alternative approach is down conversion of light from a blue OLED through the use of separate phosphorescent layers to produce white light,^{99, 100} but, again, efficiency is ultimately limited by the performance of the blue OLED. It is clear then that the development of a simple, efficient, high quality blue OLED is an important step for the production of both displays and WOLEDs.

2.4 Organic Field-Effect Transistors (OFETs)

OFETs offer the exciting possibility of integrated organic circuits, which have already been realised to some extent with the coupling of OLEDs and OFETs. Although OFETs cannot outperform their inorganic counterparts, they will likely find a place in niche markets where their lightweight construction together with the ability to manufacture large-area, low cost devices gives them an advantage over other technology. Crucially, OFETs offer mechanically flexible electronics, something inorganic technology cannot compete with. As such, OFETs are of interest in applications ranging from electronic paper and radio frequency identification (RFID) tags to chemical and biological sensors.

OFETs are virtually identical to ordinary FETs in that they are three-terminal devices consisting of gate, source and drain electrodes. The difference lies in the semiconductor between the source and drain which in this case is composed of organic material. In a transistor structure the source and drain electrodes are contacted directly to the

semiconductor and the gate is isolated by a dielectric. The different OFET configurations available are depicted in Figure 2.9.

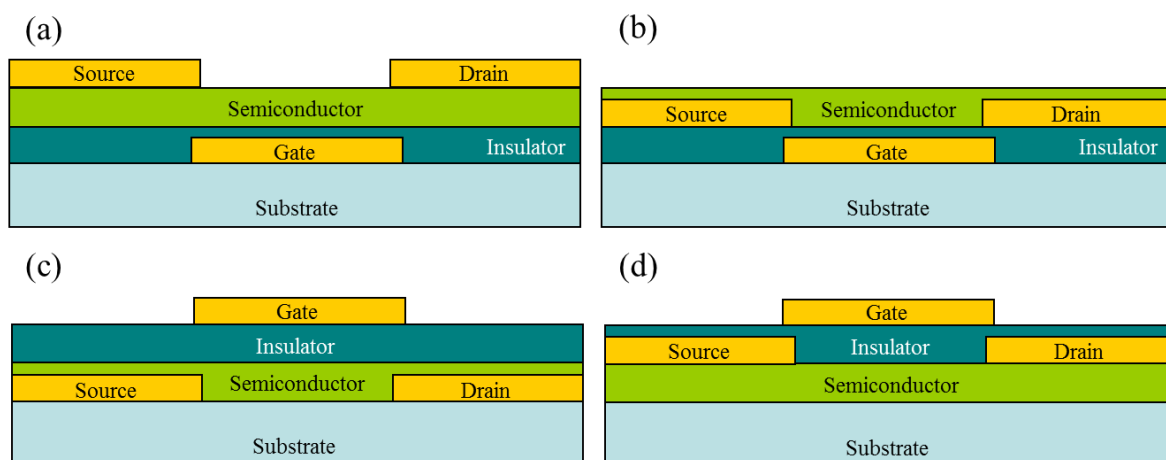


Figure 2.9: Schematic for the various structures of an OFET (a) bottom gate top contact, (b) bottom gate bottom contact, (c) top gate bottom contact, (d) top gate top contact.

In the two bottom gate configurations (Figure 2.9 (a) and (b)), the gate electrode and then the dielectric layer are first deposited onto a substrate. Subsequently, the semiconductor followed by the source and drain electrodes can be deposited, in the bottom gate top contact structure or the semiconductor can be deposited on pre-prepared source and drain electrodes in the bottom gate bottom contact configuration. The bottom contact configuration is advantageous because the source and drain electrodes can be patterned by photolithography before the semiconductor is deposited on top. However, the top contact configuration is associated with better device characteristics due to a lower contact resistance between the source and drain electrodes and the semiconductor.¹⁰¹

The alternative structures involve top gate bottom contact or top gate top contact configurations (Figure 2.9 (c) and (d)). These structures are harder to implement in OFETs due to the danger of damaging the relatively fragile semiconductor during deposition of the dielectric layer. However, this approach can be advantageous as the dielectric serves as

both the gate insulator and as an encapsulation layer to protect the organic semiconductor from ambient conditions.

By applying a voltage, V_G at the gate, current flow between the source and drain electrodes can be controlled. The gate functions to create and modify a conducting channel in the organic semiconductor between source and drain, which allows a current, I_{DS} to flow. The ability to control I_{DS} with the gate allows for the device to be switched between an on and an off state, an important feature in numerous electronic applications.

The electrical properties of both ordinary FETs and OFETs are often measured in terms of their output and transfer characteristics. The output characteristics of a device are the relationship between an applied source-drain voltage, V_{DS} and the resulting current, I_{DS} at varying applied gate voltages, V_G . An example of output characteristics obtained for an OFET based on pentacene¹⁰² are given in Figure 2.10.

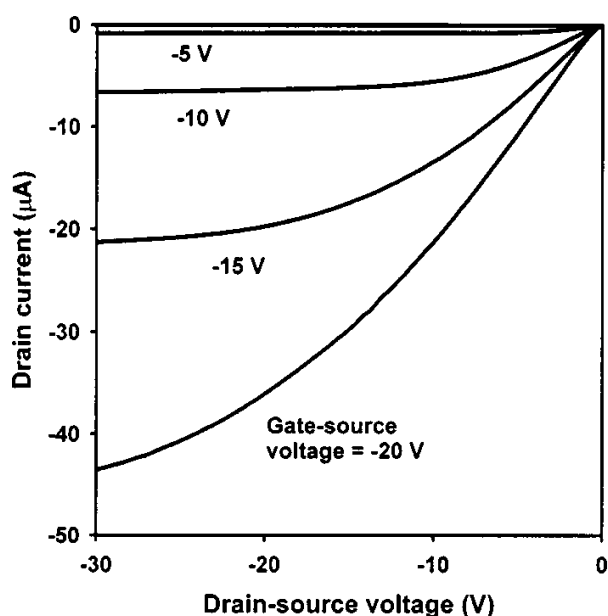


Figure 2.10: Output characteristics for an OFET based on pentacene. Modified from¹⁰².

Many organic molecules are better transporters of holes than electrons and thus the gate electrode is often negatively biased with respect to the source. Such conditions result in the accumulation of holes at the semiconductor-dielectric interface and it is these holes that

carry charge when V_{DS} is applied to drive them between source and drain. At low drain voltages the drain current, I_{DS} varies roughly linearly with increasing V_{DS} and the channel therefore exhibits a resistance and Ohm's Law is approximately obeyed. A more thorough, but still approximate representation of the linear behaviour is explained by Equation 2.10:¹⁶

$$I_{DS} = \frac{WC_i}{L} \mu \left(V_G - V_T - \frac{V_{DS}}{2} \right) V_{DS} \quad (2.10)$$

where L is the length of the conducting channel and W the width. C_i is the capacitance per unit area of the dielectric, μ the field-effect charge carrier mobility (drift velocity per unit of electric field) and V_T the threshold voltage, or turn-on voltage. V_T is constant for a particular device and represents the gate-source voltage beyond which a conductive channel forms.

From Figure 2.10, it is clear that larger values of V_{DS} cause I_{DS} to saturate at a constant value. This phenomenon is caused by 'pinch-off', which occurs when the combination of V_{DS} and V_G result in a wedge-shaped accumulation layer. The conducting channel narrows at the drain until it has a cross-sectional area of zero. Further increases in V_{DS} do not generate a rise in I_{DS} as the increased driving force is cancelled out by widening of the depletion region produced by the absence of charge carriers at the drain. The overall effect is described by Figure 2.11.¹⁶

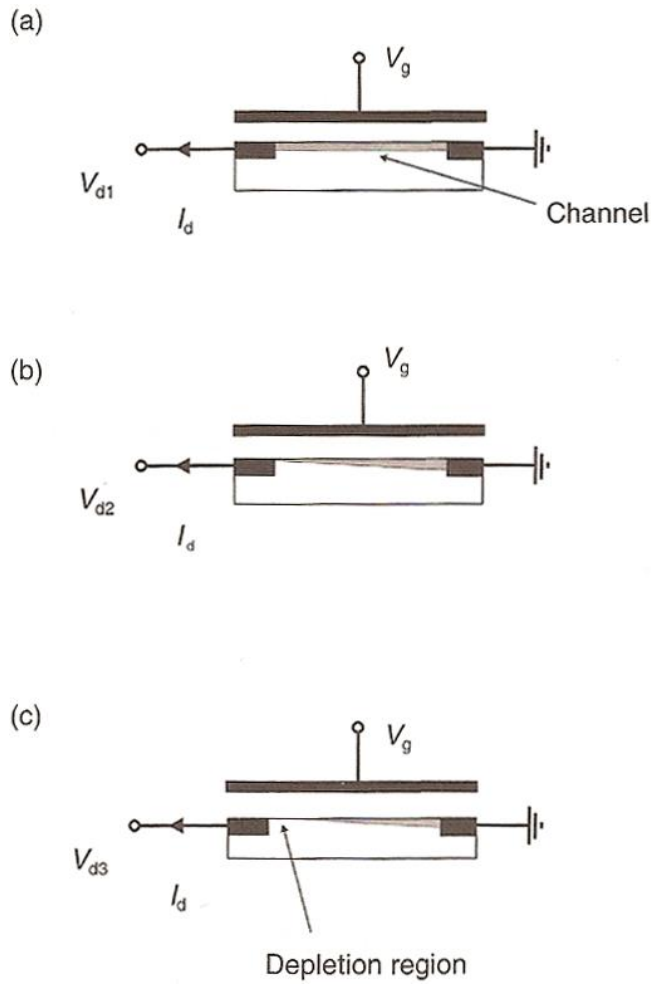


Figure 2.11: The effect of increasing the magnitude of V_{DS} on the conducting channel in an OFET. (a) The linear regime where the channel connects source and drain. (b) Pinch-off – the conducting channel has a cross-sectional area of zero at the drain. (c) Further application of V_{DS} cause the formation of a depletion region, causing current saturation.¹⁶

Beyond the pinch-off point the saturated current, I_{DS} can be modelled using Equation 2.11.¹⁶

$$I_{DS} = \frac{WC_i}{2L} \mu(V_G - V_T)^2 \quad (2.11)$$

Applying Equation 2.11 to the saturated regime allows for the calculation of carrier mobility and the value of V_T , if it is rearranged into the form $y = mx + c$ (Equation 2.12).

$$\sqrt{|I_{DS}|} = \left(\sqrt{\frac{WC_i}{2L}} \mu \right) V_G - \left(\sqrt{\frac{WC_i}{2L}} \mu \right) V_T \quad (2.12)$$

A plot of $\sqrt{|I_{DS}|}$ against V_G therefore results in a straight line within the saturated regime. Clearly, the calculation of μ from the gradient and subsequent calculation of V_T is a relatively simple affair if the values of W , L and C_i are known. Figure 2.12 shows an example of such a plot obtained for a pentacene OFET.¹⁰²

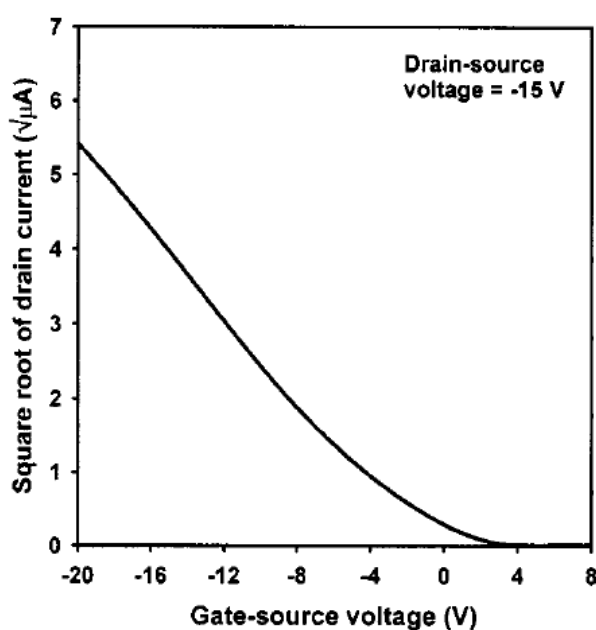


Figure 2.12: Plot of $\sqrt{|I_{DS}|}$ against V_G for a pentacene OFET. The x-intercept relates to the value of V_T and slope in the linear region to the charge-carrier mobility. Modified from¹⁰².

Based on Figure 2.10, it is evident that larger gate voltages result in both increased I_{DS} for a set V_{DS} and a delay in the onset of the pinch-off. Such behaviour shows that increasing V_G results in a greater concentration of charge carriers at the semiconductor-dielectric interface and thus greater conduction. The fact that pinch-off appears later at greater gate voltages is explained by Equation 2.13, which shows the approximate value of V_G that must be applied for I_{DS} to change from the linear to the saturated regime.¹⁶

$$V_{DS} = V_G - V_T \quad (2.13)$$

Transfer characteristics of OFETs are displayed on a graph of V_G against $\log(I_{DS})$. An example of the transfer characteristics obtained for the same pentacene OFET is shown in Figure 2.13.¹⁰²

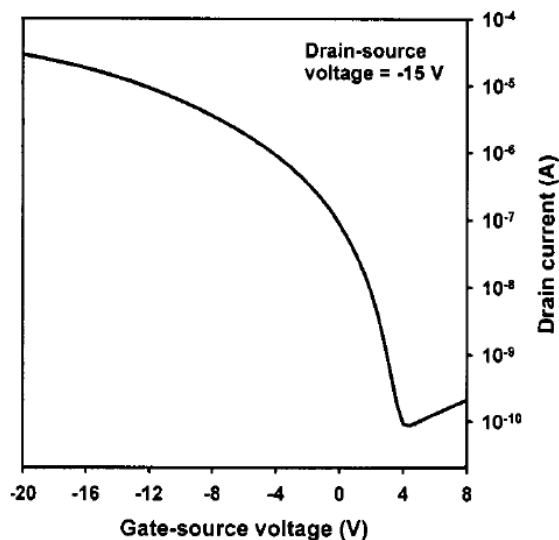


Figure 2.13: Transfer characteristics obtained for a pentacene OFET. Modified from ¹⁰².

Transfer characteristics show how sensitive a transistor is to an applied voltage at the gate, and how the device behaves. A transistor is said to be ‘on’ when V_G is greater than V_T , in Figure 2.13 this situation is reflected by the gentle curve at higher values of V_G . The lowest point of the curve is regarded as the ‘off’ state and usually occurs at more positive values of V_G . Such behaviour occurs due to a depletion of charge carriers in the conducting channel as the gate is positively biased and hence a reduction in I_{DS} . It is very common for studies regarding transistors to quote the I_{on}/I_{off} ratio of a device, which refers to the difference between observed values of I_{DS} in the accumulation and depletion regimes of a particular transistor.

Below the threshold voltage, I_{DS} falls rapidly. However, there is still clearly some current flow and this is referred to as subthreshold conduction, which relates to the conductivity of the organic semiconductor. The value of subthreshold conduction can be estimated from the slope of the curve in Figure 2.13 in the subthreshold region, at which point the I_{DS} - V_G

characteristics are fairly linear. In the subthreshold region, small changes in V_G usually result in significant increases in I_{DS} and the subthreshold slope is typically measured as the voltage required to increase I_{DS} by an order of magnitude. For the pentacene transistor shown in Figure 2.13, the subthreshold slope is approximately 0.9 V per decade. The smaller the value of voltage required to change I_{DS} by one decade, the more sensitive a transistor is as a switch. The best inorganic FETs show a subthreshold slope of 70 mV per decade,¹⁶ which is significantly better than that seen in OFETs. Whilst it is clear that OFETs can serve as electronic switches, they are not as sensitive as inorganic FETs.

The characteristics of pentacene OFETs outlined above serve as a good example of research in the area due to the huge amount of research that has been undertaken on the molecule. In their 2008 review, Kitamura and Arakawa noted that over a thousand articles were related to pentacene transistors.¹⁰³ Pentacene has been widely studied primarily due to its availability and good hole mobility. The charge carrier mobility has markedly improved for pentacene devices from $2 \times 10^{-3} \text{ cm}^2 \text{ V}^{-1} \text{ s}^{-1}$ as reported in 1991¹⁰⁴ up to $5.5 \text{ cm}^2 \text{ V}^{-1} \text{ s}^{-1}$ in 2006.¹⁰⁵ Pentacene transistors based on a PMMA dielectric typically show low mobilities less than $0.1 \text{ cm}^2 \text{ V}^{-1} \text{ s}^{-1}$, although this was improved to between 0.3 and 0.4 by reducing the thickness of the PMMA.¹⁰⁶

Despite improving hole transport, electron transport is poor in pentacene, although Unni et al showed a bilayer OFET based on pentacene and an electron transporting material could be used to increase electron mobility.¹⁰⁷ They reported hole and electron mobilities of $0.09 \text{ cm}^2 \text{ V}^{-1} \text{ s}^{-1}$ and $9.3 \times 10^{-3} \text{ cm}^2 \text{ V}^{-1} \text{ s}^{-1}$, respectively. In a similar fashion, Noever et al recently used a C_{60} layer to achieve greater carrier mobility, reporting hole and electron mobilities of $0.28 \text{ cm}^2 \text{ V}^{-1} \text{ s}^{-1}$ and $0.18 \text{ cm}^2 \text{ V}^{-1} \text{ s}^{-1}$, respectively.¹⁰⁸ Interestingly, these transistor structures possess similarities to light-emitting OFETs, (see OLEFET section below) but no light emission was reported.

Research in OFETs is still strongly motivated towards improving their characteristics, particularly with a view to improve applicability to current OLED displays. Qian et al¹⁰⁹ have recently worked on improving the quality of rubrene OFETs with an aim to allow for large-area devices. Interest has also shifted to focus upon the multifunctional properties of the devices for use in sensors and novel applications.¹¹⁰ One example of a multifunctional OFET that is of particular interest in this work is the light-emitting OFETs described below.

2.5 Organic Light-Emitting Field-Effect Transistors (OLEFETs)

OLEFETs offer the exciting possibility of a single device possessing the combined properties of an OLED and an OFET. In theory, such devices would simplify the design of organic displays by removing the need for a backplane of TFTs. They could also make such products cheaper by further reducing the amount of material required to manufacture a working device whilst still retaining the useful property of thin, flexible films that can be deposited on most substrates. Furthermore, OLEFETs could be utilised in entirely new optoelectronic applications.

OLEFETs are very similar in structure to OFETs but the semiconducting layer is composed of an electroluminescent (EL) material in which holes and electrons injected from the source and drain electrodes recombine to emit light. One of the key factors that must be considered when designing OLEFETs is the ability of the semiconductor to transport both holes and electrons.

OLEFETs are typically studied using EL spectra, output characteristics and transfer characteristics in much the same way as these methods are applied to OLEDs and OFETs. Transfer characteristics are particularly useful for revealing how effective a device is at

transporting both holes and electrons. A fairly symmetrical plot such as the example shown later in Figure 2.17 demonstrates virtually even conduction of both holes and electrons – a desirable property for an OLEFET. The minimum on the graph corresponds to the transition from electron to hole dominated current.

The first OLEFET based on tetracene¹¹¹ in fact only showed effective conduction of holes between the source and drain. EL was observed but occurred only in the vicinity of the electron injecting electrode where electrons were trapped at the metal-tetracene interface. Such devices are referred to as unipolar as they involve the transport of only one charge carrier through the semiconductor. Unipolar OLEFETs typically show poor emission as the excitons produced tend to be quenched by the nearby electrode.¹¹²

Ambipolar OLEFETs that transport both holes and electrons are the preferred device as recombination can theoretically occur at the centre of the semiconductor, far from either electrode, thus reducing losses due to quenching. A schematic of an ambipolar OLEFET is included in Figure 2.14.²⁸

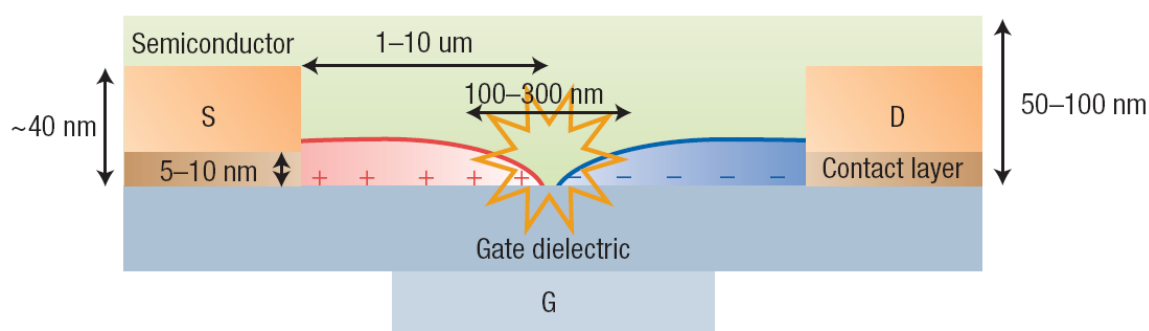


Figure 2.14: Schematic of an ambipolar OLEFET with light emission occurring equidistant from source and drain, where + represents holes and – represents electrons.²⁸

The first ambipolar OLEFET was actually based on a heterojunction,¹¹³ where the active layer was composed of P13 (N,N'-ditridecylperylene-3,4,9,10-tetracarboxylic diimide), a

good hole transporter and T5 (α -quinquethiophene), a good electron transporter. The molecular structures of P13 and T5 are given in Figure 2.15.

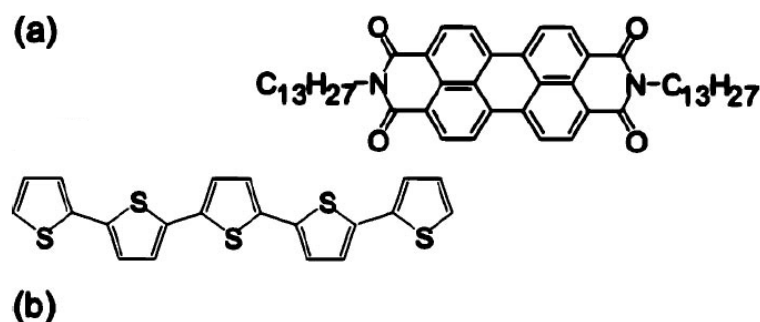


Figure 2.15: Structures of (a) P13 and (b) T5. Modified from ¹¹³.

A schematic of the heterojunction device is included in Figure 2.16. Heterojunctions are designed to balance the carrier injection and transport of holes and electrons in the conduction channel without the need for an ambipolar molecule. At present, these bilayer devices offer the best mobility values for both holes and electrons but, interestingly, recombination actually occurs close to the electron injecting drain electrode, much like is seen for unipolar devices. The most likely cause of this behaviour is due to the fact that the active layer was deposited onto a SiO_2 gate dielectric, which is now known to trap electrons.

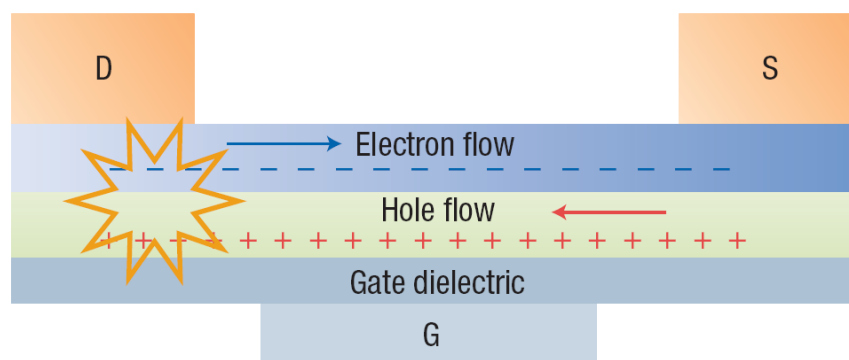


Figure 2.16: OLEFET based on a bilayer structure. Positively charged holes are transported at the dielectric-HTL interface and electrons at the ETL-HTL interface.²⁸

It is worth noting that most OLEFET research has been demonstrated with the device operated under vacuum. More recently, Seo et al¹¹⁴ demonstrated a heterojunction OLEFET operating under ambient conditions. The device was based on hole transporting pentacene and electron transporting perylene encapsulated in a wide band gap protecting layer. Movement of the recombination zone from source to drain at different gate bias was also demonstrated, although light emission was not reported to originate from the centre of the device.

Other ambipolar OLEFETs have been designed based on active layers of polyphenylene vinylene (PPV) derivatives such as Super Yellow¹¹⁵ and OC₁C₁₀-PPV.¹¹⁶ A key feature of these devices was the inclusion of an organic dielectric that served to reduce electron trapping at the semiconductor-dielectric interface, hence allowing ambipolar transport in materials previously considered to be poor electron transporters. The ambipolar transfer characteristics are highlighted in Figure 2.17 and show how the drain-source current rises from less than 7×10^{-10} A at the off-state to 1×10^{-7} A or 5×10^{-8} A when more positive and more negative gate voltages are applied, respectively. This contrasts with the transfer characteristics shown for the unipolar semiconductor pentacene in Figure 2.13, where conduction is only observed for more negative gate voltages relative to the off-state.

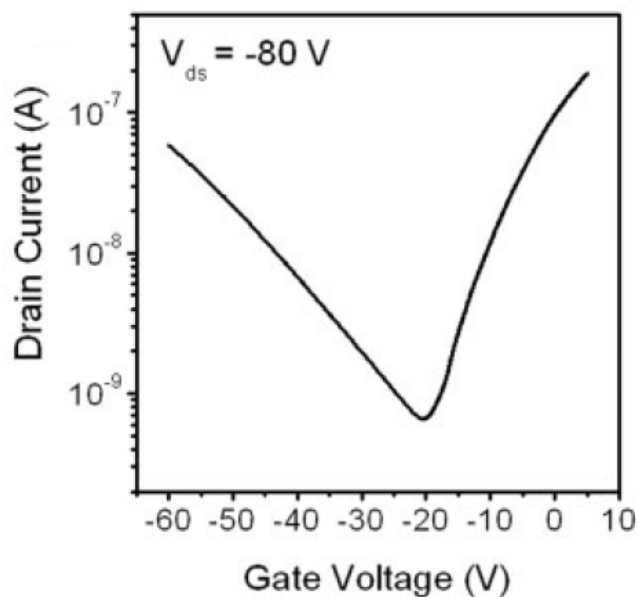


Figure 2.17: Transfer characteristics for a OC₁C₁₀-PPV ambipolar OLEFET showing roughly identical electron and hole transport properties.¹¹²

It should also be noted that the source and drain electrodes were based on a high work function metal (usually Au) to inject holes and a low work function metal (often Ca) to inject electrons more efficiently into the organic, much like in OLEDs.

An alternative approach has involved the use of ambipolar molecules in a single organic layer device. This is a useful direction for OLEFET research to take, where ambipolar charge transfer characteristics may be observed within a single molecule without the need for heterojunctions or multiple layers. As for OLEDs, incorporating the desirable properties into a simple organic layer is preferable for OLEFETs to be considered in commercial applications.

In one study, Zaumseil et al¹¹⁷ showed that OLEFETs were possible using molecules with unbalanced transport of holes and electrons but that the position of the recombination zone depended on the relative mobilities of the charge carriers. This is similar to the observations of light emission centred on one electrode for unipolar OLEFETs. In the same study, using the fluorene based compound, F8BT, deposited atop a PMMA dielectric with

gold electrodes they also demonstrated an OLEFET where the region of light emission was successfully controlled by varying the gate voltage. This suggests that there was an efficient injection of both holes and electrons from the gold electrodes. The ability to visualise directly electroluminescence moving across the F8BT film has been used as a basis for a fundamental study into charge transport in the organic transistor structure.¹¹⁷

F8BT is a very promising polymer for use in OLEFETs as it combines good hole and electron transporting moieties within a single molecule that can be deposited easily by spin-coating. The Zaumseil paper remains the benchmark to which other OLEFETs are compared, for example the recent work by Melucci et al.¹¹⁸

Addition of zinc oxide as an electron injection layer in F8BT devices was shown to improve the ambipolar characteristics and light emission further.¹¹⁹ Other, more recent work has considered the incorporation of metal oxides into the OLEFET channel region to improve light emission using a different organic semiconductor,¹²⁰ but EQE values remain significantly lower than the value of 0.55% reported for F8BT.

A selection of fluorene polymers including F8BT were studied in OLEFETs consisting of ITO source and drain electrodes by Kajii et al.¹²¹ The simple fluorene backbone F8 polymer was shown to produce blue OLEFETs. Furthermore a white OLEFET was produced by doping with 5% F8BT.

The great interest that remains in F8BT and related compounds shows how fluorene is a useful moiety in compounds intended for OLEFETs, primarily due to its ambipolar charge transport properties.

2.6 Conclusions

The review of the literature has shown how research into OLEDs, OFETs and OLEFETs has expanded in recent years. Much progress has been made in improvements to efficiency and charge transfer qualities but several key areas have been identified that require further attention. OFETs remain an area of active research, not least for integration with OLED technology into fully organic displays.

For OLED displays, efficient blue devices that meet the high colour standards set out by the NTSC remain an issue. Whilst progress has been made in the area it has typically been at the expense of simplicity of fabrication – a serious concern for the ultimate commercialisation of OLED displays. OLEDs for white light emission face similar challenges and, again, it is the lack of good quality blue emitting devices that causes many of the problems encountered.

The realisation of a blue-emitting electroluminescent molecule was therefore a key aim of the research presented in this thesis. The combination of both electron and hole transporting moieties into single molecular structures was designed to simplify the final OLED architecture whilst retaining efficient blue emission. The ambipolar nature of the molecule is also attractive to OLEFET devices and was expected to allow for simpler device structure and thus fabrication.

2.7 References

- 1) S. M. Kelly in *Flat Panel Displays: Advanced Organic Materials*, **2000**, RSC Monographs, The Royal Society of Chemistry, Chapter 4.

- 2) A. C. Grimsdale, K. L. Chan, R. E. Martin, P. G. Jokisz, A. B. Holmes, *Chem. Rev.*, 109, 897-1091, **2009**.
- 3) Z. H. Kakafi, *Organic Electroluminescence*, **2005**, CRC Press.
- 4) K. Müllen, U. Scherf, *Organic Light-Emitting Devices*, **2006**, Wiley VCH.
- 5) Z. Li, H. Meng, *Organic Light-Emitting Materials and Devices*, **2006**, CRC Press.
- 6) K. T. Kamtekar, A. P. Monkman, M. R. Bryce, *Adv. Mater.*, 22, 572-582, **2010**.
- 7) S. Beaupré, P.-L. T. Boudreault, M. Leclerc, *Adv. Mater.*, 22, E6-E27, **2010**.
- 8) Lecture by A Hunze, *Device Physics of White OLEDs for lighting Applications*, Vth International Krutyn Summer School, Poland, **2009**, 02/06/09.
- 9) Sony **2007** Flexible OLED Display. Last accessed 03/11/13.
http://www.digitaltechnews.com/news/2007/05/sonys_flexible_.html
- 10) Toshiba **2011**. Last accessed 03/11/13. <http://www.oled-info.com/toshiba-shows-ultra-thin-flexible-3-oled-display-prototype>
- 11) Samsung **2013**. Last accessed 03/11/13.
<http://global.samsungtomorrow.com/?p=28863>
- 12) LG Chem **2013**. Last accessed 03/11/13. <http://www.oled-info.com/flexible-oled>
- 13) T. Komoda, K. Yamae, V. Kittichungchit, H. Tsuji, N. Ide, *SID12 Digest*, 610, **2012**.
- 14) K. Sugi, T. Ono, D. Kato, T. Yonehara, T. Sawabe, S. Enomoto, I. Amemiya, *SID 12 Digest*, 1548, **2012**.
- 15) H. Sasabe, J. Kido, *J. Mater. Chem. C*, 1, 1699-1707, **2013**.

- 16) M. C. Petty in *Molecular Electronics: From Principles to Practice*, **2007**, John Wiley & Sons Ltd., Chapter 9.
- 17) J. H. Burroughes, D. D. C. Bradley, A. R. Brown, R. N. Marks, K. Mackay, R. H. Friend, P. L. Burns, A. B. Holmes, *Nature*, 347, 539-541, **1990**.
- 18) T. Smith, J. Guild, *Trans. Opt. Soc.*, 33, 73-134, **1931**.
- 19) M. Zhu, C. Yang, *Chem. Soc. Rev.*, 42, 4963-4976, **2013**.
- 20) RS stock no. 308-067. Sheet F14784.
- 21) K. Leo, *Nature Photonics*, 5, 716-718, **2011**.
- 22) S. Möller, S. R. Forrest, *J. App. Phys.*, 91, 3324-3327, **2002**.
- 23) Y. Sun, S. R. Forrest, *J. App. Phys.*, 100, 073106, **2006**.
- 24) A. R. Brown, D. C. C. Bradley, J. H. Burroughes, R. H. Friend, N. C. Greenham, P. L. Burn, A. B. Holmes, A. Kraft, *Appl. Phys. Lett.*, 61, 2793-2795, **1992**.
- 25) J. Chan, A. D. Rakić, C. Y. Kwong, Z. T. Liu, A. B. Djurišić, M. L. Majewski, W. K. Chan and P. C. Chui, *Smart Mater. Struct.*, 15, S92, **2006**.
- 26) R. A. Klenkler, H. Aziz, A. Tran, Z. D. Popovic, G. Xu, *Organic Electronics*, 9, 285-290, **2008**.
- 27) M. A. Khan, W. Xu, F. Wei, Y. Bai, X. Y. Jiang, Z. L. Zhang, W. Q. Zhu, *Solid State Communications*, 144, 343-346, **2007**.
- 28) M. Muccini, *Nature Materials*, 5, 605-613, **2006**.
- 29) C. W. Tang, S. A. VanSlyke, *Appl. Phys. Lett.*, 51, 913-915, **1987**.

- 30) J. C. Scott, S. A. Carter, S. Karg, M. Angelopoulos, *Synth. Met.*, 85, 1197-1200, **1997**.
- 31) P. Piromreun, H. Oh, Y. Shen, G. G. Malliaras, J. C. Scott, P. J. Brock, *Appl. Phys. Lett.*, 77, 2403-2405, **2000**.
- 32) (a) C. Yang, H.-S. Song, D.-B. Liu, *J. Mater. Sci.*, 48, 6719-6727, **2013**. (b) N. Prachumrak, S. Namuangruk, T. Keawin, S. Jungsuttingwong, T. Sudyoadsuk, V. Promarak, *Eur. J. Org. Chem.*, 3825-3834, **2013**.
- 33) T. Tsujimura in *OLED Displays: Fundamentals and Applications*, **2012**, John Wiley & Sons, Chapter 4.
- 34) Y. Yang, P. Cohn, A. L. Dyer, S.-H. Eom, J. R. Reynolds, R. K. Castellano, J. Xue, *Chem. Mater.*, 22, 3580-3582, **2010**.
- 35) T.-C. Tsai, W.-Y. Hung, L.-C. Chi, K.-T. Wong, C.-C. Hsieh, P.-T. Chou, *Org. Electron.*, 10, 158-162, **2009**.
- 36) H. Sasabe, J. Takamatsu, T. Motoyama, S. Watanabe, G. Wagenblast, N. Langer, O. Molt, E. Fuchs, C. Lennartz, J. Kido, *Adv. Mater.*, 22, 5003-5007, **2010**.
- 37) G. M. Farinola and R. Ragni, *Chem. Soc. Rev.*, 40, 3467-3482, **2011**.
- 38) C. W. Lee and J. Y. Lee, *Adv. Mater.*, 25, 5450-5454, **2013**.
- 39) Q.-X. Tong, S.-L. Lai, M.-Y. Chan, Y.-C. Zhou, H.-L. Kwong, C.-S. Lee, S.-T. Lee, *Chem. Mater.*, 20, 6310-6312, **2008**.
- 40) M. T. Lee, H. H. Chen, C. H. Liao, C. H. Tsai, C. H. Chen, *Appl. Phys. Lett.*, 85, 3301-3303, **2004**.

- 41) C.-G. Zhen, Z.-K. Chen, Q.-D. Liu, Y.-F. Dai, R. Y. C. Shin, S.-Y. Chang, J. Kieffer, *Adv. Mater.*, 21, 2425-2429, **2009**.
- 42) A. Kraft, A. C. Grimsdale, A. B. Holmes, *Angew. Chem. Int. Ed.*, 37, 402-428, **1998**.
- 43) M.-Y. Lai, C.-H. Chen, W.-S. Huang, J. T. Lin, T.-H. Ke, L.-Y. Chen, M.-H. Tsai, C.-C. Wu, *Angew. Chem., Int. Ed.*, 47, 581-585, **2008**.
- 44) P.-I. Shih, C.-Y. Chuang, C.-H. Chien, E. W.-G. Diau, C.-F. Shu, *Adv. Funct. Mater.*, 17, 3141-3146, **2007**.
- 45) Z. Jiang, Z. Liu, C. Yang, C. Zhong, J. Qin, G. Yu and Y. Liu, *Adv. Funct. Mater.*, 19, 3987-3995, **2009**.
- 46) C.-H. Chien, C.-K. Chen, F.-M. Hsu, C.-F. Shu, P.-T. Chou, C.-H. Lai, *Adv. Funct. Mater.*, 19, 560-566, **2009**.
- 47) J. Wan, C.-J. Zheng, M.-K. Fung, X.-K. Liu, C.-S. Lee, X.-H. Zhang, *J. Mater. Chem.*, 22, 4502-4510, **2012**.
- 48) Y.-I. Park, J.-H. Son, J.-S. Kang, S.-K. Kim, J.-H. Lee, J.-W. Park, *Chem. Commun.*, 2143-2145, **2008**.
- 49) B. Chen, J. Ding, L. Wang, X. Jing and F. Wang, *Chem. Commun.*, 48, 8970-8972, **2012**.
- 50) Y.-H. Kim, H.-C. Jeong, S.-H. Kim, K. Yang, S.-K. Kwon, *Adv. Funct. Mater.*, 15, 1799-1805, **2005**.
- 51) J. N. Moorthy, P. Venkatakrisnan, D.-F. Huang, T. J. Chow, *Chem. Commun.*, 2146-2148, **2008**.

- 52) S.-L. Lin, L.-H. Chan, R.-H. Lee, M.-Y. Yen, W.-J. Kuo, C.-T. Chen and R.-J. Jeng, *Adv. Mater.*, 20, 3947-3952, **2008**.
- 53) Y. Zhang, S.-L. Lai, Q.-X. Tong, M.-F. Lo, T.-W. Ng, M.-Y. Chan, Z.-C. Wen, J. He, K.-S. Jeff, X.-L. Tang, W.-M. Liu, C.-C. Ko, P.-F. Wang, C.-S. Lee, *Chem. Mater.*, 24, 61-70, **2012**.
- 54) J H. Huang, Q. Fu, S. Zhuang, Y. Liu, L. Wang, J. Chen, D. Ma, C. Yang, *J. Phys. Chem. C*, 115, 4872-4878, **2011**.
- 55) C.-G. Zhen, Z.-K. Chen, Q.-D. Liu, Y.-F. Dai, R. Y. C. Shin, S.-Y. Chang, J. Kieffer, *Adv. Mater.*, 21, 2425-2429, **2009**.
- 56) Y. H. Kim, D. C. Shin, S.-H. Kim, C.-H. Ko, H.-S. Yu, Y.-S. Chae, S. K. Kwon, *Adv. Mater.*, 13, 1690-1693, **2001**.
- 57) C.-H. Wu, C.-H. Chien, F.-M. Hsu, P.-I. Shih, C.-F. Shu, *J. Mater. Chem.*, 19, 1464-1470, **2009**.
- 58) C.-J. Kuo, T.-Y. Li, C.-C. Lien, C.-H. Liu, F.-I. Wu, M.-J. Huang, *J. Mater. Chem.*, 19, 1865-1871, **2009**.
- 59) S. Tao, Y. Zhou, C.-S. Lee, X. Zhang, S.-T. Lee, *Chem. Mater.*, 22, 2138-2141, **2010**.
- 60) W.-Y. Hung, L.-C. Chi, W.-J. Chen, Y.-M. Chen, S.-H. Chou, K.-T. Wong, *J. Mater. Chem.*, 20, 10113-10119, **2010**.
- 61) A. L. Fisher, K. E. Linton, K. T. Kamtekar, C. Pearson, M. R. Bryce, M. C. Petty, *Chem. Mater.*, 23, 1640-1642, **2011**.
- 62) J C. Liu, Y. Li, Y. Zhang, C. Yang, H. Wu, J. Qin, Y. Cao, *Chem.-Eur. J.*, 18, 6928-6934, **2012**.

- 63) S.-K. Kim, B. Yang, Y. Ma, J.-H. Lee, J.-W. Park, *J. Mater.Chem.*, 18, 3376-3384, **2008**.
- 64) S. J. Lee, J. S. Park, K.-J. Yoon, Y.-I. Kim, S.-H. Jin, S. K. Kang, Y.-S. Gal, S. Kang, J. Y. Lee, J.-W. Kang, S.-H. Lee, H.-D. Park, J.-J. Kim, *Adv. Funct. Mater.*, 18, 3922-3930, **2008**.
- 65) J M. Zhu, Q. Wang, Y. Gu, X. Cao, C. Zhong, D. Ma, J. Qin, C. Yang, *J. Mater. Chem.*, 21, 6409-6415, **2011**.
- 66) J. Huang, J.-H. Su, X. Li, M.-K. Lam, K.-M. Fung, H.-H. Fan, K.-W. Cheah, C. H. Chen, H. Tian, *J. Mater. Chem.*, 21, 2957-2964, **2011**.
- 67) S. Gong, Y. Zhao, M. Wang, C. Yang, C. Zhong, J. Qin, D. Ma, *Chem.-Asian J.*, 5, 2093-2099, **2010**.
- 68) A. P. Kulkarni, C. J. Tonzola, A. Babel, S. A. Jenekhe, *Chem. Mater.*, 16, 4556-4573, **2004**.
- 69) G. Hughes, M. R. Bryce, *J. Mater. Chem.*, 15, 94-107, **2005**.
- 70) Y. Shirota, H. Kageyama, *Chem. Rev.*, 107, 953-1010, **2007**.
- 71) N. Tamoto, C. Adachi, K. Nagai, *Chem. Mater.*, 9, 1077-1085, **1997**.
- 72) S. Takizawa, V. A. Montes, P. Anzenbacher Jr, *Chem. Mater.*, 21, 2452-2458, **2009**.
- 73) L. C. Zeng, T. Y. H. Lee, P. B. Merkel, S. G. Chen, *J. Mater. Chem.*, 19, 8772-8781, **2009**.
- 74) S. L. Gong, Y. B. A. Zhou, C. L. Yang, C. Zhong, J. G. Qin, D. G. Ma, *J. Phys. Chem. C*, 114, 5193-5198, **2009**.
- 75) L. Duan, J. Qiao, Y. Sun, Y. Qui, *Adv. Mater.*, 23, 1137-1144, **2011**.

- 76) A. Chaskar, H.-F. Chen, K.-T. Wong, *Adv. Mater.*, 23, 3876-3895, **2011**.
- 77) J. M. Hancock, A. P. Gifford, Y. Zhu, Y. Lou, S. A. Jenekhe, *Chem. Mater.*, 18, 4924-4932, **2006**.
- 78) Y. Zhu, A. P. Kulkarni, P. T. Wu, S. A. Jenekhe, *Chem. Mater.*, 20, 4200-4211, **2008**.
- 79) A. P. Kulkarni, Y. Zhu, A. Babel, P. T. Wu, S. A. Jenekhe, *Chem. Mater.*, 20, 4212-4223, **2008**.
- 80) C.-C. Chi, C.-L. Chiang, S.-W. Liu, H. Yueh, C.-T. Chen, C.-T. Chen, *J. Mater. Chem.*, 19, 5561-5571, **2009**.
- 81) A. Patra, M. Pan, C. S. Friend, T.-C. Lin, A. N. Cartwright, P. N. Prasad, *Chem. Mater.*, 14, 4044-4048, **2002**.
- 82) K. T. Kamtekar, C. Wang, S. Bettington, A. S. Batsanov, I. F. Perepichka, M. R. Bryce, J. H. Ahn, M. Rabinal, M. C. Petty, *J. Mater. Chem.*, 16, 3823-3835, **2006**.
- 83) K. R. K. Thomas, J. T. Linn, Y.-T. Tao, C.-H. Chuen, *Chem. Mater.*, 16, 5437-5444, **2004**.
- 84) H. Doi, M. Kinoshita, K. Okumoto, Y. Shirota, *Chem. Mater.*, 15, 1080-1089, **2003**.
- 85) H. Zhang, C. Huo, J. Zhang, P. Zhang, W. Tian, Y. Wang, *Chem. Commun.*, 281-283, **2006**.
- 86) K. R. J. Thomas, J. T. Lin, M. Velusamy, Y.-T. Tao, C.-H. Chuen, *Adv. Funct. Mater.*, 14, 83-90, **2004**.
- 87) T.-H. Huang, J.-T. Lin, L.-Y. Chen, Y.-T. Lin, C.-C. Wu, *Adv. Mater.*, 18, 602-606, **2006**.

-
- 88) J. Du, Q. Fang, D. Bu, S. Ren, X. Chen, *Macromol. Rapid Commun.*, 26, 1651-1656, **2005**.
- 89) O. Stéphan, J.-C. Vial, *Synth. Met.*, 106, 115-119, **1999**.
- 90) P.-L. T. Boudreault, S. Beaupré, M. Leclerc, *Polym. Chem.*, 1, 127-136, **2010**.
- 91) S. C. Lo, P. L. Burn, *Chem. Rev.*, 107, 1097-1116, **2007**.
- 92) C. Wang, G.-Y. Jung, A. S. Batsanov, M. R. Bryce, M. C. Petty, *J. Mater. Chem.*, 12, 173-180, **2002**.
- 93) J.-H. Lee, H.-H. Tsai, M.-K. Leung, C.-C. Yang, C.-C. Chao, *Appl. Phys. Lett.*, 90, 243501, **2007**.
- 94) S. Reineke, F. Lindner, G. Schwartz, N. Seidler, K. Walzer, B. Lüssem, K. Leo, *Nature*, 459, 234-239, **2009**.
- 95) J. Kido, M. Kimura, K. Nagai, *Science*, 267, 1332, **1995**.
- 96) Y.-L. Chang, Z.-H. Lu, *J. Display Technology*, 9, 459-468, **2013**.
- 97) C. Pearson, D. H. Cadd, M. C. Petty, Y. L. Hua, *J. Appl. Phys.*, 106, 064516, **2009**.
- 98) H. Kanno, R. Holmes, Y. Sun, S. Kena-Cohen, S. Forrest, *Adv. Mater.*, 18, 339-342, **2006**.
- 99) A. R. Duggal, J. J. Shiang, C. M. Heller, D. F. Foust, *Appl. Phys. Lett.*, 80, 3470-3472, **2002**.
- 100) V. Gohri, T. C. Rosenow, S. Reineke, B. Lüssem, K. Leo, *White OLEDs Based On Down Conversion Of Blue Light*, Poster presentation, Vth International Krutyn Summer School, Poland, **2009**.

-
- 101) Y. Yun in *Pentacene Based Organic Electronic Devices*, PhD thesis, Durham University, **2010**, Chapter 2.
- 102) H. Klauk, M. Halik, U. Zschieschang, F. Eder, G. Schmid, C. Dehm, *Appl. Phys. Lett.*, 82, 4175, **2003**.
- 103) M. Kitamura, Y. Arawaka, *J. Phys.: Consens. Matter*, 20, 184011, **2008**.
- 104) G. Horowitz, D. Fichou, X. Peng, F. Garnier, *Synth. Met.*, 41, 1127-1130, **1991**.
- 105) S. Lee, B. Koo, J. Shin, E. Lee, H. Park, H. Kim, *Appl. Phys. Lett.*, 88, 162109, **2006**.
- 106) Y. Yun in *Pentacene Based Organic Electronic Devices*, PhD thesis, Durham University, **2010**, Chapter 4.
- 107) K. N. N. Unni, A. K. Pandey, S. Alem, J.-M. Nunzi, *Chem. Phys. Lett.*, 421, 554-557, **2006**.
- 108) S. J. Noever, S. Fischer, B. Nickel, *Adv. Mater.*, 25, 2147-2151, **2013**.
- 109) X. Qian, T. Wang, D. Yan, *Organic Electronics*, 14, 1052-1056, **2013**.
- 110) C. Di, F. Zhang, D. Zhu, *Adv. Mater.*, 25, 313-330, **2013**.
- 111) A. Hepp, H. Heil, W. Weise, M. Ahles, R. Schmechel, H. von Seggern, *Phys. Rev. Lett.*, 91, 157406, **2003**.
- 112) F. Cicoira, C. Santanto, *Adv. Funct. Mater.*, 17, 3421-3434, **2007**.
- 113) C. Rost, S. Karg, W. Riess, M. A. Loi, M. Muriga, M. Muccini, *Appl. Phys. Lett.*, 85, 1613-1615, **2004**.
- 114) H.-S. Seo, D.-K. Kim, J.-D., Oh, E.-S. Shin, J.-H. Choi, *J. Phys. Chem. C*, 117, 4764-4770, **2013**.

- 115) J. S. Swensen, C. Soci, A. J. Heeger, *Appl. Phys. Lett.*, 87, 253511, **2005**.
- 116) J. Zaumseil, R. H. Friend, H. Sirringhaus, *Nat. Mater.*, 5, 69-74, **2006**.
- 117) J. Zaumseil, C. R. McNeil, M. Bird, D. L. Smith, P. P. Ruden, M. Roberts, M. J. McKiernan, R. H. Friend, H. Sirringhaus, *J. Appl. Phys.*, 103, 064517, **2008**.
- 118) M. Melucci, L. Favaretto, M. Zambianchi, M. Durso, M. Gazzano, A. Zanelli, M. Monari, M. G. Lobello, F. De Angelis, V. Biondo, G. Generali, S. Troisi, W. Koopman, S. Toffanin, R. Capelli, M. Muccini, *Chem. Mater.*, 25, 668-676, **2013**.
- 119) M. C. Gwinner, Y. Vaynzof, K. K. Banger, P. K. H. Ho, R. H. Friend, H. Sirringhaus, *Adv. Funct. Mater.*, 20, 3457-3465, **2010**.
- 120) K. Yamada, T. Yamao, S. Hotta, *Adv. Mater.*, 25, 2860-2866, **2013**.
- 121) H. Kajii, K. Koiwai, Y. Hirose, Y. Ohmori, *Organic Electronics*, 11, 509-513, **2010**.

3 Experimental

3.1 In this Chapter...

This chapter begins with a description of the materials used to fabricate devices in this project. As well as standard commercial materials, Katharine Linton, a PhD student in the Bryce group at the Department of Chemistry, Durham University synthesised some compounds specifically for use in this project. These are tabulated in Table 3.1. From here the chapter moves on to discuss laboratory methods of depositing these materials and why certain methods were chosen over other options. Finally, details of how each type of device was fabricated are listed clearly in their own separate sections with a full description for each step in the process.

3.2 Materials

A number of standard materials were used to fabricate the devices. All of these are shown in the following pages and some information is given in bullet points below. Where applicable, a chemical structure of the material is given adjacent to the information. The materials are listed in alphabetical order by name or acronym.

3.2.1 Commercial Materials

Aluminium

- ⇒ Purchased from BDH
- ⇒ AnalaR grade
- ⇒ Used as a top contact in OLEDs

⇒ Used as a gate, source or drain in transistors

⇒ Work function = -4.06 – -4.26 eV (depending on crystal orientation)¹

Caesium Fluoride (CsF)

⇒ Purchased from Sigma-Aldrich, purity 99.99%

⇒ Electron injector in OLEDs

Calcium

⇒ Purchased from Acros Organics, purity 99%

⇒ Work function = -2.87 eV¹

⇒ Used as an electron injector in OLEDs

Poly(9,9-di-*n*-octylfluorene-*alt*-benzothiadiazole (F8BT) (Figure 3.1)

⇒ Purchased from American Dye Source, Inc.

⇒ Molecular Weight = 157,000 g mol⁻¹

⇒ Appearance: Yellow fibres

⇒ Absorption maximum = 455 nm

⇒ Photoluminescent maximum = 531 nm

⇒ Literature shows that F8BT makes good OLEFETs²

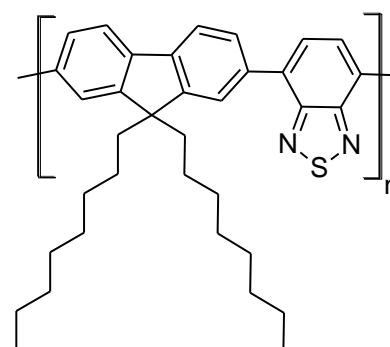


Figure 3.1: Structure of F8BT.

- ⇒ Transports holes and electrons
- ⇒ Electroluminescent – emitting green light, with peak wavelength of 550 nm

Gold

- ⇒ Purchased from Kurt J. Lesker, purity 99.99%
- ⇒ Used as a gate, source or drain in transistor structure.
- ⇒ Work function = 5.1 eV

Ionic Liquid (IL) (Figure 3.2)

- ⇒ Name: trihexyltetradecylphosphonium-bis(trifluoromethylsulfonyl)amide
- ⇒ Purchased from Sigma-Aldrich
- ⇒ Molecular Weight = 678.83 g mol⁻¹

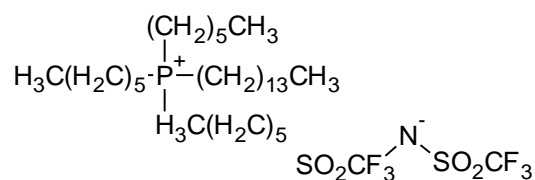


Figure 3.2: Structure of Ionic Liquid.

Indium-tin Oxide (ITO)

- ⇒ Ready-coated on glass substrates supplied by Merck and VisionTek Systems
- ⇒ Sheet resistance of 8 Ω sq⁻¹ and 7 Ω sq⁻¹
- ⇒ Used as the anode in OLEDs
- ⇒ Work function = -4.8 eV

- ⇒ High conductivity, low resistivity of approx. $10^{-4} \Omega \text{ cm}$
- ⇒ Optical transparency $> 80\%$ transmittance of incident light
- ⇒ Rough surface

1,3-bis[2-(4-tert-butylphenyl)-1,3,4-oxadiazol-5-yl]benzene (OXD7) (Figure 3.3)

- ⇒ Purchased from Luminescence Technology Corp.
- ⇒ Molecular Weight = $478.58 \text{ g mol}^{-1}$
- ⇒ Used as the electron transport material in OLEDs

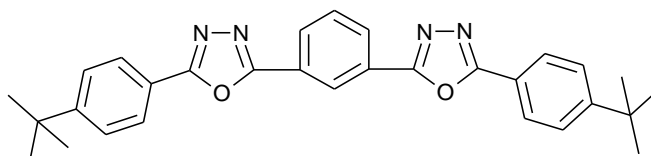
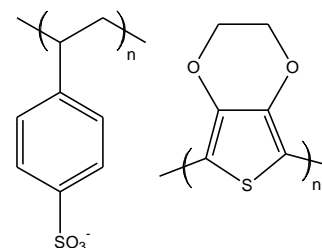


Figure 3.3: Structure of OXD7.

Poly(3,4-ethylenedioxythiophene) poly(styrenesulfonate) (PEDOT:PSS) (Figure 3.4)

- ⇒ Supplied by H. C. Starck (later Heraeus)
- ⇒ Appearance: dark blue solution in water
- ⇒ Conducting polymer that acts as a hole injection layer in OLEDs



- ⇒ Work function = -5.2 eV approx.

Figure 3.4: Structure of PEDOT:PSS.

- ⇒ Polymer mixture of two ionomers in ratio 1:6 by weight:

1. poly(3,4-ethylenedioxythiophene) (PEDOT)
2. polystyrene sulfonate (PSS)

- ⇒ Smooths out the ITO layer, therefore prevents short circuiting
- ⇒ Improves contact to the emissive layer
- ⇒ Degrades on exposure to UV light

Pentacene (Figure 3.5)

- ⇒ Purchased from Sigma-Aldrich, purity 99%
- ⇒ Molecular Weight = $278.35 \text{ g mol}^{-1}$
- ⇒ Planar molecule
- ⇒ Good hole transporter
- ⇒ Poor electron transporter

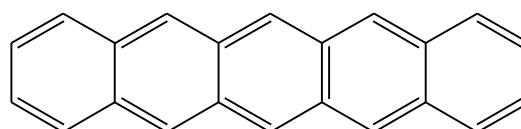


Figure 3.5: Structure of Pentacene.

PO-01 (Figure 3.6)

- ⇒ Purchased from LumTec
- ⇒ Full name: Iridium(III)bis(4-phenylthieno[3,2-c]pyridinato-N,C2')acetylacetonate
- ⇒ Molecular Weight = $712.08 \text{ g mol}^{-1}$
- ⇒ Well-known phosphorescent iridium dye complex
- ⇒ For use in OLEDs

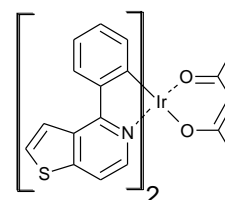


Figure 3.6: Structure of PO-01.

Poly(methyl methacrylate) (PMMA) (Figure 3.7)

⇒ Purchased from Sigma-Aldrich

⇒ Molecular Weight = 93,000 g mol⁻¹

⇒ Transparent plastic

⇒ Used as insulator/gate dielectric in transistor devices

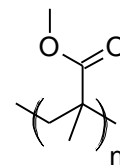


Figure 3.7: Structure of PMMA.

Super Yellow (Figure 3.8)

⇒ Purchased from Merck

⇒ Proportions of moieties is x = 50%, y = 35%, z = 15%

⇒ Also known as PDY-132

⇒ Well-known fluorescent polymer

⇒ For use in OLEDs

⇒ Highly efficient yellow emitter

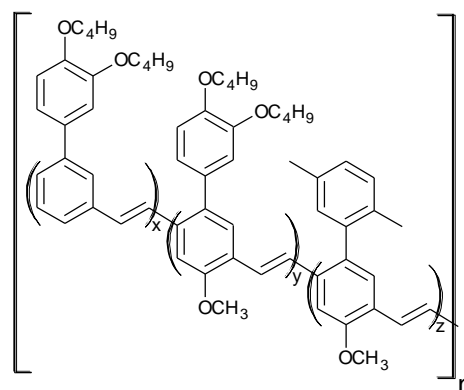


Figure 3.8: Structure of Super Yellow

Solvents

⇒ Chlorobenzene purchased from VWR, AnalaR-Normapur

⇒ Toluene purchased from Fisher Scientific, Analytical Reagent Grade

⇒ Chloroform purchased from VWR, AnalaR

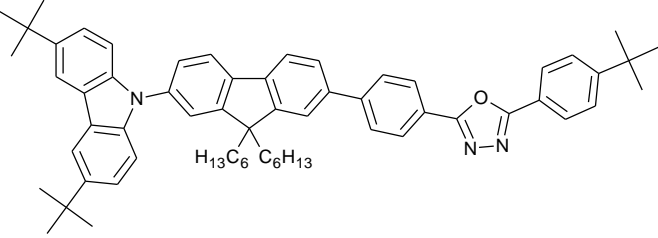
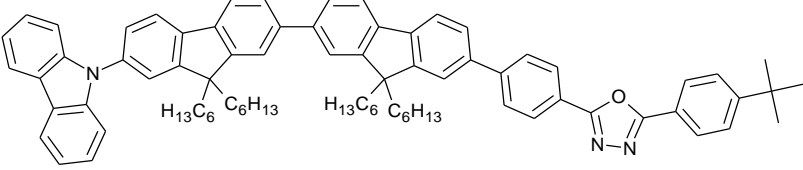
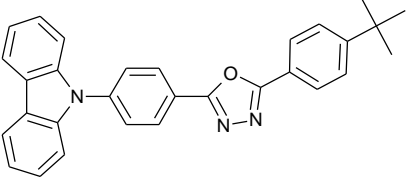
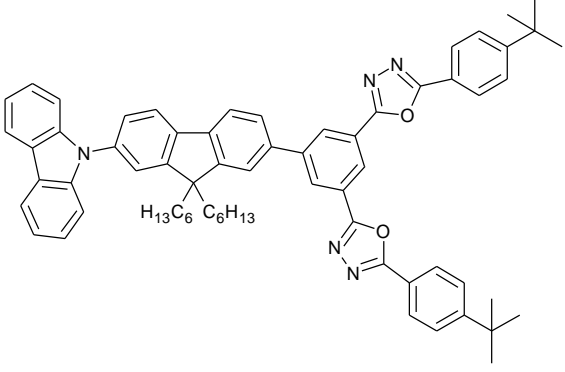
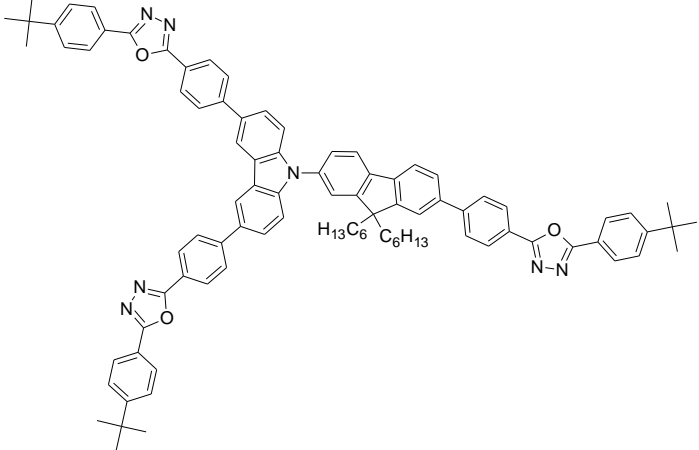
⇒ Xylene purchased from BDH, AnalaR

3.2.2 Synthesised Compounds

In this work, the materials chosen to be synthesised contained carbazole, fluorene and oxadiazole moieties. Previous experimental work at Durham University,³ which used Compound **1** (see Table 3.1), as well as recent publications,⁴⁻⁶ were key factors in the decision to synthesise these types of materials, which would then be used for new blue OLEDs. Since **1** was used successfully in the previous publication, Compound **1A** was synthesised in an attempt to recreate these OLEDs whilst also making the compound more soluble. With the goal of creating deep blue OLEDs in mind, Compounds **2-8** were designed to include an oxadiazole group and experiment with modifications to the chemical structure. Materials **1A** and **2-8** were all synthesised and purified in the Department of Chemistry, exclusively for this work. See publications^{7, 8} for further details.

Table 3.1: List to identify synthesised compounds used throughout this study. Molecular weights are also given.

Compound	Chemical Structure	Molecular Weight (g mol ⁻¹)
1		778.08
1A		806.13
2		776.06
3		777.05
4		782.09
5		836.11

Compound	Chemical Structure	Molecular Weight (g mol ⁻¹)
6	 H ₁₃ C ₆ C ₆ H ₁₃	888.27
7	 H ₁₃ C ₆ C ₆ H ₁₃ H ₁₃ C ₆ C ₆ H ₁₃	1108.58
8		443.54
9	 H ₁₃ C ₆ C ₆ H ₁₃	976.30
10	 H ₁₃ C ₆ C ₆ H ₁₃	1328.73

3.3 Equipment and Techniques

3.3.1 Spin-Coating

Spin-coating involves dropping an excess volume of a solution onto a substrate and then spinning the substrate at high speed. Centrifugal forces spread the solution across the substrate while the solvent evaporates, leaving a uniform thin film. It is important to use an appropriate spin speed for the solution, which is determined by the solvent (i.e. how volatile it is), how concentrated the solution is and the fluid viscosity. This is described in Equation 3.1.⁹

$$d = \left(\frac{\eta}{4\pi\rho\omega^2} \right)^{1/2} t^{-1/2} \quad (3.1)$$

Where:

d = thickness of the spun film

η = viscosity coefficient of the solution

ρ = density of the solution

ω = angular velocity of the spinning

t = spinning time

An image of a spin-coater is shown in Figure 3.9.

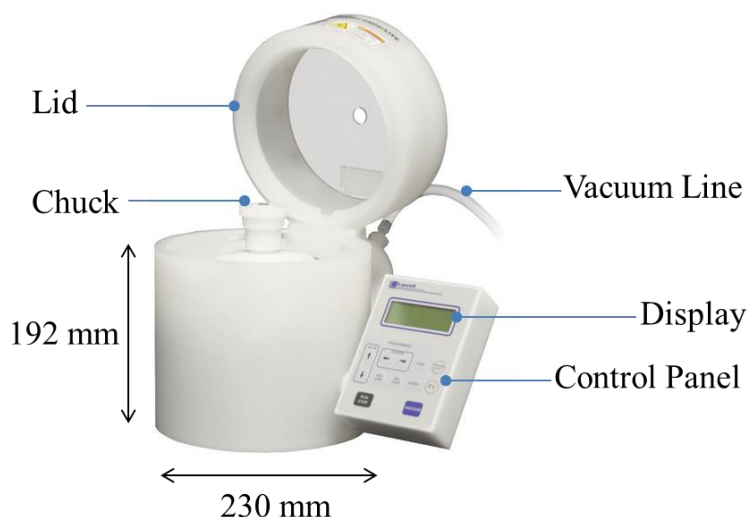


Figure 3.9: Labelled photograph of a spin-coater.

This is a common technique in the fabrication of micro and nanoelectronics, the advantages being that it is very simple, quick to do, gives uniform films and is reliable. Low material utilisation is one disadvantage in that only a small percentage of the material is left on the substrate at the end of the process.

This method consists of four stages (also see Figure 3.10):

Stage 1: Deposition – Dispense solution onto the substrate and spread across the whole area.

Stage 2: Spin-up – Once up to speed, fluid is expelled off the substrate.

Stage 3: Spin-off – Fluid is spun off the edges, creating a uniform film.

Stage 4: Evaporation – The film thins as the solvent evaporates.

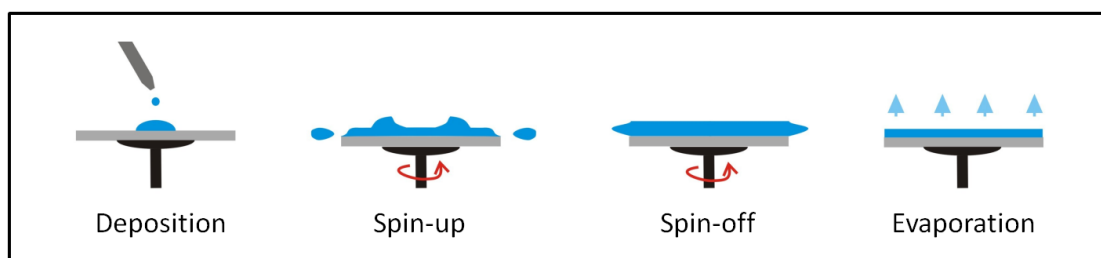


Figure 3.10: Schematic showing the four steps in the spin-coating process.

It is important to be aware of potential thickness differences at the very edge of the substrate, known as edge bead. This should be removed or only the inner area of the substrate film used.

In this work, spin-coating provides an effective method for substrate coverage. Any devices made are kept away from the edge, removing any possibility of edge bead or similar effects.

Two spin-coaters were used in this project.

- Laurell Technologies WS-400A-6NPP-LITE. This was used to spin-coat PMMA layers.
- Glovebox Spin-Coater. This home-made spin-coater was set up in the nitrogen glovebox and used to spin-coat all other spun materials.

A Brand Transferpette micropipette was used to deposit the solutions onto the substrates prior to spinning.

3.3.2 Thermal Evaporation

This technique involves heating a material to the point of evaporation, usually at pressures of around 10^{-6} mbar. The high vacuum is created by a diffusion pump, backed by a rotary pump. At this pressure, the mean free path of the atoms is of the same order as the chamber dimensions. As the power (filament current) is increased, the tungsten filament heats up and the material begins to evaporate. The material evaporates and condenses on the substrate. The rate of this deposition can therefore be controlled by an increase or decrease in power. This and the thickness of material evaporated can be monitored using a film

thickness monitor – a quartz crystal, placed in the path of the source. A diagram of a thermal evaporator is shown in Figure 3.11 below.

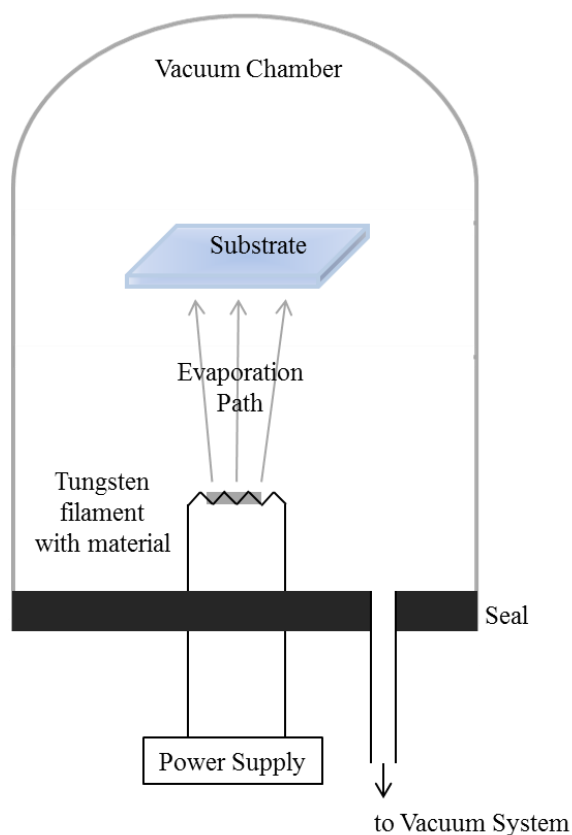


Figure 3.11: Diagram of a thermal evaporator.

This is a technique often used in microfabrication. Advantages are it is quick to set up, thickness can be accurately monitored once calibrated and it is a reliable, repeatable process.

A disadvantage may be that if the vacuum is poor and oxygen remains in the chamber, oxides may form in the film. In the case of this work, the evaporator stands in a nitrogen glovebox, so a negligible amount of oxygen is present, even when the chamber is vented.

Alternative techniques include sputter coating and electron beam evaporation. For this work, thermal evaporation was chosen. There are a number of advantages to each method and access has been available to each throughout the project. However, this work was

carried out as far as possible in a nitrogen glovebox which contained a thermal evaporator. This nitrogen environment is essential in ensuring the layers are kept moisture-free and do not oxidise.

In this work, three evaporators were used:-

- Edwards Auto306. This was used for pentacene evaporations and some metal evaporations. An Edwards RV12 rotary pump was used for roughing the chamber down to $\sim 10^{-2}$ mbar and an Edwards EXT255H compound molecular pump was used to reach a pressure below 1×10^{-6} mbar.
- Edwards 306. This was used for some metal evaporations. A high vacuum was achieved using an Edwards RV12 rotary pump and an Edwards E04K diffusion pump. Material thickness and rate were monitored by an Edwards film thickness monitor (FTM7).
- Glovebox evaporator. This Edwards 306 with E04 diffusion pump and RV8 rotary pump, set up inside a nitrogen-containing glovebox, was used for all other evaporations not mentioned above.

3.4 Device Characterisation

3.4.1 Atomic Force Microscope (AFM)

An AFM scans the surface of a sample with a sharp probe attached to a cantilever and builds up a map of the topography of the sample's surface. The main components of an AFM are shown over in Figure 3.12.

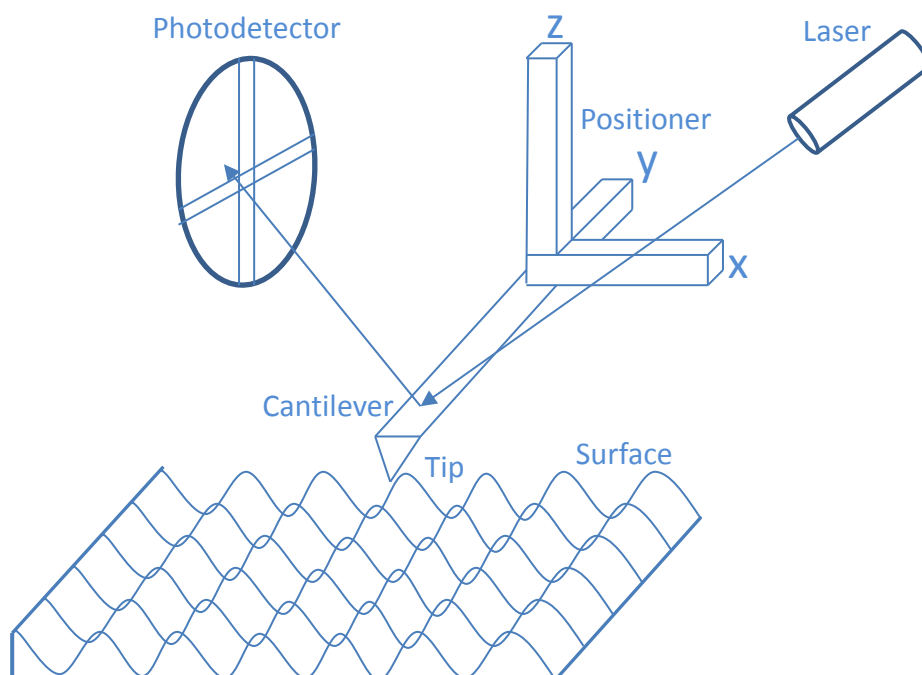


Figure 3.12: Schematic of an AFM.

There are three main components to how an AFM operates. These are the piezoelectric transducers (scanners), force transducers (sensors) and feedback control.¹⁰ The piezoelectric transducers provide fine control of movement in the x, y, and z directions relative to the sample surface. Force is measured from the deflection of the cantilever as the probe scans the surface and is monitored with a laser beam reflected off the back of the cantilever onto a photodetector. In order to maintain a fixed force between the tip and the sample during scanning, the feedback control sends a signal to the z-scanner to maintain a constant signal on the photodetector.

There are three modes in which the AFM can be used to look at the surface of a film.

These are contact, tapping and non-contact mode:-

- Contact Mode: The tip contacts the surface during the scan, keeping the force between the tip and the surface constant.

- Tapping Mode: The cantilever is oscillated between 20 and 100 nm. The tip lightly taps the surface and contacts on every oscillation.
- Non-Contact Mode: The cantilever is oscillated at less than 10 nm. The tip does not tap or contact the surface, but simply oscillates during the scan.

AFM can be used to image almost any sample, whether the material is hard or soft. It is possible to see the surface of the sample from any angle and it is simple to measure the dimensions of any features and the arithmetic mean of the surface roughness (R_a). There is minimal sample preparation, no vacuum is required and it is a relatively low cost method of imaging, when compared to the Scanning Electron Microscope (SEM) or Transmission Electron Microscope (TEM). AFM has high accuracy when positioning the probe on the surface and high sensitivity. This means that it can be difficult to set up the probe correctly and tip problems are common, however once operational, it can give superb images of a sample on the nanometre or micrometre scale.

In this project, a Digital Instruments Nanoscope IVa, Dimension 3100 was used in tapping mode using a 1 Ω cm silicon cantilever with a 7 nm radius tip (Veeco OTESPA) to image the surface of the organic material, as well as to check the thickness of the evaporated materials, including calcium, gold and aluminium, when calibrating the film thickness monitor in the evaporator. In order to measure the thickness of organic material deposited on individual devices, scratches were made in the film with a sharp set of tweezers. This approach produced scratches with a width of several microns that penetrated to the underlying electrode. AFM scans in the region of each scratch provided a clear edge profile from which the film thickness could be measured.

3.4.2 Electrical Characterisation of OLEDs

The setup for electrical and photocurrent measurements of OLEDs is shown in Figure 3.13. All measurements were carried out under vacuum ($\sim 10^{-1}$ mbar) in a screened metal chamber. Devices were mounted emissive-side down over a large-area photodiode (1 cm^2) and electrical connection to the anode and cathode was provided with adjustable contacts. D.C. bias voltages were supplied and sample currents measured using a Keithley model 2400 sourcemeter. The light output of each device was measured from the photocurrent generated at the photodiode, as recorded by a Keithley model 485 digital picoammeter. The instruments were connected, via a General Purpose Interface Bus (GPIB), to a Personal Computer which was used to automate the measurement process.

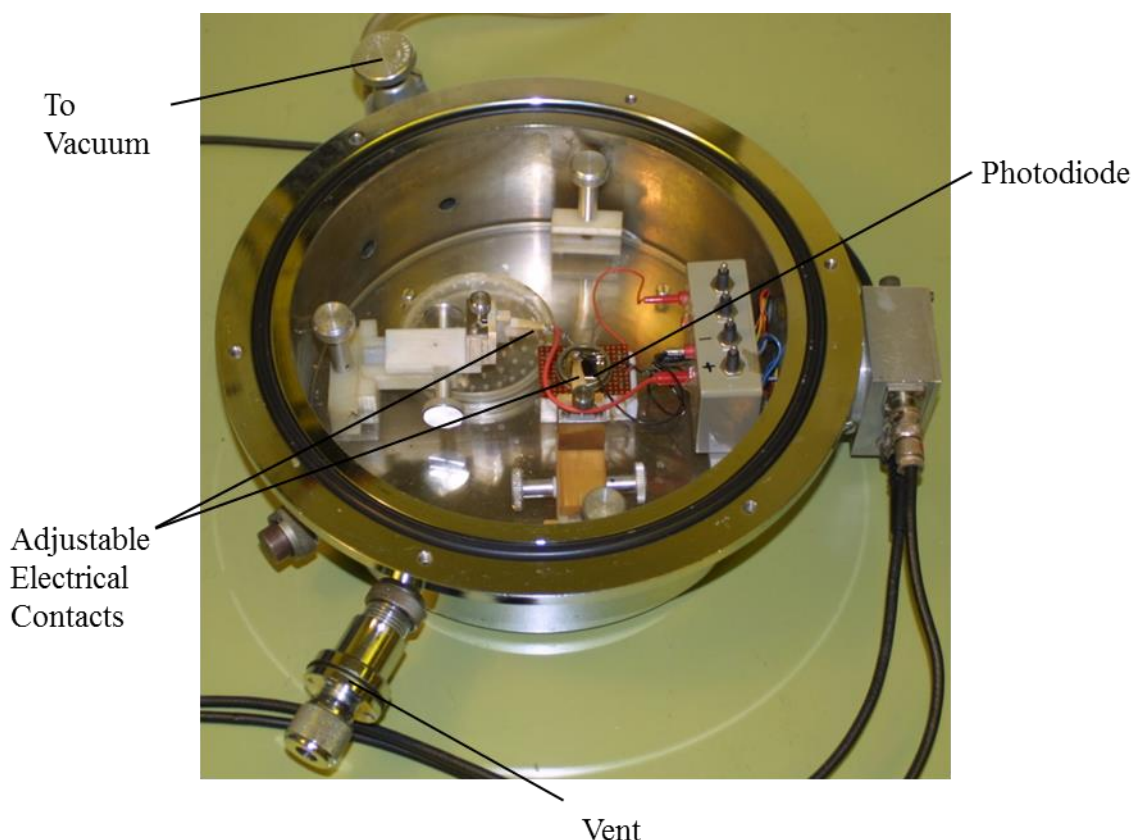


Figure 3.13: Photograph of the setup for electrical and photocurrent measurements of OLEDs.

Photometric and colourimetric measurements were performed using a Photo Research Inc. PR-655 SpectraScan spectroradiometer fitted with a FP-655 flexible probe (3.18 mm tip

diameter). Some (more detailed) electroluminescence spectra were measured using an Ocean Optics USB2000 Miniature Fibre Optic Spectrometer.

Devices on each slide were characterised and graphs generated of electroluminescence, external quantum efficiency, current and photocurrent vs voltage curves and a CIE chromaticity diagram. Turn-on voltages from current and photocurrent vs voltage plots were quoted at the point when photocurrent reached 1 nA.

For external quantum efficiency measurements the radiant power of each OLED was quantified using the photocurrent measured by the photodiode. This photocurrent has a wavelength-dependent relationship to the radiant power emitted and a typical spectral response curve for the photodiode is given in Figure 3.14 and shows the current produced per watt of light power at each wavelength. This curve was used together with the wavelength of the peak emission measured for the device to obtain a photodiode conversion ratio in AW^{-1} , which was then used to calculate the EQE (see also Section 2.3.3).

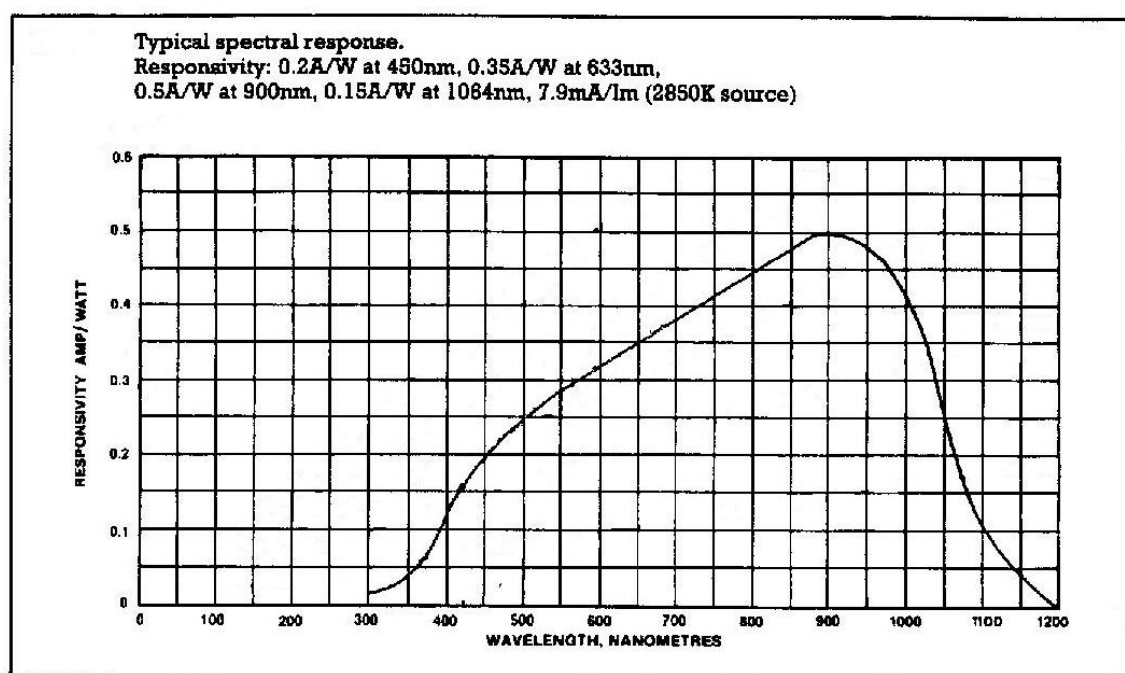


Figure 3.14: Photodiode responsivity curve used to calculate photodiode conversion ratio. Modified from ¹¹.

3.4.3 Electrical Characterisation of OFETs

A Hewlett Packard 4140B pA Meter / DC Voltage Source was used to measure the output and transfer characteristics of each device.

3.5 Device Fabrication

All device fabrication was undertaken in a Class 1000 Cleanroom. Devices were stored under vacuum and kept out of white light in order to reduce degradation.

3.5.1 Standard OLEDs

Step 1: Substrate Preparation

Glass ready-coated in ITO was cut to the required size and cleaned by sonication in propan-2-ol, acetone, 2% Decon 90 solution in deionised water and finally deionised water, each for 15 minutes and dried with a nitrogen gun.

Step 2: PEDOT:PSS

This involved spin-coating PEDOT:PSS onto the clean glass substrate. First it was filtered through a 0.2 μm PTFE syringe filter. A micropipette was then used to drop 200 μl on to the slide, which was then spin-coated at 2500 rpm for 45 seconds and dried on a hot plate at 180 $^{\circ}\text{C}$ for 2 minutes to give a layer 45 nm thick.

Step 3: Active Layer

The active layer that was used here depends on the experiment. The following active layers were used and deposition details given.

⇒ Spin-coated Compound **2** OLED (Chapter 4)

For spin-coated **2** devices, the compound was dissolved in toluene (15 mg ml^{-1}) and spin-coated at 1000 rpm for 1 minute to give a 70 nm thick layer. This was annealed on a hot plate at 80 °C for 30 minutes.

⇒ Evaporated triad molecule OLEDs (Chapter 4)

On top of the PEDOT:PSS layer, a calculated mass of material was evaporated at a certain rate in order to give a thickness of approximately 80 nm (± 20 nm). Experimental details are given in Table 3.2.

Table 3.2: Evaporation conditions for each synthesised compound.

Compound	Mass (mg)	Evaporation Temperature (°C)	Rate (nm s⁻¹)
1	2.5	195-220	0.04-0.06
1A	3.8	230-250	0.05-0.20
2	2.7	265-275	0.02-0.05
3	2.5	265-275	0.14-0.16
4	2.5	275-285	0.10-0.30
5	2.7	270-280	0.10-0.20
6	2.4	230-240	0.15-0.20
7	2.5	340-360	0.15-0.25
8	2.5	210-220	0.20-0.40
9	2.8	320-340	0.10-0.15

⇒ Spin-coated Compound **10** (Chapter 5)

150 μl of the solution (10.61 mg ml^{-1} in chloroform) was spun at 1000 rpm for 1 minute and annealed at 80 $^{\circ}\text{C}$ for 30 minutes, to obtain a thickness of 112 nm, with a range between 75 nm to 161 nm with half of all measurements being 112 ± 20 nm.

⇒ WOLEDs (Chapter 6)

The OXD7 compound was dissolved in chlorobenzene while separate solutions of Compound **2**, Super Yellow and PO-01 were made up in toluene. The individual solutions were then mixed in the proportions necessary to achieve a blended solution of the required concentration and composition. The resulting solvent was toluene (for all compositions not including OXD7) or 1:1 (by volume) toluene: chlorobenzene (for mixtures including OXD7). Devices based on Compound **9** were prepared from chlorobenzene. Approximately 150 μl of the appropriate solution was applied to the surface of the substrate which was then spun for 60 s at 1000 rpm. The coated substrates were annealed at 80 $^{\circ}\text{C}$ for 30 minutes to remove any residual solvent. The total thicknesses of the organic layers in the WOLED devices (i.e. including the PEDOT layer) were around 120-150 nm.

⇒ Spin-coated F8BT OLED (Chapter 8)

These were made by spinning a solution of 5 mg ml^{-1} in chloroform at 1000 rpm for 60 seconds onto the PEDOT:PSS layer and annealed at 230 $^{\circ}\text{C}$ for 30 minutes, to create an 80 nm thick layer of F8BT.

Step 4: Cathode Deposition

Calcium (15 nm) followed directly by aluminium (80 nm) were thermally evaporated at rates of 0.05-0.10 nm s^{-1} to complete the devices. A shadow mask with six holes of radius 2.5 mm was used, yielding six devices per substrate. Six substrates could be put into the

evaporator at any one time, giving a total of 36 devices which could be made in one batch. One such substrate is shown below in Figure 3.15. In Chapter 6, CsF was experimented with as an alternative to the calcium layer in “WOLED 3”. For this, 1 nm of CsF was thermally evaporated at a rate of 0.05-0.10 nm s⁻¹.

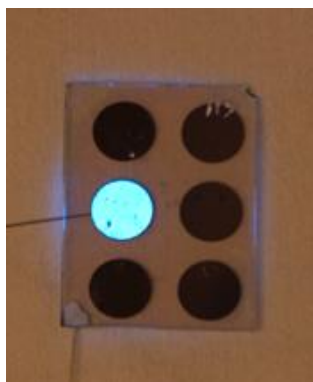


Figure 3.15: Photograph of six devices (based on a phosphorescent blue emitter). One connected to a circuit. Each device has a diameter of 5 mm.

The general structure for each OLED is shown in Figure 3.16 below, the only difference between each being the type of organic material used (represented by the blue striped layer).

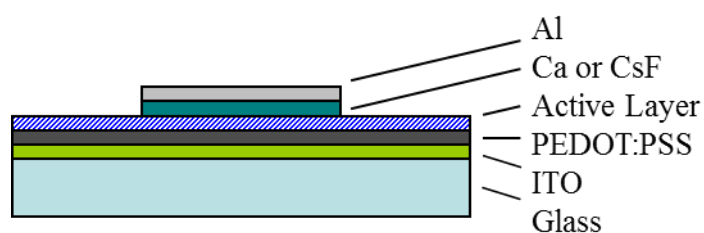


Figure 3.16: Standard OLED structure.

3.5.2 F8BT:IL OLEDs

A modified OLED architecture was used to experiment with the addition of IL blends to F8BT OLEDs. F8BT-only devices were also produced. The different device architectures

are shown below and were produced using identical techniques to those outlined for the Standard OLEDs.

- 1) ITO / F8BT:IL / Al
- 2) ITO / F8BT / Al
- 3) ITO / PEDOT:PSS / F8BT:IL / Al
- 4) ITO / PEDOT:PSS / F8BT / Al

The F8BT:IL layers were prepared from a stock solution of 10 mg F8BT and 0.5 mg IL all dissolved in a total of 2 ml chloroform. The 5 wt% solution was pipetted on to the substrate, which was then spin-coated at 1000 rpm for 60 seconds and annealed at 230 °C for 30 minutes to give a layer approx. 80 nm thick. A later study also experimented with annealing ITO / F8BT:IL / Al and ITO / F8BT / Al devices at 30 °C and 80 °C.

3.5.3 Production of Dissimilar Electrodes

Part of this thesis looks into in-plane devices with dissimilar metal electrodes. In order to deposit these electrodes without breaking the vacuum, the following setup was used inside the evaporator (Figure 3.17).

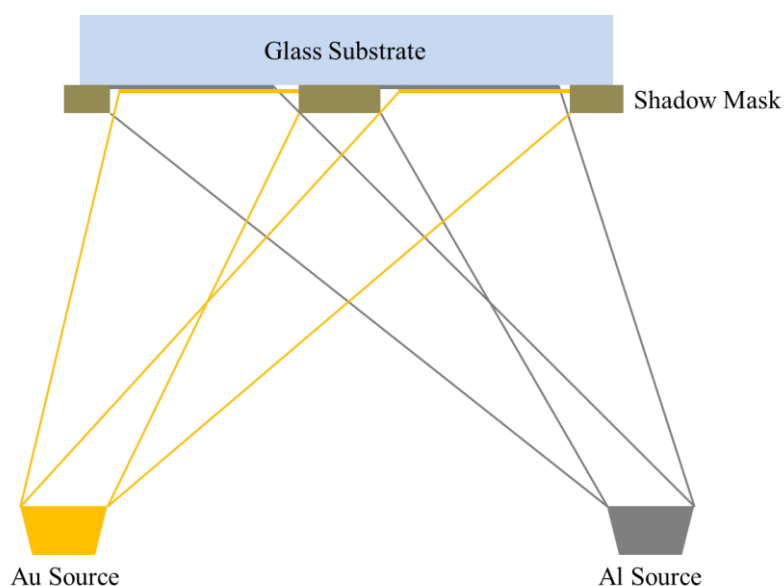


Figure 3.17: Schematic showing the set up and evaporation path of the gold and aluminium inside the evaporator.

This allowed for the structure shown in Figure 3.18(c). Figure 3.18(a) and (b) show microscope images of two different sets of these electrodes.

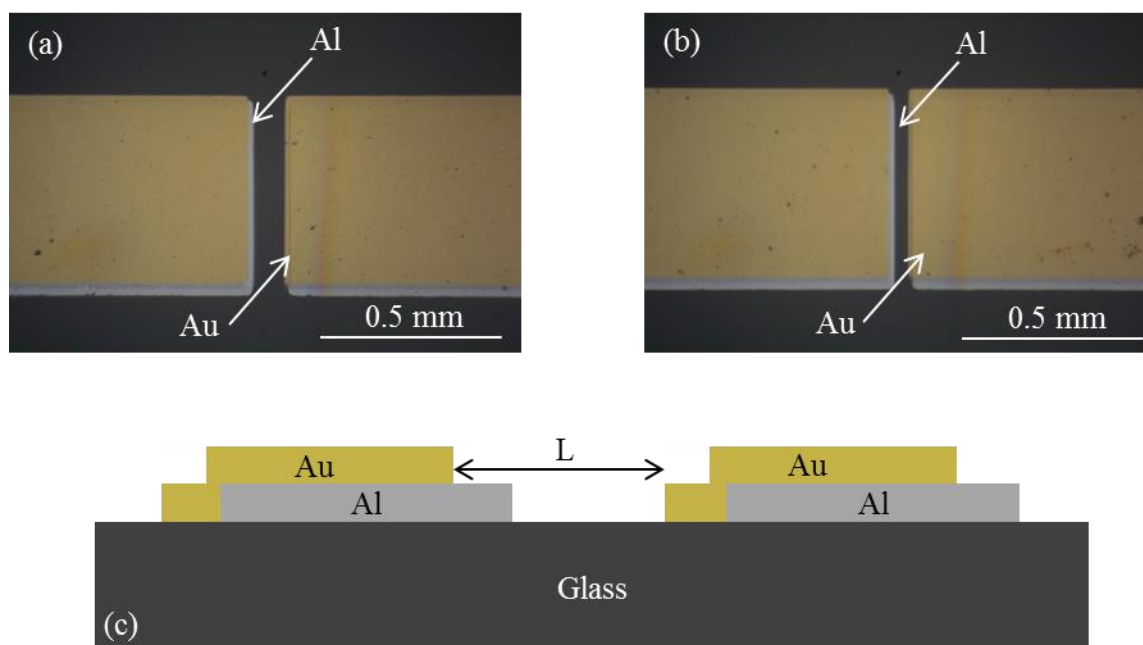


Figure 3.18: (a) and (b) are microscope images of the electrodes on glass where $L = 100 \mu\text{m}$ and $L = 50 \mu\text{m}$ respectively and (c) shows a cross-section schematic of the electrodes on glass.

These dissimilar electrodes were used for in-plane OLEDs and in some OFETs.

3.5.4 F8BT:IL In-Plane OLED with Dissimilar Electrodes

The structure of these devices is given below in Figure 3.19.

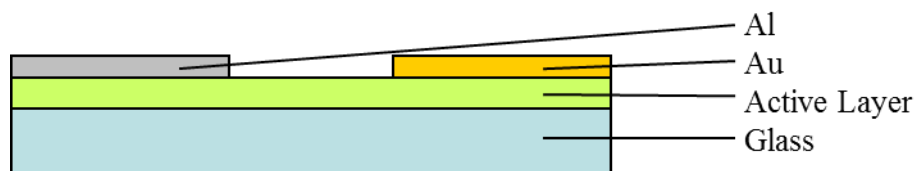


Figure 3.19: Structure of F8BT:IL in-plane OLEDs produced using the technique for dissimilar electrodes.

The solution used was from a stock of 10 mg F8BT and 0.5 mg IL all dissolved in a total of 2 ml chloroform. The solution was pipetted on to a glass slide, which was then spin-coated at 1000 rpm for 60 seconds and dried at 30 °C for 30 minutes to give a layer approx. 80 nm thick. The Al/Au electrodes were evaporated on top using the dissimilar electrode technique described above.

3.5.5 Standard OFETs

The structure of a “Standard OFET” in this thesis, with a bottom gate contact, is given in Figure 3.20 below.

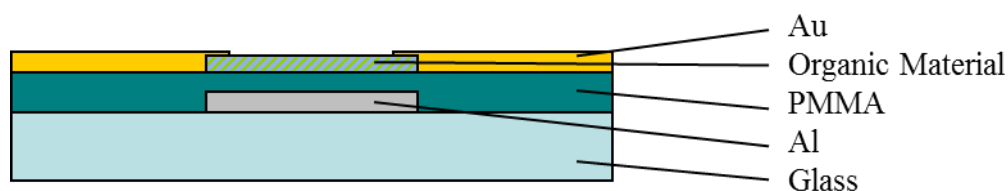


Figure 3.20: Schematic of a Standard OFET.

Step 1: Substrate Preparation

A standard microscope slide (VWR International) was cleaned by sonication in acetone, propan-2-ol and finally deionised water, each for 15 minutes. It was then dried in a stream of nitrogen and baked on a hot plate at 95 °C for 30 minutes.

Step 2: Gate electrode

Al (30 nm) was thermally evaporated through a shadow mask (Figure 2.11) at a rate of 0.1-0.15 nm s⁻¹ at approximately 5-8 x 10⁻⁶ mbar pressure.

Step 3: Gate dielectric

PMMA solution in anisole (50 mg ml⁻¹) was spin-coated on top (500 rpm for 10 seconds then 3000 rpm for 50 seconds) and annealed for 30 minutes at 120 °C to give a thickness of 150 nm.

Step 4: Organic Material

Pentacene, Compound **1**, Compound **2**, or Compound **8** (approx. 30 nm) were thermally evaporated through a shadow mask at a rate of approximately 0.02-0.15 nm s⁻¹ at around 1-4 x 10⁻⁶ mbar pressure.

Step 5: Gold source and drain

To complete the devices, 30 nm of gold was thermally evaporated through a shadow mask (Figure 3.21) at a rate of $0.1\text{-}0.15\text{ nm s}^{-1}$ at approximately $5\text{-}8 \times 10^{-6}$ mbar pressure.

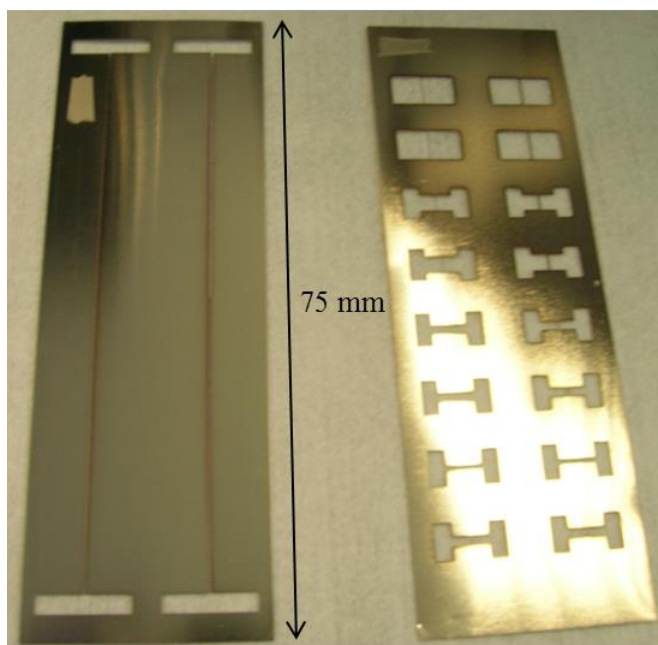


Figure 3.21: Gate mask (left) and source-drain mask (right).

This process yielded 16 transistors per substrate with various channel dimensions as shown in Figure 3.22 and Table 3.3.

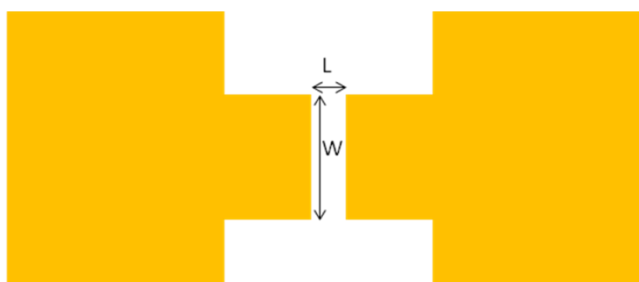


Figure 3.22: Plan view of source and drain electrodes showing the channel dimensions where L is channel length and W is channel width.

Table 3.3: Channel dimensions of the 16 devices that can be produced using the shadow masks shown in Figure 3.22.

Length (μm)	Width (μm)	Length (μm)	Width (μm)
200	4000	50	4000
200	4000	50	4000
200	2000	50	2000
200	2000	50	2000
100	1000	50	1000
100	1000	50	1000
100	500	50	500
100	1000	50	1000

3.5.6 F8BT Transistors with Top Gate (Chapter 8)

F8BT transistors were made with the top gate bottom contact structure given in Figure 3.23.

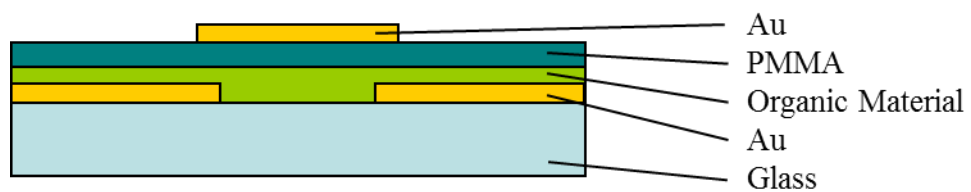


Figure 3.23: F8BT transistors with top gate structure.

Step 1: Source-drain

Gold (30 nm) was thermally evaporated at $5\text{-}8 \times 10^{-6}$ mbar pressure.

Step 2: Organic layer

F8BT (5 mg ml⁻¹ in chloroform) was spin-coated at 1000 rpm for 60 seconds and annealed at 230 °C for 30 minutes to give an 80 nm thick layer.

Step 3: Gate dielectric

PMMA solution in anisole (50 mg ml⁻¹) was spin-coated on top (500 rpm for 10 seconds then 3000 rpm for 50 seconds) and annealed for 30 minutes at 120 °C to give a thickness of 150 nm.

Step 4: Gate

The devices were completed by evaporating a gold gate electrode on top.

3.5.7 OFETs with Dissimilar Electrodes

Compound **2** was also incorporated into a transistor device with dissimilar electrodes deposited using the techniques described in Section 3.5.3, to see if the efficiency could be improved. The bottom gate top contact structure given in Figure 3.24 was obtained.

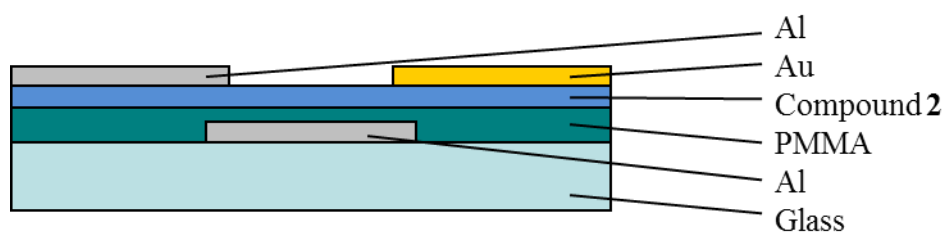


Figure 3.24: Dissimilar electrode Compound **2** device.

F8BT transistors were also produced using the structure in Figure 3.24, but with an F8BT:IL blend in place of Compound **2**. See Section 3.5.2 for details of how to make the F8BT:IL solution.

3.5.8 Progression Towards Multilayer OFET Structure

As part of a study into preparing a multilayer OFET structure,¹² in Chapter 7 a systematic approach was adopted, which started with adding an evaporated layer of pentacene as a hole transport layer between the PMMA and Compound **2** as shown in Figure 3.25. The pentacene was evaporated at $0.10\text{--}0.15\text{ nm s}^{-1}$ and two different thicknesses were experimented with; 7 nm and 40 nm.

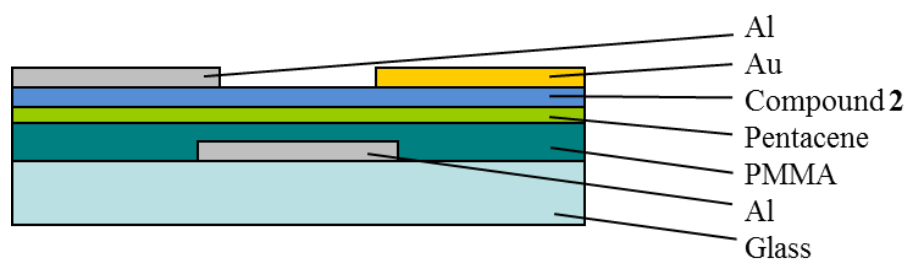


Figure 3.25: Dissimilar electrode device with pentacene hole transport layer: Al / PMMA / Pentacene / Compound **2** / Al/Au.

An alternative structure was also considered where Compound **2** was evaporated as the top layer in the device and is given in Figure 3.26.

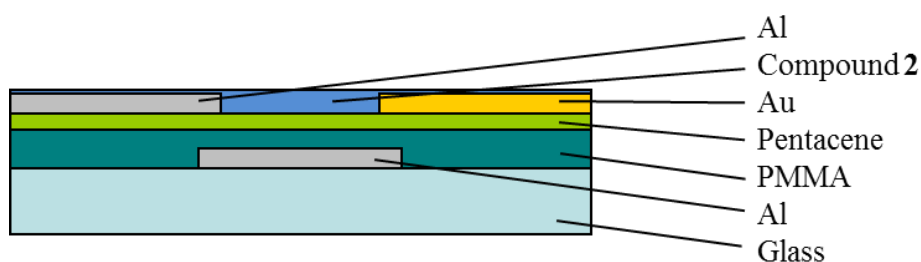


Figure 3.26: Alternative structure with Compound **2** as top layer above dissimilar electrodes.

The final step in preparing the multilayer OFET device with comparable structure to that reported in Capelli et al¹² involved the deposition of the electron transporting material OXD7 to give the structure shown in Figure 3.27. 2 mg of OXD7 was evaporated on top of Compound **2** at a rate of 0.05-0.15 nm s⁻¹ to give a 40 nm thick layer.

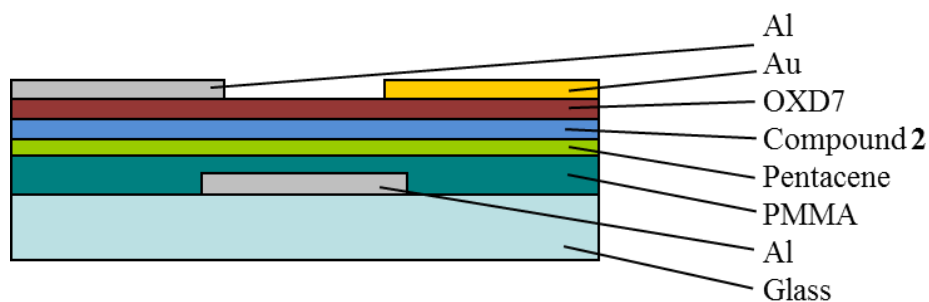


Figure 3.27: Dissimilar electrode OFET structure with pentacene hole transporting layer and OXD7 electron transporting layer: Al / PMMA / Pentacene / Compound **2** / OXD7 / Al/Au.

3.5.9 Nanogap Devices

A number of devices with a 500 nm gap or less were made on silicon wafers by a new photolithographic technique.¹³ Thanks are due to Mark Rosamond for producing these contacts. Materials were then incorporated into the structure as shown in Figure 3.28 below, by thermal evaporation or spin-coating.

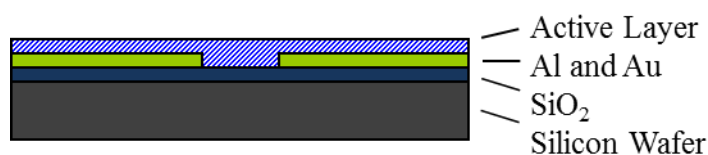


Figure 3.28: Nanogap structure.

3.6 Conclusions

This chapter has described the key properties of materials used throughout the thesis. Experimental methods and characterisation were discussed and a detailed description of device fabrication has been presented for OLEDs and OFETs.

3.7 References

- 1) Editor: D. R. Lide, *CRC Handbook of Chemistry and Physics*, 86th Ed.
- 2) J. Zaumseil, C. R. McNeill, M. Bird, D. L. Smith, P. P. Ruden, M. Roberts, M. J. McKiernan, R. H. Friend, H. J. Siringhaus, *J. Appl. Phys.*, 103, 064517, **2008**.
- 3) K. T. Kamtekar, C. Wang, S. Bettington, A. S. Batsanov, I. F. Perepichka, M. R. Bryce, J. H. Ahn, M. Rabinal, M. C. Petty, *J. Mater. Chem.*, 16, 3823-3835, **2006**.
- 4) Q.-X. Tong, S.-L. Lai, M.-Y. Chan, Y.-C. Zhou, H.-L. Kwong, C.-S. Lee, S.-T. Lee, *Chem. Mater.*, 20, 6310-6312, **2008**.
- 5) C.-G. Zhen, Z.-K. Chen, Q.-D. Liu, Y.-F. Dai, R. Y. C. Shin, S.-Y. Chang, J. J. Kieffer, *Adv. Mater.*, 21, 2415-2429, **2009**.
- 6) K. R. J. Thomas, J. T. Linn, Y.-T. Tao, C.-H. Chuen, *Chem. Mater.*, 16, 5437-5444, **2004**.
- 7) A. L. Fisher, K. E. Linton, K. T. Kamtekar, C. Pearson, M. R. Bryce, M. C. Petty, *Chem Mater. Commun.*, 23, 1640-1642, **2011**.
- 8) K. E. Linton, A. L. Fisher, C. Pearson, M. A. Fox, L.-O. Pålsson, M. R. Bryce, M. C. Petty, *J. Mater. Chem.*, 22, 11816-11825, **2012**.

-
- 9) M. C. Petty in *Molecular Electronics: From Principles to Practice*, **2007**, John Wiley & Sons Ltd., Chapter 7.
 - 10) P. Eaton and P. West in *Atomic Force Microscopy*, **2010**, Oxford University Press, Chapter 2.
 - 11) RS stock no. 308-067. Sheet F14784.
 - 12) R. Capelli, S. Toffanin, G. Generali, H. Usta, A. Facchetti, M. Muccini, *Nat. Mater.*, **9**, 496-503, **2010**.
 - 13) M. C. Rosamond, A. J. Gallant, M. C. Petty, O. Kolosov, D. A. Zeze, *Adv. Mater.*, **23**, 5039-5044, **2011**.

4 Simple OLEDs Incorporating Triad Molecules

4.1 In this Chapter...

The effect of introducing a carbazole moiety into a previously reported ambipolar triad molecule was investigated and the new molecular structure incorporated into a simple OLED device architecture. The influence of the molecular change was studied by measuring fundamental properties of the OLED – emission colour, brightness, power efficiency, current efficiency and external quantum efficiency. In addition, a series of analogous carbazole-containing triad molecules was studied to show how chemical changes could enable tuning of the emission colour in OLEDs.

4.2 Improvement of Device Characteristics with Carbazole

Kamtekar et al¹ have previously reported OLEDs based on a D-A molecule incorporating a triphenylamine hole transporting moiety, oxadiazole electron transporting group and fluorene emitter. This molecule showed ambipolar characteristics and produced green-blue OLEDs. The original Kamtekar molecule is referred to as Compound **1** in this study and was used as a basis for the further development of the new molecule, Compound **2**. Both structures are given in Figure 4.1 and were synthesised by the Bryce group at the Department of Chemistry, Durham University. The subtle difference in the molecular structure of Compound **2** results in a carbazole-oxadiazole D-A molecule still incorporating fluorene. The carbazole group has previously been associated with deep blue OLEDs² and, as a good hole conductor, was expected to improve the ambipolar characteristics of the molecule, which in turn was expected to lead to an efficiency improvement when incorporated into an OLED. Also, the additional bond compared to Compound **1** was expected to flatten the molecule, which may allow closer packing and

thus improve transport of both holes and electrons throughout the organic layer when built into an OLED.

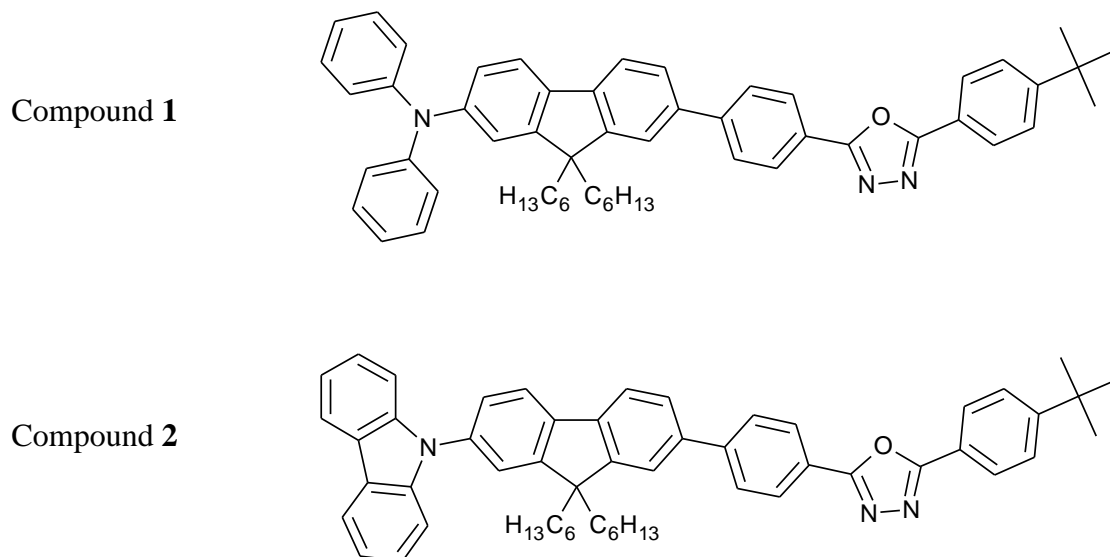


Figure 4.1: Structures of compounds **1** and **2**.

A computational study (Appendix A) using Density Functional Theory (DFT) calculations on analogous molecules to **1** and **2** (thanks to Dr Mark Fox in the Department of Chemistry, Durham University) showed that both the Highest Occupied Molecular Orbital (HOMO) and Lowest Unoccupied Molecular Orbital (LUMO) levels were lowered in Compound **2**, and the overall band gap was increased from 3.22 eV in Compound **1** to 3.48 eV in Compound **2** (Figure 4.2). The decrease in HOMO for Compound **2** is predicted to increase the energy barrier for holes from the ITO / PEDOT:PSS anode into the emitting layer by around 0.4 eV.

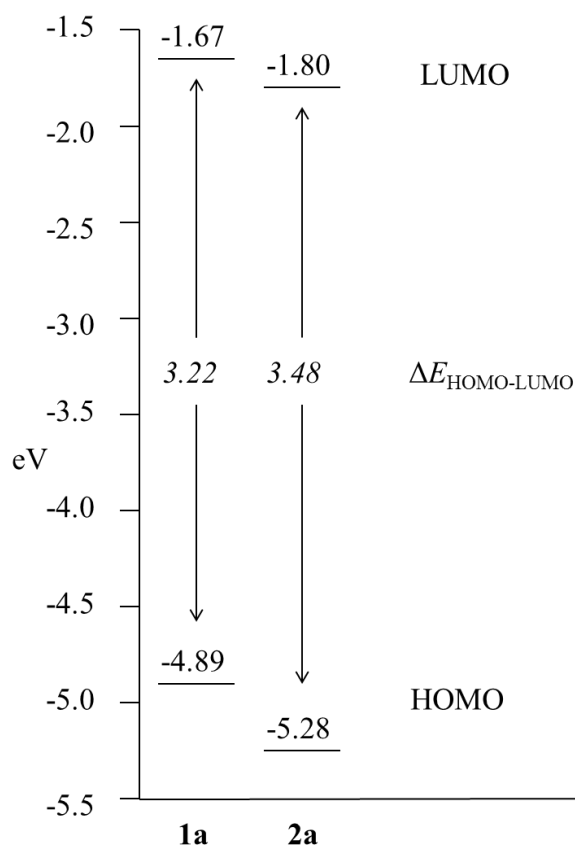


Figure 4.2: Orbital energy level diagrams for the compounds **1a** and **2a**. The **a** denotes that the optimised geometries contain C_2H_5 groups instead of C_6H_{13} groups to reduce computational efforts.

The full energy diagram for all the triad compounds can be found on page 104. Although independent values for the carrier concentrations and mobilities of the compounds were beyond the scope of this work, the conductivity data are consistent with holes being the majority carriers in both compounds. Presented in Figure 4.3 are the results for OLEDs made with spin-coated layers of compounds **1**¹ and **2**. To correct for variations in thickness and allow for direct comparison between devices, voltages were converted to electric field and current to current density.

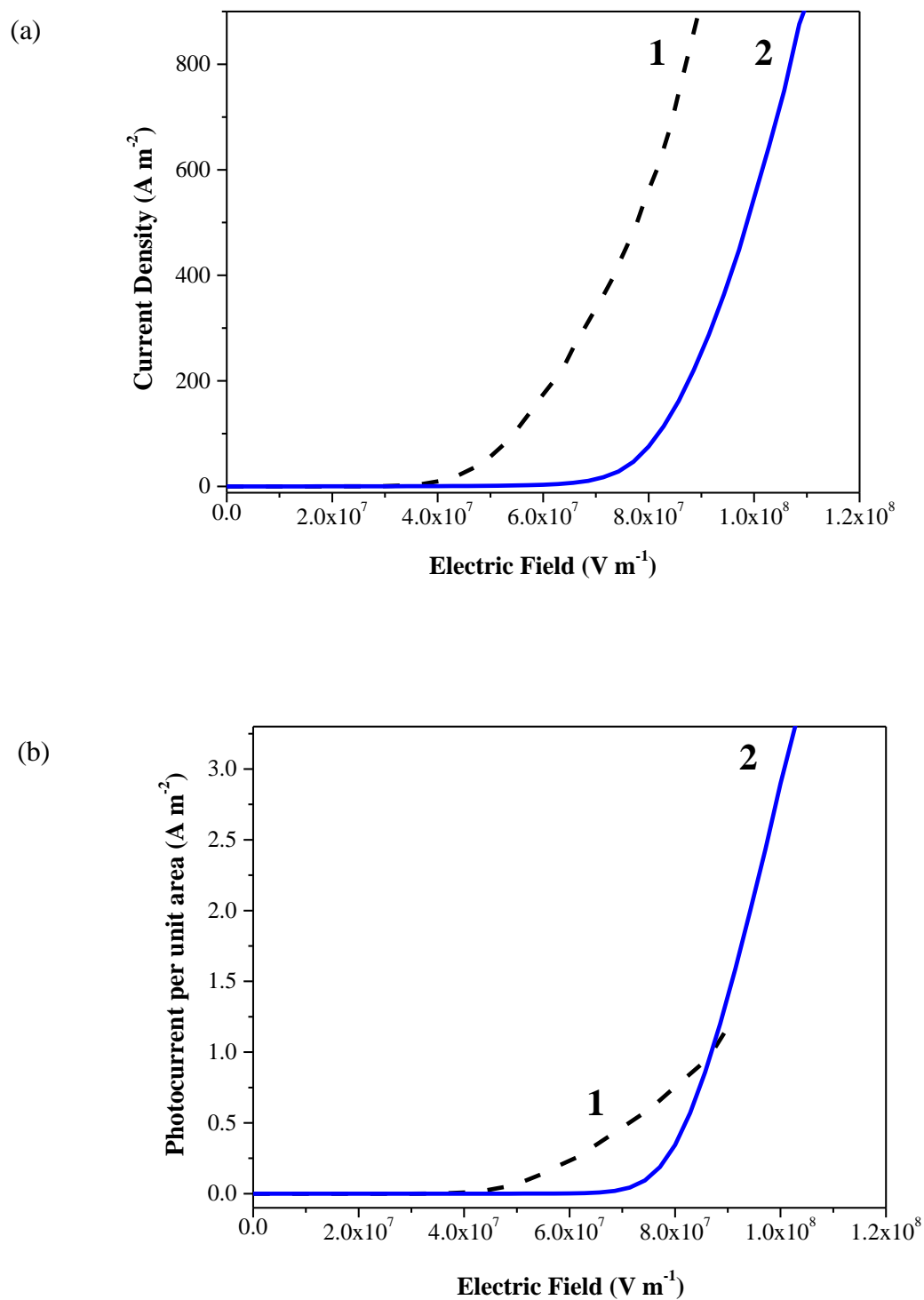


Figure 4.3: (a) Current density as a function of electric field; (b) photocurrent per unit area as a function of electric field. Active layers in OLEDs produced by spin-coating. Note numbers **1** and **2** refer to the compounds in Figure 4.1. Device architecture: ITO / PEDOT:PSS / Compound **X** / Ca / Al where **X** refers to Compound **1** or **2**.

Results shown for devices containing Compound **2** are amongst the best performing devices of all batches made in this study. Other devices showed a similar trend and magnitude in IV plots. From Figure 4.3(a) it is clear that the conductivity of **2** is lower than **1**. This could be explained by the increased energy barrier between the HOMO of **2** and the ITO / PEDOT:PSS as discussed earlier. This is also the likely cause of the higher turn-on electric field observed for films of Compound **2**. Figure 4.3(b), above reveals a smaller photocurrent per unit electric field for **2** below $\sim 9 \times 10^{-7} \text{ V m}^{-1}$. However, J_{ph} is not reduced as much as J . It may be that the improved balance between the electron and hole current for **2** leads to the significant increase in the external quantum efficiency (EQE) as shown in Figure 4.4 below. A fivefold enhancement in EQE is achieved, from 0.26% for **1** to 1.25% in the case of Compound **2**. Typical variations between devices containing Compound **2** were from ca. 0.85% to 1.25%.

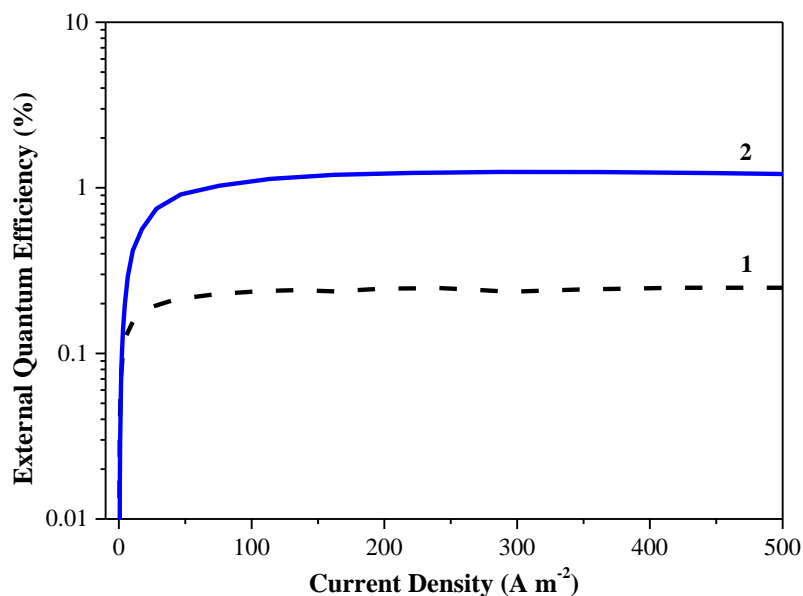


Figure 4.4: External quantum efficiencies of OLED devices based on spin-coated compounds **1** and **2**.

Figure 4.5 compares the electroluminescence (EL) spectra for **1** and **2**, revealing a blue shift of around 56 nm in the peak emission of **2** relative to **1**. For **1**, the peak emission is 487 nm while for **2** peak emission occurs at a lower wavelength of 431 nm. This shift suggests an increased HOMO-LUMO separation for Compound **2**. Again, this is confirmed by the DFT calculations which show a HOMO-LUMO separation of 3.48 eV for **2** in comparison with 3.22 eV for **1**.

The shape of the emission spectra also varies slightly between the two analogues, with **1** exhibiting three main peaks at 458 nm, 487 nm and 517 nm together with a shoulder at around 555 nm. In contrast, Compound **2** shows four peaks at 413 nm, 431 nm, 452 nm and 480 nm and a shoulder at approximately 520 nm.

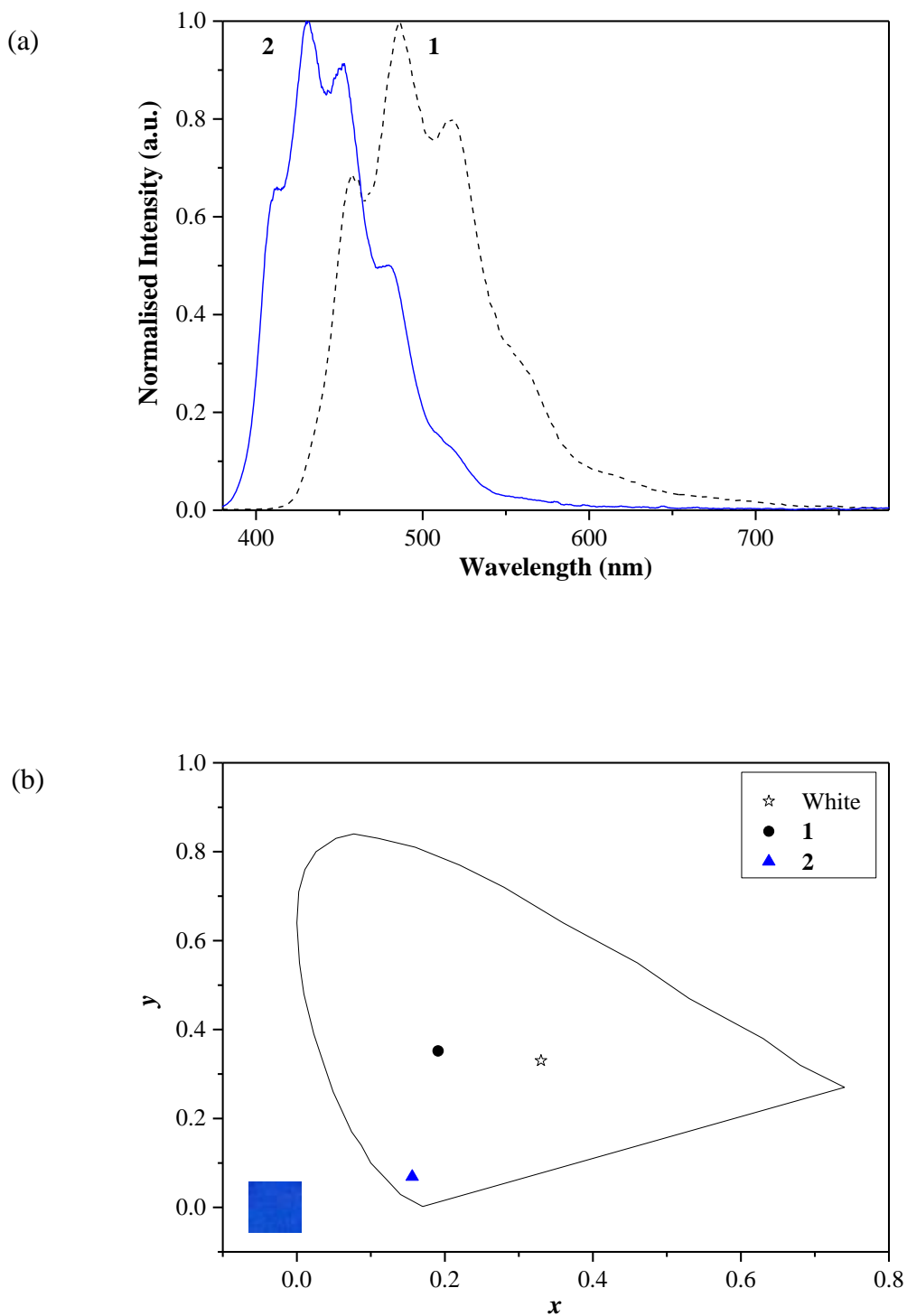


Figure 4.5: (a) EL spectra of devices based on spin-coated layers of **1** and of **2**; (b) comparison of CIE coordinates of devices comprising **1** and **2**, measured at $J \sim 150 \text{ A m}^{-2}$ for **1** and $J \sim 50 \text{ A m}^{-2}$ for **2**. Active layers in OLEDs produced by spin-coating. Inset is a photograph of the deep-blue OLED of **2**.

The blue shift for **2** becomes further apparent on inspection of the CIE diagram (Figure 4.5(b)). Compound **2** shows a particularly saturated deep blue emission (0.16, 0.07) compared to **1** (0.19, 0.35). This is very close to the National Television System Committee (NTSC) standard blue CIE coordinates of (0.14, 0.08), as seen in Table 2.1 in Chapter 2. A photograph of the light output from an OLED of **2** is given as an inset in the CIE diagram and further illustrates both the depth of the blue colour and its uniformity across the OLED.

4.3 Effect of Processing Technique on Device Characteristics

The effect of the processing technique used to deposit the active layer was considered by comparing spin-coated and evaporated films of compounds **1** and **2**. The impact on device characteristics is summarised in Table 4.1. Data for the spin-coated device of **1** have been taken from measurements of a device from the previous Kamtekar et al publication.¹

Table 4.1: Comparison of results for **1** and **2** with spin-coated and evaporated layers.

Compound	Deposition Method	Emissive Layer Thickness (nm)	Peak Emission (nm)	FWHM (nm)	CIE ^a _x	CIE ^a _y	Turn-on Electric Field (V m ⁻¹) (Turn-on Voltage, V)	EQE ^b (%)	Current Efficiency ^c (cd A ⁻¹)	Power Efficiency ^c (lm W ⁻¹)	Brightness ^c (cd m ⁻²)
1	Spin-coated	110	487	87	0.19	0.35	2.96 x 10 ⁷ (3.5)	0.26	-	-	-
1	Evaporated	70	484	105	0.16	0.25	6.24 x 10 ⁷ (4.3)	0.63	0.93	0.30	943
2	Spin-coated	70	431	67	0.16	0.07	4.50 x 10 ⁷ (3.2)	1.25	0.47	0.18	483
2	Evaporated	105	431	81	0.16	0.08	3.99 x 10 ⁷ (4.2)	4.71	1.49	0.53	1520

^aCIE coordinates of spin-coated **1** measured at an applied current of 0.5 mA (J ~ 150 A m⁻²). All other OLEDs measured at an applied current of 1 mA (J ~50 A m⁻²). ^bEQE measured at 100 ± 30 cd m⁻². ^cMeasured under an applied current of 20 mA (J ~ 10³ A m⁻²).

The surface morphologies of the different layers used in this study are shown by the AFM images in Figure 4.6 below.

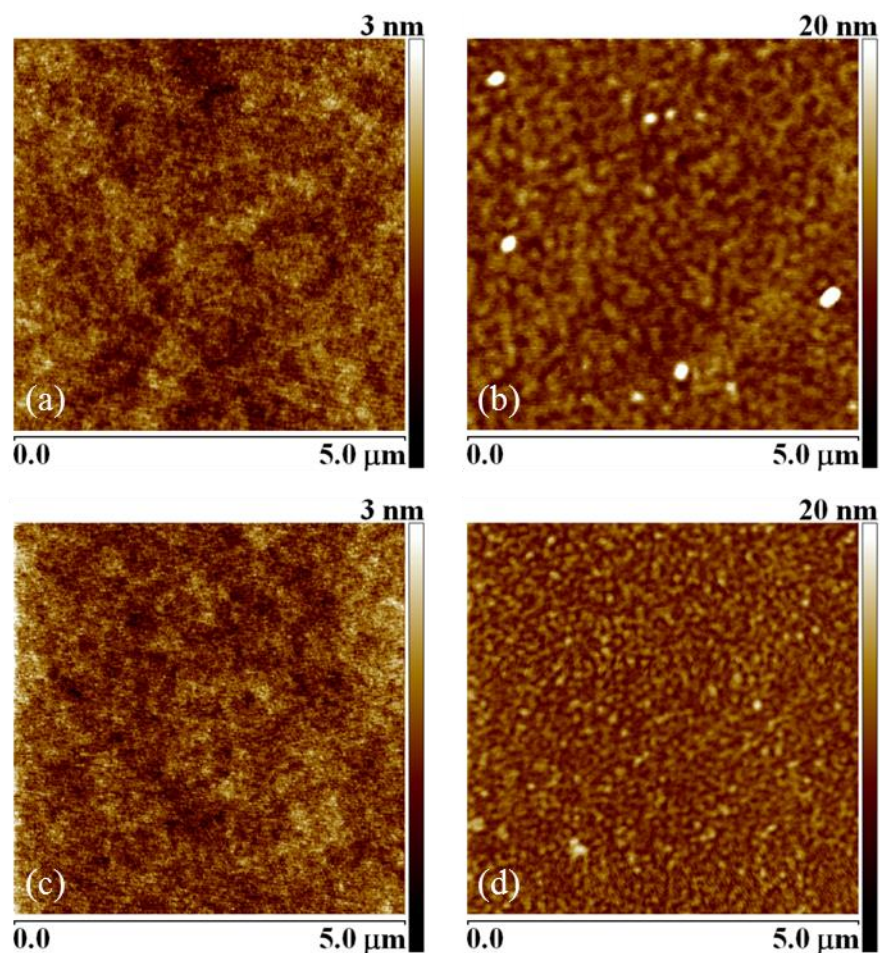


Figure 4.6: AFM images of films of (a) spin-coated **1** (film thickness = 53 nm); (b) evaporated **1** (64 nm); (c) spin-coated **2** (61 nm); and (d) evaporated **2** (59 nm). The film thickness values were obtained using the scratch test technique discussed in Chapter 3.4.1

Relatively smooth, apparently amorphous surfaces are evident for the spin-coated layers of both compounds, however distinct grains are apparent in the AFM images of the evaporated materials, suggesting these films are crystalline, although this has not been conclusively proven. Comparing R_a (surface roughness) values (see Experimental chapter) shows spin-coated layers to be the smoothest, showing a roughness of 0.26 nm for

Compound **1** and 0.30 nm for Compound **2**. Evaporated films of Compound **1** were rougher at 1.33 nm and evaporated Compound **2** showed a roughness of 1.24 nm.

Photoluminescence measurements carried out by the Department of Chemistry, Durham University are given in Appendix B and reveal no major differences in the fluorescence quantum efficiencies for the films despite their different morphological forms. The more ordered polycrystalline structure of the thermally evaporated organic layers should lead to improved carrier mobilities for both holes and electrons as carriers can move more easily through a crystalline structure than an amorphous structure. For example, single crystal silicon can show mobilities of greater than $1000 \text{ cm}^2 \text{ V}^{-1} \text{ s}^{-1}$,³ whereas amorphous silicon typically shows values of $0.5\text{-}1.0 \text{ cm}^2 \text{ V}^{-1} \text{ s}^{-1}$; as a comparison, some organic single crystals have been reported with mobilities greater than $10 \text{ cm}^2 \text{ V}^{-1} \text{ s}^{-1}$.⁴ Indeed devices based on the evaporated emitters were found to possess a significantly higher conductivity than those fabricated by spin-coating, as shown in Figure 4.7.

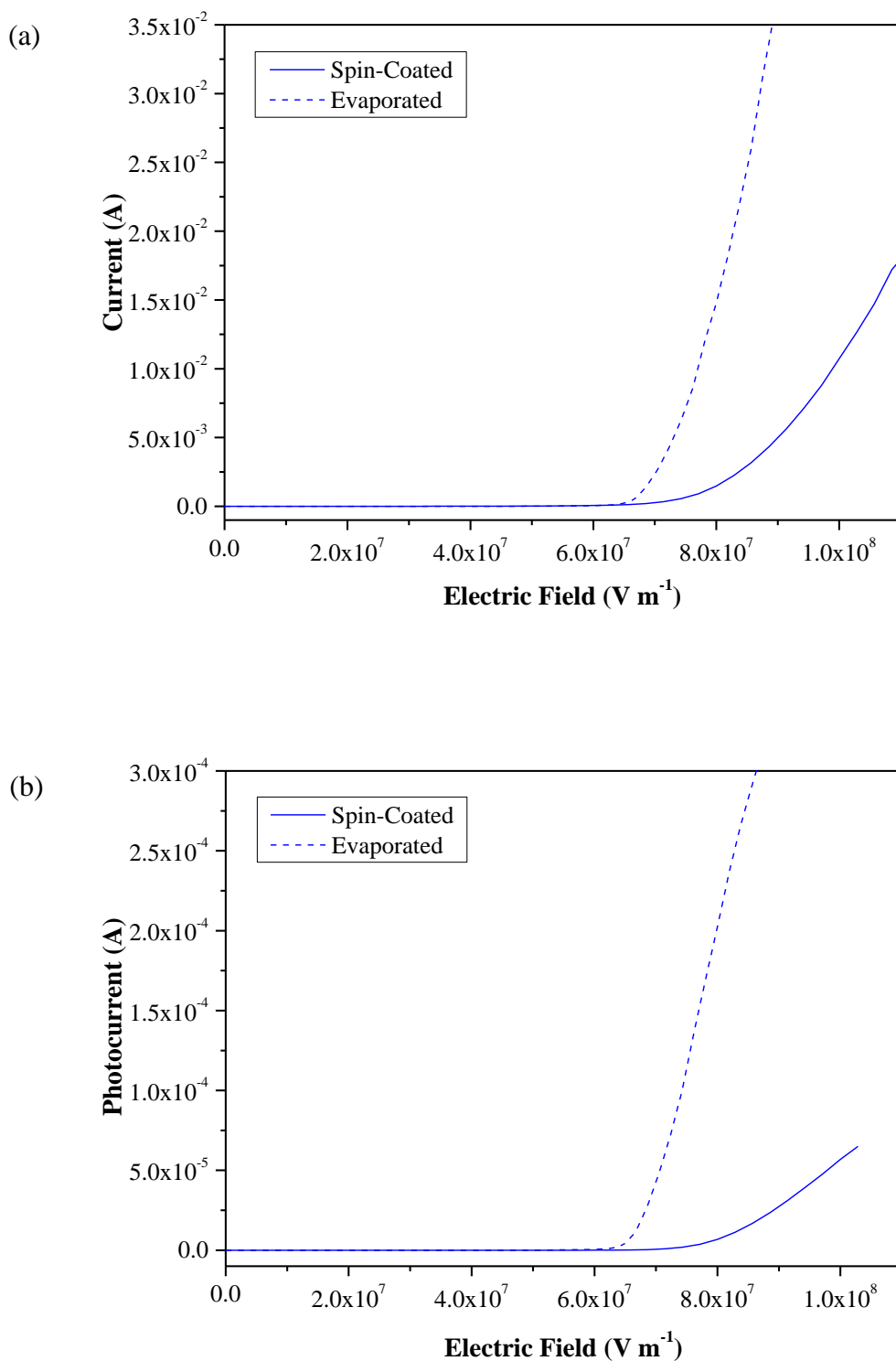


Figure 4.7: Comparison of the current (a) and photocurrent (b) versus electric field for spin-coated and evaporated devices of Compound 2.

Table 4.1 indicates that the efficiencies of **2** are improved more (ca. 4 times in the case of EQE) than those of **1** (ca. 2.5 times for the EQE) by using thermal evaporation. It is suggested that the electron mobility is in fact more enhanced than the hole mobility, leading to a better balance between the electron and hole currents and, consequently, to the increase in the efficiency, as shown in Figure 4.8. Additionally, the better balance of charge carrier mobility may have moved the emission zone further away from the Ca/Al cathode, reducing the EL quenching effects.

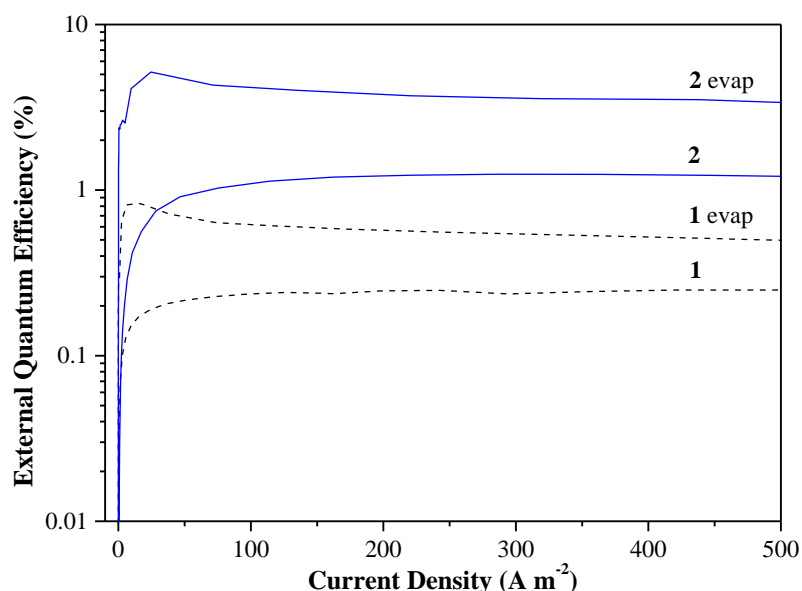


Figure 4.8: External quantum efficiencies of OLED devices based on **1** and **2**. Data are shown for OLEDs in which the active layer has been deposited by both spin-coating and thermal evaporation (data denoted as **1** evap and **2** evap).

It is not believed that the small variations in thickness explain the differences in EQE. For both **1** and **2** the use of evaporated layers enhances the device EQE. Furthermore, the current and power efficiencies are both improved for the evaporated layer of **2**. The

efficiencies of these single-active-layer devices compare very favourably with those reported in multilayer blue emitting devices based on ambipolar compounds.⁵

Figure 4.9 shows that while the different processing methods have little influence on the colour of the OLEDs incorporating **2**, the evaporated OLEDs containing **1** reveal a blue shift in the CIE coordinates when compared to devices fabricated using spin-coating. This is possibly related to microcavity effects resulting from the different film thicknesses.⁶ Microcavity effects refer to how light is trapped by the edges of layers inside the OLED. It is known that the thickness of the layer forming the microcavity influences the colour of emitted light, with thinner layers producing a blue shift.⁶

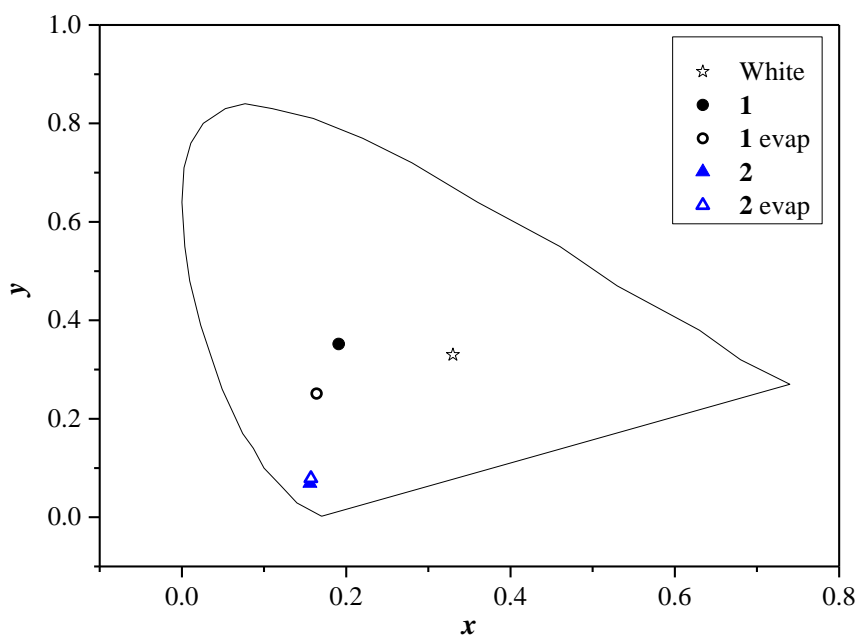


Figure 4.9: Comparison of CIE coordinates of devices comprising **1** and **2**, measured at $J \sim 150 \text{ A m}^{-2}$ for **1** and $J \sim 50 \text{ A m}^{-2}$ for **2**. Active layers in OLEDs produced by spin-coating and thermal evaporation.

In summary, the new ambipolar molecule **2** was successfully integrated into a simple, single-active-layer OLED to produce devices which are amongst the highest performing

deep-blue OLEDs. Using thermal evaporation to produce layers of **2**, devices with an EQE of over 4% and CIE coordinates of (0.16, 0.08) were achieved. This combination of highly efficient deep-blue emission and a simple device architecture is very attractive for further development. Recently Lee et al⁷ have reported a device with 5.6% external quantum efficiency, however the device structure is complex and the colour is not as deep-blue, with CIE coordinates (0.146, 0.148). Devices close to the NTSC blue standard, with efficiencies near 7.18% and CIE coordinates (0.156, 0.088) have also been reported, but again based on complex stack structures.⁸ Most deep blue OLEDs based on a single active layer show lower efficiencies of 0.8-2.5%.⁹⁻¹¹

Some preliminary data indicating an improved stability for unencapsulated OLEDs based on evaporated layers of **2** over evaporated layers of **1** were collected and are shown below in Figure 4.10.

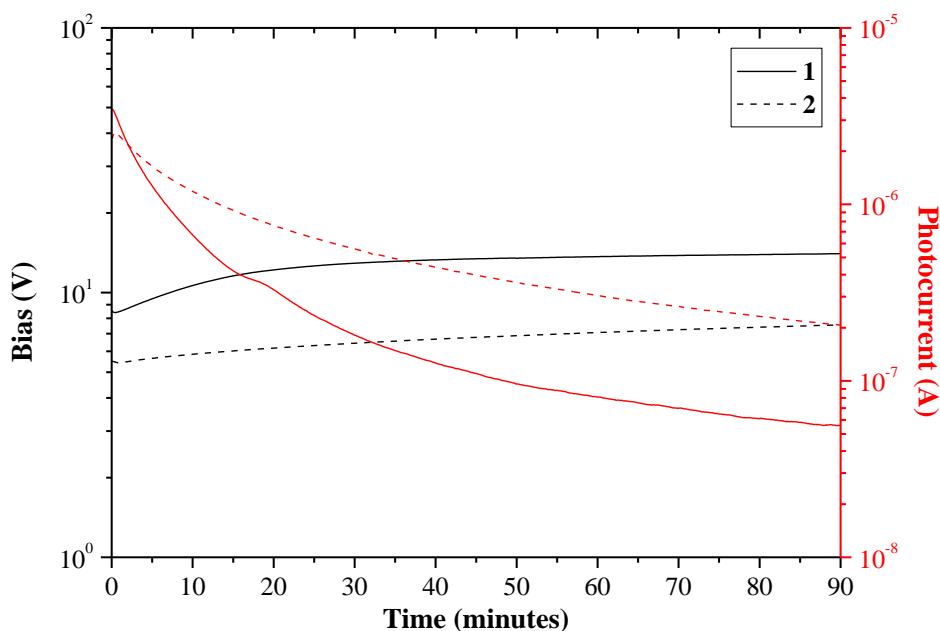


Figure 4.10: Stability data of OLEDs containing evaporated layers of Compound **1** and Compound **2**. Current maintained at 1mA.

Comparing OLEDs based on **1** and **2**, it can be seen that the light output for Compound **1** falls off more rapidly for the first 50 minutes of operation, after which time the rate of device degradation appears equal for both materials. Simultaneously, the voltage required to maintain a constant device current of 1 mA increased for both materials, but initially at a higher rate for OLEDs based on **1**. Based on these observations, it can be concluded that Compound **2** is the more stable of the two molecules. Apart from the first three minutes of operation, the light output from the OLED based on **2** is consistently higher and the operating voltage required to maintain the device current is always lower. Thus the OLED fabricated using Compound **2** achieves higher light output for a lower applied voltage, which likely aids the stability as the electric field applied across the compound is lower throughout device operation.

4.4 Colour Tuning Study

The success with the carbazole moiety encouraged further research into these types of compounds. The next stage was to synthesise a number of compounds analogous to **2**, to investigate if any further improvements could be made using the same device structure and techniques employed in the development of devices containing **2**. This idea led the way to the synthesis of compounds **3-8**, again by colleagues in the Department of Chemistry at Durham University. These compounds can be found in the Experimental chapter and are included again in Table 4.2 for ease of reference.

Table 4.2: Structures of compounds 3-8.

Compound	Structure
3	<p>Chemical structure of compound 3: A triad molecule consisting of a carbazole core substituted with a tert-butylphenyl group and a pyridine ring, which is further substituted with a tert-butylphenyl group and an oxadiazole ring.</p>
4	<p>Chemical structure of compound 4: A triad molecule consisting of a carbazole core substituted with a tert-butylphenyl group and a thiophene ring, which is further substituted with a tert-butylphenyl group and an oxadiazole ring.</p>
5	<p>Chemical structure of compound 5: A triad molecule consisting of a carbazole core substituted with two methoxy groups and a phenyl ring, which is further substituted with a tert-butylphenyl group and an oxadiazole ring.</p>
6	<p>Chemical structure of compound 6: A triad molecule consisting of a carbazole core substituted with two tert-butylphenyl groups and a phenyl ring, which is further substituted with a tert-butylphenyl group and an oxadiazole ring.</p>
7	<p>Chemical structure of compound 7: A triad molecule consisting of two carbazole cores linked by a phenyl ring, with tert-butylphenyl groups and an oxadiazole ring.</p>
8	<p>Chemical structure of compound 8: A triad molecule consisting of a carbazole core substituted with a tert-butylphenyl group and a phenyl ring, which is further substituted with a tert-butylphenyl group and an oxadiazole ring.</p>

Compounds **3-8** each possess a donor carbazole and an acceptor oxadiazole unit. 9,9-dihexylfluorene was chosen as the spacer component in **3-7** as fluorene derivatives are highly fluorescent and serve as efficient π -conjugating units.¹² The hexyl chains at the C(9) position of fluorene improve the solubility of the molecules in organic solvents. The molecular structures in the series were systematically varied in the following ways to probe structure/property relationships.

- 1) The spacer moieties by the oxadiazole electron acceptor were changed, from phenylene (**2**) to pyridyl (**3**) and thienyl (**4**) units in order to modify the HOMO and LUMO levels of this portion of the molecules.
- 2) The electron donor ability and electrochemical stability of the carbazole unit was enhanced with the attachment of dimethoxy substituents (**5**) and *t*-butyl substituents (**6**).
- 3) The number of fluorene units was changed from one (**2-6**) to two (**7**) to none (**8**) to probe the effects of the conjugation length of the spacer.

Molecular orbital calculations were carried out by Dr Mark Fox in the Department of Chemistry, Durham University. Ethyl groups were used instead of hexyl groups in molecules **3-7** to reduce computational efforts (as previously for molecules **1** and **2**) and are denoted by an **a**. The full diagram showing the calculated energy levels for the compounds synthesised for this project, **2-8** is given in Figure 4.11.

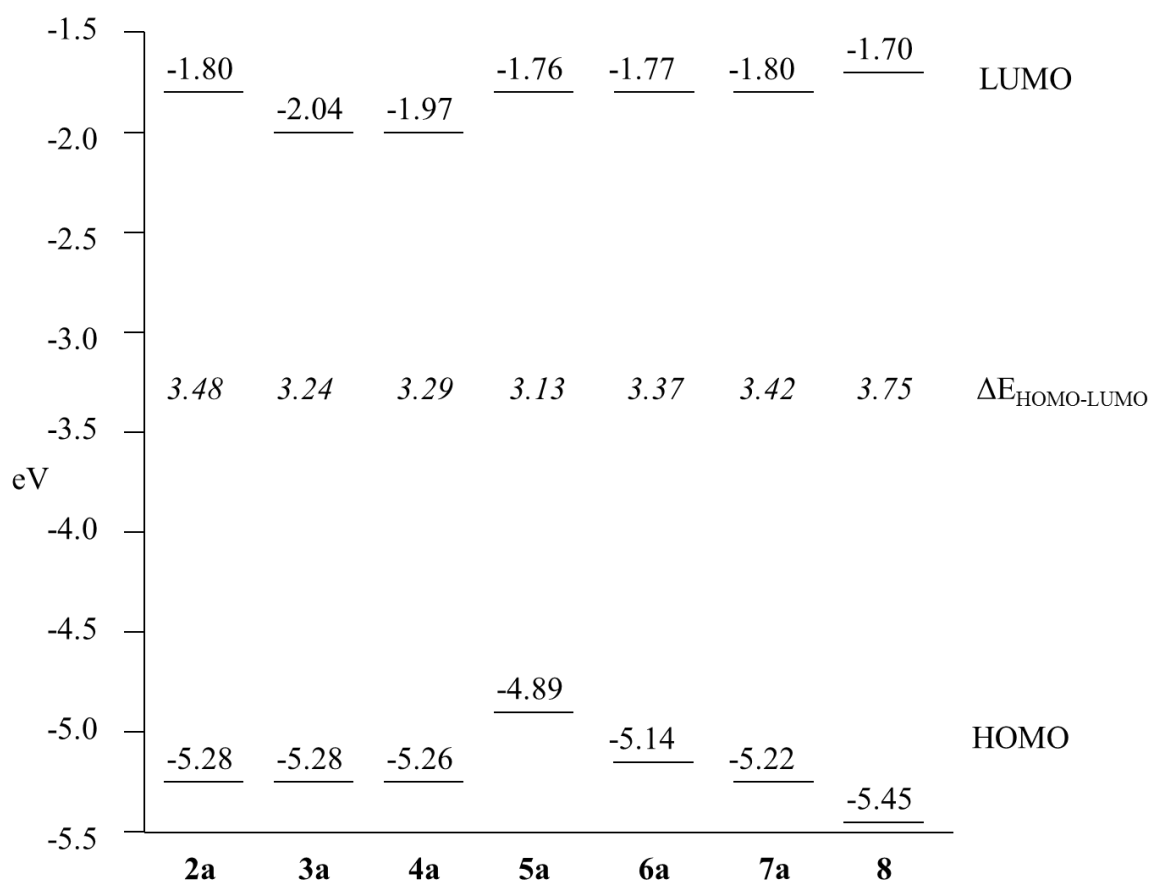


Figure 4.11: Molecular orbital energy diagram of HOMO and LUMO levels for compounds **2a-8**.

It was anticipated that the systematic modifications to the molecular structure of **2** and the resulting changes in energy levels, would enable a degree of tuning on the OLED output colour, turn-on voltage and efficiency. The current versus voltage, IV, and EL (measured by the photocurrent in the photodiode detector) versus voltage, LV, characteristics of OLEDs based on **2-8** are contrasted in Figure 4.12. The device architecture in all cases is: ITO / PEDOT:PSS / **X** / Ca / Al (**X** = **2-8**) and further details can be found in the Experimental chapter. The corresponding EQEs and EL spectra are shown in Figures 4.13 and 4.14, respectively, while the CIE coordinates of the various devices are depicted in Figure 4.15. Important electro-optical characteristics of the various OLEDs are collated in Table 4.3.

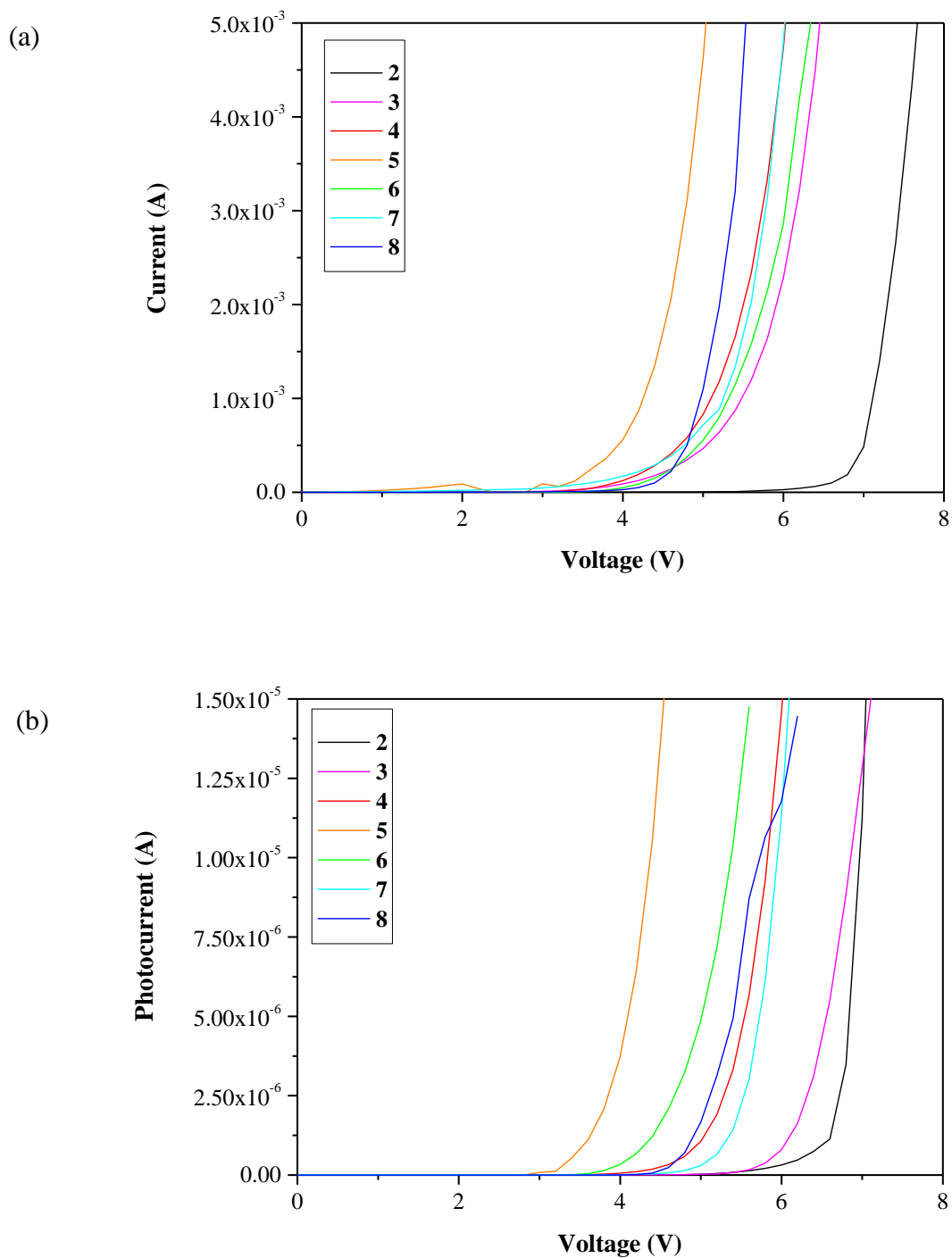


Figure 4.12: (a) Current-voltage and (b) photocurrent-voltage characteristics of the devices incorporating the new materials. Device architecture: ITO / PEDOT:PSS / X / Ca / Al (X = 2-8).

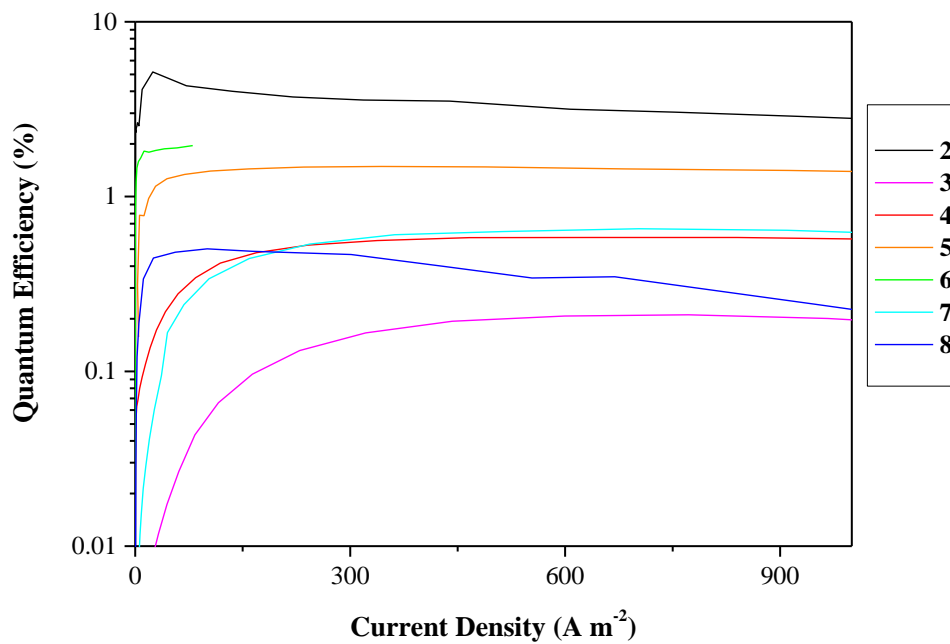


Figure 4.13: External quantum efficiency of devices incorporating materials 2-8.

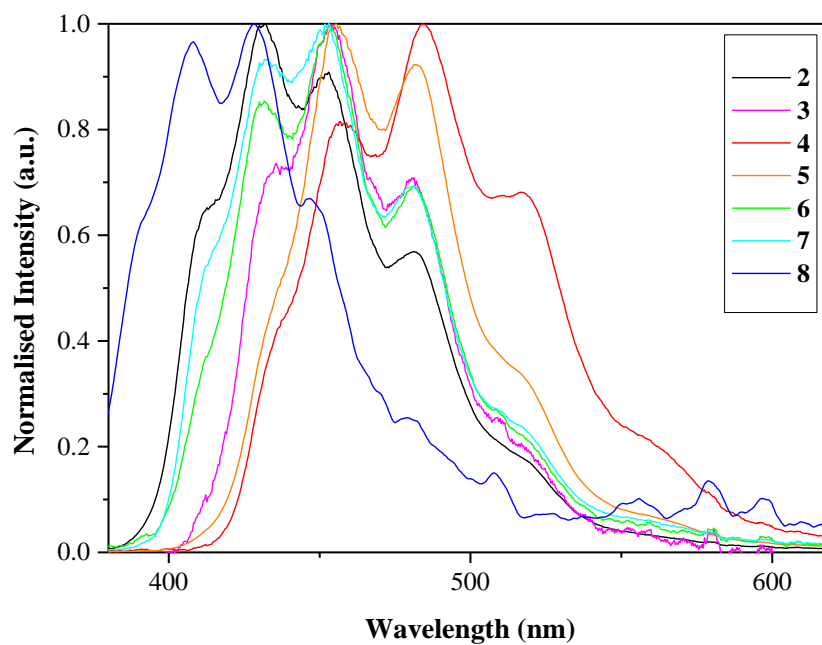


Figure 4.14: Electroluminescence spectra of devices incorporating materials 2-8.

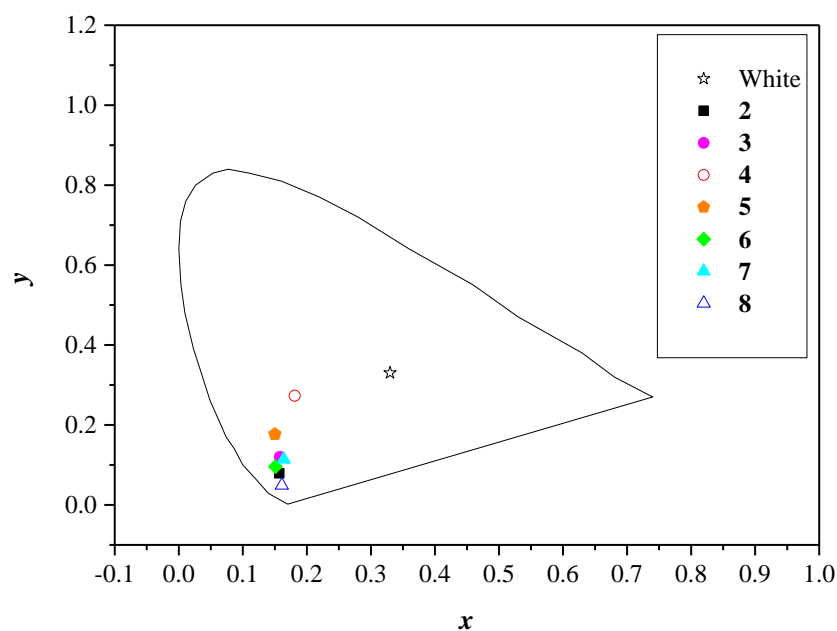


Figure 4.15: CIE diagram indicating the colour emission of devices **2-8** compared to standard white light. Measured at an applied current of 1 mA.

Table 4.3: Electroluminescence data for OLEDs based on compounds **2-8**.

Compound	2	3	4	5	6	7	8
Turn on Voltage ^a (V)	4.2	3.9	3.0	2.8	3.0	3.2	3.7
EQE ^b (%)	4.7	0.2	0.4	1.5	1.9	0.5	0.4
Wavelength of max emission ^c (nm)	431	453	484	455	453	452	428
FWHM (nm)	81	66	87	63	73	81	70
CIE ^d <i>x</i> at 1 mA	0.16	0.16	0.18	0.15	0.15	0.16	0.16
CIE ^d <i>y</i> at 1 mA	0.08	0.12	0.27	0.18	0.10	0.11	0.05
Brightness ^e (cd m ⁻²)	72.3	1.74	35.8	7.51	99.6	7.77	6.31
Current efficiency ^e (cd A ⁻¹)	1.42	0.03	0.70	0.15	1.96	0.15	0.12
Power efficiency ^e (lm W ⁻¹)	0.67	0.01	0.41	0.13	0.96	0.08	0.08

^aTurn on voltage given at 1 nA of photocurrent. ^bEQE measured at 100 ± 30 cd m⁻². ^cPeak emission of **5** and **7** measured under an applied current of 10 mA and 2 mA, respectively. All other OLEDs measured at 20 mA ($J \sim 10^3$ A m⁻²). ^dCIE coordinates measured at an applied current of 1 mA. ^eBrightness, current efficiency and power efficiency measured under an applied current of 1 mA.

The electrical data in Figure 4.12 reveal similar IV characteristics for **3** and **4** (i.e. within experimental error), but with currents significantly higher than those measured for the OLED based on **2**. The addition of pyridine and thiophene groups increases the electron affinity and lowers the LUMO levels whilst the HOMO levels for these three compounds are approximately the same (Figure 4.11). Thus it is easier to inject electrons into **3** and **4** than into **2**, suggesting that the increased currents measured for these devices are electron currents. Only the device based on **4** reveals an enhanced EL output and a reduced turn-on voltage for EL (Figure 4.12(b) and Table 4.3). However, the overall device efficiencies for OLEDs based on **3** and **4** are both significantly lower than that measured for OLEDs based on **2**. Lowering the LUMO level of the active molecule in the OLED architectures resulted in the peak EL emission moving from the blue end of the spectrum (Figure 4.14), so the output colour of the OLED was no longer confined to the deep-blue region of the CIE diagram (Figure 4.15). This is consistent with the reduced HOMO-LUMO separations of **3** and **4** (Figure 4.11).

Compound **5** has increased donor strength relative to compound **2** due to the methoxy groups on the 3,6-positions of the carbazole rings. The predicted LUMO levels of **2** and **5** are similar, but the HOMO level of **5** is significantly increased (Figure 4.11). The OLED based on compound **5** exhibited green rather than blue EL as expected from a reduced HOMO-LUMO separation, with an EQE of 1.5%. This device possessed the lowest turn-on voltage (2.8 V) of all the OLEDs studied. Compound **6** has a higher HOMO-LUMO gap compared to **5**, and, as expected, **6** retains the blue emission. Moreover, the current and EL output are both increased for the OLEDs manufactured with **6** compared to **2** (Figure 4.12), leading to an EQE of 1.9% (Figure 4.13) – the second highest of all the compounds studied in this work.

Compounds **7** and **8** provided the means to study the influence of the fluorene group on the OLED behaviour. Figure 4.14 shows that the additional fluorene group in **7** has no impact on the device colour as supported by DFT predictions. In contrast, **8**, which does not contain fluorene, provides the deepest blue OLEDs of all the compounds synthesised for this study, again supported by HOMO-LUMO predictions. However, the EQE of OLEDs based on this compound is low (0.4%). The above results suggest that the fluorene group is not itself responsible for the deep blue emission in some of the compounds but it is necessary for high efficiency. The deep blue colour must therefore arise from the presence of the carbazole group. This is consistent with results obtained in the previous study of **1** and **2**,¹³ where the diarylamine donor was replaced with a carbazole and the colour of emission moved from greenish-blue to deep-blue. Figures 4.12 and 4.13 reveal that OLEDs based on **7** and **8** possess similar IV, LV and EQE characteristics. The key difference is the much deeper blue EL from devices based on **8**. Although the predicted greater HOMO-LUMO separation explains the deeper blue EL for **8**, it cannot account for their similar electrical behaviour. It is possible that the more difficult charge carrier injection into **8** (raised LUMO and lowered HOMO in relation to **2**) is compensated by much higher carrier mobilities for thin films of **8**.

The most significant correlation that has emerged from our studies of OLEDs based on this series of bipolar carbazole-oxadiazole molecules is that between the EL maxima and the bandgap $E_g (= E_{\text{LUMO}} - E_{\text{HOMO}})$ predicted by molecular orbital calculations. Figure 4.16 shows a plot of E_g versus the reciprocal of the CIEy coordinate. The OLEDs based on molecules with the largest HOMO-LUMO separations generally show the largest values of $1/\text{CIEy}$ for the deepest blue EL. Two exceptions are compounds **4** and **7**. Figure 4.14 shows that OLEDs using compound **4** possess the most red-shifted EL spectra of all the molecules studied. The peaks in the EL emissions from **4** and **5** are quite similar; however,

the broad shoulder on the low energy side of the peak emission for **4** results in dissimilar CIE coordinates.

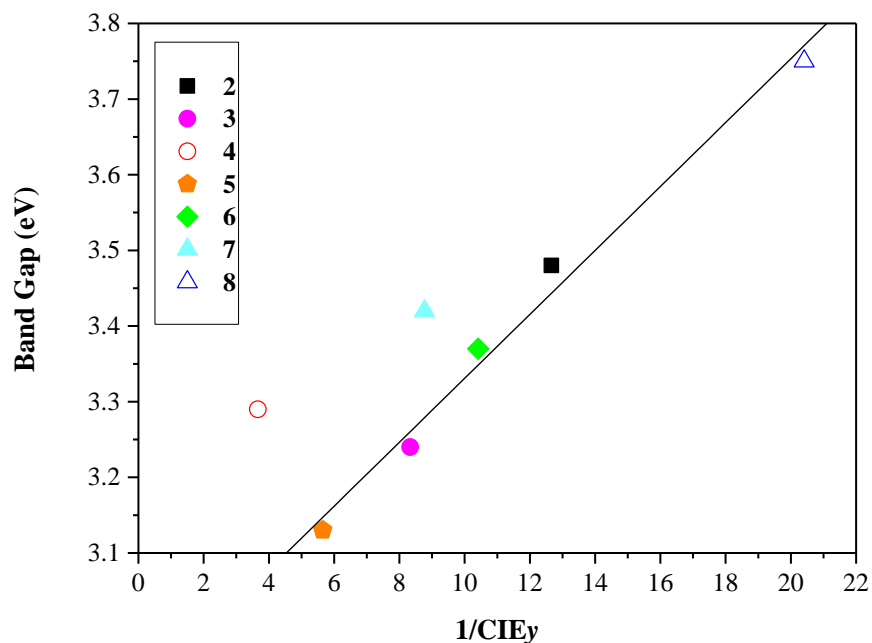


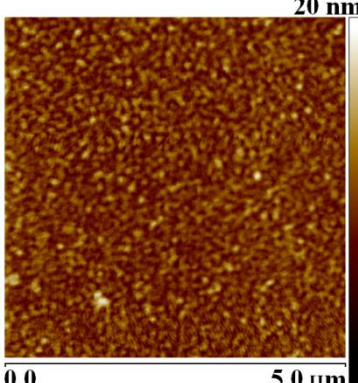
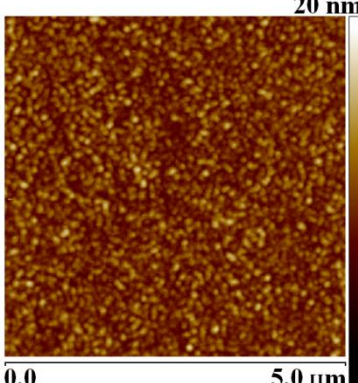
Figure 4.16: Relationship between band gap, E_g (from Figure 4.11) and $1/CIE_y$ for OLEDs based on molecules **2-8**. The solid line is a line of best fit, ignoring compounds **7** and **8**.

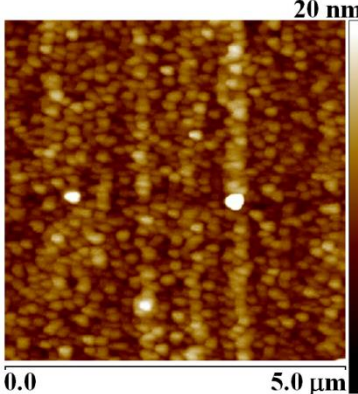
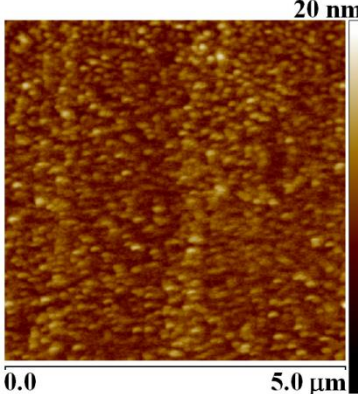
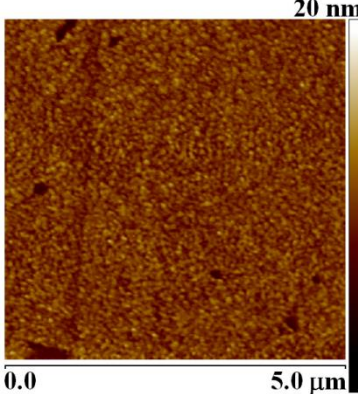
From Figure 4.16 it can be seen that the data points for each compound appear to fall on a line, except for compounds **4** and **7**. If these two are assumed to be anomalous, the remaining data suggest that a linear relationship may exist between band gap and CIE_y . The line of best fit through this data is shown in Figure 4.16 and implies that the relationship between band gap, E_g (in eV) and CIE_y may be described by Equation 4.1, which is derived from the best fit.

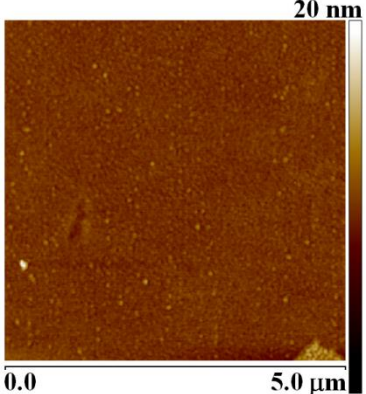
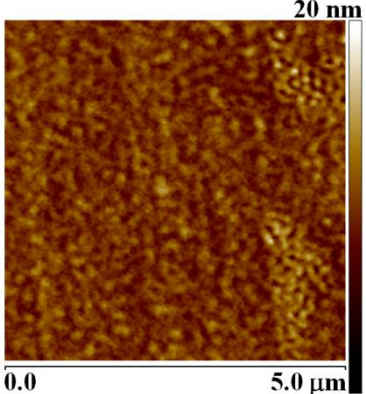
$$CIE_y = \frac{0.0423}{E_g - 2.9084} \quad (4.1)$$

AFM images were measured for each compound in the series, revealing that the small structural changes to each molecule had an impact on the film properties, as measured by roughness values and grain size. The AFM data are summarised in Table 4.4. The table shows a variation in roughness from 0.43 nm to 1.70 nm. The rougher films tend to have the larger grain size. The surface of compounds **4**, **5** and **8** show the largest grain size, however there appears to be no correlation between this and the chemical structure. The film thickness values given in Table 4.4 were measured using the scratch technique described in Section 3.4.1.

Table 4.4: AFM images of evaporated films for each compound in the series of compounds **2-8**.

Compound Number	AFM Image	Thickness (nm) ^a	Surface Roughness, Ra (nm) ^a	Grain Size (nm) ^b
2		59	1.24	179
3		64	1.25	152

Compound Number	AFM Image	Thickness (nm) ^a	Surface Roughness, Ra (nm) ^a	Grain Size (nm) ^b
4		63	1.70	278
5		59	1.19	217
6		67	0.97	147

Compound Number	AFM Image	Thickness (nm) ^a	Surface Roughness, Ra (nm) ^a	Grain Size (nm) ^b
7		64	0.43	125
8		65	1.06	208

^a ±5%; ^b ±10%

From this study, important design rules have emerged:

- 1) the most balanced carrier transport in the OLEDs (i.e. similar electron and hole currents, providing a high device efficiency) is achieved with a 2,5-diphenyl-1,3,4-oxadiazole acceptor and a carbazole donor, i.e. Compound **2**.
- 2) the deep blue emission from the molecules originates from the carbazole group, as the deepest blue emission occurred in Compound **8** where no fluorene was present.
- 3) the presence of a fluorene group adjacent to the carbazole donor, and separated from the oxadiazole moiety by a phenylene ring spacer, is required to achieve a high device efficiency (i.e. compounds **2**, **5** and **6**).

The links between other electro-optical parameters measured for the OLEDs (e.g. device currents and EL turn-on voltages) and their predicted electronic band structures are less clear. This indicates that different factors, for example, electron and hole carrier mobilities are a major influence in controlling the electro-optical parameters of these single-active-layer OLEDs.

To place this work in a broader context, it should be noted that the OLEDs from compounds **2** and **6** are competitive with the most efficient deep-blue OLEDs based on all-organic small-molecule fluorophores⁹⁻¹¹ and have been identified as such.^{14, 15} There are very few literature reports of OLEDs of this type with emission close to the NTSC standard blue coordinates of (0.14, 0.08) that achieve EQE values >1%.

4.5 Conclusions

DFT calculations have established that molecules **2-8** possess molecular orbitals which favour bipolar charge-transport. Single-active-layer organic light-emitting devices have been fabricated by thermal evaporation using the bipolar compounds as the emitters in the architecture ITO / PEDOT:PSS / **X** / Ca / Al (**X** = **1-8**). The results reveal an excellent correlation between the emitted EL spectrum and the $E_{\text{LUMO}}-E_{\text{HOMO}}$ separation predicted by the molecular orbital calculations. OLEDs based on **2**, incorporating a 2,5-diphenyl-1,3,4-oxadiazole acceptor group and a carbazole donor unit emitted deep-blue electroluminescence, with CIE (x, y) coordinates of (0.16, 0.08), close to the NTSC standard blue coordinates of (0.14, 0.08). Important design rules that have emerged from this study are that the deep blue emission from the molecules originates from the carbazole group and that the presence of a fluorene group adjacent to the carbazole donor, and separated from the oxadiazole acceptor by a phenylene ring (i.e. compounds **2**, **5** and **6**) is

required to achieve a high device efficiency (EQE > 1%). These materials are very attractive for further development due to the combination of good processability of the molecules, their bipolar structure, colour tuneability and efficient performance of OLEDs using a simple non-doped device architecture.

4.6 References

- 1) K. T. Kamtekar, C. Wang, S. Bettington, A. S. Batsanov, I. F. Perepichka, M. R. Bryce, J. H. Ahn, M. Rabinal, M. C. Petty, *J. Mater. Chem.*, 16, 3823-3835, **2006**.
- 2) Q.-X. Tong, S.-L. Lai, M.-Y. Chan, Y.-C. Zhou, H.-L. Kwong, C.-S. Lee, S.-T. Lee, *Chem. Mater.*, 20, 6310-6312, **2008**.
- 3) M. C. Petty in *Molecular Electronics: From Principles to Practice*, **2007**, John Wiley & Sons Ltd. Chapter 3.
- 4) H. Sirringhaus, *Adv. Mater.*, 26, 1319-1335, **2014**.
- 5) H. Zhang, C. Huo, J. Zhang, P. Zhang, W. Tian, Y. Wang, *Chem. Commun.*, 281-283, **2006**.
- 6) V. Bulović, V. B. Khalfin, G. Gu, P. E. Burrows, D. Z., Garbuzov, S. R. Forrest, *Phys. Rev. B*, 58(7), 3730-3740, **1998**.
- 7) C.-W. Lee, J.-G. Jang, M.-S. Gong, *Dyes and Pigments*, 98, 471-478, **2013**.
- 8) S.-K. Kim, B. Yang, Y. Ma, J.-H. Lee, J.-W. Park, *J. Mater. Chem.*, 18, 3376-3384, **2008**.

- 9) M.-Y. Lai, C.-H. Chen, W.-S. Huang, J. T. Lin, T.-H. Ke, L.-Y. Chen, M.-H. Tsai, C.-C. Wu, *Angew. Chem., Int. Ed.*, 47, 581-585, **2008**.
- 10) B. Chen, J. Ding, L. Wang, X. Jing and F. Wang, *Chem. Commun.*, 48, 8970-8972, **2012**.
- 11) J. Huang, J.-H. Su, X. Li, M.-K. Lam, K.-M. Fung, H.-H. Fan, K.-W. Cheah, C. H. Chen, H. Tian, *J. Mater. Chem.*, 21, 2957-2964, **2011**.
- 12) C.-G. Zhen, Z.-K. Chen, Q.-D. Liu, Y.-F. Dai, R. Y. C. Shin, S.-Y. Chang, J. Kieffer, *Adv. Mater.*, 21, 2425-2429, **2009**.
- 13) A. L. Fisher, K. E. Linton, K. T. Kamtekar, C. Pearson, M. R. Bryce, M. C. Petty, *Chem. Mater.*, 23, 1640-1642, **2011**.
- 14) J. Khunchalee, R. Tarsang, N. Prachumrak, S. Jungsuttiwong, T. Keawin, T. Sudyoadsuk, V. Promarak, *Tetrahedron*, 68, 8416-8423, **2012**.
- 15) M. Zhu, T. Ye, C.-G. Li, Z. Cao, C. Zhong, D. Ma, J. Qin, C. Yang, *J. Phys. Chem. C*, 115, 17965-17972, **2011**.

5 Devices Based on Novel D-A Compounds

5.1 In this Chapter...

This short chapter contains a number of proof of concept experiments involving the incorporation of new molecules into OLEDs, focusing on analogues of compounds **1** and **2** reported in Chapter 4. Compound **1A** was prepared via a simpler synthetic route and was therefore studied with a view to using it as a replacement for Compound **1**. Compounds **9** and **10** experimented with the addition of OXD groups to the molecular structure of Compound **2** with an aim to improve the efficiency of the OLED without the need for additional layers within the device structure. These experiments have their own conclusions and do not need any further investigation at present or for this thesis.

5.2 Compound 1A

This molecule (Figure 5.1(a)) was synthesised by the Bryce group at Durham University. It has a very similar structure to Compound **1**, but with additional methyl groups on the phenyl rings. The synthesis of Compound **1A** compared to Compound **1** is much simpler and the electrical properties of the molecule were expected to be almost identical. Thus incorporation of this new material into an OLED structure was seen as very attractive.

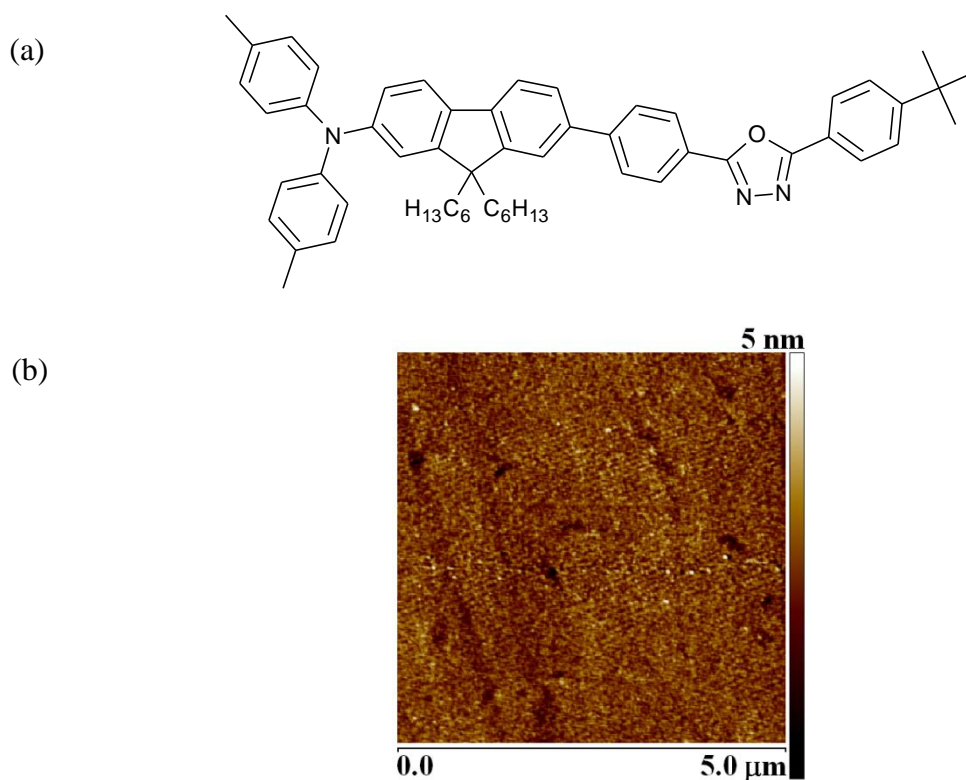


Figure 5.1: (a) Molecular structure of Compound **1A** and (b) AFM image of a 42 nm thick layer of Compound **1A** deposited by evaporation.

The morphology of the deposited film is shown in the AFM scan in Figure 5.1(b). It was interesting to note that approximately twice as much mass of this material was required to obtain the same thickness of the evaporated organic layer in the OLED structure as other materials in the family. (See Experimental.) This suggests that the density of the film is higher and implies that Compound **1A** forms a closely-packed film whereas the other compounds studied (compounds **1-8**) must have produced highly porous films. Figure 5.2 shows the current and photocurrent vs bias data for devices incorporating Compound **1A**. The turn-on voltage for this device at 1 nA of photocurrent was 2.52 V.

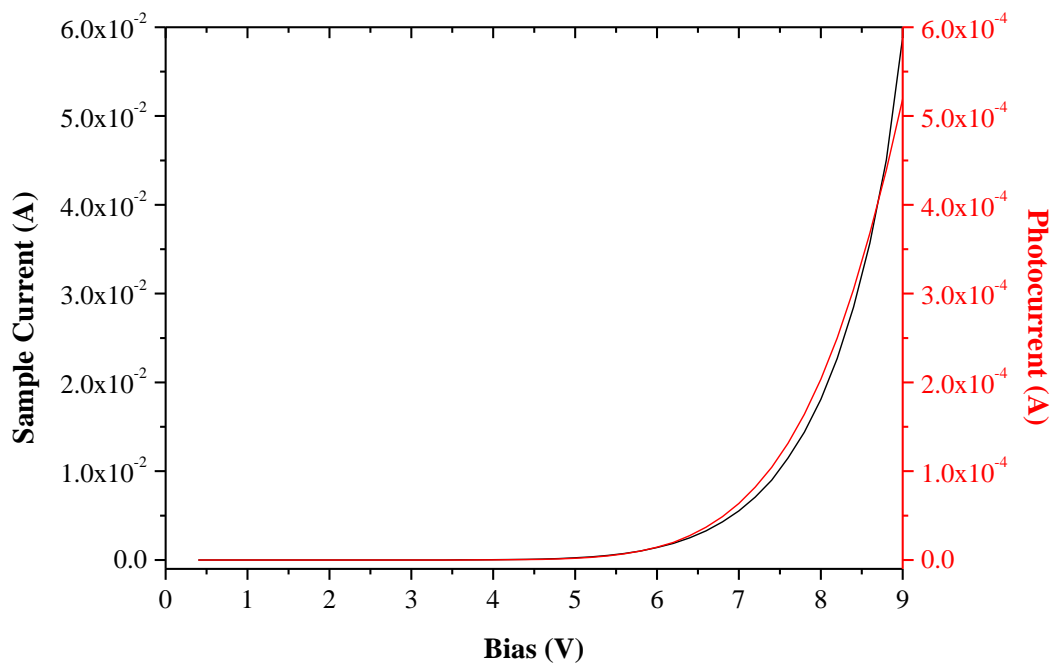


Figure 5.2: Current and photocurrent vs bias graph of a typical device with structure ITO / PEDOT:PSS / Compound **1A** / Ca / Al.

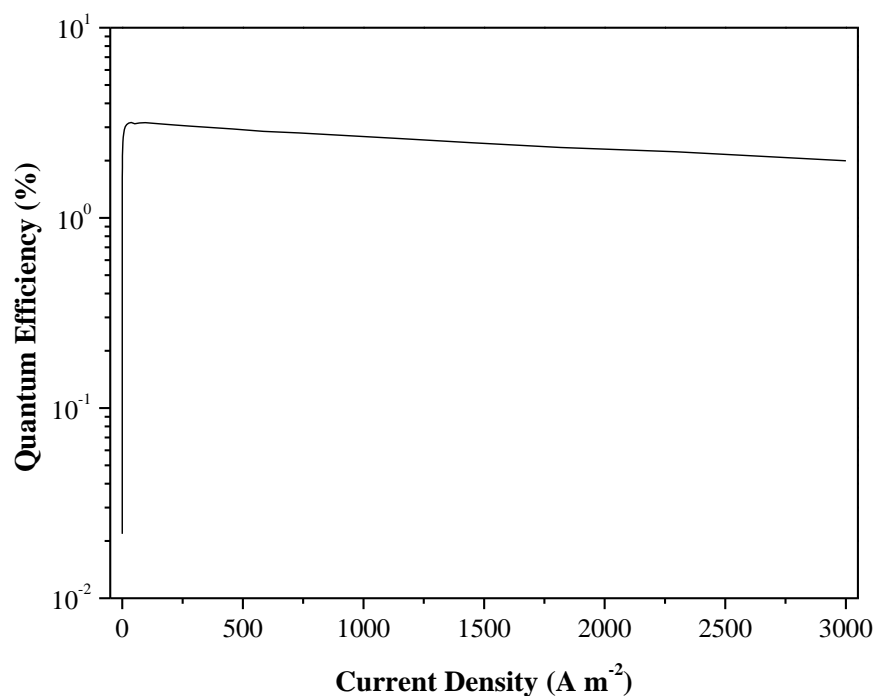


Figure 5.3: Best efficiency graph of OLED incorporating Compound **1A**.

The efficiency of this material, shown in Figure 5.3, is very promising at 3.09% at 100 cd m⁻². At its peak, the EQE measures 3.18%. This is an improvement in comparison with Compound **1** (EQE = 0.63%) and also most of the other materials in the series considered in Chapter 4. However, the EL spectrum (Figure 5.4) shows a shift towards green in the peak emission (486 nm) compared to that generally observed for the other molecules in the series. It is however similar to the peak emission observed for compounds **1** and **4**. The CIE coordinates in Figure 5.5 show a more significant shift towards the green region at (0.171, 0.390) compared with compounds **2-8** and the move away from blue likely explains the increase in efficiency.

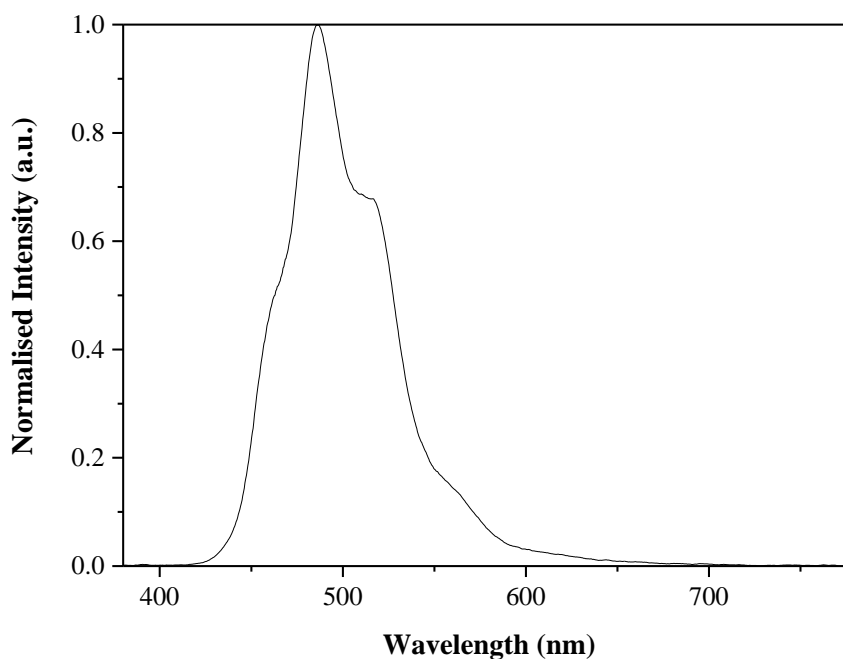


Figure 5.4: Electroluminescence spectrum showing peak emission at 486 nm for a device with structure ITO / PEDOT:PSS / Compound **1A** / Ca / Al.

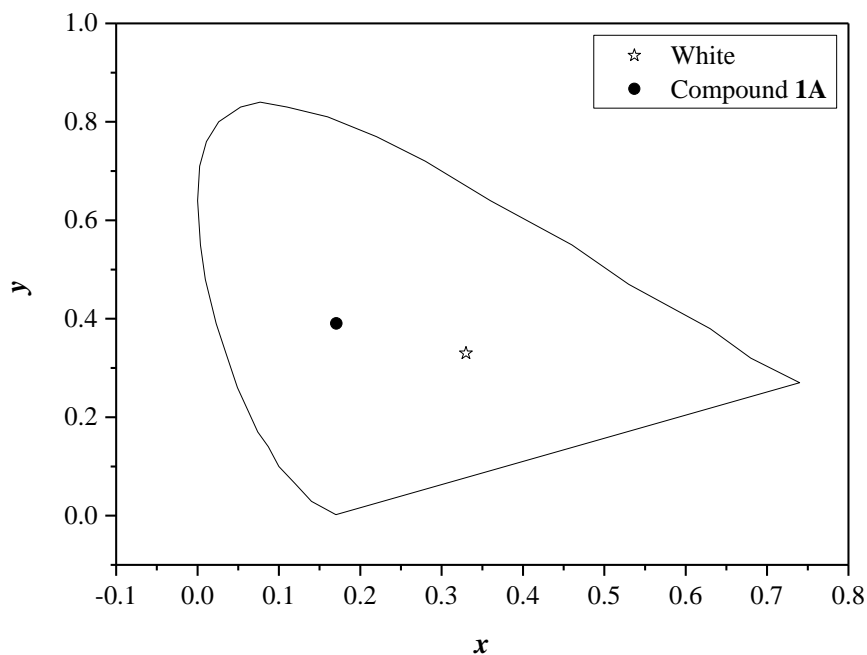


Figure 5.5: CIE diagram showing device with coordinates (0.17, 0.39) for the OLED structure ITO / PEDOT:PSS / Compound **1A** / Ca / Al.

The current efficiency for this device was 7.0 cd A^{-1} and power efficiency 3.7 lm W^{-1} . The brightness at 1 mA of applied current was found to be 355 cd m^{-2} . Computational calculations (Appendix A) on the molecular structure of Compound **1A** predicted a band gap for this molecule of 3.12 eV, explaining its move away from the deep blue colour seen in the other compounds in the series and into the bluish green region.

Conclusions

The results for Compound **1A** underline how slight modifications in chemical structure affect emission properties of OLED compounds. The addition of two methyl groups to Compound **1** results in a significant shift from (0.16, 0.25) to (0.17, 0.39). This compound is easier to synthesise and still retains a good efficiency of over 3% although this may be explained by the move away from the blue region.

5.3 Further Manipulations to Carbazole Compound 2

The remainder of this chapter focuses on modifications to the successful OLED molecule Compound **2** from Chapter 4. Addition of electron transport compounds has previously been shown by J. Ahn and S. Oyston et al to result in a marked improvement in the efficiency of poly(2-methoxy-5-(2-ethylhexyloxy)-1,4-phenylenevinylene) (MEH-PPV) OLEDs.¹⁻³ Similarly, blending of the electron transporting molecule, OXD7 in WOLEDs in Chapter 6 was shown to improve devices characteristics.

It was considered that direct chemical attachment could improve electron transport and thus performance in the whole molecule, eliminating the need for blending. Therefore, these molecules were designed to incorporate additional oxadiazole (OXD) groups, with an aim to improve the efficiency of the deep blue device.

5.3.1 Compound 9

This structure (Figure 5.6(a)) was designed to experiment with the effect of an additional electron transport group to Compound **2** to create an OXD7 moiety.

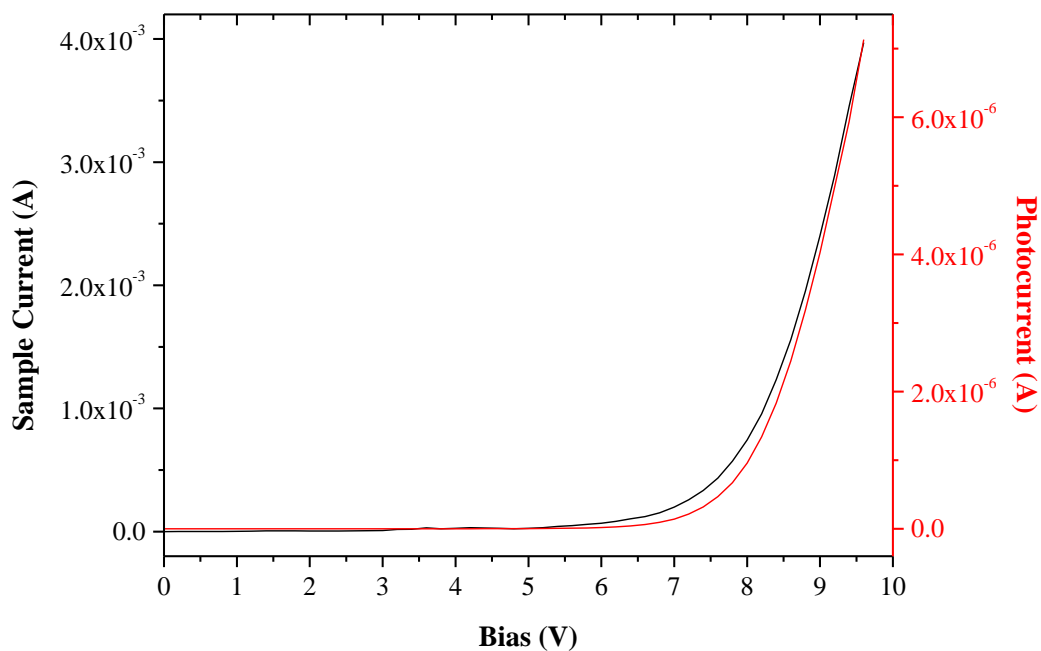


Figure 5.7: Current and photocurrent vs bias graph of device with structure ITO / PEDOT:PSS / Compound **9** / Ca / Al.

The current and photocurrent vs bias data shown in Figure 5.7 show a turn-on voltage of 4.4 V at 1 nA of photocurrent. The results for the external quantum efficiency (Figure 5.8) for these devices was relatively low at around 0.4%. Overall the electrical and efficiency measurements are poor, showing resistive properties that prevent significant emission of photons for the amount of electrons being injected. This is also shown in the EL spectra shown in Figure 5.9 where the low light output results in a noisy spectrum. The peak emission occurred at 428 nm, which would suggest a deep blue, on par with Compound **8**, the deepest blue emitter studied. However, the CIE coordinates of (0.17, 0.11) in Figure 5.10, show that the colour is a less deep blue. This discrepancy is not explained with the Full Width Half Maximum (FWHM) for the emission, which measures 67 nm (72 nm including shoulder peak), similar to the other deep blue materials.

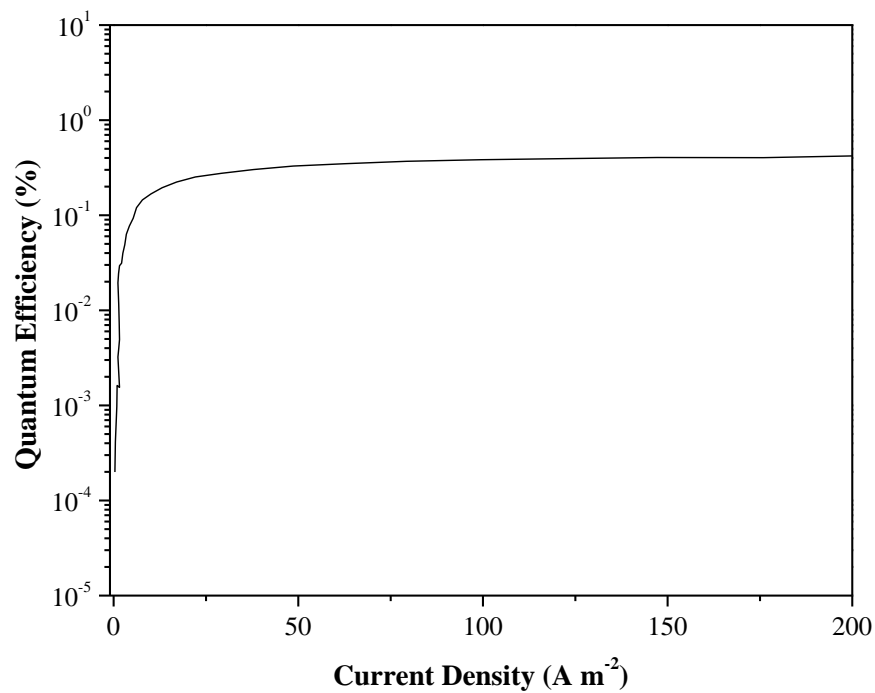


Figure 5.8: External quantum efficiency graph of device with structure ITO / PEDOT:PSS / Compound **9** / Ca / Al with EQE at 0.43%.

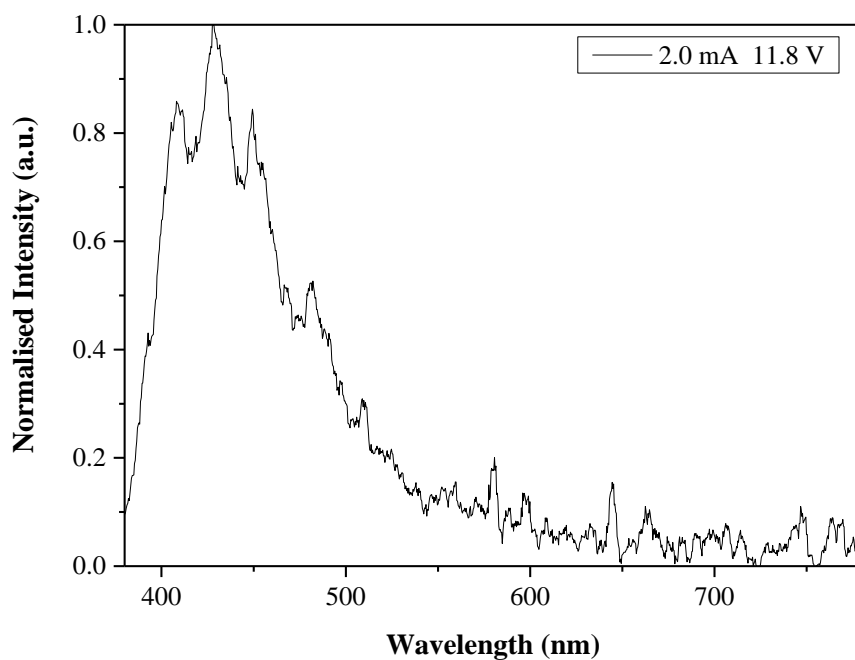


Figure 5.9: Electroluminescence spectrum of a device with structure ITO / PEDOT:PSS / Compound **9** / Ca / Al.

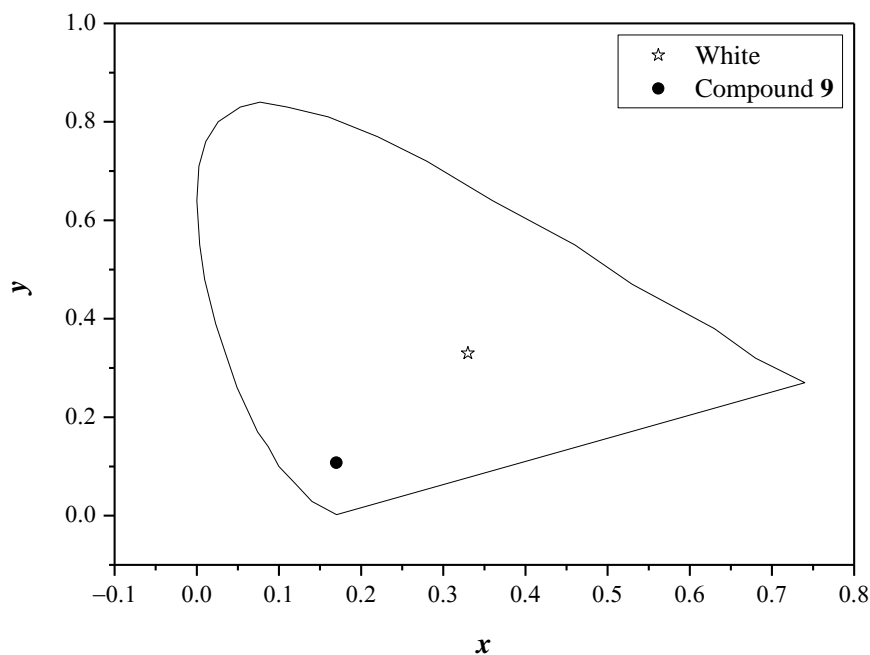


Figure 5.10: CIE diagram showing the colour of a device with structure ITO / PEDOT:PSS / Compound **9** / Ca / Al.

Conclusions

Overall OLEDs based on Compound **9** showed poor characteristics with high turn-on voltage and a lower efficiency compared to carbazole devices without the chemical addition of OXD. However, it was promising that the emission colour had not shifted far from deep blue suggesting that the new structure did not alter the band gap far from the value of 3.48 eV for Compound **2**. It was considered that addition of an extra OXD group could be necessary to improve device efficiency, so a new chemical structure was designed.

5.3.2 Compound 10

There are in fact several options of where to attach another OXD group. One possibility was to insert the third OXD group between the carbazole and fluorene groups of Compound 2. However, this structure would be very conjugated which would reduce the band gap and therefore result in a more red emission. Instead, the carbazole-fluorene linker was left intact and the OXD groups added at the terminal positions as shown in Figure 5.11(a). In this location, the OXD groups are in the same position as the methoxy groups in compound 5, (Chapter 4) but would be expected to have the opposite effect with OXD being electron accepting. This in turn should lower the Highest Occupied Molecular Orbital (HOMO) and thus increase the band gap.

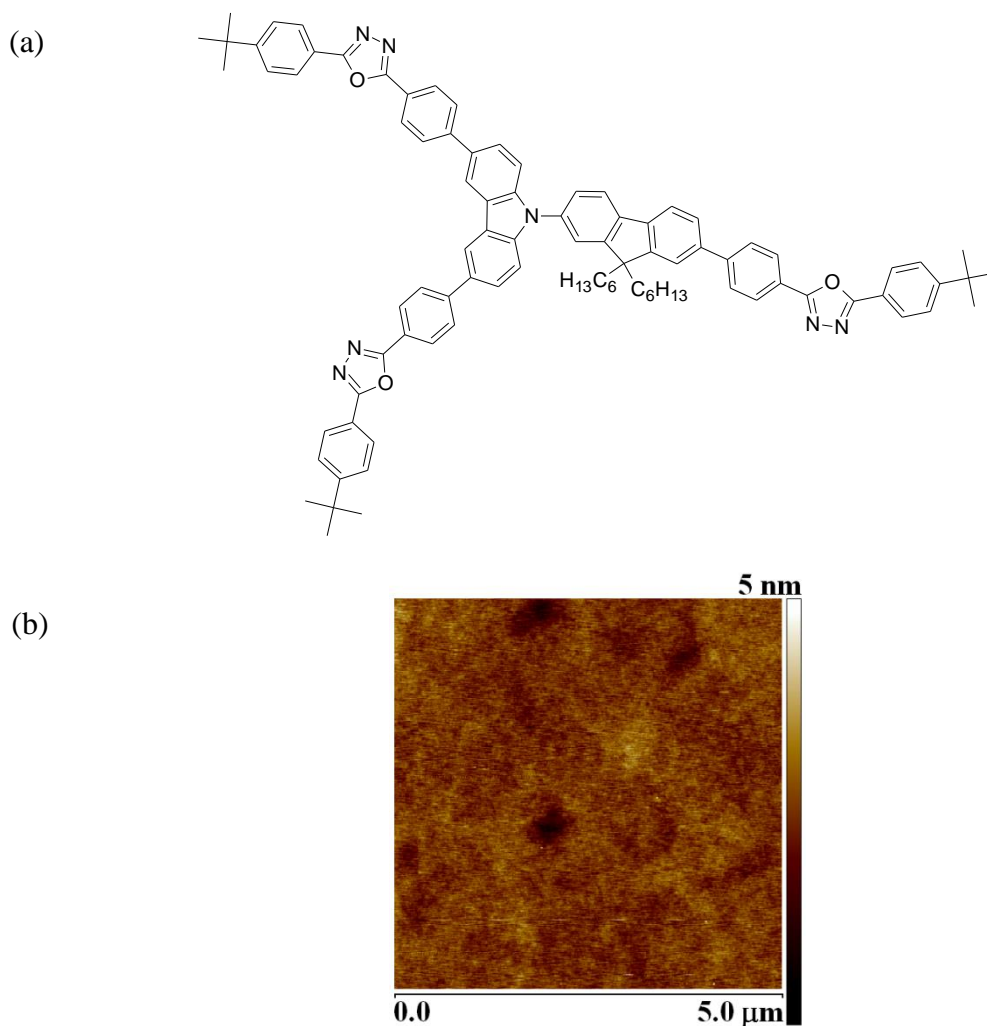


Figure 5.11: (a) Structure of Compound **10** and (b) Topography of a spin-coated film of Compound **10**. Thickness = 75 nm. Other films of higher thickness looked very similar under AFM.

As for earlier OLEDs, standard device architectures were attempted incorporating an evaporated layer of this material. However, it proved impossible to evaporate this compound. Following heating to 500 °C in the vacuum chamber, the crucible became discoloured and the white powder of Compound **10** had apparently decomposed, appearing black and tar-like and showing no evidence of evaporating. The conclusion was that this material cannot be evaporated, probably due to its relatively high molecular weight, resulting in low volatility.

As a result, devices were produced based on a spin-coated layer of Compound **10**. The material was first dissolved in chloroform to a concentration of 15 mg/ml but the thickness

of the spun layer (150 μl spread, spin at 1000 rpm, for 1 minute, bake at 80 $^{\circ}\text{C}$ for 30 minutes) was 163 nm as measured by AFM. This is far too thick to get reasonable electrical characteristics so the concentration was reduced for spinning onto the devices and a concentration of $15/\sqrt{2}= 10.61 \text{ mg ml}^{-1}$ was used. These repeat devices possessed an average thickness of the Compound **10** layer (as measured using AFM) of 112 nm, with a range between 75 nm to 161 nm with half of the measurements being $112 \pm 20 \text{ nm}$. The topography of these devices is shown in Figure 5.11(b) and is very smooth, as has been seen in all previously spin-coated devices in the series. Resulting device characteristics are given below.

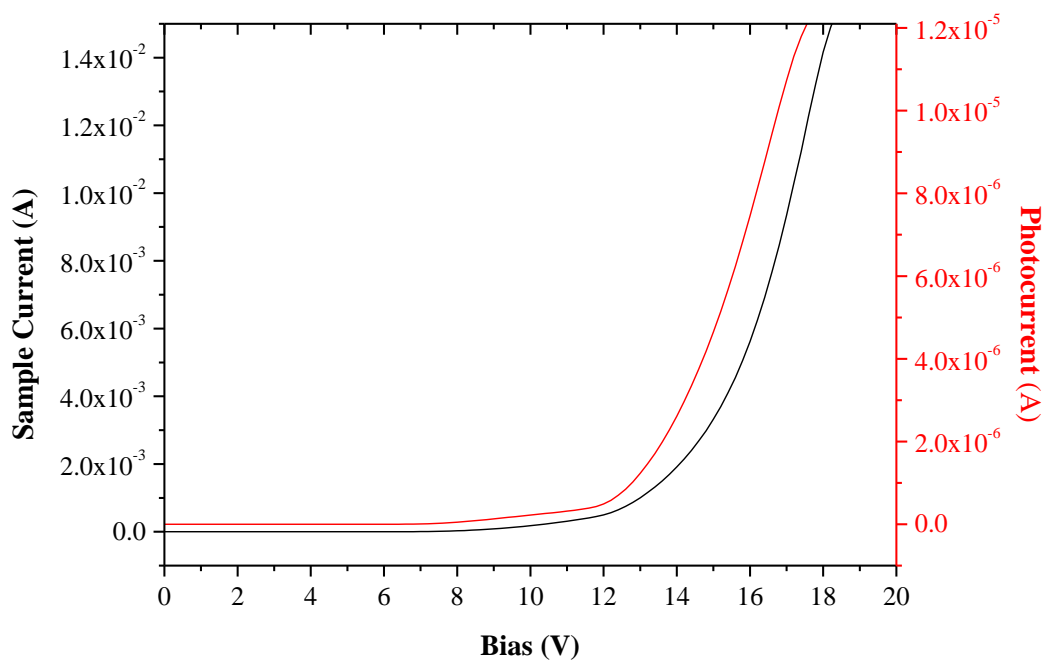


Figure 5.12: Current and photocurrent vs bias graph of device with structure ITO / PEDOT:PSS / Compound **10** / Ca / Al.

The current and photocurrent vs bias characteristics in Figure 5.12 show a high turn-on voltage of 6.45 V at 1 nA of photocurrent. The sample current at turn-on was 1.91 μA . The

external quantum efficiency shown in Figure 5.13 is similar to devices based on Compound **9** with two OXD groups and is low at 0.36%.

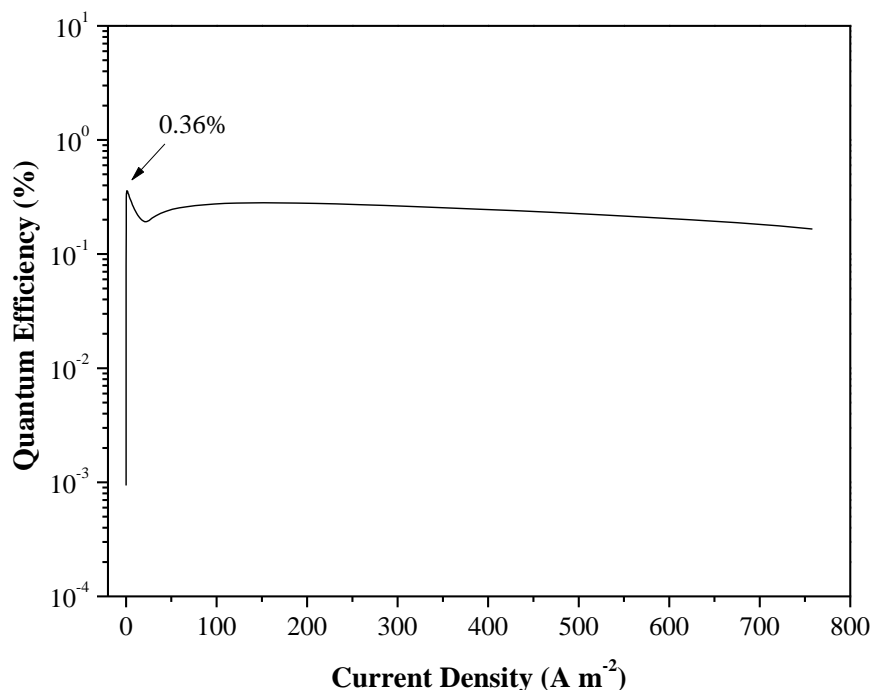


Figure 5.13: External quantum efficiency graph of device with structure ITO / PEDOT:PSS / Compound **10** / Ca / Al.

The EL spectrum shown in Figure 5.14 shows five peaks in emission at 435 nm, 450 nm, 484 nm, 422 nm and 560 nm. The peak emission occurs at 484 nm. This compound shows the most complicated electroluminescence spectrum of the compounds studied. The CIE diagram (Figure 5.15) reveals that there is a drift in the colour with applied current from a blue-white towards pure white. For comparison with other devices, the CIE coordinates at 1 mA were (0.24, 0.23). At 20 mA the coordinates are (0.27, 0.26) and this whiter emission is reflected in the huge FWHM of 149 nm in Figure 5.14. This complex emission might be a result of the three OXD acceptors all being conjugated to the single carbazole donor. Increase in the applied voltage might encourage emission between different LUMO levels of the three OXD groups to the HOMO of the carbazole. It would therefore be useful to perform DFT calculations on this molecule to further understand its electronic properties.

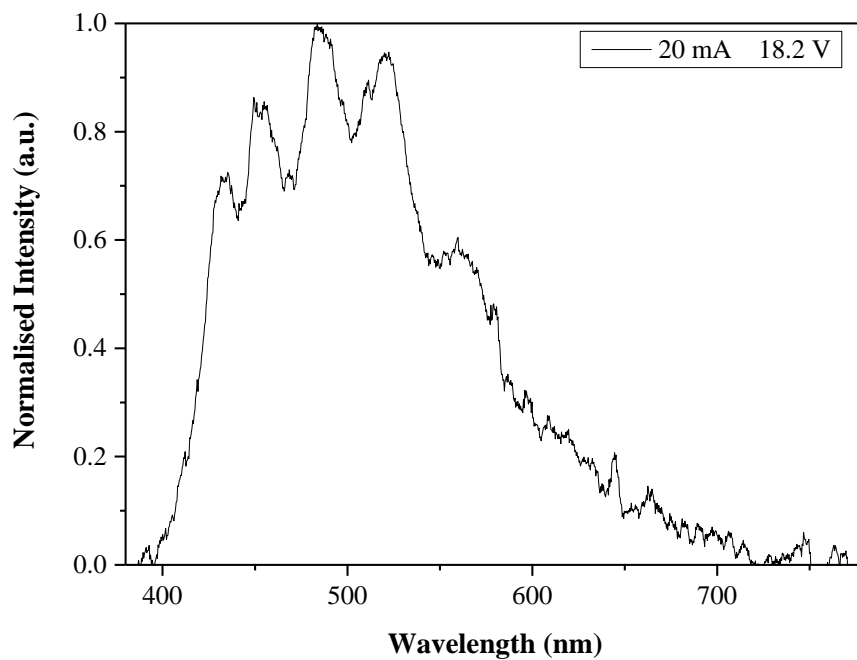


Figure 5.14: Electroluminescence spectrum of a device with structure ITO / PEDOT:PSS / Compound **10** / Ca / Al.

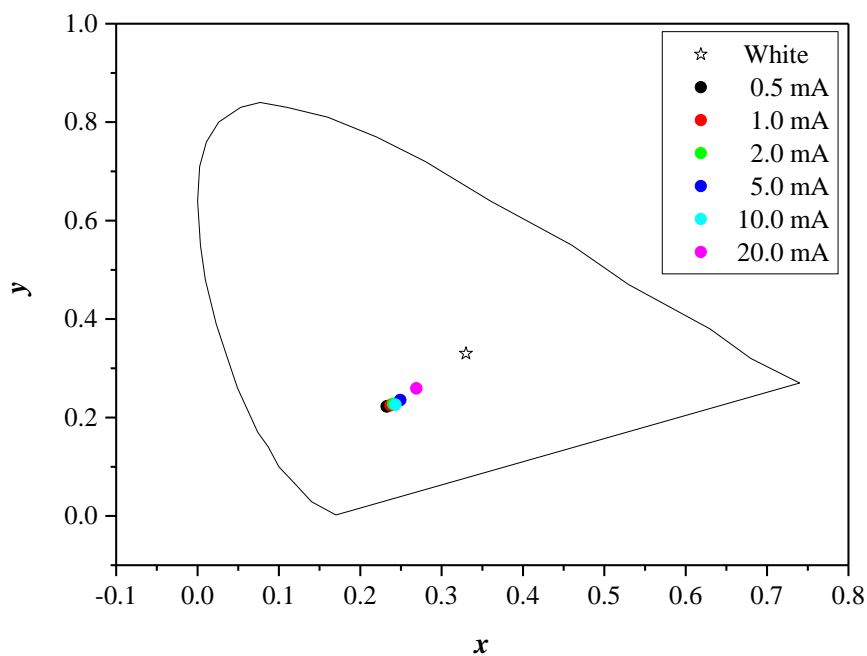


Figure 5.15: CIE diagram of a device with structure ITO / PEDOT:PSS / Compound **10** / Ca / Al.

Conclusions

This section has explored new molecular structures based on the chemical addition of OXD groups to the blue emitting molecule Compound **2**, in contrast with the physical blending of Compound **2** with OXD7 in Chapter 6, with the aim to improve efficiency. Compared to devices incorporating Compound **9**, Compound **10** shows a higher turn-on voltage of 6.45 V. Both compounds however show similarly low efficiencies. The most striking difference is in the EL spectra and CIE coordinates with extra peaks appearing in the green region for Compound **10** and an overall emission colour closer to white and further from blue. It is interesting to note that evaporated Compound **9** showed similar efficiency to spin-coated Compound **10**. As seen in Chapter 4, OLEDs prepared by spin-coating exhibit lower device efficiency and in fact a comparison with the results for spin-coated Compound **9** in Chapter 6 shows a lower efficiency for Compound **9** of 0.27%.

A comparison of device characteristics for Compound **2**, Compound **2** blended with OXD7, Compound **9** and Compound **10** OLEDs is given in Table 5.1. The results for both compounds, Compound **9** and Compound **10**, which incorporate additional OXD groups show higher turn-on and lower efficiency compared to devices of unmodified Compound **2**. Similarly, the efficiencies of OLEDs based on compounds **9** and **10** are an order of magnitude lower compared to blended Compound **2** and OXD7 and also lower than the external quantum efficiency for unblended OLEDs comprising only Compound **2**, which measure 0.9% (Chapter 6). Interestingly, the turn-on voltage for Compound **9** is lower than that observed for the blend of OXD7 with Compound **2**.

Overall, it would then appear that the chemically attached OXD groups have no beneficial effects on the deep blue OLEDs. Based on the higher turn-on voltages and low efficiencies measured for these compounds, it is suggested that charge transport is inhibited compared to in Compound **2**. One reason may be steric effects from the relatively bulky molecules,

which hinder intermolecular charge transport. Alternatively the OXD groups may interfere with the electronic structure and energy levels of the donor-acceptor compound, resulting in unfavourable electroluminescence. Some evidence for this is observed for Compound **10**, which reveals a complex emission dependent upon applied current. The shift towards white for Compound **10** does open the possibility however of chemical modifications towards WOLEDs.

Table 5.1: Comparison of key optical and electrical properties for pure Compound **2** devices with OXD7 blended devices and chemical attachment of OXD groups.

Device	Turn-on Voltage (V)	EQE _{max} ^b (%)	Luminance ^c (cd m ⁻²)	Luminous Power Efficiency ^c (lm W ⁻¹)	CIE (x, y) ^c
2 spin-coated	3.2 ^a	0.90	21	0.26	0.16, 0.09
2 : 30% OXD7 spin-coated	5.6 ^a	3.00	49	0.44	0.16, 0.09
9 spin-coated	4.4 ^a	0.27	2.8	0.0019	0.17, 0.07
9 evaporated	4.4	0.43	12.21	0.087	0.17, 0.11
10 spin-coated	6.5	0.36	25.42	0.12	0.24, 0.23

^aTaken from Chapter 6. ^bMaximum value for external quantum efficiency. ^cAt a current intensity of 1mA.

5.4 Conclusions

This chapter has considered several different materials in OLED structures. Compound **1A**, an analogue to the previously published Compound **1**, showed promising results, with improved efficiency. This new analogue is attractive due to a more facile synthesis, although the addition of the methyl groups also appeared to adjust the emission colour to more green. Analogues to the successful deep blue OLED Compound **2** were also considered, incorporating OXD groups with an aim to improve efficiency. Despite blended devices of OXD7 showing improved efficiencies as demonstrated in Chapter 6, the

chemical attachment of OXD did not improve the efficiency of the OLEDs studied. However, attachment of two OXD groups to the compound did result in a complex, more white emission.

5.5 References

- 1) J. H. Ahn, C. Wang, C. Pearson, M. R. Bryce, M. C. Petty, *Appl. Phys. Lett.*, 85, 1283-1285, **2004**.
- 2) S. Oyston, C. Wang, G. Hughes, A. S. Batsanov, I. F. Perepichka, M. R. Bryce, J. H. Ahn, C. Pearson, M. C. Petty, *J. Mater. Chem.*, 15, 194-203, **2004**.
- 3) S. Oyston, C. Wang, I. F. Perepichka, A. S. Batsanov, M. R. Bryce, J. H. Ahn, M. C. Petty, *J. Mater. Chem.*, 15, 5164-5173, **2005**.

6 White OLEDs based on Spin-Coated Blends

6.1 In this Chapter...

The majority of this work was carried out in collaboration with a visiting student, Cristina Roldan-Carmona, on a summer placement in 2010, over who I had a supervisory role. With Compound **2**, in Chapter 4, producing efficient deep blue OLEDs a further study was undertaken to assess whether this material could be combined with a yellow emitter, and create white light. As stated in Chapter 4, The CIE coordinates of **2** were found to be (0.16, 0.07). The idea was that if the yellow emitters, Super Yellow and the iridium dye PO-01, were combined with **2** in the correct proportions, white light emission in a simple device architecture would be possible.

Two systems were compared.

- 1) Compound **2** mixed with a fluorescent phenyl-substituted poly(*p*-phenylene vinylene) polymer, PDY-132, or “Super Yellow”.
- 2) Compound **2** mixed with a phosphorescent complex, iridium(III)bis(4-phenylthieno[3,2-*c*]pyridinato-N,C2')acetylacetonate, PO-01.

A further part of the study looked at improving the efficiency of the fabricated white OLEDs (WOLEDs) by blending with the electron transport compound OXD7. Finally, the effect of the chemical attachment of OXD7 (Compound **9**, as seen in Chapter 5) was considered as an alternative for improving the efficiency of WOLEDs.

A reminder of the materials used in this chapter (also listed on pages 56-61) can be found over in Figure 6.1. Fabrication details are described earlier in the Experimental chapter.

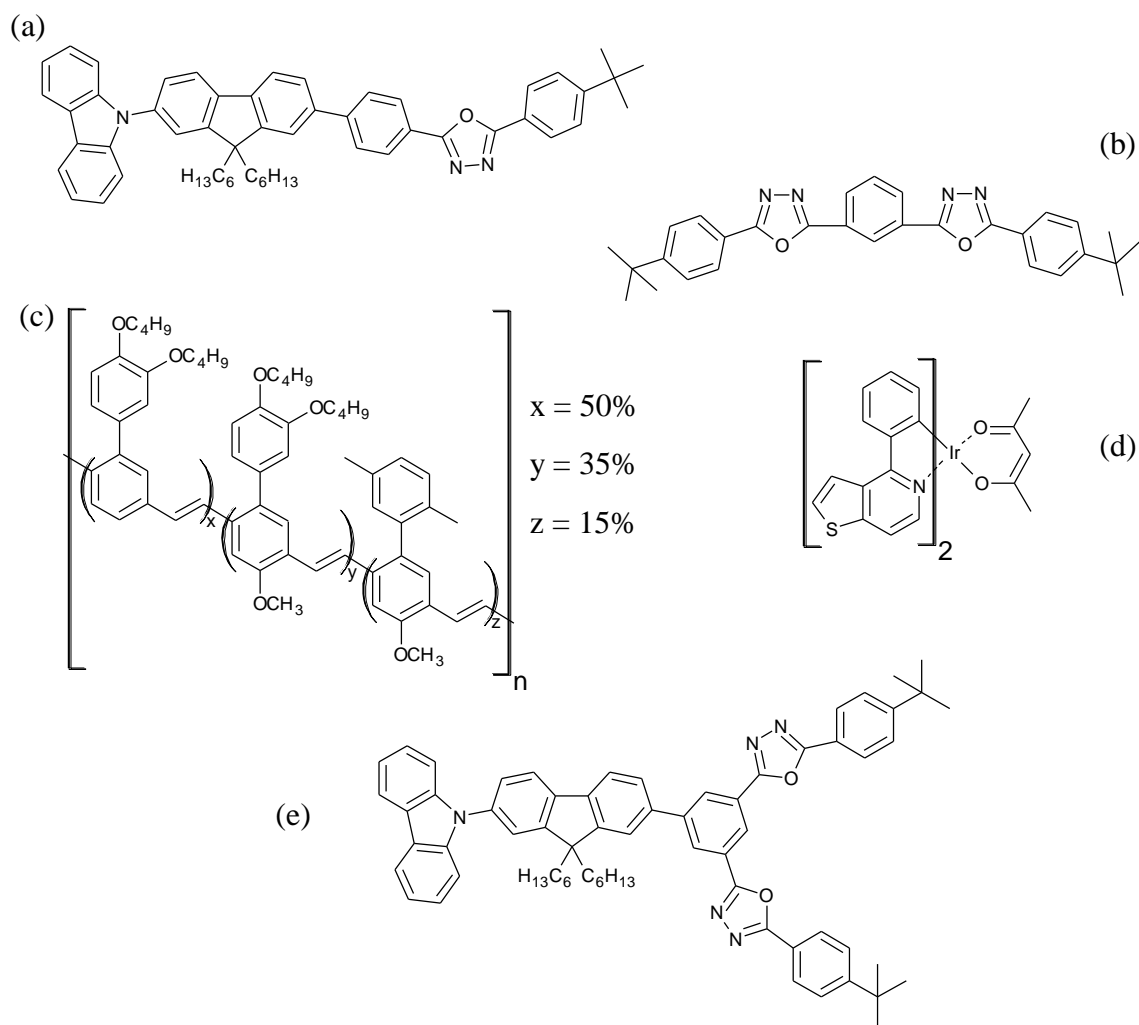


Figure 6.1: Structures of materials used in this study; (a) Compound 2, (b) OXD7, (c) Super Yellow, (d) PO-01, (e) Compound 9.

6.2 Super Yellow

6.2.1 Devices Incorporating Super Yellow

Figure 6.2 shows the normalised electroluminescence (EL) spectra for devices prepared with different proportions of Compound 2 and Super Yellow. In all cases, the spectra were recorded for a device current of 1 mA.

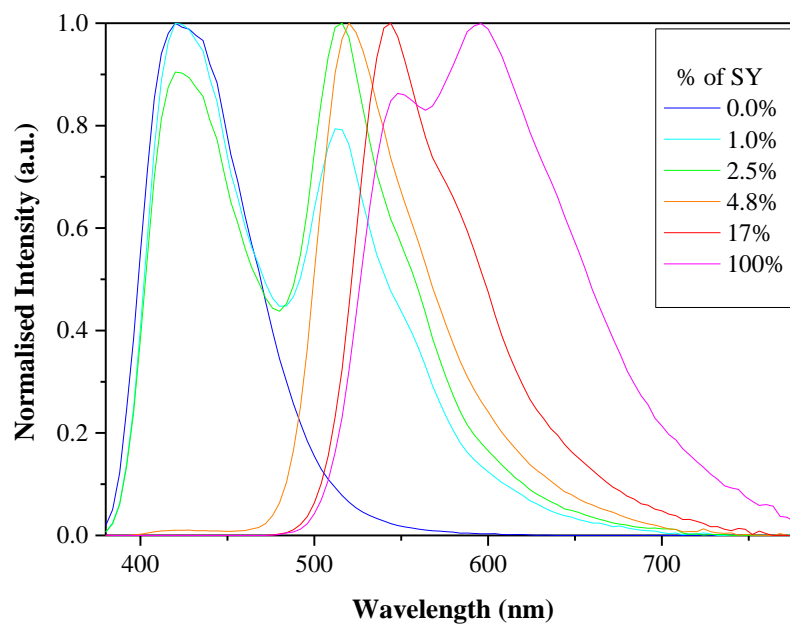


Figure 6.2: Normalised EL spectra for the Compound **2** devices, blended with different percentages of Super Yellow (SY), expressed in weight ratios. All samples spin-coated from toluene solutions. In all cases, spectra were recorded for a current of 1 mA.

As before, the device based on **2** produced a deep-blue emission,¹ while the spectrum of the OLED incorporating only the pure Super Yellow compound reveals two emissions, at approximately 550 nm and 595 nm.² The addition of the blue emitter to the device results, initially, in a reduction in the intensity of the 595 nm peak relative to those at higher energy. As further quantities of blue dye are added, the 550 nm emission begins to shift towards smaller wavelengths. The net result is a change in the emission colour of the OLED, from yellow to deep-blue. However, as evident from the CIE diagram in Figure 6.3, the colour change is not along a line directly connecting the emission coordinates of the two pure dyes. As Compound **2** is added to Super Yellow, the emission shifts from yellow to green and, then, to deep-blue. Although it is not possible to achieve the pure white point in the CIE diagram (0.33, 0.33) by varying the relative amounts of these

molecules, a blue-white device with CIE coordinates (0.23, 0.36) was achieved using a blend containing 1% of Super Yellow.

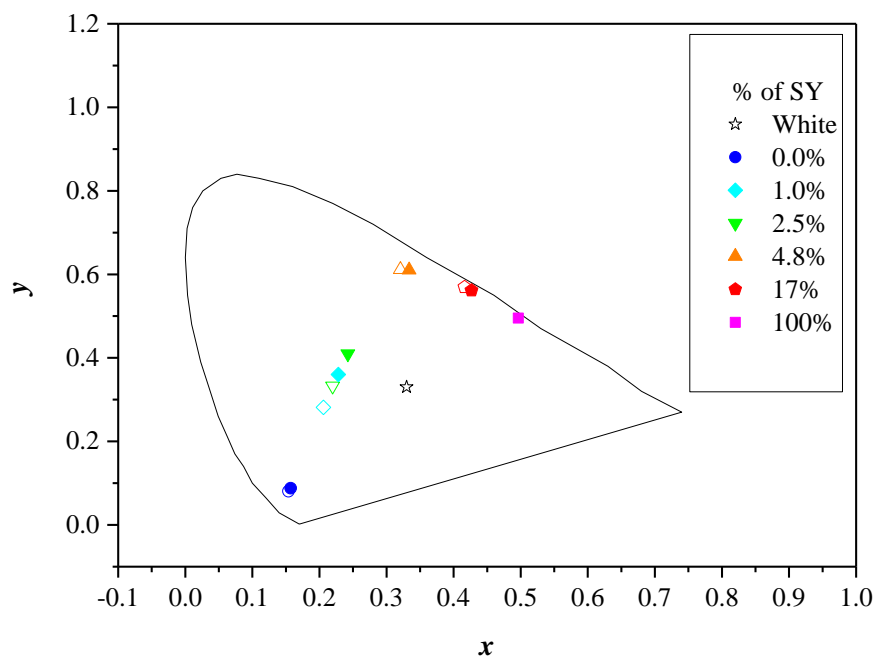


Figure 6.3: CIE (x , y) coordinates for devices prepared with different amounts of Compound **2** and Super Yellow (the spectra of which have been presented in Figure 6.2) at 1 mA. All samples spin-coated from toluene solutions. The open symbols represent the CIE (x , y) coordinates for the devices operated at 10 mA. The CIE coordinates of standard white are also included for reference.

The colour changes in these blended-layer devices is probably related to structural reorganisation of the Super Yellow polymer chains as these are mixed with the molecules of Compound **2**. For example, Shi et al have reported on the influence of the spin speed on the organisation of polymer films of poly(2-methoxy-5-(2-ethylhexyloxy)-1,4-phenylenevinylene) (MEH-PPV).³ It was found that when the polymer solution was cast at high spin speeds, the resulting OLEDs possessed a strong yellow EL emission peak and a weak red shoulder. This was attributed to a more extended and less coiled configuration of the polymer chains formed at high spin speeds. The yellow emission was related to single

chain excitons from the more extended polymer chains. In contrast, the red emissive species were thought to be interchain excimers, associated with aggregates, which are broken up at high spin speeds. Cea et al⁴ have also noted that red shifts in the EL spectra of annealed blended MEH-PPV films are probably related to an increase in interchain interactions and thereby to an increase of excimer formation. It is therefore suggested that aggregates are present in the films of the pure Super Yellow dye. These are then broken up on addition of the blue dye. From a blending viewpoint, the ‘intrinsic’ (single chain exciton) EL from the Super Yellow is green rather than yellow. Once the aggregates are destroyed, by mixing with the blue dye, the emission colour varies in a linear fashion between this green colour and the blue dye coordinates in the CIE diagram.

Table 6.1: Optoelectronic properties of ITO / PEDOT:PSS / 2:Super Yellow / Ca / Al devices with different concentrations of Super Yellow. All samples spin-coated from toluene solutions.

Weight concentration of Super Yellow (%)	EQE _{max} (%) ^a	Luminous		Luminous		CIE (x, y) ^b
		Luminance (cd m ⁻²)	Power Efficiency (lm W ⁻¹)	Luminance (cd m ⁻²)	Power Efficiency (lm W ⁻¹)	
0.0	0.90	21	0.26	289	0.29	0.16, 0.09
1.0	1.00	120	1.05	990	0.70	0.23, 0.36
2.5	1.10	161	1.44	1373	1.05	0.24, 0.40
4.8	1.35	234	1.98	2564	1.72	0.33, 0.61
17.0	2.73	540	3.44	4004	1.87	0.43, 0.56
100.0	1.73	159	0.58	565	0.17	0.50, 0.49

^aMaximum value for external quantum efficiency. ^bAt a current intensity of 1 mA.

Table 6.1 provides the brightness and efficiency data for the OLEDs fabricated by blending compounds **2** and Super Yellow. The external quantum efficiency (EQE) of the OLED

based on the pure blue compound is 0.90%, which is slightly lower than the value of 1.25% reported previously in Chapter 4 and our paper¹ for OLEDs manufactured by spin-coating, but within the typical experimental variation found in different batches of samples. This efficiency increases with the amount of the Super Yellow compound to a maximum of 2.73%, measured for a device containing 17% of Super Yellow, and then decreases to a figure of 1.73%, measured for the structure containing only the yellow dye. The luminous power efficiencies, measured at drive currents of 1 mA and 10 mA, show similar trends. The brightness for the blended-layer devices also appears to be optimum for the blended-layer containing 17% of Super Yellow. This green/yellow-emitting device exhibits an output of 540 cd m⁻² when driven at 1 mA; this increases by approximately an order of magnitude (to 4004 cd m⁻²) for an order of magnitude increase in the drive current. Figure 6.3 reveals that the colour output of these OLEDs depended on the device operating current. Higher currents resulted in the light output shifting to higher energies. Devices with CIE coordinates closest to the white (0.33, 0.33) reference point were those with 1% and 2.5% of Super Yellow mixed with **2** and operated at 1 mA (Figure 6.3).

6.2.2 OXD7 Blend with Super Yellow

As mentioned in Chapter 5, in previous work, J. Ahn and S. Oyston et al reported on a marked improvement of the efficiency of MEH-PPV OLEDs on the addition of electron transport compounds.⁵⁻⁷ A similar strategy was examined in this work. The chemical structure of the electron transport compound that was used, OXD7, is given in Figure 6.1. Figure 6.4 is a potential energy diagram for the materials studied in this work, comparing the Lowest Unoccupied Molecular Orbitals (LUMOs) and the Highest Occupied Molecular Orbitals (HOMOs) for the different molecules: Compound **2**;¹ Super Yellow;⁸ PO-01;⁹ and OXD7.¹⁰

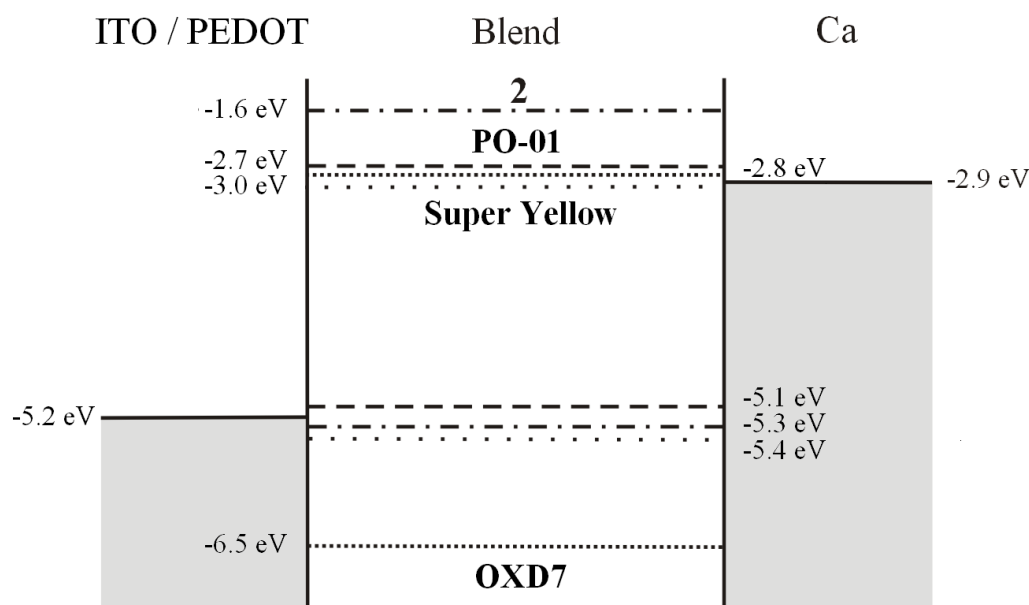


Figure 6.4: Potential energy diagram indicating the HOMO and LUMO levels for the different molecules used in this work.

The LUMO and HOMO levels for the fluorescent and phosphorescent dyes are both similar, consistent with the similar CIE coordinates of their EL emissions. The LUMO level for OXD7 is also similar to those of the yellow dyes. However, the low lying HOMO level for OXD7 is expected to reduce the hole transport in the blended layer OLEDs, providing an enhanced electron to hole current ratio and thereby improving the device internal quantum efficiency.

The EL spectra for blended-layer devices incorporating Compound **2**, Super Yellow and OXD7 are shown in Figure 6.5. The amount of Super Yellow was fixed at 1% while the proportion of OXD7 was varied from 0% to 30% (by weight of the entire blend). It is evident that the addition of the electron transport compound has resulted in a marked reduction in the emission from the yellow dye. Simultaneously, the blue emission from Compound **2** is considerably enhanced. In a related experiment (data not shown) it was confirmed that the addition of OXD7 to Super Yellow does enhance the OLED efficiency, in a similar manner to the experiments with MEH-PPV.⁵⁻⁷ The explanation for the results shown in Figure 6.5 lies in the relative proportions of the OXD7 to the two dyes. The EL

for Compound **2** is enhanced because the relative amount of OXD7 is less than the proportion of Compound **2** (approx. 19% and 29% for the data shown). However, the amount of OXD7 considerably exceeds the amount of Super Yellow present (1% of the entire blend), effectively quenching the yellow EL in the three-component blend, i.e. the electron current flows predominantly through the electron transport compound (OXD7) rather than through the Super Yellow, which is isolated from both electrodes.

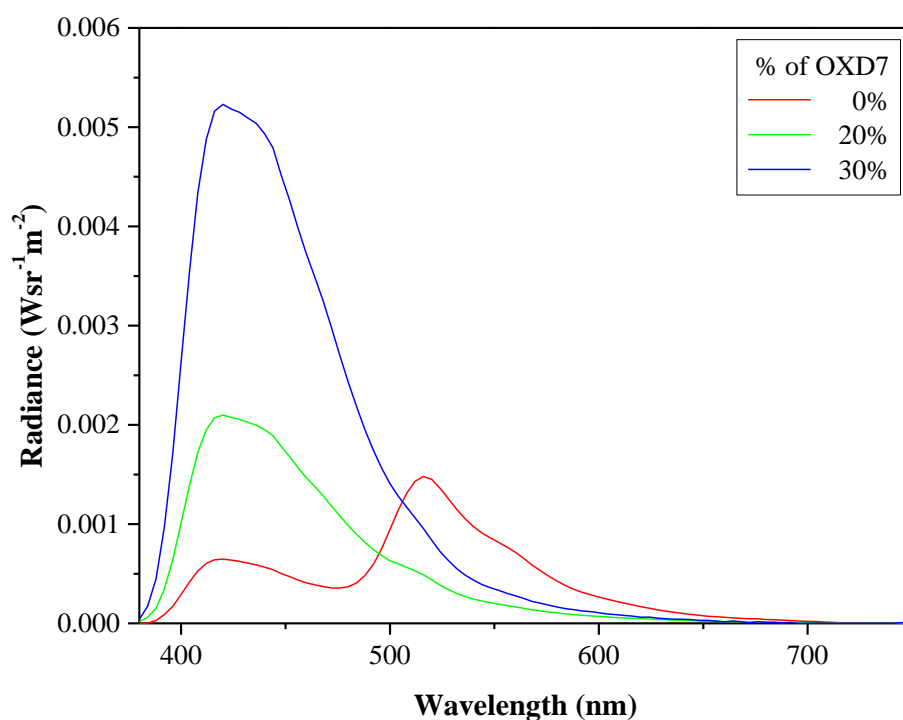


Figure 6.5: Electroluminescence spectra (not normalised) for blended-layer devices incorporating compound **2**, Super Yellow and OXD7. The amount of Super Yellow was fixed at 1% while the proportion of OXD7 is as indicated in the figure.

6.2.3 Conclusions to Super Yellow

This study has shown that the colour of OLEDs based on Compound **2** can be tuned towards white using the fluorescent compound, Super Yellow. However, the emission colour is observed to ‘sweep around’ the (0.33, 0.33) white point towards green. This

effect was attributed to structural reorganisation of the polymer chains in the yellow material.

Addition of OXD7 to the blend of Compound **2** and Super Yellow enhanced the blue emission, whilst reducing the emission from Super Yellow, resulting in primarily blue OLEDs.

6.3 PO-01

6.3.1 Devices Incorporating the Yellow Phosphorescent Dye, PO-01

Figure 6.6 shows the normalised EL spectra for devices prepared with different proportions of Compound **2** with the phosphorescent yellow dye PO-01. In all cases, the spectra were recorded for a device current of 1 mA. The addition of the yellow phosphorescent dye to Compound **2** resulted in a rapid decrease in the blue emission, which disappeared completely when the concentration of PO-01 exceeded 0.4% (by weight).

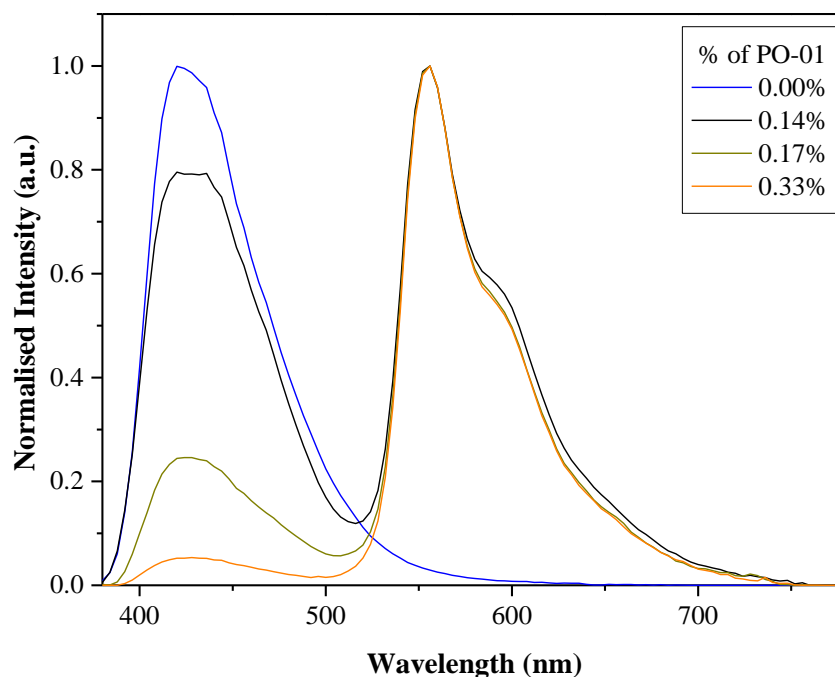


Figure 6.6: Normalised electroluminescence spectra for the devices prepared with different amounts of compounds **2** and PO-01, expressed in weight ratios, at a device current of 1 mA. All samples spin-coated from toluene solutions.

As shown in the CIE diagram in Figure 6.7(a), the coordinates of the emission from the blended-layer OLEDs pass quite close to the pure white point of (0.33, 0.33). The optimum blend concentration for this white emission (0.32, 0.31) at a drive current of 1 mA contains 0.14% of the PO-01. The EQE of this device, referred to as WOLED 1 in Table 6.2, was 0.72%, with an output of about 58 cd m^{-2} at a drive current of 1 mA. Although the luminance increased to 721 cd m^{-2} when the drive current was increased to 10 mA, the peak emission was found to move towards the red part of the spectrum. This phenomenon was found to be irreversible, and is shown in Figure 6.7(b). After the OLED had been subjected to higher drive currents, the EL peak in the blue part of the spectrum had decreased in relation to the red emission. This resulted in an irreversible shift in the CIE coordinates from (0.32, 0.31) to (0.36, 0.37), possibly the result of a change in the morphology of the blended-layer.

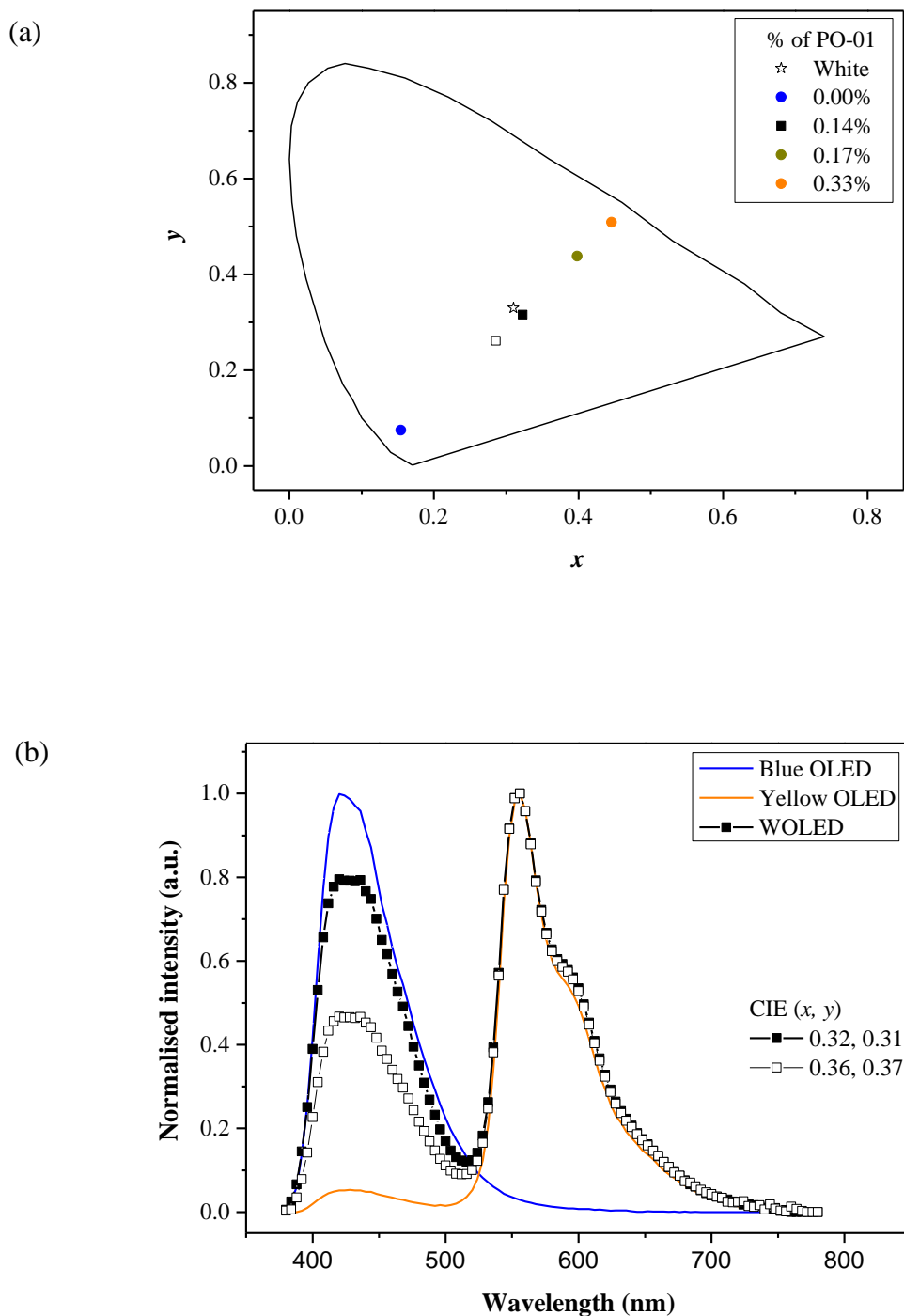


Figure 6.7: (a) CIE (x, y) coordinates for devices, prepared with different amounts of compounds **2** and PO-01 (the spectra of which have been presented in Figure 6.6) at 1 mA. The symbol with the open square is for a WOLED containing 0.14% of PO-01, measured at 10 mA. The pure white reference point (0.33, 0.33) is indicated by the star. (b) Normalised EL spectra for the white OLED at 1 mA before (filled squares) and after (open squares) the application of a 10 mA current. The EL spectra of the blue and yellow OLEDs (0.0% and 0.33% compound PO-01, respectively) are also shown.

6.3.2 OXD7 Blend with PO-01

In contrast to experiments using blended layers based on Super Yellow, the addition of OXD7 to the phosphorescent-based OLEDs did not significantly affect the colour of the light output. The results of adding different amounts of OXD7 to a blend of **2** with PO-01, containing 0.14% (by weight) of the latter, are shown in Figure 6.8.

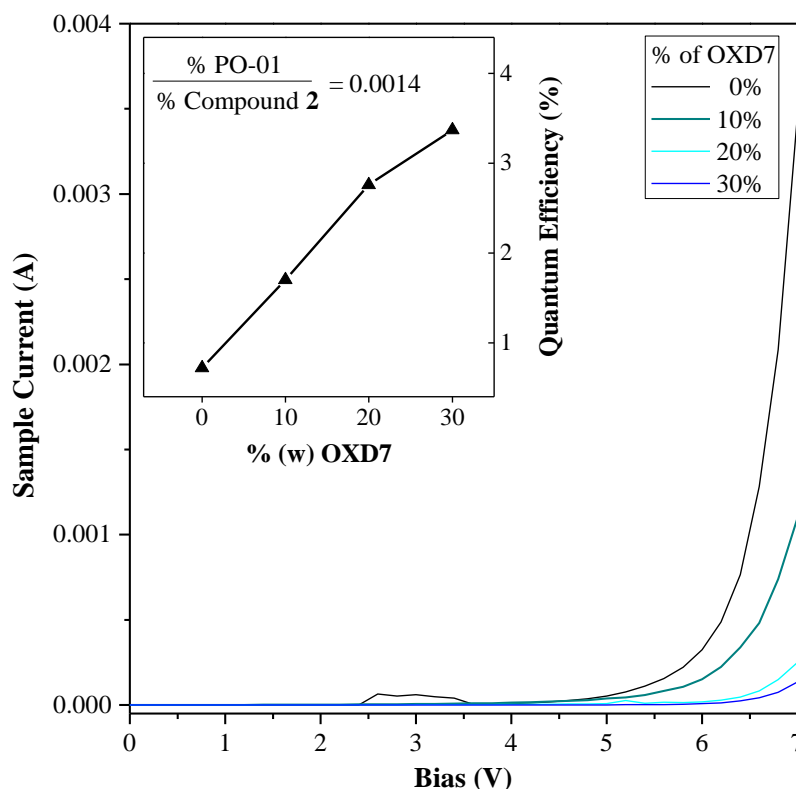


Figure 6.8: Current versus bias data for PO-01:2 OLEDs with different percentages of OXD7 in the blended film. All samples spin-coated from 1:1 (by volume) toluene:chlorobenzene solutions. In all cases, the yellow:blue dye ratio is 0.14% (by weight). The inset shows the external quantum efficiency variation with the weight concentration of OXD7.

The sample current clearly decreases with the addition of OXD7, as expected from the hole-blocking characteristic of this molecule (Figure 6.4). The reduced device current is accompanied by a significant increase in the EQE of the OLED. Such effects are very similar to those reported in previous experiments on the addition of electron transport materials to MEH-PPV.⁵⁻⁷ An EQE figure of approximately 3.4% is achieved using 30% of

OXD7. The very different behaviour on adding the electron transport compound to the blend between Super Yellow and Compound **2** (Figure 6.5) results from the different excitation mechanisms of the fluorescent and phosphorescent dyes. The latter is likely to occur by energy from excitons formed on the host molecule (Compound **2**) being transferred to the triplet emitter. Consequently, if the EL emission from Compound **2** is increased, so is that from the PO-01.

It should be noted that a different solvent (1:1 toluene:chlorobenzene mixture) was used to spin-coat the blended-layer devices incorporating OXD7. This was necessary to provide a good dispersion of all the compounds. As a consequence, the colour of the resulting OLEDs was found to be shifted towards yellow, with CIE coordinates of (0.45, 0.51) for all mixtures shown in Figure 6.8. Using the mixed solvent, it was therefore possible to achieve white emission using significantly lower concentrations of PO-01. For example, the CIE coordinates from a structure, WOLED 2 in Table 6.2, with an architecture ITO / PEDOT:PSS / **1**:PO-01(0.021%):OXD7(30%) / Ca / Al, was (0.30, 0.31), very close to white reference point of (0.33, 0.33). The EQE of this device was 2.5%, significantly greater than the figure of 0.72% achieved for WOLED 1.

Devices containing the OXD7 also showed an emission colour dependence on applied bias, with a shift towards the blue at high currents. In contrast to the previous results for WOLED 1, it is evident that this effect is reversible. This phenomenon is revealed by the data in Figure 6.9, which show the CIE coordinates and the EL spectra at 1 mA (inset) for WOLED 2 before and after passing a forward current of 5 mA, followed by 10 mA.

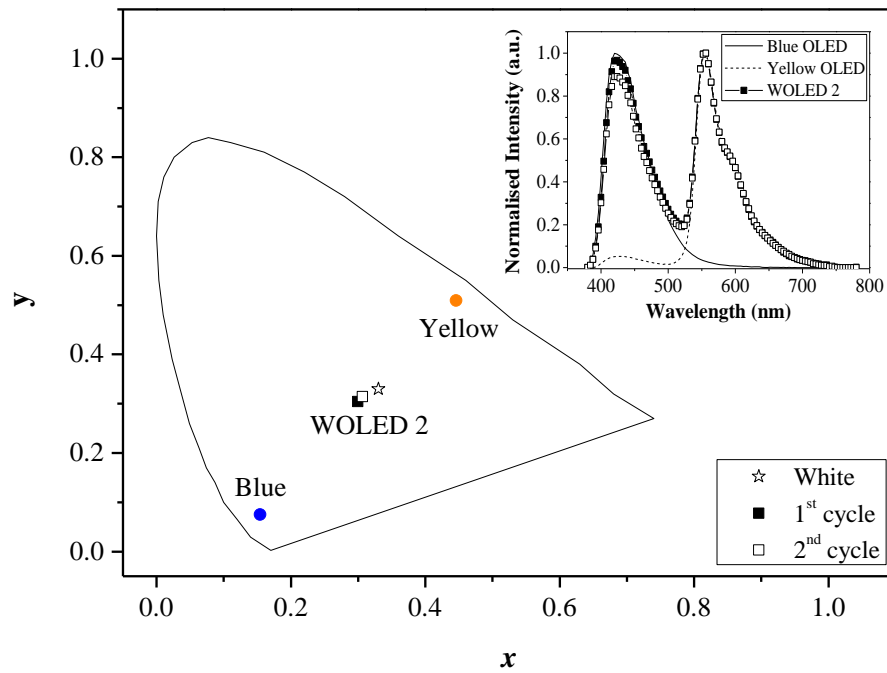


Figure 6.9: CIE diagram showing coordinates for WOLED 2 at 1mA before and after applying higher current intensities (filled and open circles respectively). The CIE (x , y) coordinates for the blue and yellow OLEDs are also included. The inset shows the normalised spectra for the devices at 1 mA.

The high currents have led to no permanent changes in the devices. Thus, the addition of OXD7 to the phosphorescent blended-layer devices appears to have two significant advantages: an efficiency increase and an improvement in the device stability.

Table 6.2: Optoelectronic properties of ITO / PEDOT:PSS / 2:PO-01:OXD7 / Ca / Al OLEDs for different concentrations of PO-01 and OXD7 molecules. WOLED 3 is prepared in the same conditions of WOLED 2 but using a cathode of CsF/Al.

Devices	Solvent ^a	OXD7 ^b	PO-01 ^b	EQE _{max} (%) ^c	Luminance (cd m ⁻²)	Luminous		CIE (x,y) ^d	
						Power Efficiency (lm W ⁻¹)	Luminance (cd m ⁻²)		Power Efficiency (lm W ⁻¹)
					1 mA	10 mA			
Blue OLED	Toluene	-	-	0.90	21	0.26	289	0.29	0.16, 0.09
	T:C	30	-	3.00	49	0.44	394	0.26	0.16, 0.09
WOLED 1	Toluene	-	0.140	0.72	58	0.53	721	0.56	0.32, 0.31
WOLED 2	T:C	30	0.021	2.50	221	1.83	1582	0.98	0.30, 0.31
WOLED 3	T:C	30	0.021	2.25	219	2.16	1620	1.18	0.30, 0.31
Yellow OLED	Toluene	-	0.330	0.70	171	1.43	2426	1.64	0.45, 0.51
	T:C	30	0.140	3.37	910	6.45	7819	4.50	0.45, 0.51

^aSolvent used in the spinning solution. (T:C) represents toluene :chlorobenzene1:1 (v/v). ^bWeight concentration (%). ^cMaximum value for the external quantum efficiency. ^dAt a current intensity of 1 mA.

Table 6.2 lists the important electro-optical properties of OLEDs fabricated from blends of compounds **2**, PO-01 and OXD7. Included are the characteristics of a further device, WOLED 3, in which the cathode material was CsF/Al instead of Ca/Al. These alternative devices were produced to remove the Ca, which is unstable in air, a necessary step for further development. The properties of WOLED 2 and WOLED 3 are very similar showing the CsF gives comparable devices, without the need for the Ca injector. The EQE of the optimised WOLED was 2.5%, with a luminance of 221 cd m⁻² and a luminous power efficiency of 1.83 lm W⁻¹ (all measured with a 1 mA drive current). The CIE coordinates were (0.30, 0.31). Figure 6.10 shows photographs of the optical output of the blue (pure **2**), yellow (0.33% PO-01) and WOLED 2 devices.

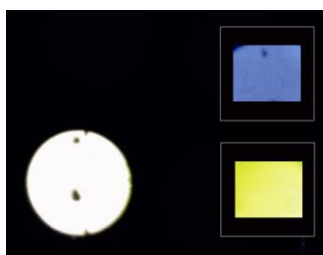


Figure 6.10: Photographs of the light output of the reference blue (top right) and yellow (bottom right) devices and WOLED 2 (left) recorded at a constant current of 1 mA.

6.3.3 Conclusions to PO-01

Similar to the results for Super Yellow, blending the yellow phosphorescent material PO-01 with Compound **2** allows the colour to be tuned towards white. For this blend the colour passes quite close to the pure white point. It was also observed that at drive currents of 10 mA the peak emission undergoes an irreversible shift towards the red end of the spectrum.

In contrast to the Super Yellow blends, addition of OXD7 had little effect on the emission colour of these devices but did improve the overall efficiency. A dependence of colour on drive current was again observed but for these devices was found to be reversible.

6.4 Blended-layer Devices Incorporating Compound 9

Further to the encouraging results described with OXD7, OLEDs based on active layers with blends of Compound 9 with Super Yellow, and Compound 9 with PO-01 (both in chlorobenzene solutions) were also studied. Compound 9 is described in Chapter 5 and builds on the idea of addition of OXD7 blends by chemically attaching an OXD group directly to the molecular structure. The results are summarised in the CIE diagram in Figure 6.11, with the full data given in Tables 6.3 and 6.4.

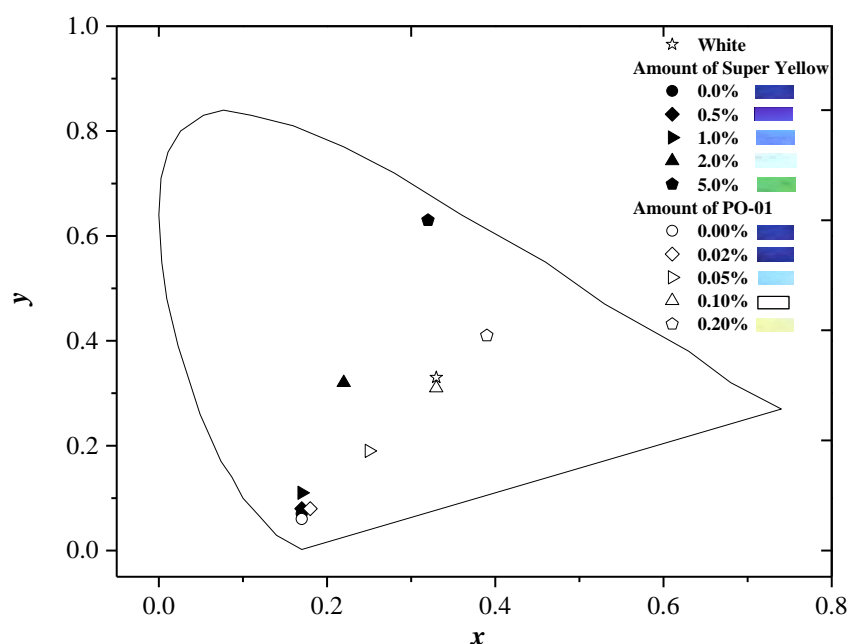


Figure 6.11: CIE (x , y) coordinates for devices prepared with different amounts of Compound 9 and Super Yellow (filled symbols) and Compound 9 and PO-01 (open symbols) at 1 mA. All samples spin-coated from chlorobenzene solutions. The CIE coordinates of pure white (0.33, 0.33) are also included for reference. Photographs of the emission are included in the legend.

Table 6.3: Optoelectronic properties of ITO / PEDOT:PSS / Compound **9**:Super Yellow / Ca / Al devices with different concentrations of Super Yellow. All samples spin-coated from chlorobenzene solutions.

Weight concentration of Super Yellow (%)	EQE _{max} (%) ^a	Luminous			CIE (x, y) ^b	
		Luminance (cd m ⁻²)	Power Efficiency (lm W ⁻¹)	Luminance (cd m ⁻²)		Power Efficiency (lm W ⁻¹)
		1 mA		10 mA		
0.0	0.27	2.8	0.0019	71	0.057	0.17, 0.07
0.5	0.34	6.5	0.060	94	0.070	0.17, 0.08
1.0	0.48	12	0.11	133	0.097	0.17, 0.11
2.0	0.58	62	0.55	541	0.36	0.22, 0.32
5.0	1.47	394	2.4	3505	1.6	0.32, 0.63

^aMaximum value for the external quantum efficiency. ^bAt a current intensity of 1 mA.

Table 6.4: Optoelectronic properties of ITO / PEDOT:PSS / Compound **9**:PO-01 / Ca / Al devices with different concentrations of PO-01. All samples spin-coated from chlorobenzene solutions.

Weight concentration of PO-01 (%)	EQE _{max} (%) ^a	Luminous			CIE (x, y) ^b	
		Luminance (cd m ⁻²)	Power Efficiency (lm W ⁻¹)	Luminance (cd m ⁻²)		Power Efficiency (lm W ⁻¹)
		1 mA		10 mA		
0.0	0.27	2.8	0.0019	71	0.057	0.17, 0.07
0.02	0.25	2.5	0.017	62	0.036	0.18, 0.08
0.05	0.33	1.7	0.011	153	0.085	0.25, 0.19
0.1	0.42	14	0.088	353	0.19	0.33, 0.31
0.2	0.46	27	0.17	692	0.33	0.39, 0.41

^aMaximum value for the external quantum efficiency. ^bAt a current intensity of 1 mA.

Devices based on pure Compound **9** (i.e. device architecture ITO / PEDOT:PSS / Compound **9** / Ca / Al) possess a similar deep-blue colour to those based on Compound **2** (CIE coordinates 0.17, 0.07); however, as seen in Chapter 5, the device external quantum efficiency, 0.27%, was significantly less than the value of 0.9% measured above for OLEDs based on pure **2**. The trends in the CIE coordinates as Compound **9** is blended with the Super Yellow and with PO-01 dye are similar to those reported above with Compound **2**. As Compound **9** is added to Super Yellow, the OLED colour shifts from yellow to green, and finally to blue; the locus of the data points misses the pure white point. Interestingly, the EL from Super Yellow is not quenched by Compound **9**, in contrast to the findings using OXD7 blended with Compound **2**.

The EL outputs from blends of Compound **9** with PO-01 pass very close to the white point. The efficiency values of the latter category of WOLEDs are, however, disappointing. For a device containing 0.1% of PO-01, which possesses CIE coordinates of (0.33, 0.31), the EQE is 0.42%, almost an order of magnitude less than WOLED2 (Table 6.2) in which the OXD7 was added separately to Compound **2**.

The above results suggest that the detailed orientation of the oxadiazole moieties with respect to the carbazole and fluorene groups is important. It is perhaps significant that, whereas the topologies of **2** and OXD7 are similar (linear molecules), Compound **9** is quite different (Y-shaped). This is likely to lead to different blended-layer morphologies with different interactions between the various sub-units in the electro-active molecules. A further issue may be the mixed solvent that was used to process the blends of **2**, PO-01 and OXD7. It is now apparent that solvent effects play key roles in other organic blended devices, for example photovoltaic cells.^{11, 12} Clearly, further experiments are needed to clarify such issues.

6.4.1 Conclusions to Compound 9

Devices based on Compound 9, incorporating chemical addition of OXD moieties to the structure of Compound 2 show that blending with Super Yellow and PO-01 allows the colour of emission to be tuned. Blends with Super Yellow miss the white point, as observed for Compound 2, but interestingly the yellow emission is not quenched as was observed for Compound 2 blended with OXD7 and Super Yellow.

Blending with PO-01 allows the emission colour to be tuned very close to the white point, similar to results with Compound 2 and PO-01. However, the efficiency of the white devices was low compared with white devices based on blends of Compound 2, OXD7 and PO-01. Although only low efficiency WOLEDs were produced, the approach has demonstrated that WOLEDs may be fabricated based on a simple single-layer device.

6.5 Conclusions

Single-active-layer blended OLEDs in which a deep blue carbazole-based dye, 2, is mixed with yellow emitting materials have been fabricated and their electro-optical behaviour studied as a function of blend composition. Two different yellow dyes were used: a commercial fluorescent phenyl-substituted poly(*p*-phenylene-vinylene) polymer, Super Yellow, and an iridium-based phosphorescent dye, PO-01. Although OLEDs based on the pure yellow compounds possessed similar CIE coordinates, the blended-layer devices behaved very differently. As Compound 2 was added to Super Yellow, the OLED colour shifted from yellow to green, and finally to blue; the locus of the data points missed the (0.33, 0.33) white point. The effect was attributed to structural reorganisation of the polymer chains in the yellow material. In contrast, blends of 2 with PO-01 passed very close to the white point, and achieved CIE coordinates of (0.30, 0.31). The efficiency of

these devices could be optimised by the addition of the electron transport compound OXD7 to the blend of the two dyes. The result was a simple white OLED architecture with an external quantum efficiency of about 2.5%, a luminance of 221 cd m⁻² and a luminous power efficiency of 1.83 lm W⁻¹, all measured at a drive current of 1 mA. Although these data fall a long way short of the highest values currently reported in the literature, the device should be fabricated at a relatively low cost and high reproducibility compared with multilayer device architectures, including applicability to large-area panels.

Devices using blends of yellow emitters and Compound **9** (a structure based on **2** with chemically attached OXD groups) were also experimented with and for the phosphorescent molecule PO-01, white OLEDs were produced, although the efficiency was low at 0.42%. As seen in Chapter 5, the chemical attachment of the OXD group does not lead to an improvement in device efficiency compared to the blends of OXD7 for the blue devices.

The results clearly indicate the effects that the morphologies of the blended-layer devices have on their electro-optical properties. Further work, therefore, needs to be directed at understanding the subtleties of the interactions of the various molecular species with each other and with the processing solvents.

6.6 References

- 1) A. L. Fisher, K. E. Linton, K. T. Kamtekar, C. Pearson, M. R. Bryce, M. C. Petty, *Chem. Mater. Commun.*, **23**, 1640-1642, **2011**.
- 2) K. H. Shen, S. T. Yeh, H. L. Huang, I. H. Shen, M. T. Chu, T. S. Hsieh, **2008**, US Patent 7445857.
- 3) Y. Shi, J. Liu, Y. Yang, *J. Appl. Phys.*, **87**, 4254-4263, **2000**.

- 4) P. Cea, Y. Hua, C. Pearson, C. Wang, M. R. Bryce, F. M. Royo, M. C. Petty, *Thin Solid Films*, 408, 275-281, **2002**.
- 5) J. H. Ahn, C. Wang, C. Pearson, M. R. Bryce, M. C. Petty, *Appl. Phys. Lett.*, 85, 1283-1285, **2004**.
- 6) S. Oyston, C. Wang, G. Hughes, A. S. Batsanov, I. F. Perepichka, M. R. Bryce, J. H. Ahn, C. Pearson, M. C. Petty, *J. Mater. Chem.*, 15, 194-203, **2004**.
- 7) S. Oyston, C. Wang, I. F. Perepichka, A. S. Batsanov, M. R. Bryce, J. H. Ahn, M. C. Petty, *J. Mater. Chem.*, 15, 5164-5173, **2005**.
- 8) S. R. Tseng, Y. S. Chen, H. F. Meng, H. C. Lai, S. F. Horng, H. H. Liao, C. S. Hsu, *Synth. Met.*, 159, 137-141, **2009**.
- 9) S.-Y. Huang, H.-F. Meng, H.-L. Huang, T.-C. Chao, M.-R. Tsenf, Y.-C. Chao, S.-F. Horng, *Synth. Met.*, 160, 2393-2396, **2010**.
- 10) C. Yang, G. He, R. Wang, Y. Li, *Thin Solid Films*, 363, 211-213, **2000**.
- 11) G. Li, Y. Hao, H. Yang, V. Shrotriya, G. Yang, Y. Yang, *Adv. Funct. Mater.*, 17, 1636-1644, **2007**.
- 12) L. Chang, H. W. A Lademann, J.-B. Bonekamp, K. Meerholz, A. J. Moule, *Adv. Funct. Mater.*, 21, 1779-1787, **2011**.

7 Transistor Development

7.1 In this Chapter...

Initial studies were carried out on a simple pentacene transistor to provide a proof of concept for the further development of transistors based on three novel materials, compounds **1**, **2** and **8**, synthesised by the Bryce group in the Department of Chemistry at Durham University. Pentacene was also incorporated into OLEDs as an initial study into pentacene OLEFETs. See Appendix C.

7.2 Pentacene

Pentacene transistors were made using the standard OFET structure shown in Section 3.5.5 of the Experimental chapter. The output characteristics (Figure 7.1) for the pentacene OFETs were as expected from simple transistor theory, with a linear regime at low drain voltages, becoming a saturated regime at higher drain voltages. As the gate voltage was increased, the pinch-off point occurred at higher drain voltages. Hysteresis was observed at low V_{DS} with a V_G of -30 V, which could be due to temporary charge build up in the device.

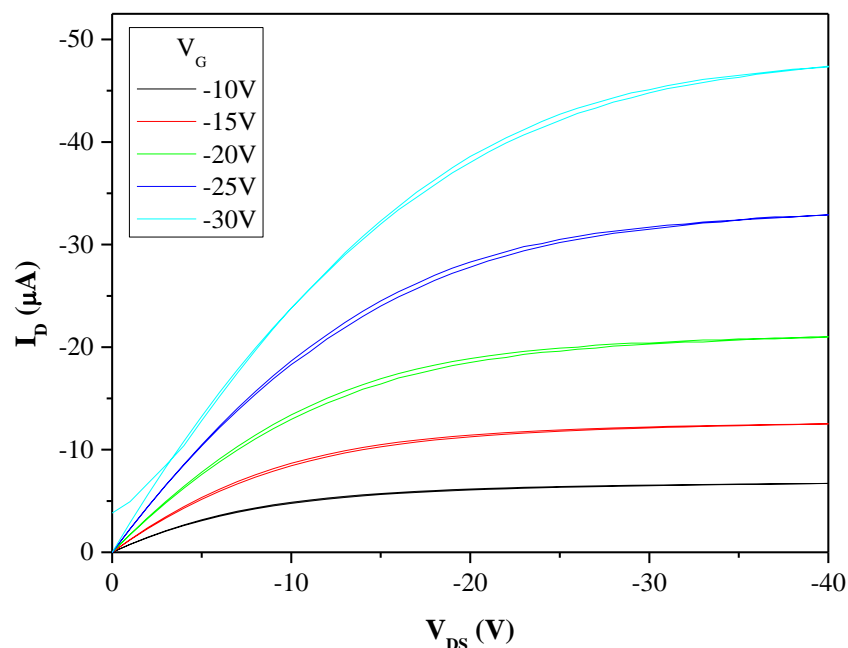


Figure 7.1: Output characteristics for a pentacene OFET with channel dimensions $L = 200 \mu\text{m}$ and $W = 4000 \mu\text{m}$.

There was some evidence that increasing channel lengths reduced the magnitude of the drain current, whilst increasing channel widths increased the drain current. However, this pattern was difficult to identify as there was significant variation in the drain current even for devices with identical channel dimensions. Nonetheless, this trend was expected based on Equations 2.10 and 2.11 (see Chapter 2) which show that I_{DS} is proportional to W and inversely proportional to L .

Some output characteristics (data not shown) of other devices in the batch showed unusually high currents, which could be due to two different reasons. First, the pentacene crystals could have a larger than normal grain size caused by slow evaporation. Secondly, the PMMA insulator could be too thin. The optimum thickness of the layer is 150 nm ,¹ films of 100 nm or less result in higher currents. This possibility was explored and the thickness found to be 160 nm (based on AFM images of scratches) which is close to 150 nm and therefore cannot be a cause. The cause of the high drain currents in the output

characteristics is most likely due to the grain size of pentacene.² This could be further proven with AFM images.

The transfer characteristics were obtained at $V_{DS} = -20$ and -30 V and V_G from 20 to -40 V for all devices.¹ In the ‘on’ state of the device, above a threshold voltage of around 2-4 V all the graphs showed a similar trend to published data for pentacene OFETs.³ However, the characteristic off state where the gradient of I_{DS} changes rapidly in the subthreshold region was not as clearly defined and most devices showed no conduction below ~ 60 nA I_{DS} . Only one device showed behaviour similar to what would be expected and is given in Figure 7.2. It is noteworthy that even this graph only showed clear subthreshold conduction at $V_{DS} = -30$ V and additionally only on the first voltage sweep.

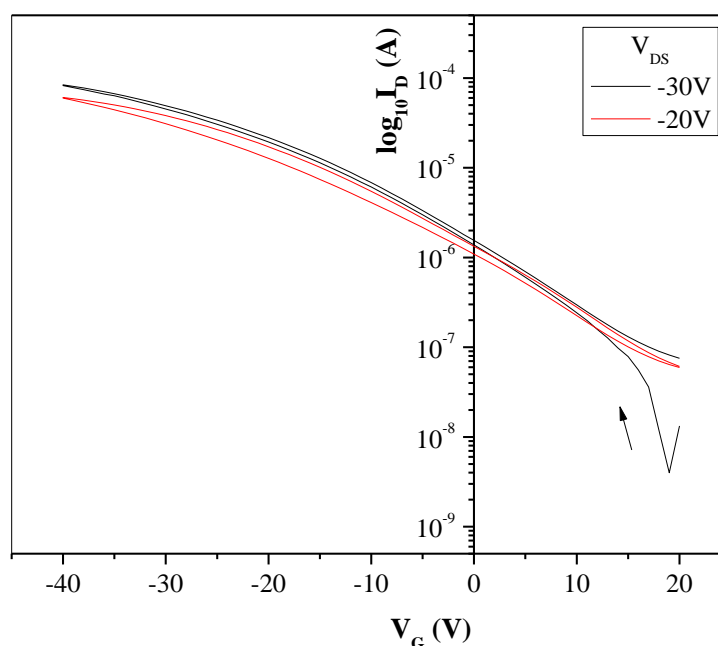


Figure 7.2: Transfer characteristics for a pentacene OFET with channel dimensions $L = 200$ μm and $W = 4000$ μm .

It is clear from the graph that pentacene is a good hole transporter, based on the rise in drain current with increasing negative gate voltage. The mobility and threshold voltage

mentioned earlier were calculated from the $\sqrt{|I_{DS}|}$ vs V_G graph. Mobility was found to be $0.3 \text{ cm}^2 \text{ V}^{-1} \text{ s}^{-1}$. (See Figure 7.3.) Previous work³ reported a mobility of $0.7 \text{ cm}^2 \text{ V}^{-1} \text{ s}^{-1}$ for a similar OFET with a gate dielectric thickness of 120 nm. The difference could be partly explained by the fact that the devices studied here possessed a slightly thicker dielectric at 160 nm. As for the output characteristics, some hysteresis was again observable.

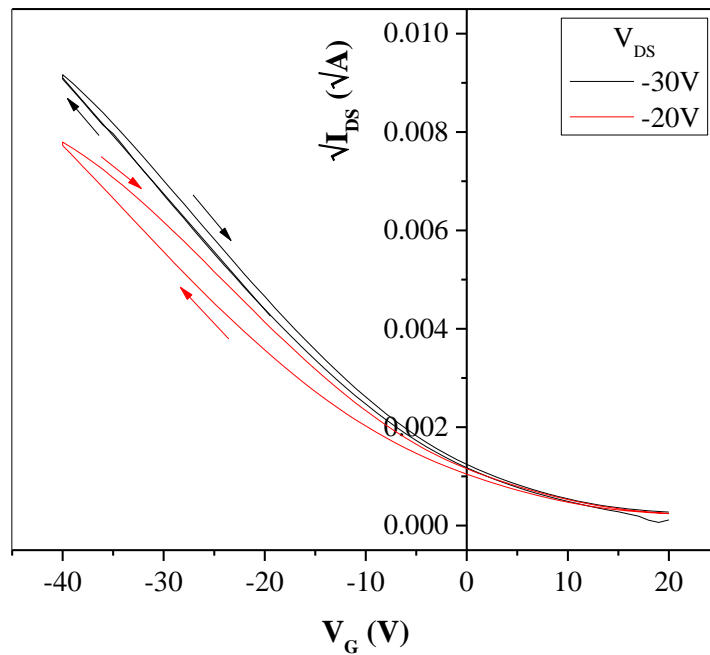


Figure 7.3: Graph of $\sqrt{|I_{DS}|}$ vs V_G for pentacene OFET with channel dimensions $L = 200 \text{ }\mu\text{m}$ and $W = 4000 \text{ }\mu\text{m}$.

Previous studies on a pentacene transistor¹ showed that it was important to ensure that the PMMA layer was as close to the optimum thickness of 150 nm as possible in order to be certain of good, reliable results. To do this, the PMMA recipe on page 78 was henceforth strictly followed.

This study has shown that the basic processing techniques are valid to produce transistors.

7.3 Compound 8

Compound **8** is part of a series of materials synthesised by the Bryce group in the Department of Chemistry at Durham University for use in OLEDs.⁴ This material is designed to possess hole and electron transporting as well as emissive properties in one single molecular structure. The ambipolar nature of the molecule suggested that it may function in a transistor architecture. Also of interest was whether the holes and electrons could recombine to emit light.

The output characteristics for these devices, Figure 7.4, show no field-effect and are dominated by leakage. There is no dependence of I_D on V_{DS} but the current does increase with increasing gate voltage.

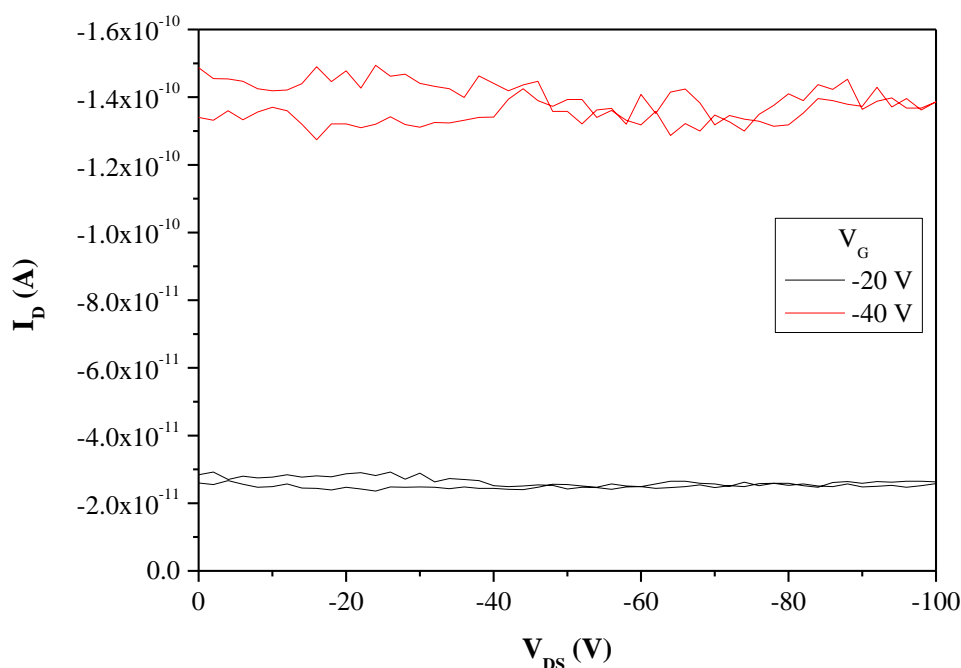


Figure 7.4: Output characteristics measured for OFETs based on Compound **8** showing no dependence of I_D on V_{DS} .

An initial inspection of the $\log I_D$ in the transfer characteristics suggested promising transistor properties. However, this is misleading. In processing the I_D vs V_G graph, to

obtain the log plot, the modulus of I_D was used but the current at negative gate voltage was always negative, again showing that the drain current is solely dependent on the gate voltage, implying leakage from the gate to the drain.

The previous work on pentacene has shown that the processing techniques are good to produce transistors and it has been shown that Compound **8** works in an OLED architecture. Therefore it must be concluded that this particular molecule is unsuitable for transistors.

7.4 Compound 1

Results based on Compound **1** follow. As for the Compound **8** devices, the output characteristics showed no evidence of field-effect and the drain current was again dominated by the gate voltage. However, in this case, the observed I_D is not solely dependent on the gate voltage but in some cases a combination of V_G and V_D . I_{DS} remained at zero for increasing V_G until V_G was -15 V and V_{DS} was -39 V, at which point the drain current spikes. Subsequent sweeps of V_G at -20 and -30 V show a non-linear increase in I_D with V_{DS} , after -30 V V_{DS} when gate voltage was -20 V, and after -10 V V_{DS} when the gate voltage was -30 V. Strangely, at an applied gate voltage of -25 V I_{DS} remained at zero throughout the V_{DS} voltage sweep. One possibility to explain the observed behaviour is a poor electrical connection between the source and drain electrodes.

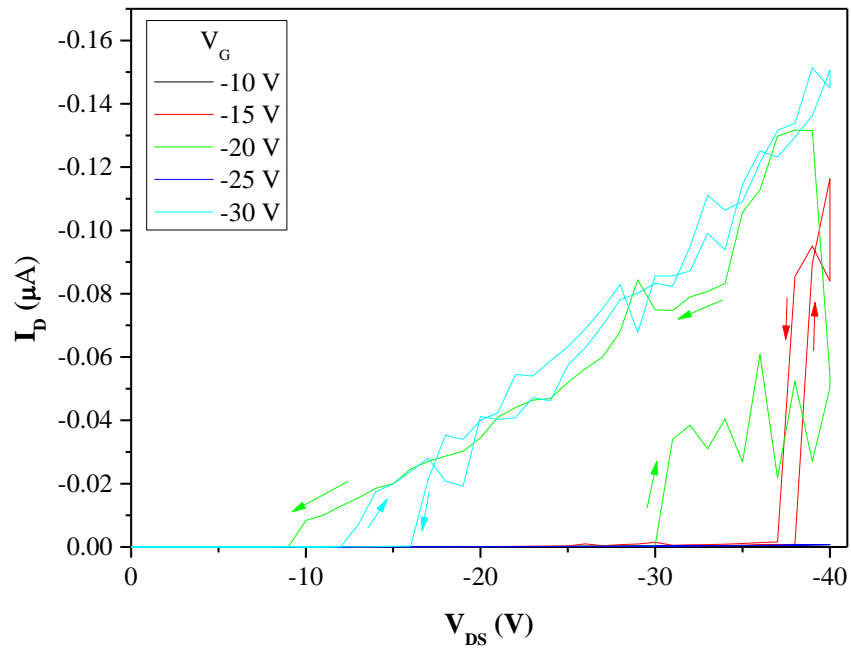


Figure 7.5: Output characteristics obtained from a $L = 50 \mu\text{m}$ and $W = 4000 \mu\text{m}$ Compound **1** device.

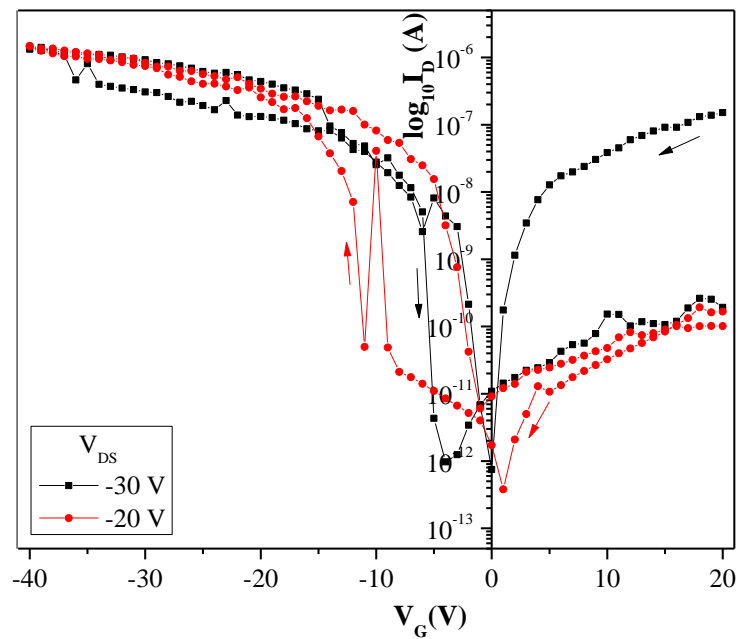


Figure 7.6: Transfer characteristic of Compound **1** transistor with channel dimensions $L = 50 \mu\text{m}$ and $W = 4000 \mu\text{m}$.

In the transfer characteristics (Figure 7.6), the values of I_D observed at negative gate voltage are in reality also negative. Since the current only appears negative at negative values of V_G the effect must be due to leakage from the gate. Thus the devices are not behaving as transistors. Other complex behaviour was noted in the transfer characteristics. At a V_{GS} of -10 V, a sudden peak in the curve is observed. This occurred on a number of measurements and it was considered that a switching effect may have been observed. Two devices showed this switching effect in the transfer characteristics. It was decided that the switching effect was most likely a polymer effect, as polystyrene has shown similar effects in the past.⁵

AFM measurements on Compound 1 (Figure 7.7) revealed small holes of approximately 20 nm diameter and unknown depth in the film. If these holes penetrate into the PMMA, they could be the source of the leakage.

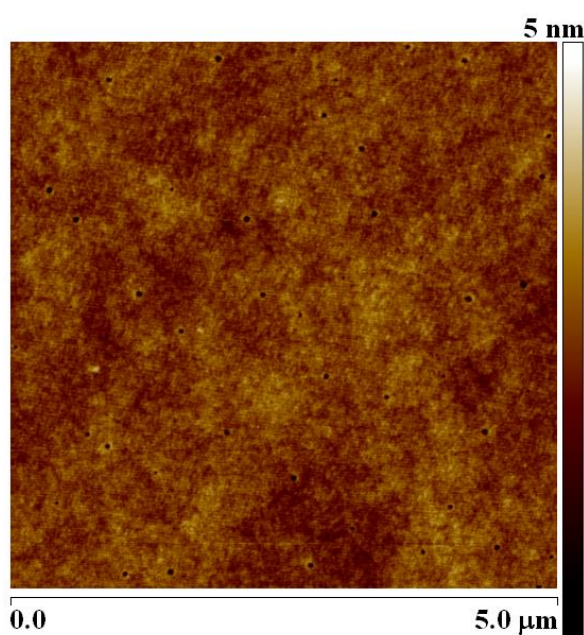


Figure 7.7: AFM image of Compound 1 film.

Despite these problems, the characteristics obtained did show evidence of in-plane conduction in the film, with V_G of -30 V reaching I_D of -0.16 μA . Unfortunately the Department of Chemistry was not able to synthesise more of this material, so

measurements on additional devices was not possible. It should be possible to measure light output from these devices and further studies could be made with this material if more became available.

7.5 Compound 2

Devices were made in the same way as the successful pentacene devices. The results showed that although there was no leakage, there was poor charge injection. One reason for this could be poor alignment of the device which is especially challenging to achieve in the glove box. Thus this issue was avoided by creating all further devices without patterning the Compound 2.

A number of published articles⁶⁻¹¹ use dissimilar metal source-drain electrodes in order to improve charge injection by more closely matching the energy levels of the source/drain to the HOMO/LUMO of the organic layer. It was decided to use gold and aluminium as the source and drain. An initial experiment was designed to verify that it was possible to pattern the devices using a thermal evaporator and one shadow mask. This strategy greatly depends on the angle of evaporation, however this was achieved and Figure 7.8 shows a microscope image and AFM line scan of the electrodes. See Experimental chapter, page 75 for the evaporation procedure used.

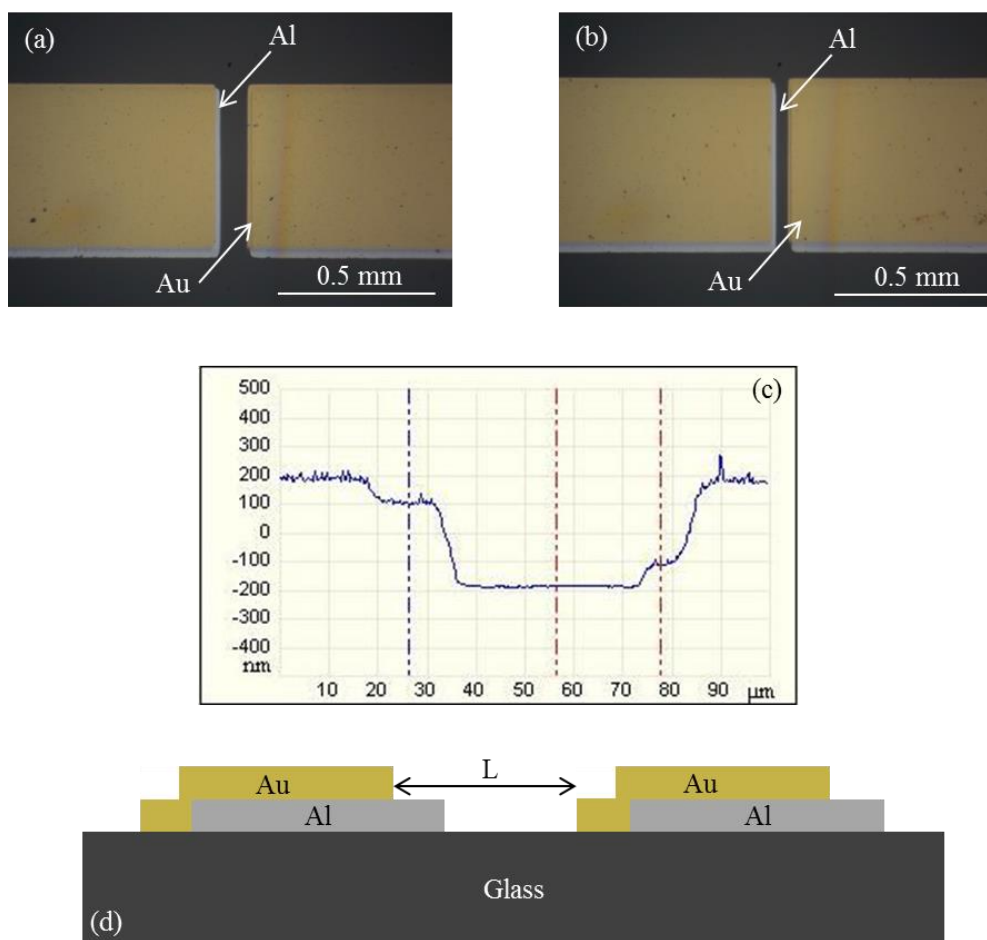


Figure 7.8: Gold (brown areas) and aluminium (grey areas) electrodes with channel dimensions approximately (a) $L = 100 \mu\text{m}$ and $W = 500 \mu\text{m}$ and (b) $L = 50 \mu\text{m}$ and $W = 500 \mu\text{m}$, evaporated through one shadow mask, as imaged by optical microscope. (c) AFM line scan of height vs length across the $L = 50 \mu\text{m}$ and $W = 500 \mu\text{m}$ device with markers showing (L-R) aluminium step, substrate and gold step. (d) Schematic diagram showing cross section of dissimilar electrode evaporation structure.

Devices incorporating Compound **2** and gold-aluminium source-drain (rather than gold-gold electrodes) were fabricated using the same method as was used for the original pentacene transistors. The output and transfer characteristics for a device with channel dimensions of $L = 200 \mu\text{m}$ and $W = 2000 \mu\text{m}$ are shown in Figure 7.9. High gate voltages of -80 to -100 V produced a very low magnitude of I_D . Although the forward voltage sweep in the output characteristics showed an anomalous peak in I_D at $V_{DS} = 0 \text{ V}$, the return sweep showed evidence of a field-effect, with I_D saturated at high V_G and apparently dependent on V_{DS} below the pinch off point. The anomalous peak at $V_{DS} = 0 \text{ V}$ is likely

due to leakage and is very low considering the high magnitude of the gate voltage, up to -100 V. The second anomalous peak on the sweep at $V_G = -100$ V at $V_{DS} = -70$ V is likely due to external noise, considering the low level of current measured. In the transfer characteristics the minima vary between the forward and return voltage sweeps. This may be due to charge being injected and stored.

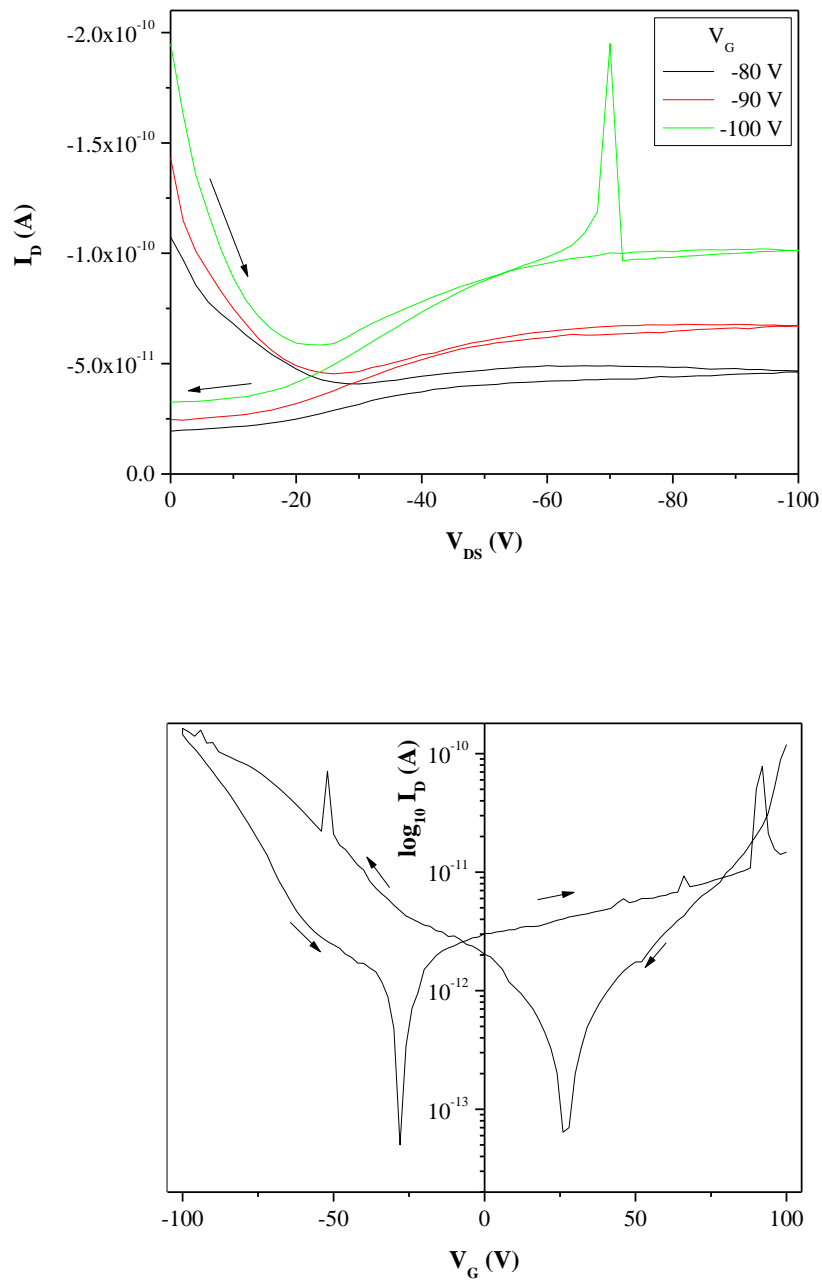


Figure 7.9: (a) Output and (b) transfer characteristics with V_{DS} at -40 V. Device architecture: Al / PMMA / Compound **2** / Al!Au. Channel dimensions: $L = 200$ μm and $W = 2000$ μm .

A device from the same substrate but with a smaller channel length of 50 μm (down from 200 μm) and a longer channel width of 4000 μm (from 2000 μm) was measured and it was expected that this device would show better results, however they were similar in shape and magnitude to the above device, even at higher values of applied V_{DS} and V_{G} .

In an attempt to improve charge injection, a more complex stack device was considered. A paper by Capelli et al.¹² was published during this research. These workers made an organic light-emitting transistor using more layers, as shown in Figure 7.10. Essentially their devices used an ITO gate, PMMA dielectric (450 nm), electron transport layer (7 nm), emissive layer, hole transport layer (15 nm) and gold source and drain contacts (50 nm).

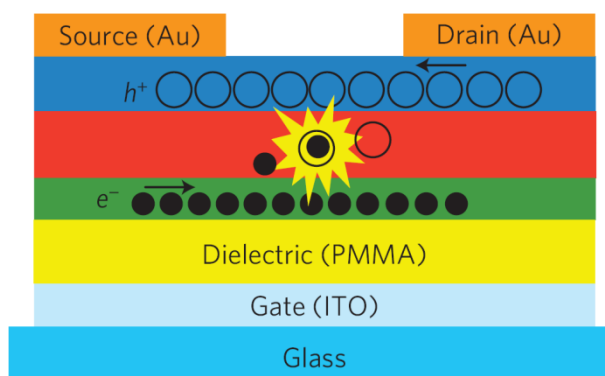


Figure 7.10: Structure of OLET by Capelli et al.¹²

The devices they reported achieved efficiencies of 5%, greatly exceeding the previous leading devices at the time, which were 2.2%.¹³ Their dielectric was much thicker at 450 nm.

To proceed using this new idea, similar layers were gradually incorporated into the basic structure to measure their individual effect on device characteristics. The equivalent emissive layer here was the Compound **2**. It was decided that the first step would be to add a hole transport layer, pentacene. In analogy to the Capelli paper, the initial experiment used a thin 7 nm layer of pentacene on top of the PMMA and below the Compound **2** as shown in Figure 7.11.

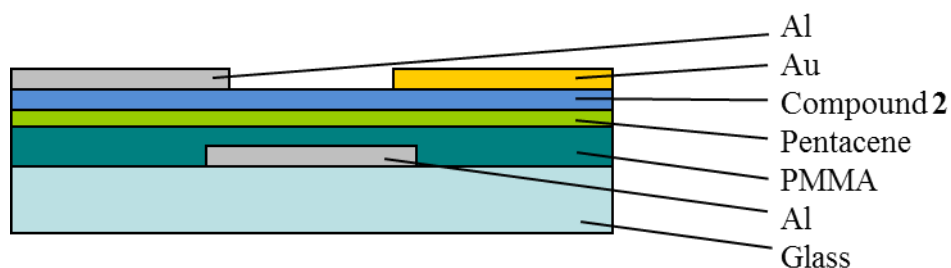
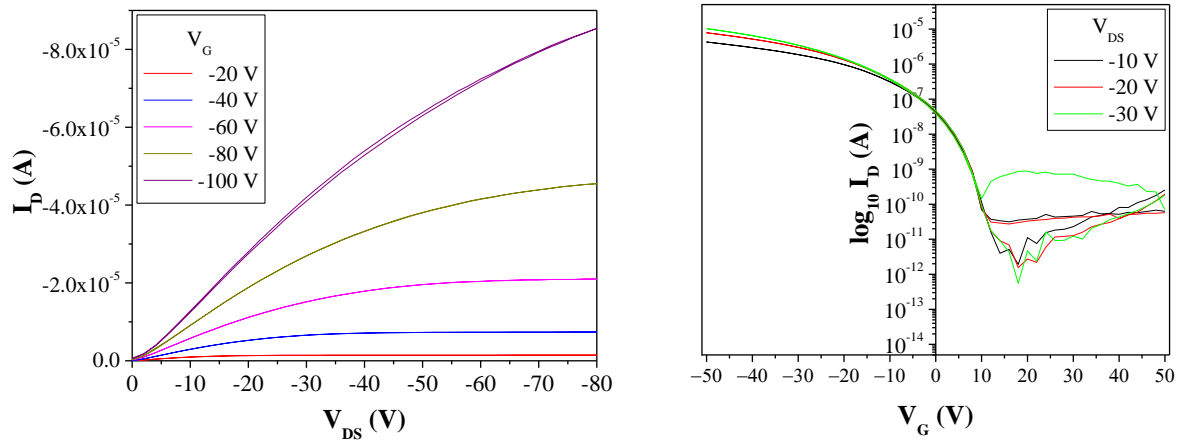


Figure 7.11: Device configuration incorporating pentacene as hole transport layer.

The electrodes were left as Al/Au due to the promising results in previous experiments. The results for these new devices with pentacene were poor and only showed leakage currents. It is possible that the poor device characteristics are partly due to the extremely thin pentacene layer, which may not be continuous. It was decided to see if increasing the thickness of the pentacene layer had any positive effect on the device. In the next set of devices, the stack was the same as previously, but the pentacene layer was 40 nm thick. It was noted that both output and transfer characteristics looked suspiciously similar to the pentacene devices described earlier on page 158, with no evidence of conduction at positive gate voltages, and thus poor electron transporting properties. To verify whether the Compound **2** was having any effect, devices with no Compound **2** were made alongside (i.e. at the exact same time) those containing Compound **2**. Results are shown in Figure 7.12 for Compound **2** containing devices having channel dimensions $L = 200 \mu\text{m}$ and $W = 2000 \mu\text{m}$ and devices without Compound **2** with dimensions $L = 50 \mu\text{m}$ and $W = 2000 \mu\text{m}$.

(a) With Compound 2



(b) Without Compound 2

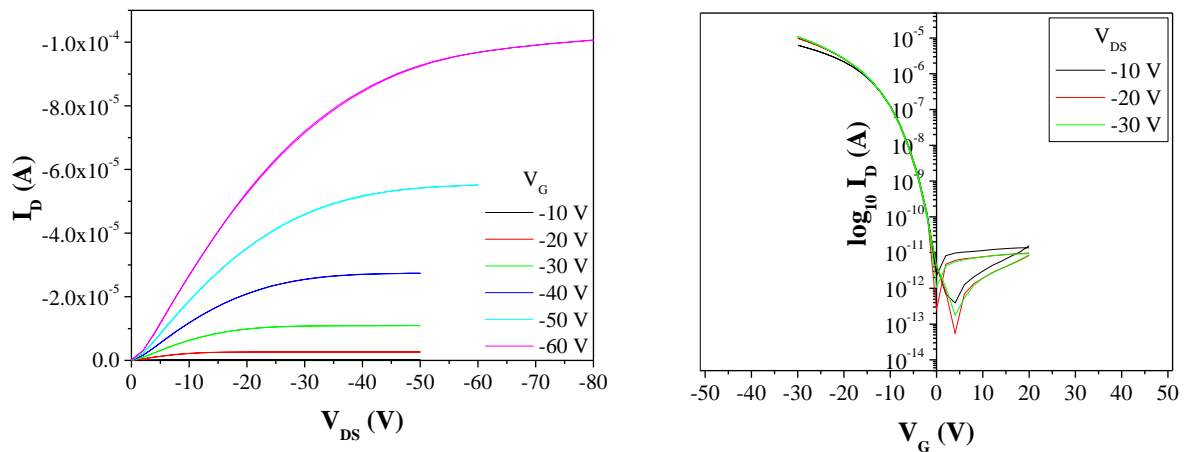


Figure 7.12: Output and transfer characteristics from a repeated set of devices (a) with Compound 2 and (b) without Compound 2. Channel dimensions $L = 200 \mu\text{m}$ and $W = 2000 \mu\text{m}$ and $L = 50 \mu\text{m}$ and $W = 2000 \mu\text{m}$, respectively.

The output characteristics for the devices containing Compound 2 showed reduced currents compared to those without Compound 2. For example, for the devices with Compound 2, $I_{DS} = -0.11 \mu\text{A}$ at $V_G = -60 \text{ V}$ and $V_{DS} = -20 \text{ V}$. The same value of V_G and V_{DS} for the devices without Compound 2 results in $I_{DS} = -0.53 \mu\text{A}$. I_{DS} is therefore five times larger for the devices without Compound 2. This difference is mostly explained by considering Equation 2.11 (see Chapter 2) for transistor characteristics and the different channel

dimensions for each device. The ratio, $W/2L$ is four times larger for the devices without Compound **2** ($L = 50 \mu\text{m}$, $W = 2000 \mu\text{m}$) compared to those with Compound **2** ($L = 200 \mu\text{m}$, $W = 2000 \mu\text{m}$).

Both transfer graphs show no electron transport showing that Compound **2** is not transporting electrons. However Compound **2** has produced a number of other differences in the electrical characteristics. Although the current in the output characteristics is relatively unchanged when taking into account channel dimensions, the off-state has shifted in the transfer graph for the device with Compound **2** to +18 V, compared to 0 V to +4 V for the device without Compound **2**. The value of V_T , as calculated from plots of $\sqrt{|I_{DS}|}$ vs V_G at $V_{DS} = -20 \text{ V}$ and -30 V , is similarly shifted. For the device without Compound **2** V_T is negative at -5.7 to -7.1 V , whereas for the device with Compound **2** V_T is positive, exhibiting values of $+5.1$ to $+7.6 \text{ V}$.

To verify that these results were not due to a degradation of the Compound **2** layer during deposition of the electrodes, devices with and without Compound **2** were compared again, but with Compound **2** evaporated as the last layer in the devices, as shown in Figure 7.13. Those with no Compound **2** had the same structure as in the set shown schematically in Figure 7.11.

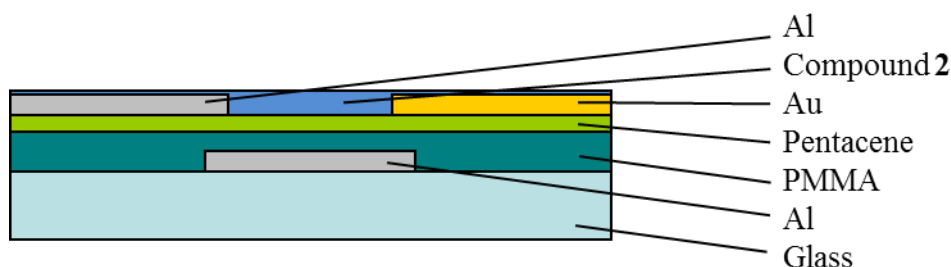
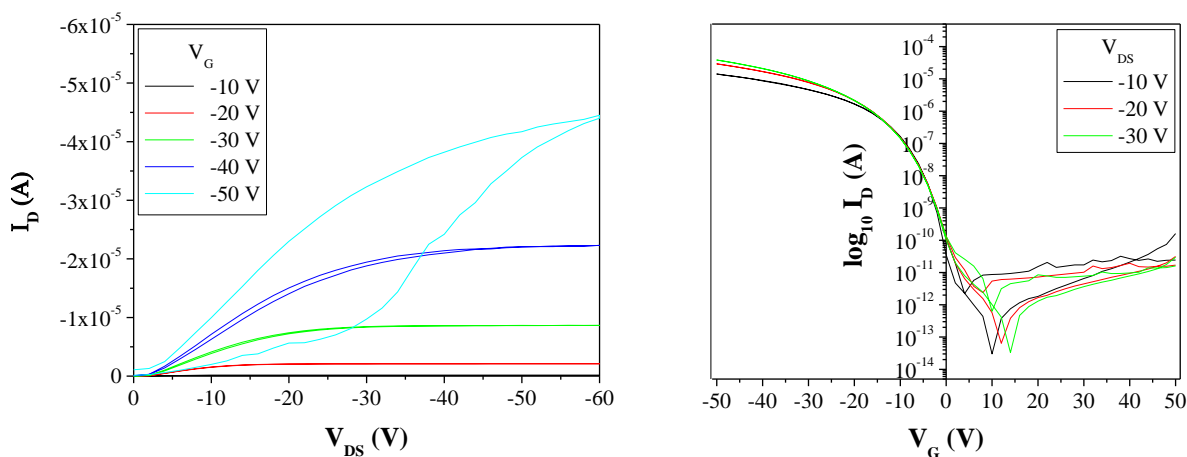


Figure 7.13: Structure of Compound **2** device with Compound **2** as the top layer.

Results are shown below in Figure 7.14 for the alternative structure Compound **2** containing devices having channel dimensions $L = 50 \mu\text{m}$ and $W = 2000 \mu\text{m}$ and devices without Compound **2** with dimensions $L = 50 \mu\text{m}$ and $W = 1000 \mu\text{m}$.

(a) With Compound **2**



(b) Without Compound **2**

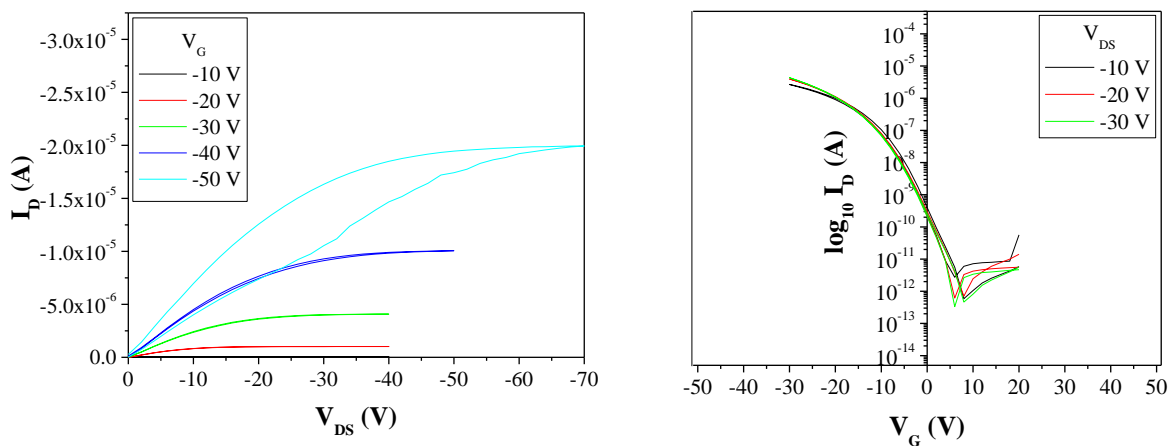


Figure 7.14: (a) Output and transfer characteristics of device with channel dimensions $L = 50 \mu\text{m}$ and $W = 2000 \mu\text{m}$, with Compound **2** deposited on top (b) Output and transfer characteristics of a pentacene-only device made alongside the pentacene / Compound **2** stack devices. Channel dimensions: $L = 50 \mu\text{m}$ and $W = 1000 \mu\text{m}$.

The output characteristics for both the devices with and without Compound **2** show significant hysteresis between the forward and reverse sweeps in V_{DS} at $V_G = -50 \text{ V}$.

Sweeps at higher values of V_G (data not shown) gave noisy and vaguely linear characteristics and large hysteresis throughout, likely indicative of an electrical breakdown of each device. Comparing the output characteristics below $V_G = -50$ V showed that Compound **2** devices gave approximately twice as much saturated current at any voltage compared to pentacene only. However, as for the earlier comparison of devices with and without Compound **2**, this difference can be explained by taking into account the channel dimensions of the separate devices. From Equation 2.11, these are predicted to follow this trend i.e. the $W/2L$ term is twice the magnitude for the Compound **2** devices as for the pentacene devices. This suggests that the Compound **2** is not having any observable effect on the output characteristics and the devices are basically pentacene transistors.

It is clear that something happens to the device when applying a gate voltage of -50 V when hysteresis is observed in the output. It is noted that the hysteresis is seen in all devices both with and without Compound **2**. This could imply that the hysteresis is due to the presence of pentacene. In the pentacene devices, subsequent measurements at lower gate voltages showed significantly reduced current with hysteresis still remaining. It was considered that this effect may be due to charge trapping at the interface. In an attempt to neutralise the traps and release the charges, the device was exposed to UV light for 3 hours to flood the conduction band with electrons. However, this had no positive effect on the characteristics indicating that the hysteresis observed at high voltages is not due to charge trapping and must be the result of an irreversible change such as breakdown.

As for the earlier comparison of devices with and without Compound **2** in Figure 7.14, transfer characteristics showed little evidence of electron transport in either type of device. However, differences in electrical characteristics were again evident. The off-state was similarly shifted to more positive values of V_G at $+10$ V to $+14$ V for the devices with Compound **2**, compared to $+6$ to $+8$ V for the devices without it. It is noted however that

the difference in V_G at the off-state is lower for these devices compared to those in Figure 7.14. As before, the value of V_T was calculated from plots of $\sqrt{|I_{DS}|}$ vs V_G at $V_{DS} = -20$ V and -30 V. For these devices V_T was negative for both types of device and was similar at -9.4 V to -4.0 V for the devices incorporating Compound **2** and -6.7 to -7.7 V for the devices without it.

In a further attempt to obtain ambipolar characteristics in these transistors it was decided to add an electron transport layer as was done by Capelli et al. The well-known electron transporting molecule OXD7 was added into the Compound **2** stack as shown in Figure 7.15.

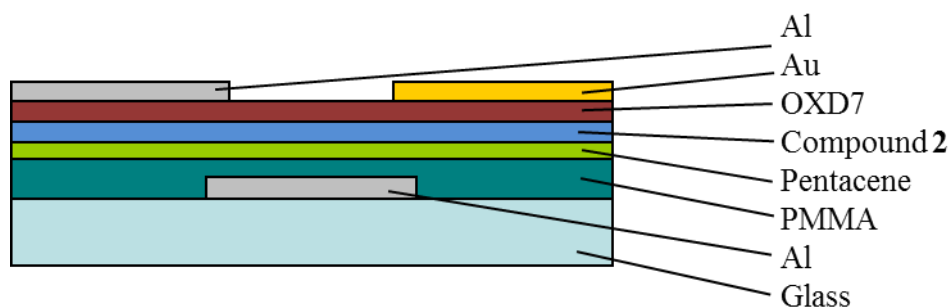


Figure 7.15: Transistor stack including both hole and electron transporting materials.

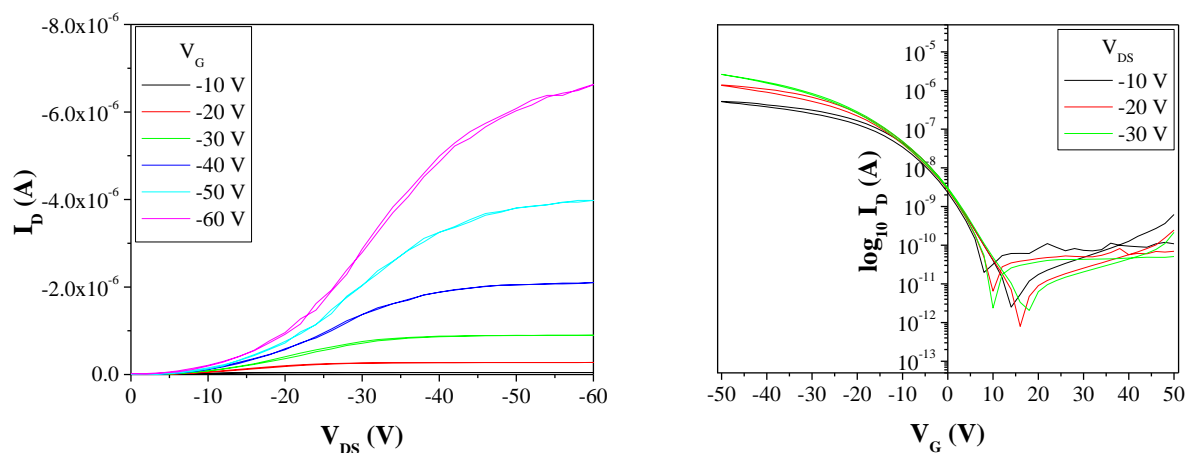
Typical results for the output and transfer characteristics from this set of devices are shown in Figure 7.16 with the device containing Compound **2** having channel dimensions $L = 100$ μm and $W = 1000$ μm and the device without having channel dimensions, $L = 50$ μm and $W = 1000$ μm .

Above $V_G = -60$ V devices both with and without Compound **2** appeared to undergo an electrical breakdown similar to that described for the devices in Figure 7.14. In the output characteristics for the devices incorporating Compound **2** and OXD7 there is an initial region for all values of V_G before the linear regime that is relatively non-conductive with low currents for increasing $-V_{DS}$. This is likely a series resistance from the current passing

through the three organic layers (OXD7, Compound **2**, pentacene) before entering the linear regime and showing more standard characteristics. The current in the pentacene devices is approximately ten times larger than that in the Compound **2** devices for the same value of V_{DS} and V_G . This difference cannot be explained solely by the differing channel dimensions for each device from which it would be predicted that the pentacene devices would have a current approximately twice as large. The difference is likely due to the relatively slow onset of current with increasing V_{DS} in the Compound **2** devices and is again indicative of an additional series resistance in these devices.

The transfer characteristics for both the pentacene and Compound **2**-OXD7-pentacene devices showed no evidence of electron transport. However, as seen for other devices combining layers of pentacene and Compound **2**, the off-state again shifted to more positive values of V_G . For the devices with Compound **2** the off-state was at +10 V to +18 V, compared with 0 V to +4 V for the pentacene-only devices. The value of V_T was also compared at $V_{DS} = -20$ V and -30 V for the pentacene device, resulting in $V_T = -7.7$ V to -9.2 V. The plots of $\sqrt{|I_{DS}|}$ vs V_G for the devices containing Compound **2** and OXD7 were not obviously linear at $V_{DS} = -20$ V, so only the plot at $V_{DS} = -30$ V was used, giving a slightly negative value of V_T of -0.8 V. As for the other devices it is clear that whilst incorporation of Compound **2** does influence the transfer characteristics, it does not produce ambipolar charge transport, even in the presence of a layer of the electron transporting OXD7.

(a) With pentacene and OXD7



(b) Pentacene only

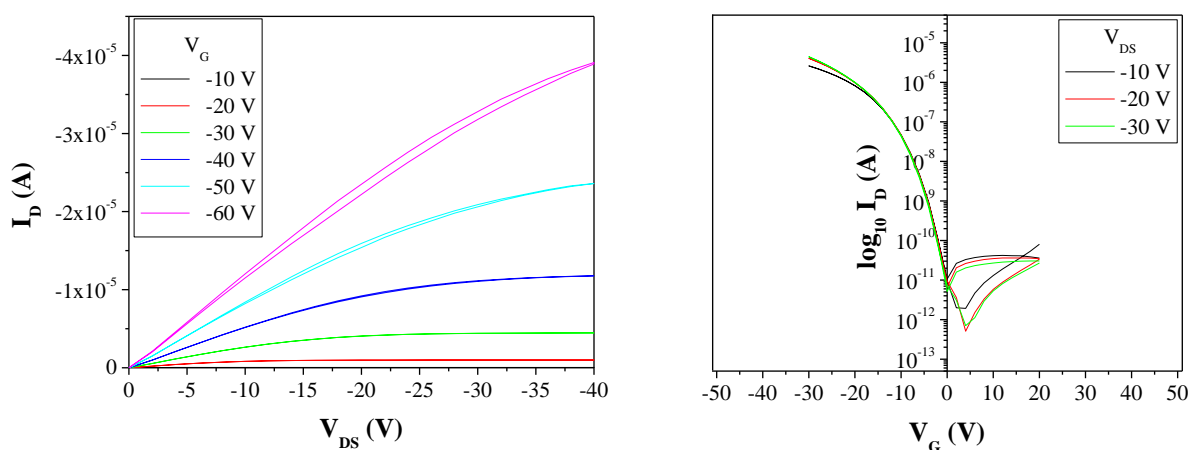


Figure 7.16: (a) Output and transfer characteristics of a device with channel dimensions $L = 100 \mu\text{m}$ and $W = 1000 \mu\text{m}$ incorporating both pentacene and OXD7. (b) Output and transfer characteristics of a pentacene-only device made alongside the full stack devices. Channel dimensions: $L = 50 \mu\text{m}$ and $W = 1000 \mu\text{m}$.

7.6 Conclusions

This chapter has experimented with transistors based on the novel compounds **8**, **1** and **2**. Initial studies with pentacene served as a proof of concept for the transistor structures. Transistors incorporating Compound **8** gave characteristics dominated by leakage, which

lead to misleading transfer characteristics that appeared to show ambipolar conduction that is in fact an artefact of current from the gate contact leaking to the drain. Transistors based on Compound **1** also showed misleading transfer characteristics however the output characteristics did not show clear evidence of leakage. A lack of synthesised Compound **1** prevented the creation of further transistors and this material could be studied further in the future.

Overall, this study has shown that transistors based on Compound **2** alone as the active layer gave very small current output even with dissimilar source and drain electrodes. Incorporating a stack structure into the transistor with a layer of the hole-transporting material pentacene, allowed for measurable transistor characteristics. However, little difference was observed between the output characteristics for devices consisting of Compound **2** and pentacene compared with pentacene-only devices. This suggests the electrical properties are dominated by the pentacene layer. Similarly, transfer characteristics for devices based on Compound **2** and pentacene only showed hole transporting properties, with no evidence of electron transport. However, the incorporation of Compound **2** did alter the value of the threshold voltage and tended to shift the off-state of the transistor to more positive values of gate voltage. The addition of an electron transporting layer consisting of OXD7 to the pentacene-Compound **2** stack also showed no evidence of electron transporting properties in the transfer characteristics obtained. Also, the output characteristics for the transistor showed evidence of additional series resistance, likely as a result of the interfaces between the pentacene, Compound **2** and OXD7 layers in the device.

7.7 References

- 1) Y. Yun in *Pentacene Based Organic Electronic Devices*, PhD thesis, **2010**, Chapter 4.
- 2) D. Kolb in *Organic Transistors based on Pentacene and Dibenzothiophene Derivatives*, PhD thesis, **2008**, Chapter 5.
- 3) H. Klauk, M. Halik, U. Zschieschang, F. Eder, G. Schmid, C. Dehm, *Appl. Phys. Lett.*, **82**, 4175-4177, **2003**.
- 4) K. E. Linton, A. L. Fisher, C. Pearson, M. A. Fox, L. O. Pålsson, M. R. Bryce, M. C. Petty, *J. Mater. Chem.*, **22**, 11816-11825, **2012**.
- 5) M. C. Petty, Organic Electronic Memory Devices in *Handbook of Organic Materials for Optoelectronic Devices* edited by O. Ostroverkhova, Woodhead Publishing Limited, **2013**, Chapter 22.
- 6) E. J. Feldmeier, M. Schidleja, C. Melzer, H. von Seggern, *Adv. Mater.*, **22**, 3568-3572, **2010**.
- 7) Y. Wang, R. Kumashiro, Z. Li, R. Nouchi, K. Tanigaki, *Appl. Phys. Lett.*, **95**, 103306, **2009**.
- 8) S. Z. Bisri, T. Takenobu, Y. Yomogida, H. Shimotani, T. Yamao, S. Hotta, Y. Iwasa, *Adv. Funct. Mater.*, **19**, 1728-1735, **2009**.
- 9) E. B. Namdas, P. Ledochowitsch, J. D. Yuen, D. Moses, A. J. Heeger, *Appl. Phys. Lett.*, **92**, 183304, **2008**.
- 10) T. Sakanoue, M. Yahiro, C. Adachi, J. H. Burroughes, Y. Oku, N. Shimoji, T. Takahashi, A. Toshimitsu, *Appl. Phys. Lett.*, **92**, 053505, **2008**.

- 11) K. Nakamura, M. Ichikawa, R. Fushiki, T. Kamikawa, M. Inoue, T. Koyama, Y. Taniguchi, *Jap. J. Appl. Phys.*, 44, 1367-1369, **2005**.
- 12) R. Capelli, S. Toffanin, G. Generali, H. Usta, A. Facchetti, M. Muccini, *Nat. Mater.*, 9, 496-503, **2010**.
- 13) T. Matsushima, C. Adachi, *Appl. Phys. Lett.*, 89, 253506, **2006**.

8 F8BT OLEDs and Transistors

8.1 In this Chapter...

This chapter begins with the description of some initial experimentation on the light-emitting polymer poly(9,9-di-*n*-octylfluorene-*alt*-benzothiadiazole) (F8BT), which has been previously incorporated in OLEFETs by Zaumseil et al.¹ The testing of different solvents and electrical measurements on OLED and OLEFET devices is included and some success with light output from the OLEFETs is reported. The chapter then moves on to discuss alternative device configurations, using nanogap contacts as well as experimenting with ionic liquid blends as a replacement for the hole injector, PEDOT:PSS.

8.2 Initial Experiments into Thin Film Processing

A number of papers have used F8BT, (the structure of which is shown in the Experimental chapter and repeated over in Figure 8.1) but each uses a different solvent, such as chlorobenzene,² chloroform,³ and different forms of xylene.^{1, 4-8} Some initial investigation was therefore carried out in order to identify the best solvent to obtain spin-coated films. A summary of the results is presented over in Table 8.1 and a discussion follows. All of the films were deposited by spinning at 1000 rpm for 60 s and then annealing at 230 °C for 5 minutes.¹ Although the referenced papers annealed at 290 °C, the hotplate available for this project reached a maximum temperature of 230 °C, so this was used.

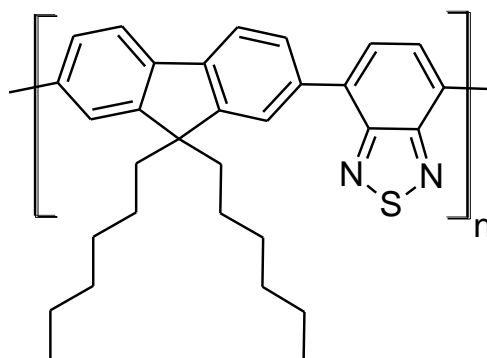
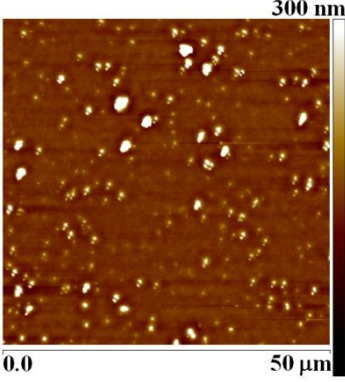
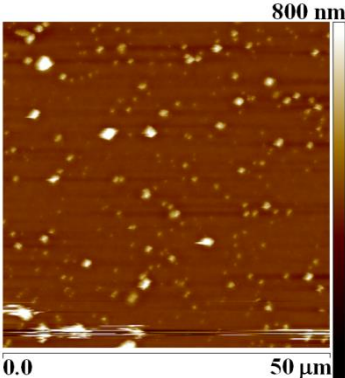
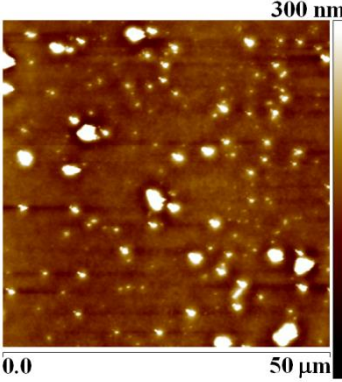
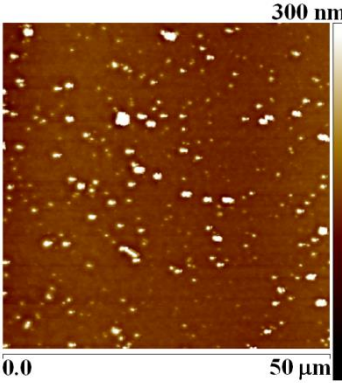


Figure 8.1: Molecular structure of F8BT.

Table 8.1: Summary of F8BT solutions, film qualities and film thicknesses.

Solvent & Concentration (mg ml ⁻¹)	Appearance of Solution	AFM Image of Film	Roughness R _a (nm)	Approx. Film Thickness (nm)
Xylene 10	Very Cloudy		12.4	10
Chlorobenzene 10	Cloudy		19.1	80

Solvent & Concentration (mg ml ⁻¹)	Appearance of Solution	AFM Image of Film	Roughness R _a (nm)	Approx. Film Thickness (nm)
Chloroform 10	Cloudy		24.2	150
Chloroform 5 FILTERED	Slightly Cloudy		12.7	80

None of the solutions were completely clear and all of the spin-coated films showed evidence of particulates in the AFM scans. Zaumseil et al¹ reported F8BT OLEFETs spun from *m*-xylene. When xylene was used in this study the resulting solution was very cloudy, suggesting poor dissolution of the F8BT. Spin-coated films were very thin, with a thickness of 10 nm and due to particulates exhibited a roughness of 12.4 nm, based on the 50 μm AFM scan given for a film prepared from this solution in Table 8.1. In addition, a trial transistor fabricated using F8BT spun from xylene revealed that, after the F8BT layer was spin-coated on top of the PMMA insulator, the surface showed an unusual appearance which seemed to be characteristic of a liquid crystal (Figure 8.2). Also, the F8BT solution became cloudy when cool (heating is a side effect of the ultrasonic bath), which could have been indicative of thermotropic or possibly lyotropic properties. However, observation of

the film between crossed polarisers showed this not to be the case, as the film did not rotate plane polarised light. The cloudy appearance upon cooling was the F8BT falling out of solution and it is likely that there was a phase segregation effect. The layer of F8BT likely mixed into the pre-coated PMMA during spin-coating, resulting in a single mixed layer of the two materials that later separated into the different phases visible in Figure 8.2. Xylene was therefore considered to be an unsuitable solvent for transistor fabrication since the layers must not mix.

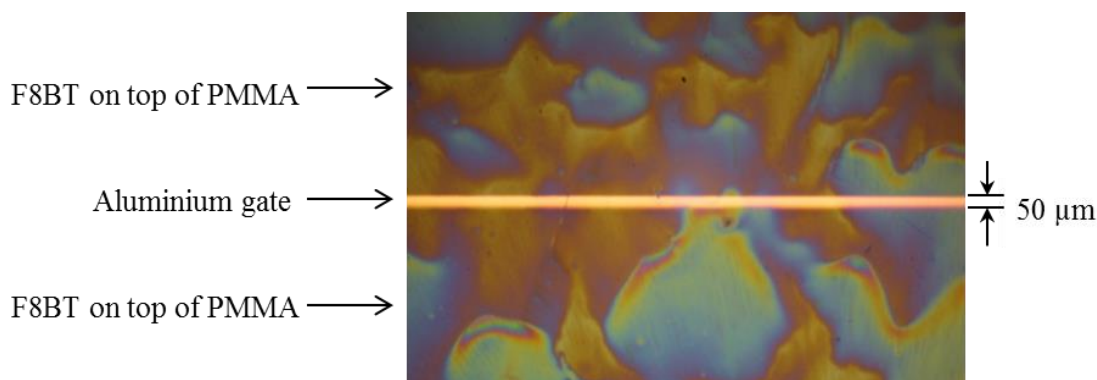


Figure 8.2: Microscope image of F8BT device prepared from xylene solution with gate electrode for scale.

Chlorobenzene has also been previously used in the literature as a solvent for F8BT.⁹ Here chlorobenzene appeared to dissolve F8BT better than xylene but still resulted in a cloudy solution. The same spin-coating method was followed and 80 nm films were successfully deposited with a roughness of 19.1 nm. The 10 mg ml⁻¹ chloroform solution was also cloudy and when imaged with AFM, the film appeared to be of poor quality, showing particles up to 2 μm in size. The roughness of the 50 μm area shown in Table 8.1 was calculated to be 24.2 nm and, in addition, the film was too thick for this application at 150 nm. A lower concentration of 5 mg ml⁻¹ F8BT in chloroform produced a slightly cloudy solution. To remove any remaining undissolved particles, the solution was filtered through a 0.2 μm syringe filter prior to spin-coating. The resulting F8BT film was also annealed for 30 minutes instead of 5 minutes as with previous F8BT batches. The film quality was

found to be smoother, with a roughness of 12.7 nm as assessed over the 50 μm AFM scan given in Table 8.1. Film thickness was determined to be approximately 80 nm.

Since the film quality vastly improved with the filtered 5 mg ml^{-1} F8BT in chloroform solution, this approach was used for all further F8BT thin film processing. Several early experiments with F8BT incorporated into transistor devices were unsuccessful. The fact that no light output was observed from the proven F8BT OLEFET structure motivated all the steps in F8BT film processing to be moved to a nitrogen-filled glove box as literature reports¹⁰ hint that F8BT is sensitive to air and/or moisture. Until this point, not all processing steps had taken place in a glove box.

8.3 F8BT Standard OLEDs (Out-of-Plane Structure)

With the film processing techniques optimised, F8BT was spun from the 5 mg ml^{-1} chloroform solution to form out-of-plane OLEDs. Here, out-of-plane refers to the standard OLED structure where the active organic material is sandwiched between a cathode and anode in a vertical, out-of-plane, stack arrangement. This terminology is used to differentiate from in-plane OLEDs used in Section 8.5, where the active organic layer was deposited on top of the cathode and anode, which were effectively in a horizontal plane, relative to each other. The out-of-plane stack formation had been very successful with a number of other materials^{11, 12} (see also Chapter 4), so this was a good experiment to measure the electroluminescent properties of F8BT as a precursor to further transistor studies.

Devices were made using the standard OLED structure described in the Experimental chapter, but with F8BT as the emissive layer. The overall configuration was ITO / PEDOT:PSS / F8BT / Ca / Al. Devices from three different substrates were measured and

data from the optimum device from each substrate is included in the graphs that follow. Current and photocurrent vs bias plots (Figure 8.3) showed excellent reproducibility and high sample currents, up to 0.125 A with no evidence of breakdown, which is promising for the development of transistors. Figure 8.3 also reveals that the devices emitted light with a turn-on voltage of 5.1-5.3 V, although the EQEs shown in Figure 8.4 were low at an average of 0.05%. The electroluminescence (Figure 8.5) was steady but fairly weak, as shown by the increased noise in the normalised intensity graph, but the shape of the graph was similar to that given in the paper by Zaumseil et al,¹ showing a peak emission of 530 nm, with a shoulder at approximately 565 nm. The light appeared a yellow-green colour with CIE coordinates of (0.38, 0.60), as shown in Figure 8.6.

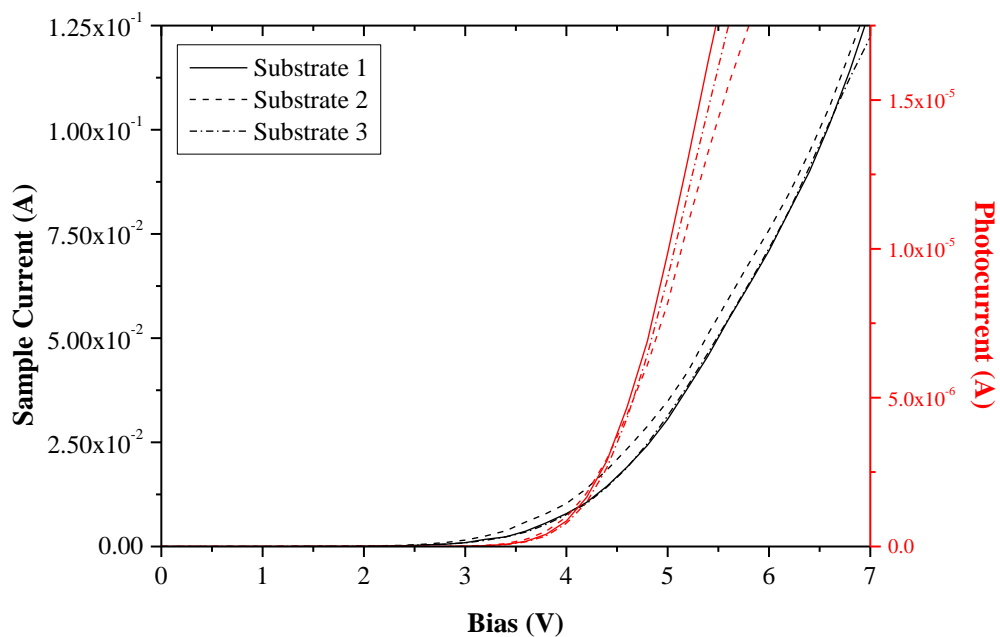


Figure 8.3: Electrical characteristics of standard F8BT OLEDs showing the best devices from three separate substrates. Device architecture: ITO / PEDOT:PSS / F8BT / Ca / Al.

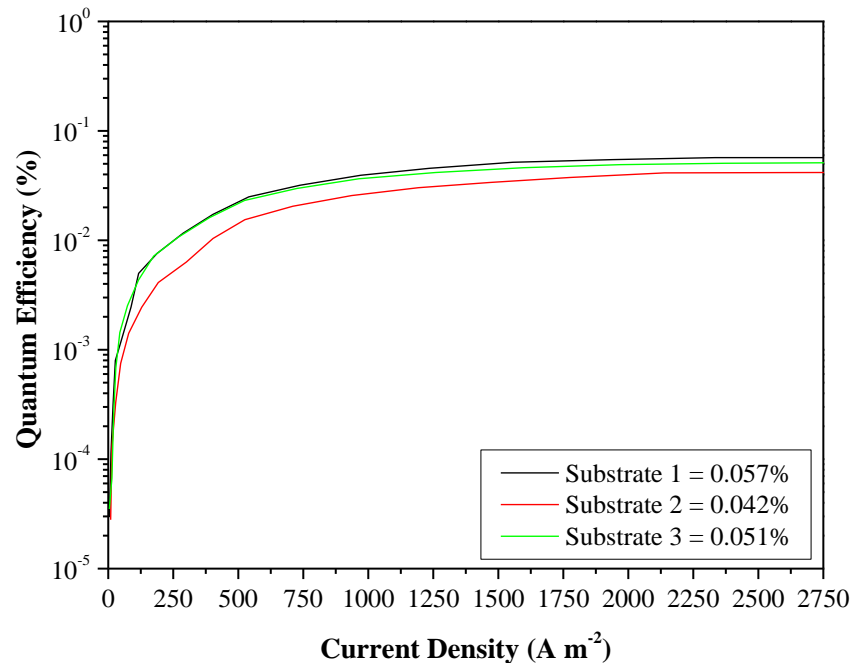


Figure 8.4: External quantum efficiency data of standard F8BT OLEDs. Device architecture: ITO / PEDOT:PSS / F8BT / Ca / Al.

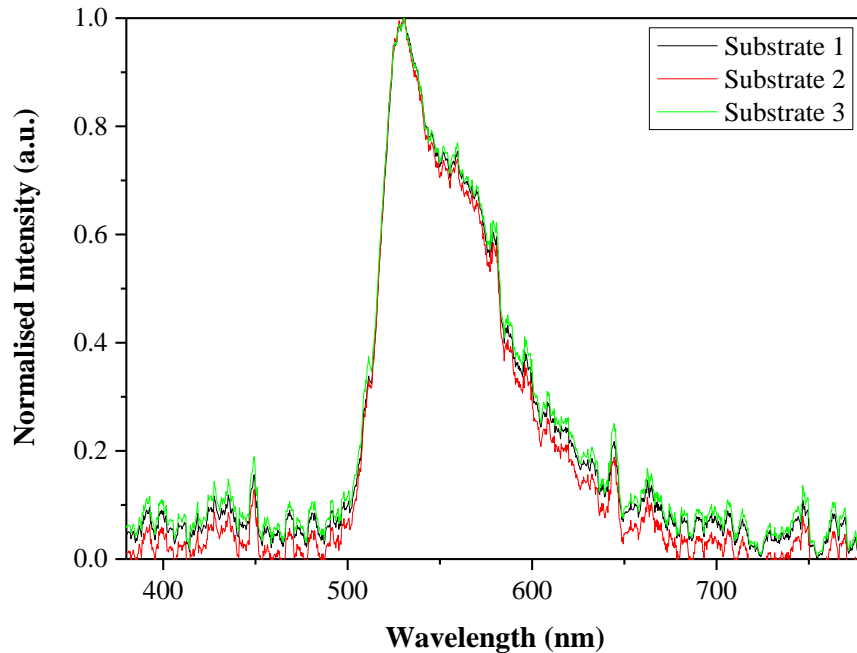


Figure 8.5: Electroluminescence spectra of standard F8BT OLEDs. Device architecture: ITO / PEDOT:PSS / F8BT / Ca / Al.

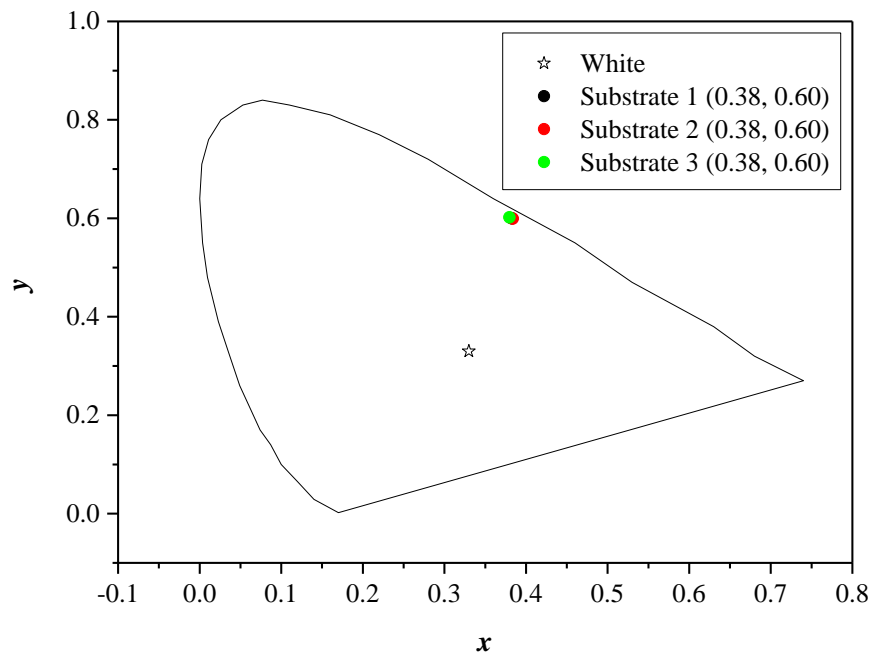


Figure 8.6: CIE coordinates of standard F8BT OLEDs measured at 20 mA. Device architecture: ITO / PEDOT:PSS / F8BT / Ca / Al.

8.4 F8BT Transistors

The out-of-plane F8BT OLEDs successfully demonstrated the electroluminescent properties of the material and encouraged incorporation of F8BT into transistors. The structure and channel dimensions of the devices are outlined in the Experimental chapter.

As mentioned in the film processing section, initial F8BT transistor experiments were partly performed in air and many of the results were poor (leakage, no current, etc.). However, a promising set of output characteristics was obtained from one device (Figure 8.7(a)). V_G of -5, -10 and -15 V clearly show pinch off, however it is clear that the V_{DS} applied was not great enough to see pinch-off and saturation at higher gate voltages. When repeated the following day, these results could not be reproduced, possibly as a result of degradation of the F8BT film due to exposure to ambient conditions. One set of transfer

characteristics was also obtained (Figure 8.7(b)) although from a different device. The mobility obtained from a plot of $\sqrt{|I_{DS}|}$ vs. V_G in the saturation region (Figure 8.8) was found to be $3 \times 10^{-6} \text{ cm}^2 \text{ V}^{-1} \text{ s}^{-1}$, about two orders of magnitude lower than mobilities quoted by Zaumseil et al¹ for F8BT.

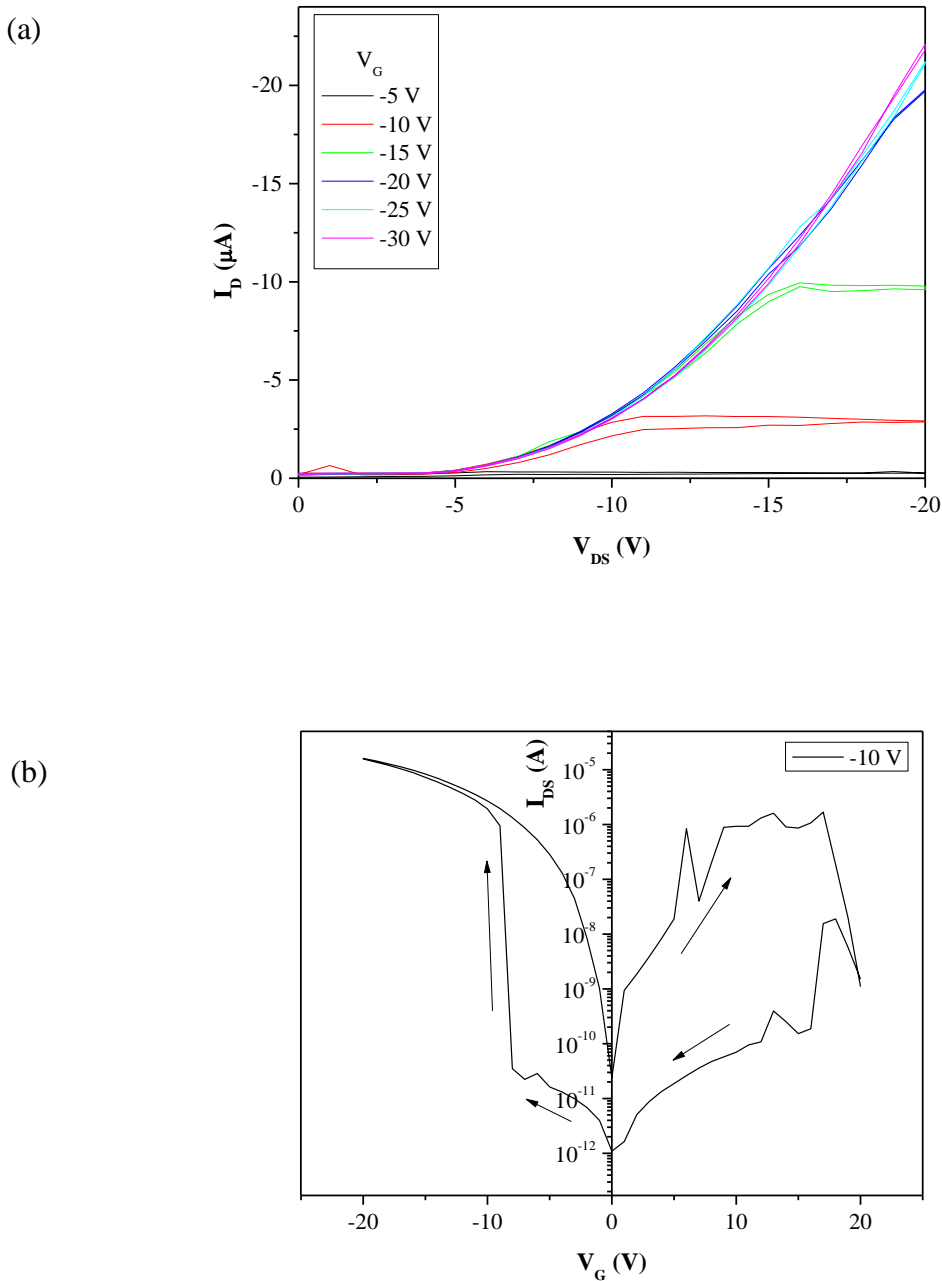


Figure 8.7: (a) Output characteristics for a standard F8BT transistor device with channel dimensions $L = 200 \mu\text{m}$ and $W = 4000 \mu\text{m}$ (b) Transfer characteristics for a device with channel dimensions $L = 200 \mu\text{m}$ and $W = 4000 \mu\text{m}$.

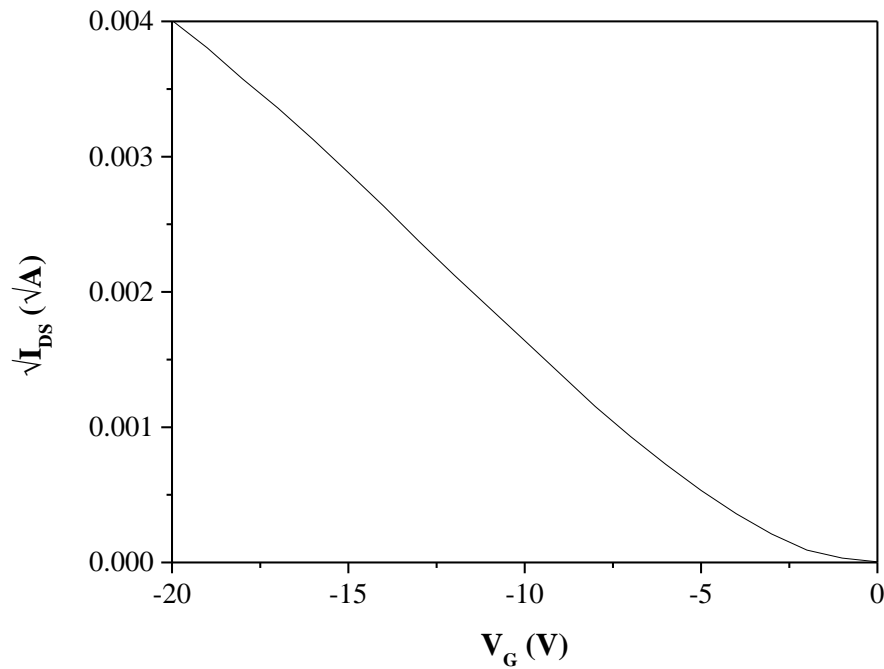


Figure 8.8: Plot of $\sqrt{|I_{DS}|}$ vs V_G for the F8BT device with channel dimensions $L = 200 \mu\text{m}$ and $W = 4000 \mu\text{m}$.

To improve reproducibility, all further fabrication was undertaken solely in a nitrogen atmosphere. F8BT transistors repeated in this way produced a number of working devices that also emitted light. However, microscope images of these devices during operation (Figure 8.9(a)) compared with images immediately after operation (Figure 8.9(b)) showed the appearance of irreversible markings on the device corresponding to the location of the light emission. It became clear that the light was not coming from the channel and was instead coming from the areas where there was overlap between the gate and source and gate and drain. In addition, output characteristics recorded for the device as shown in Figure 8.10 showed no field-effect and only leakage current. The location of the light proves that this must have been leakage current only where breakdown was occurring through the PMMA layer. There was no obvious pattern in the visible light, but it may be related to the spinning process. For example, the pattern may reflect areas of the spun F8BT film of different thickness, or areas where the spun PMMA is particularly thin.

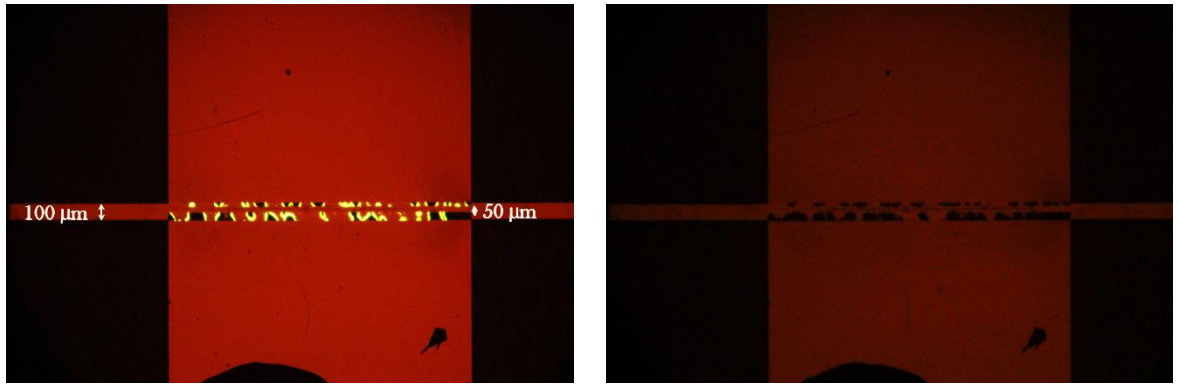


Figure 8.9: Photographs taken through a microscope of (a) device switched on and (b) the same device switched off. Channel dimensions: $L = 50 \mu\text{m}$ and $W = 2000 \mu\text{m}$.

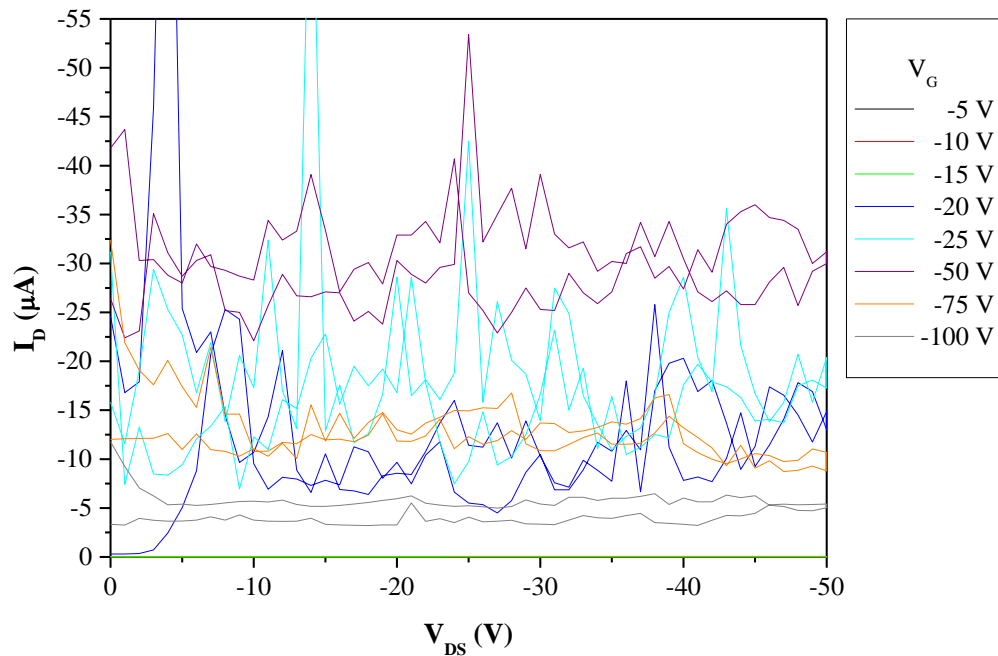


Figure 8.10: Output graph from device showing leakage and no field-effect. Channel dimensions: $L = 50 \mu\text{m}$ and $W = 2000 \mu\text{m}$.

Electroluminescence spectra were obtained for the light emission from two different devices with channel dimensions of $L = 50 \mu\text{m}$ and $W = 2000 \mu\text{m}$ and $L = 50 \mu\text{m}$ and $W = 4000 \mu\text{m}$ and are given in Figure 8.11(a). (Note a full diagram of the mask pattern with device dimensions is included in the Experimental chapter on page 79.) These showed a peak emission at 580 nm, which is slightly red-shifted compared with the emission in the

previously published work,¹ which stated that the emission peak was at 550 nm. Also included in Figure 8.11(b) are the CIE coordinates of the light emitted by the two transistors.

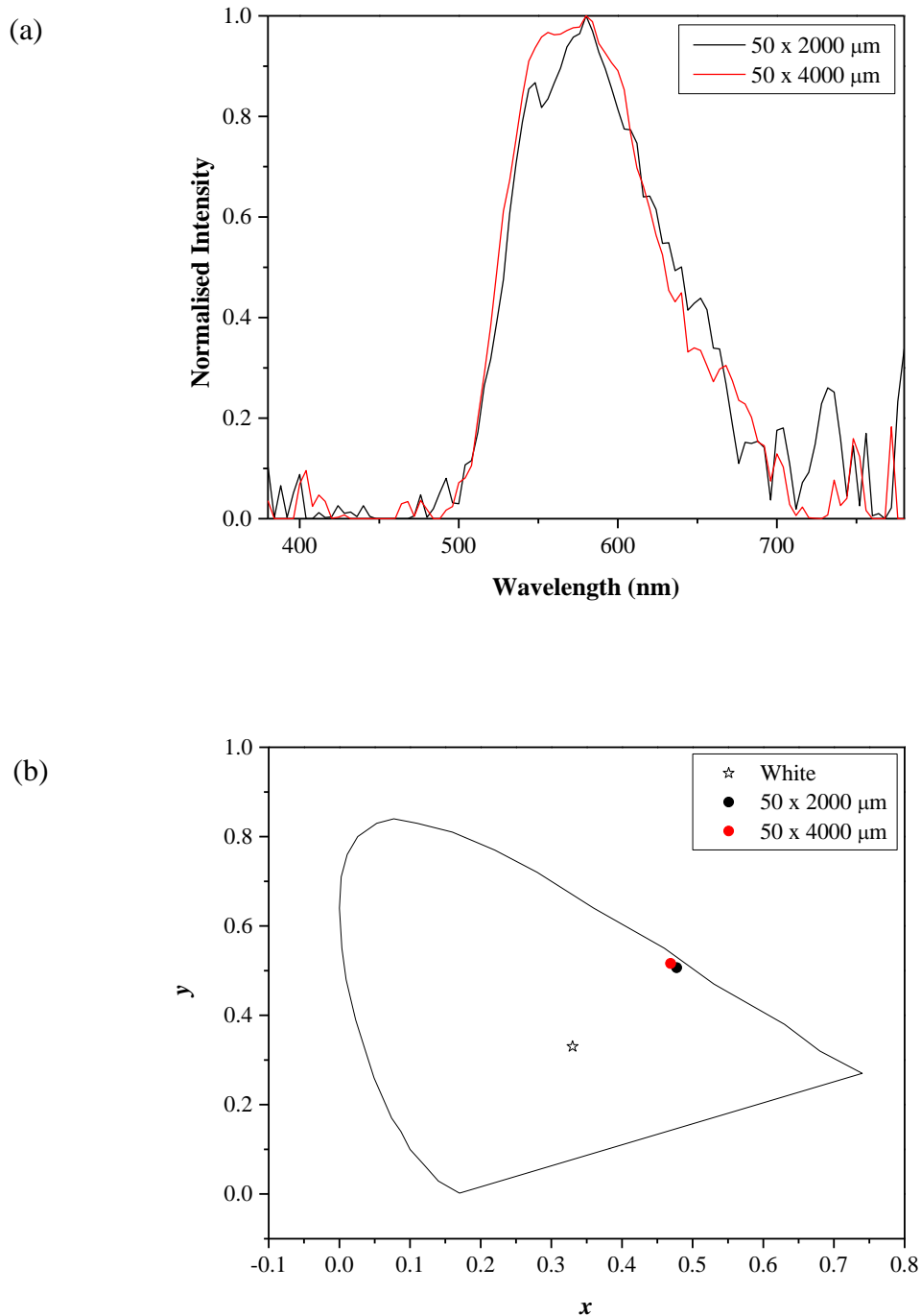


Figure 8.11: (a) Emission spectra and (b) CIE diagram of the light emitted by the transistor devices with channel dimensions of $L = 50 \mu\text{m}$ and $W = 2000 \mu\text{m}$ and $L = 50 \mu\text{m}$ and $W = 4000 \mu\text{m}$, all taken with a current of 2 mA.

Interestingly, an identical fabrication process later failed to produce repeatable device characteristics, and all the devices failed with open circuits. There was light at certain points during the measurements but not continuously as with the previous batch. Alignment of the source and drain electrodes with the gate during fabrication was considered to be one possible problem and led to experiments with a significantly wider gate of 1 mm. However, these devices all failed with open circuits and it was concluded that the narrower gate dimensions were necessary for working F8BT OLEFETs.

8.4.1 Nanogap Contacts

An alternative approach to improve device characteristics and repeatability was also explored through the preparation of Au-Al nanogap electrodes for use in transistor and in-plane OLED structures. A number of new contacts were made on a silicon wafer using a lithographic process.¹³ Thanks are due to Mark Rosamond, a Research Assistant in the School of Engineering at Durham University, for producing these. An AFM image and cross section of one such contact is shown in Figure 8.12 and reveals a nanogap with an electrode spacing on the order of 400-450 nm.

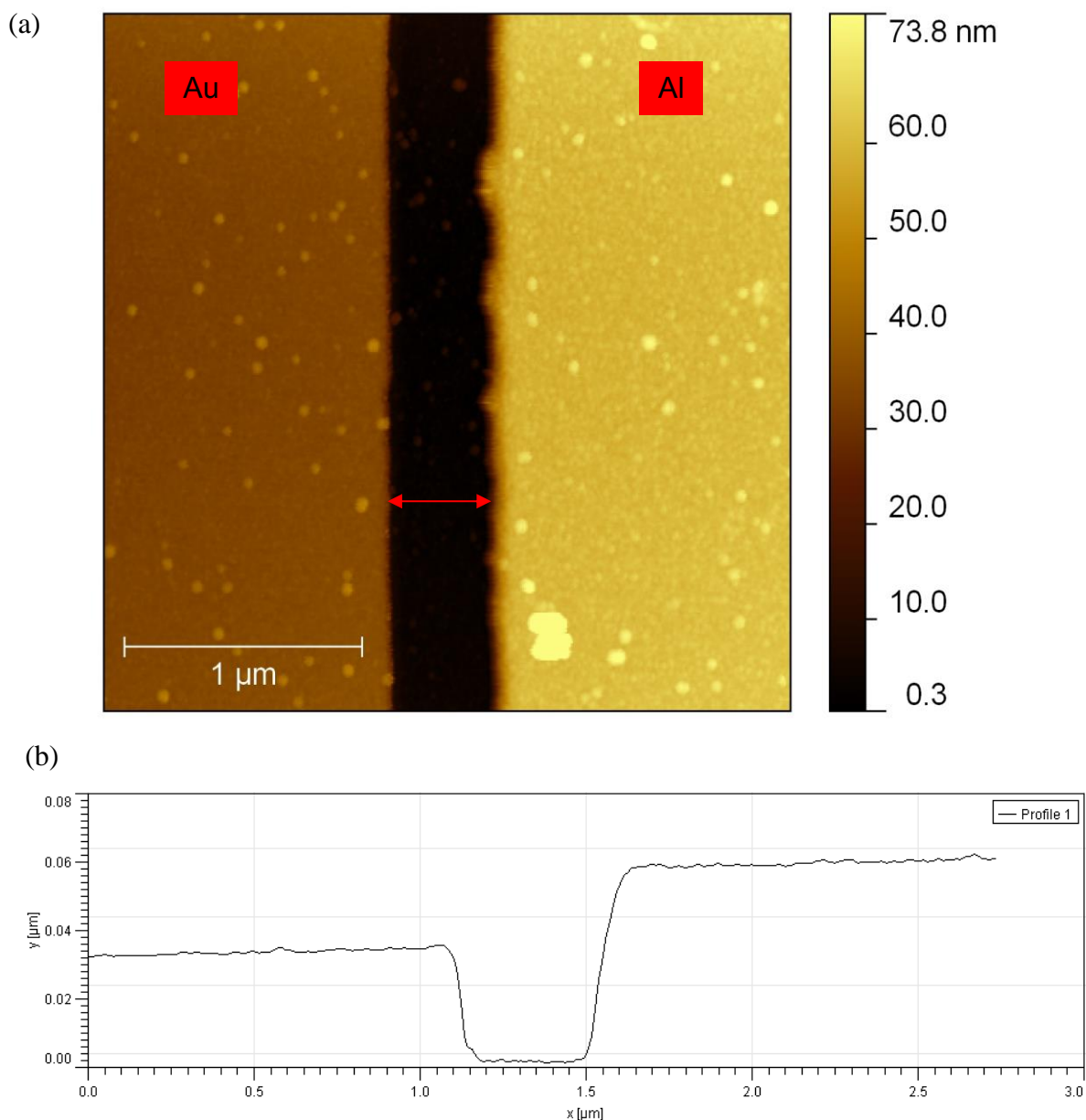


Figure 8.12: (a) Nanogap contacts as imaged by AFM and (b) Averaged cross section showing a channel length of 400-450 nm.

F8BT in chloroform (5 mg ml^{-1}) was spun onto the nanogap electrodes, however in all cases electrical measurements showed the devices to be open circuit. It was considered that the problem could not be a result of degradation in the F8BT electrical properties since the material had already been successfully incorporated into the out-of-plane OLED design. One possibility was that the F8BT failed to deposit in the nanogap during the spin-coating

process. However, AFM imaging of the gap, as shown in Figure 8.13, after F8BT deposition confirmed the presence of the material.

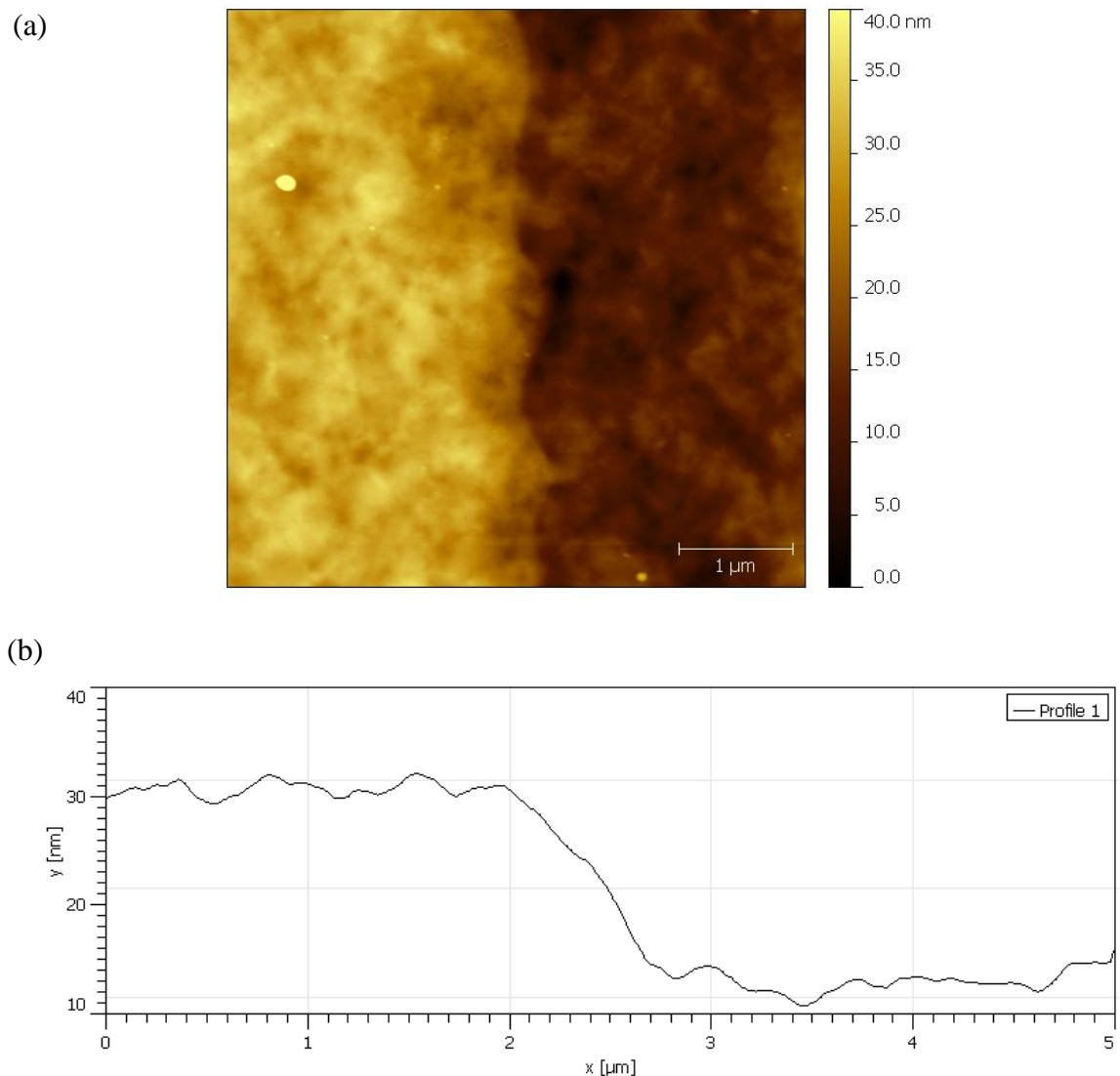


Figure 8.13: (a) AFM image confirming that F8BT was present in the nanogap. (b) The averaged cross section shows that F8BT has filled the gap, which is now no longer visible. The step profile has been preserved due to coating over the different thicknesses of the Au and Al electrodes.

Therefore it was concluded that the most likely cause of the lack of electrical contact across the F8BT nanogap devices was the presence of a layer of aluminium oxide on the Al electrode. Nanogap devices were not pursued further and instead further studies involved attempts to optimise F8BT OLEDs as a precursor to improving F8BT transistors with channel lengths on the order of microns.

8.5 Study into Ionic Liquid blends as a Replacement for PEDOT:PSS

The out-of-plane F8BT OLEDs reported in Section 8.3 demonstrated light emission and suggested that F8BT should incorporate well into an OFET structure. However, the PEDOT:PSS hole injection layer which was expected to improve the device efficiency could not be patterned on the in-plane electrodes. Thus an alternative was sought for future devices with an aim to improve their characteristics compared to F8BT OLEFETs produced without a hole injection layer.

Published work has shown that when mixed with active layer materials, ionic liquids (ILs) introduce mobile IL molecules into the layer. This is the basis of Light-emitting Electrochemical Cells (LECs).^{14, 15} The IL molecules effectively act as a hole injection and transport material¹⁶ and in this way negate the need for a PEDOT:PSS layer. It has been reported that the presence of IL can enhance the efficiency of OLED emission by one or two orders of magnitude.¹⁷⁻²² The effect of introducing IL into the F8BT film was studied systematically – first in an out-of-plane OLED structure and then in a planar OLED structure as a precursor to the final use in transistors.

8.5.1 Out-of-plane OLED Optimisation Study

Throughout these experiments the IL used was trihexyltetradecylphosphonium-bis(trifluoromethylsulfonyl)amide. Previous work in the group by Ian Kenyon, a Level 4 project student in the School of Engineering, Durham University,²³ involving the well-known polymer Super Yellow²⁴ (also used in Chapter 6) established that optimum device characteristics were obtained with a standard OLED structure in the configuration: ITO / SY:IL(5 wt%) / Al, and so this was used as a starting point for the incorporation of IL into F8BT.

5 Wt% F8BT:IL Devices (Batch 1)

To study the incorporation of IL in F8BT, standard OLEDs were fabricated with 5 wt% IL, as described in Section 3.5.2. Four different types of OLEDs were prepared on individual substrates consisting of a set of six identical devices. Separate substrates were produced with F8BT:IL and F8BT. For the purposes of comparison, two substrates consisting of F8BT:IL and F8BT-only devices were simultaneously prepared with a PEDOT:PSS layer. For clarity, the different substrates are listed below in Table 8.2 and collectively referred to as Batch 1.

Table 8.2: Device configurations for substrates in Batch 1.

Substrate	Device Configuration
1	ITO / F8BT:IL / Al
2	ITO / F8BT / Al
3	ITO / PEDOT:PSS / F8BT:IL / Al
4	ITO / PEDOT:PSS / F8BT / Al

Figure 8.14 shows the best current and photocurrent vs bias results for individual devices of each structure.

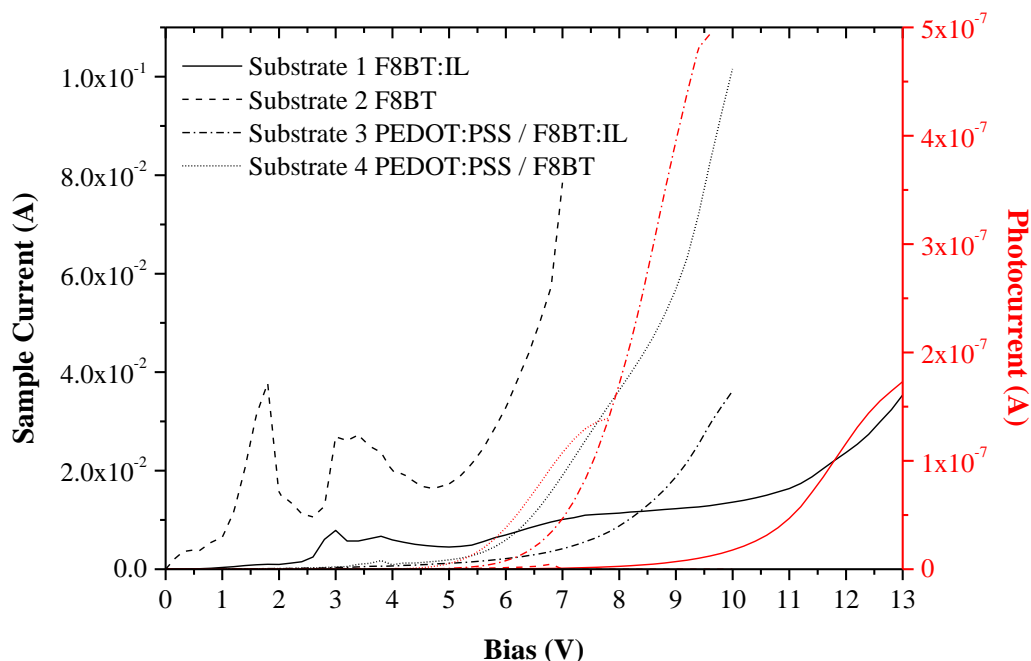


Figure 8.14: Current and photocurrent vs bias graph of best devices from Batch 1.

The F8BT:IL and F8BT devices showed poor IV characteristics and also little increase in photocurrent with increasing voltage. The turn-on voltages (at 1 nA photocurrent) for each were high at 7.1 V and 5.7 V, respectively. The two equivalent devices containing the PEDOT:PSS layer show better IV characteristics with turn-on voltages of 5.1 V and 4.4 V for the F8BT:IL and the F8BT, respectively.

On comparing this batch with the standard F8BT OLEDs with calcium (Figure 8.3), the PEDOT:PSS / F8BT device was less efficient. However, this was not unexpected as the calcium in the earlier configuration acts as an electron injector. In the configuration used in Batch 1 there is an energy mismatch between the work function of the aluminium cathode and the F8BT LUMO.²⁵

The PEDOT:PSS / F8BT:IL device shows a lower current in the IV compared to the PEDOT:PSS / F8BT OLEDs in Batch 1 and this is likely due to the interface between the PEDOT:PSS and the F8BT:IL layers. F8BT has a relatively high electron affinity with a

HOMO of 5.8 eV, which makes it harder to inject holes from the PEDOT:PSS. Therefore F8BT acts as a hole blocker.²⁶ The increase in electron current explains the higher light output. The F8BT:IL devices prepared in Batch 1 without the PEDOT:PSS layer needed a higher applied voltage to pass current due to the absence of the PEDOT:PSS hole injection layer. The devices containing only F8BT on Substrate 2 were also measured at higher voltages, up to 30 V, however they all failed at around 6-7 V.

Substrates 3 and 4, which consisted of devices based on F8BT:IL and F8BT with PEDOT:PSS were the only substrates which had devices that emitted any visible light. Therefore, external quantum efficiency and emission data were only obtainable for these devices. The best are presented in the following graphs.

EQE data are in Figure 8.15 and show the Batch 1 PEDOT:PSS / F8BT:IL devices to be three times more efficient at 0.003%, compared with 0.001% for the Batch 1 PEDOT:PSS / F8BT devices. Both devices show a lower efficiency than the PEDOT:PSS / F8BT / Ca / Al devices prepared earlier.

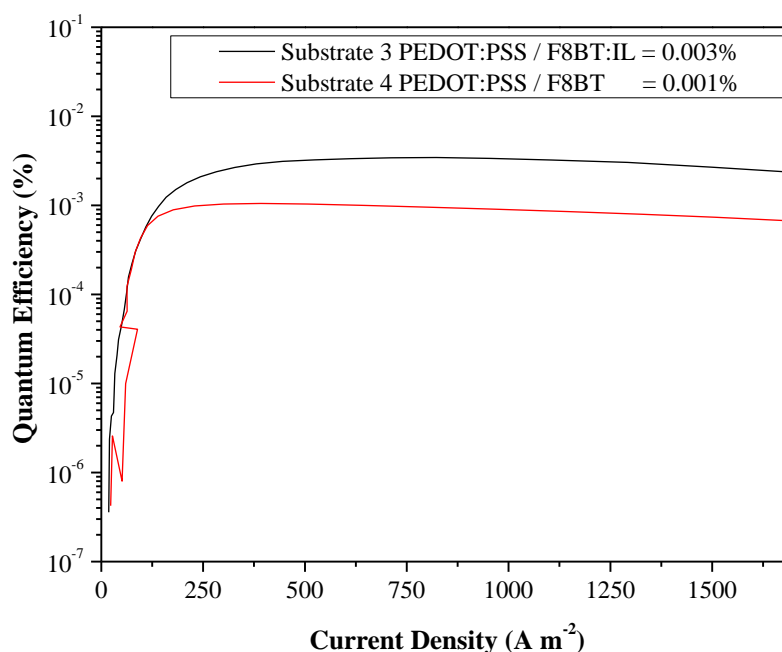


Figure 8.15: External quantum efficiency graph of Batch 1 Substrates 3 and 4.

The electroluminescence spectra in Figure 8.16 reveal that the F8BT:IL device has an identical intensity maximum as for F8BT, but a broader FWHM of 83 nm compared with 72 nm for F8BT, a difference of 11 nm, with more emission in the longer wavelengths compared with F8BT. The peak emission occurred at 535 nm, similar to the value of 530 nm measured for the standard F8BT OLEDs prepared with calcium reported in Figure 8.5. Comparing CIE coordinates (Figure 8.17) for the F8BT and F8BT:IL OLEDs prepared in this batch shows a small difference, with F8BT slightly closer to green, which may be explained by the larger FWHM observed in the electroluminescence spectra. External quantum efficiency graphs (Figure 8.15) show an improvement in efficiency.

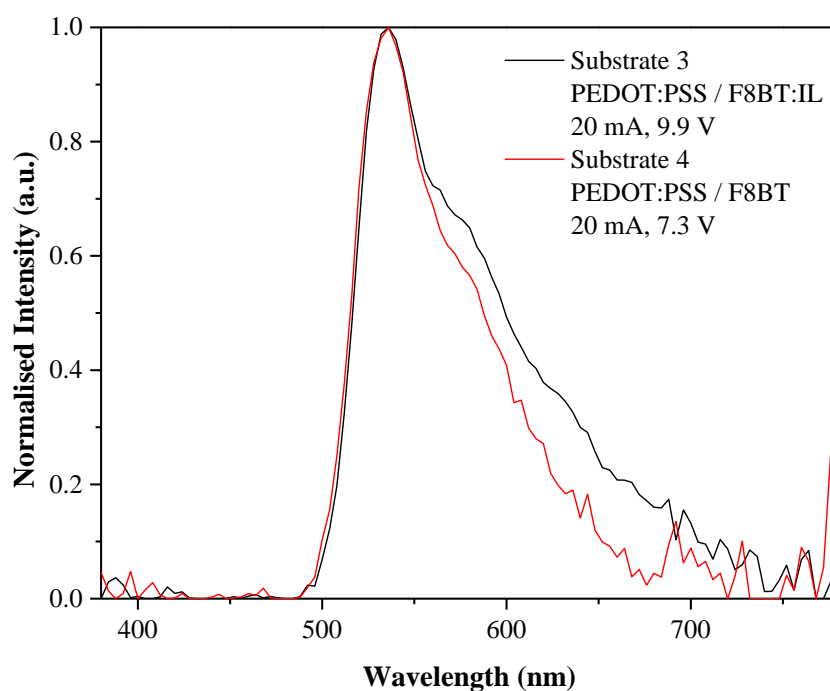


Figure 8.16: Electroluminescence data of Batch 1 Substrates 3 and 4.

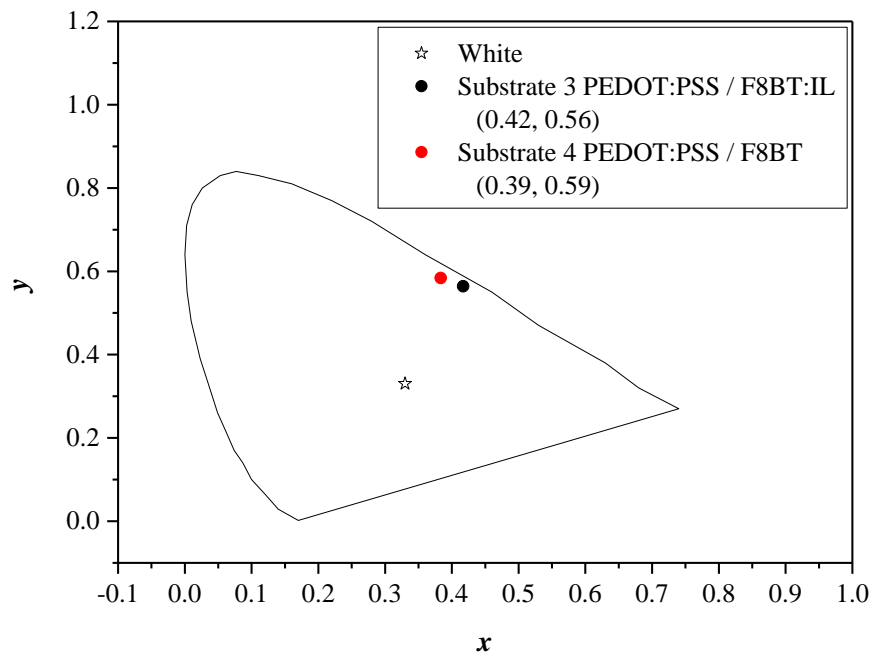
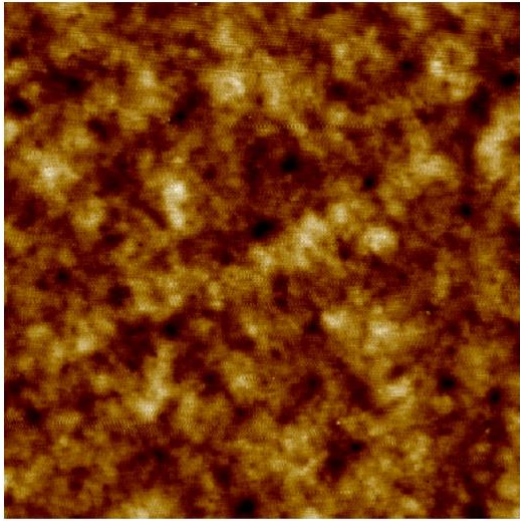
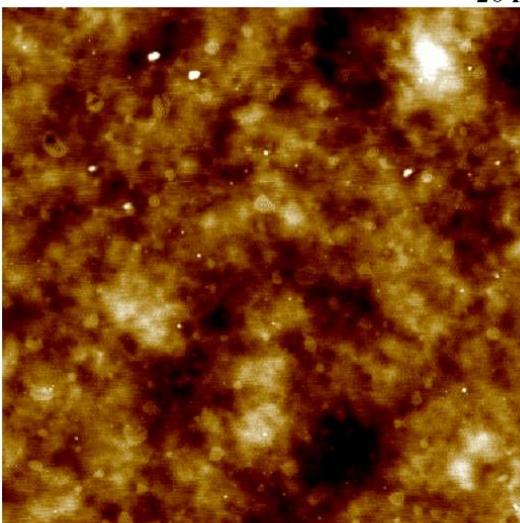


Figure 8.17: CIE coordinates of Batch 1 Substrates 3 and 4.

AFM images were also taken of the films of F8BT and the F8BT:IL. The roughness and thickness of each film were measured and found to be similar. The results of these measurements are tabulated over in Table 8.3.

Table 8.3: AFM images and thicknesses of films of F8BT:IL (5 wt%) and F8BT.

Film	AFM Image	Roughness R _a (nm)	Thickness (nm)
F8BT:IL		1.91	55
F8BT		2.29	66

5 Wt% F8BT:IL annealing temperature study (Batch 2)

It was considered that annealing the F8BT or F8BT:IL layer at 230 °C may be destroying the devices, despite published work^{1, 5, 7} reporting to have annealed at 290 °C. A second set

of devices was therefore prepared based on a 5 wt% of IL annealed at 30 °C, 80 °C and 230 °C. Again, for comparative purposes, devices without IL were also produced. This set of devices is referred to as Batch 2 and the device structures and annealing conditions are summarised in Table 8.4.

Table 8.4: Summary of the substrates in Batch 2 with device configuration and annealing temperatures. Substrates 4-6 have 5 wt% IL.

Substrate	Device Configuration	Annealing Temperature (°C)
1	ITO / F8BT / Al	30
2	ITO / F8BT / Al	80
3	ITO / F8BT / Al	230
4	ITO / F8BT:IL / Al	30
5	ITO / F8BT:IL / Al	80
6	ITO / F8BT:IL / Al	230

Current and photocurrent vs bias data for F8BT and F8BT:IL devices annealed at different temperatures are shown in Figure 8.18. The F8BT devices annealed at 30 °C and 80 °C both show diode-like characteristics with evidence of resistive effects before a rapid rise in current. The device annealed at 30 °C turns on at a lower voltage of 7.7 V compared to the device annealed at 80 °C which turns on at 10.8 V. The F8BT device annealed at 230 °C produced unusual characteristics and a lower light output. The F8BT:IL devices annealed at 30 °C and 80 °C showed an identical turn-on voltage of 3.6 V and based on the IV characteristics appear to breakdown at 6.8 V. Based on the photocurrent measurement, the F8BT:IL device annealed at 30 °C gave the greatest light output. Similar to the F8BT device, the F8BT:IL device annealed at 230 °C gave unusual IV characteristics and poor light output.

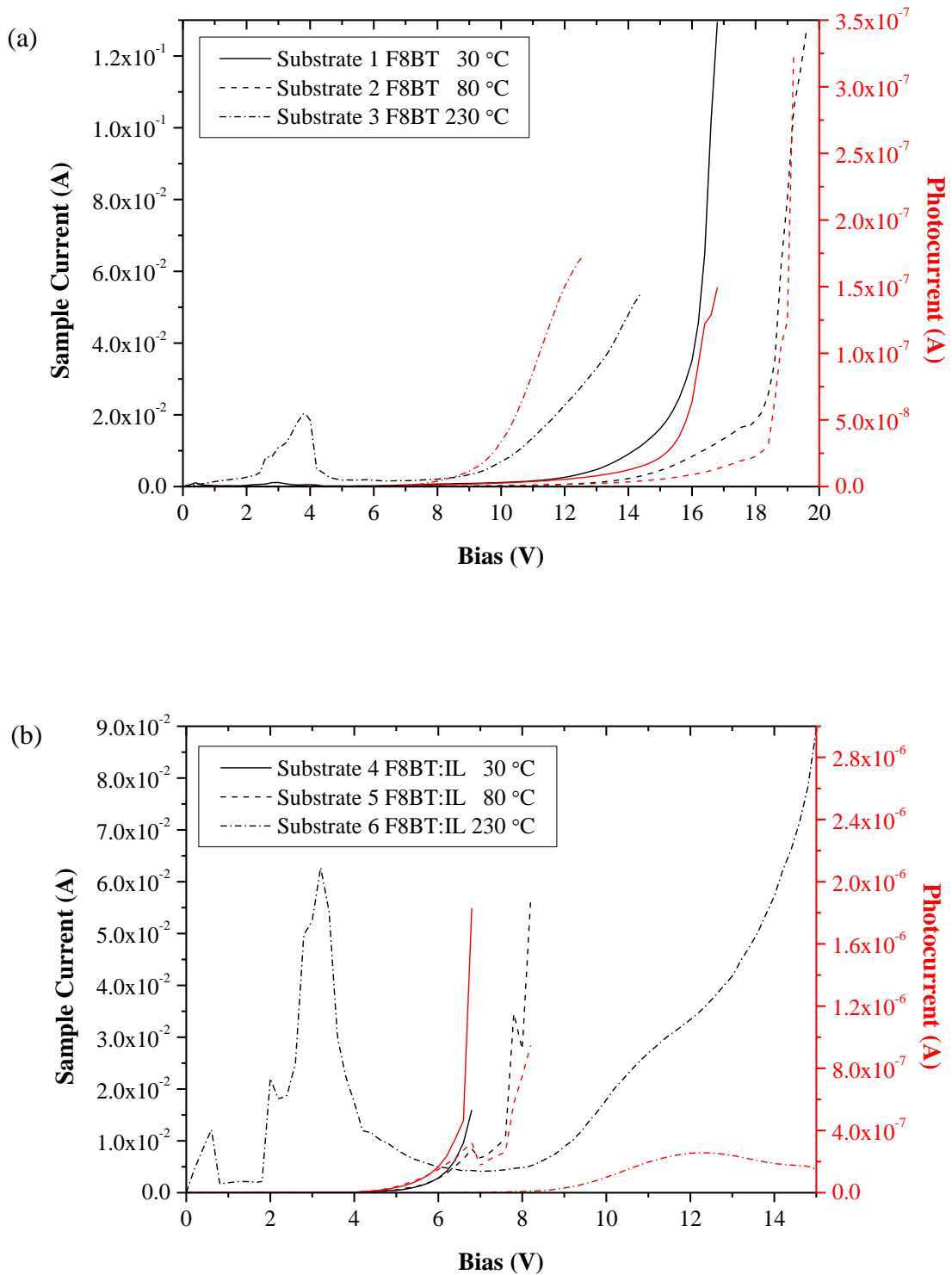


Figure 8.18: Electrical characteristics of the best devices on (a) substrates 1-3 and (b) substrates 4-6.

The ITO / F8BT / Al devices annealed at 30 °C and 80 °C emitted very little light and no reliable light measurements could be made with the spectrophotometer. Very speckly light was visible from the F8BT device annealed at 230 °C but dimmed within 2 seconds; not

long enough to measure. The F8BT:IL devices annealed at 30 °C and 80 °C were also difficult to measure however some results were obtained and the EL spectra are given in Figure 8.19. Overall light emission was poor and the spectra are mainly dominated by noise. The F8BT:IL device annealed at 230 °C emitted no visible or measureable light.

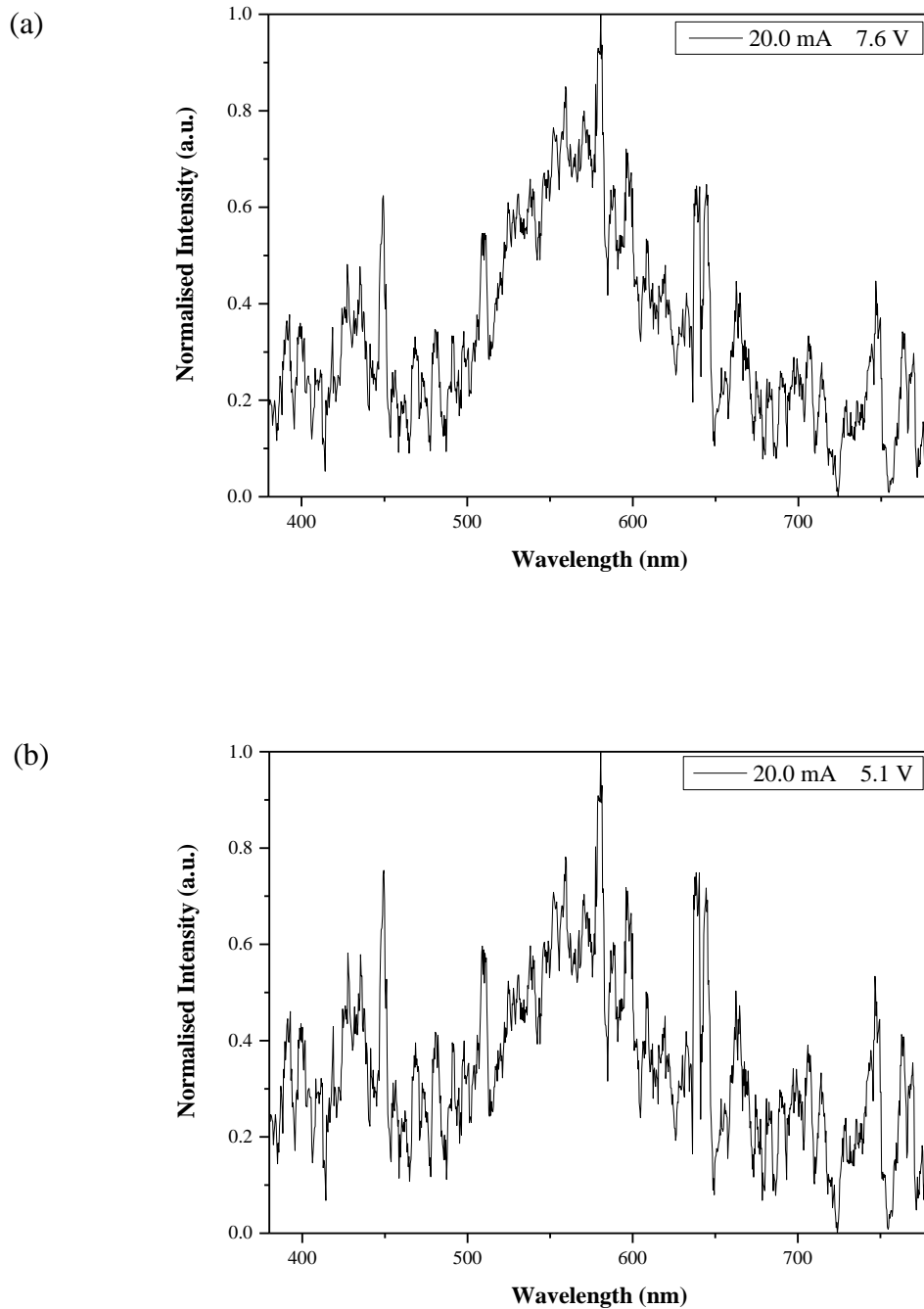


Figure 8.19: EL graphs of (a) Substrate 4 (30 °C) and (b) Substrate 5 (80 °C), both at 20 mA. Device structure: ITO / F8BT:IL / Al.

Despite the low levels of light emission, it was possible to measure CIE coordinates for the F8BT:IL devices annealed at 30 °C and 80 °C, as shown in Figure 8.20, and give a similar colour to the F8BT:IL devices incorporating a PEDOT:PSS layer, shown in Figure 8.17.

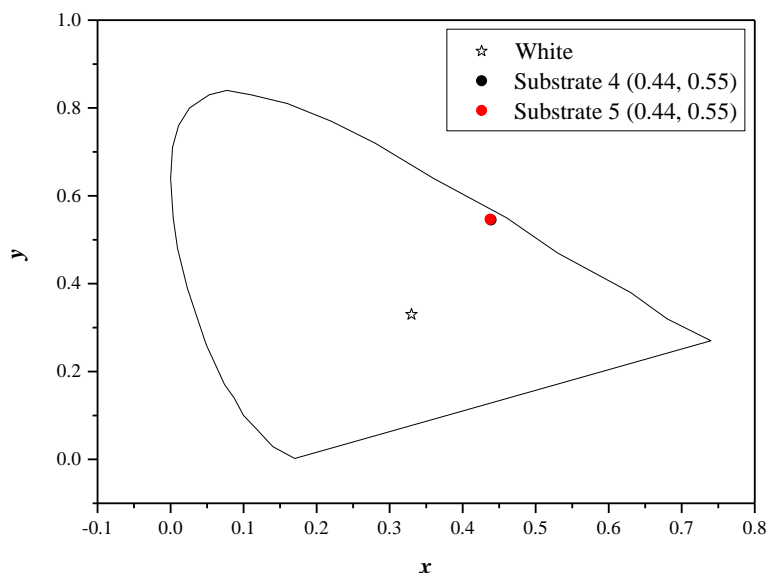
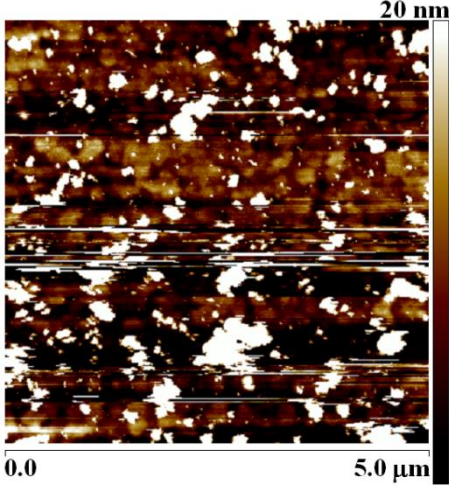
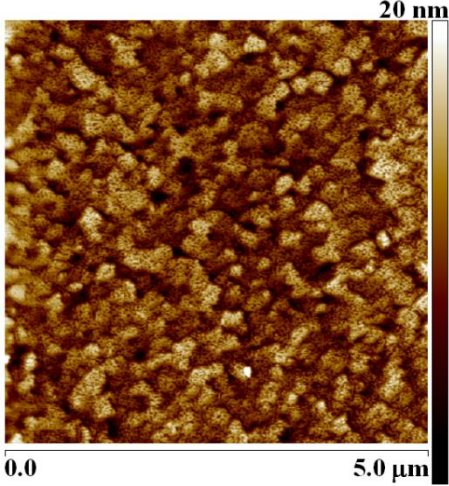
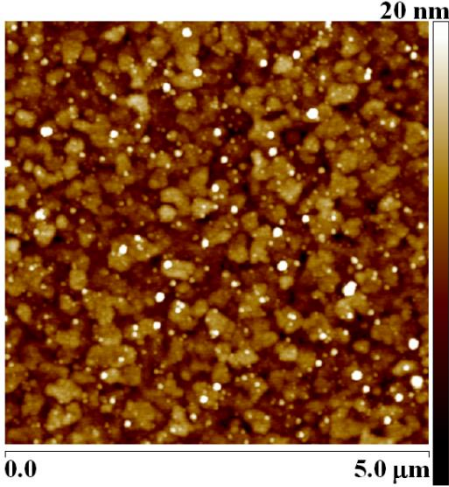
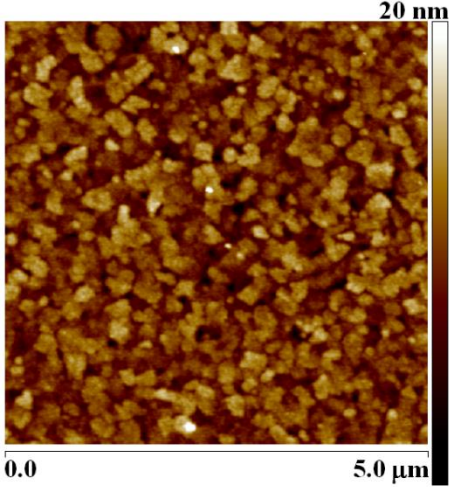
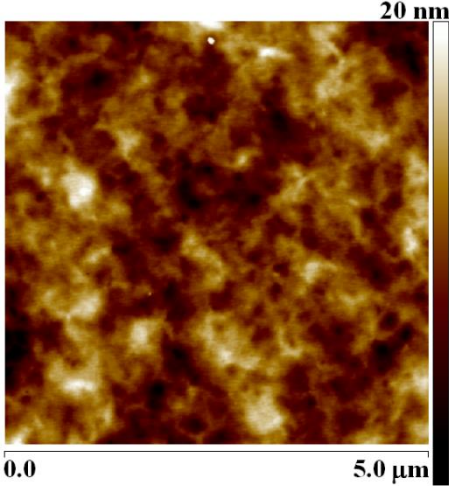
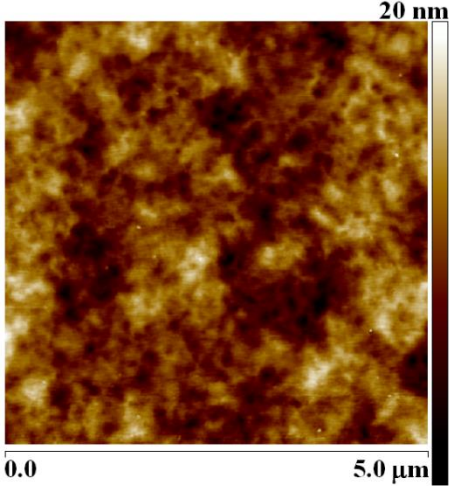


Figure 8.20: CIE diagram showing coordinates with current of 20 mA.

AFM measurements of each film are given in Table 8.5. The AFM images for F8BT annealed at 30 °C and 80 °C show similar topography consisting of crystalline structures with a surface roughness of about 2.2-2.4 nm (ignoring the large particulates on the film annealed at 30 °C). The F8BT:IL layers are similar, with a surface roughness of about 2.0-2.5 nm. The AFM images for the F8BT and the F8BT:IL annealed at 230 °C show that the high annealing temperature has a profound effect on the film structure. The annealed films reveal no evidence of crystallinity and appear amorphous with a roughness of 2.2-2.3 nm. It is now thought that annealing the F8BT or F8BT:IL layer at 230 °C causes a melting transition or a breakdown of the polymer which essentially destroys the film, rendering it useless for any devices.

The importance of annealing temperature was highlighted, with the best device results achieved for the 5% IL devices annealed at 30 °C. Therefore it was considered that the lack of light emission for the 5% IL devices prepared in Batch 1 could be due to the high annealing temperature.

Table 8.5: AFM images of each substrate in Batch 2.

Annealing T (°C)	ITO / F8BT	ITO / F8BT:IL (5 wt%)
30	 <p>Layer Thickness = 79 nm Roughness = 10.9 nm (or 2.42 without asperities)</p>	 <p>Layer Thickness = 58 nm Roughness = 2.53 nm</p>
80	 <p>Layer Thickness = 69 nm Roughness = 2.19 nm</p>	 <p>Layer Thickness = 54 nm Roughness = 2.01 nm</p>
230	 <p>Layer Thickness = 58 nm Roughness = 2.30 nm</p>	 <p>Layer Thickness = 59 nm Roughness = 2.21 nm</p>

A set of devices were also produced based on incorporating a higher weight percentage of IL (25% IL) and are given in Appendix D. Comparison of these results with the 5% IL devices in Batch 2 revealed that the 5% devices typically show smoother characteristics, particularly at lower voltages. There is also an effect from varying the annealing temperature. Devices annealed at 230 °C emitted no observable light and those at 80 °C gave noisy and irreproducible data. Devices annealed at 30 °C gave both more repeatable results and sustained a higher current.

The conclusion from these IL experiments is that IL does make a difference to F8BT devices and is similar to including a PEDOT:PSS layer. For F8BT:IL annealed at 30 °C the turn-on voltage is lowered to 3.6 V, compared with 4.4 V for F8BT with PEDOT:PSS annealed at 230 °C. There is also an improvement over devices containing both F8BT:IL and PEDOT:PSS (annealed at 230 °C) which showed turn-on at 5.1 V. Annealing at higher temperatures changes the film structure and gives noisy, irreproducible data. This effect is the reason why IL based devices without PEDOT:PSS in Batch 1, annealed at 230 °C, showed no light emission, as identical devices annealed at 30 °C do show light emission. This result appears to contradict other work in the area that anneals F8BT at 290 °C.^{1, 5, 7} Using 5 wt% IL gave the best results and was used to try to make an in-plane OLED and a transistor, where the IL would remove the problem of reduced efficiency due to the absence of PEDOT:PSS.

8.5.2 In-plane OLED and Transistor

With IL having been successfully incorporated into a standard out-of-plane OLED architecture, the next natural step towards a transistor was an in-plane OLED. The term, in-plane refers to the fact that the active organic layer was deposited on top of the electrodes

to give a device where the anode and cathode are on the same horizontal plane, as opposed to the standard OLED structure where the electrodes are out-of-plane and sandwich the active organic material. The structures of the in-plane devices are given schematically in the Experimental chapter on page 77 and involved F8BT:IL deposited between gold and aluminium electrodes.

Current and photocurrent vs bias data for all of the in-plane OLEDs were similar and showed no correlation with channel dimensions. Data for an OLED with dimensions $L = 50 \mu\text{m}$ and $W = 4000 \mu\text{m}$ are given in Figure 8.21 and show that current increased to only 0.28 nA at 200 V and no light output was observed.

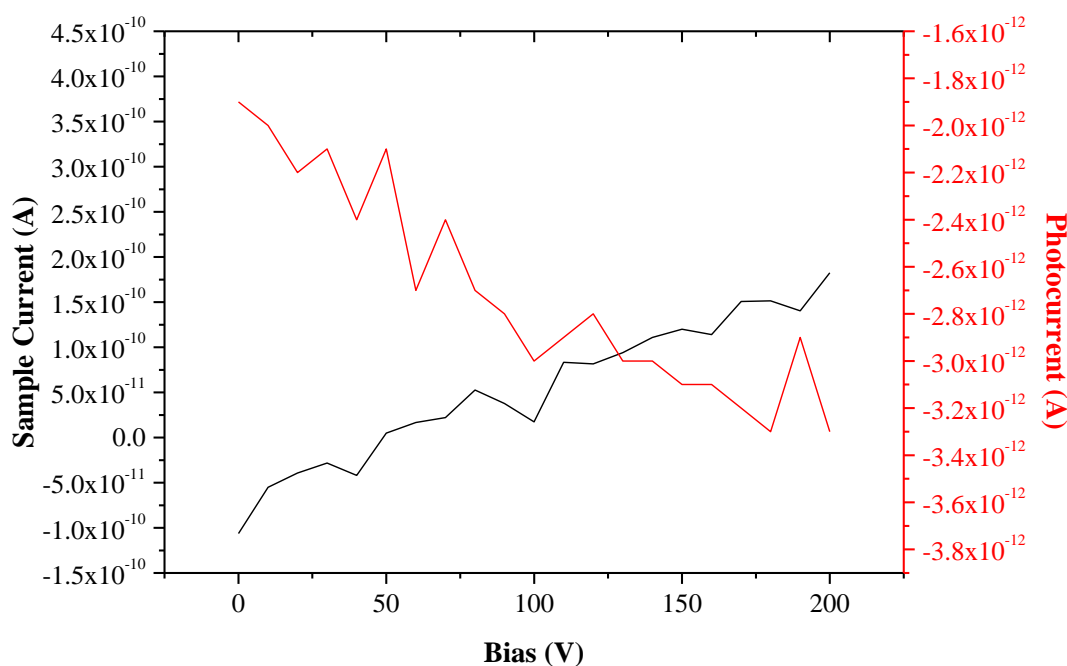


Figure 8.21: Current and photocurrent vs bias data for in-plane OLED containing F8BT:IL (5 wt%). Channel dimension: $L = 50 \mu\text{m}$ and $W = 4000 \mu\text{m}$. See Experimental chapter for device dimensions.

Although the F8BT:IL in-plane OLED was unsuccessful, incorporation of the blend into a transistor structure, with aluminium gate and PMMA insulator, showed light emission.

The transistors were measured and in this case there was some speckly green light from a number of devices. A photograph of a device with channel dimensions $L = 50 \mu\text{m}$ and $W = 4000 \mu\text{m}$ under operation inside the measurement chamber is given in Figure 8.22.

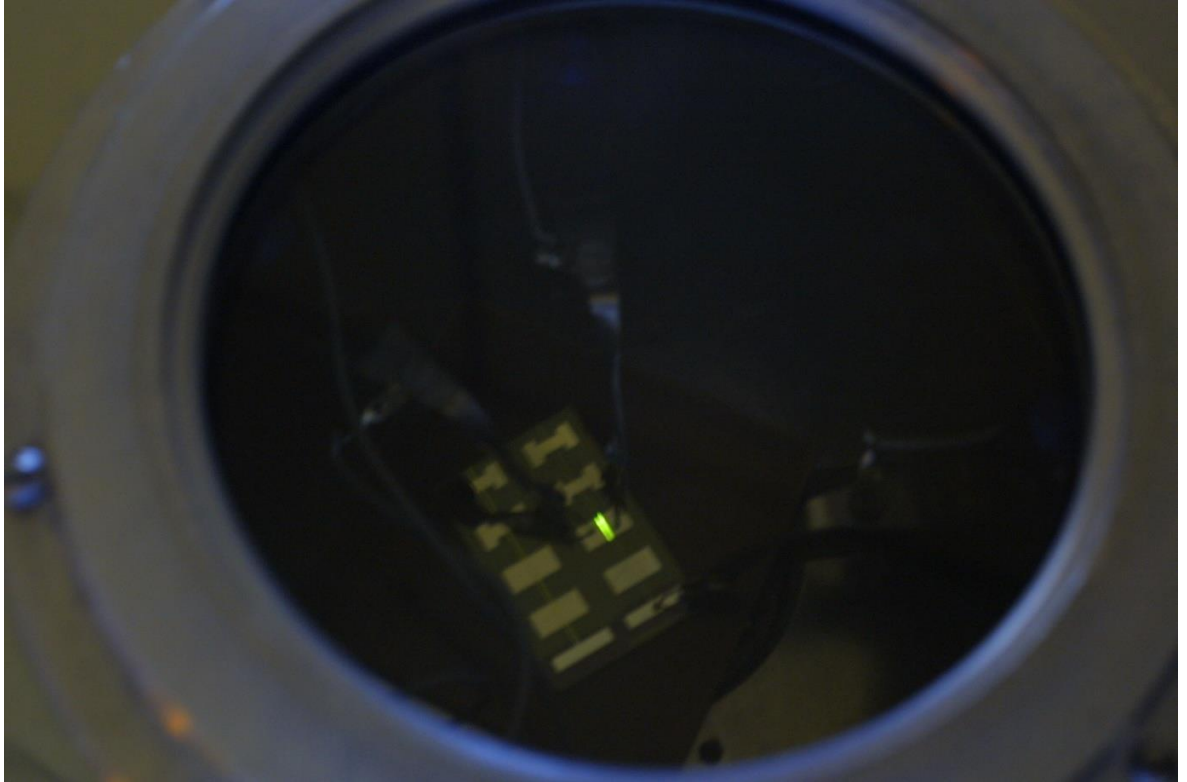
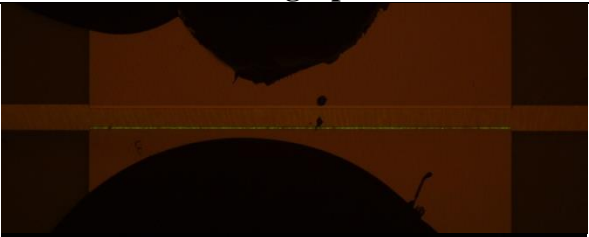

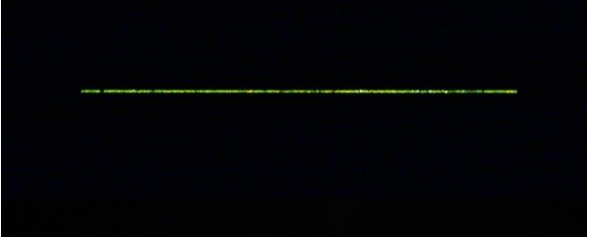
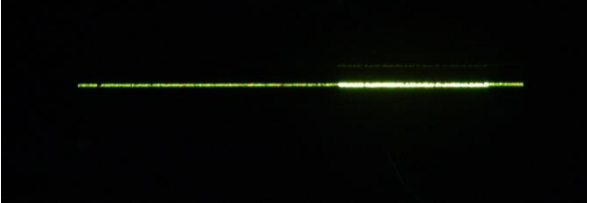
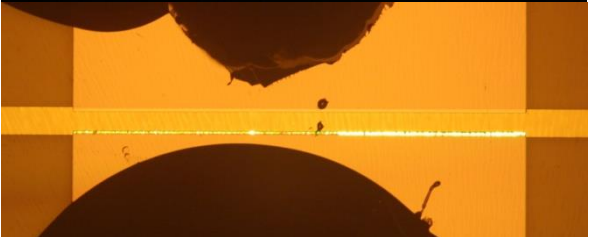
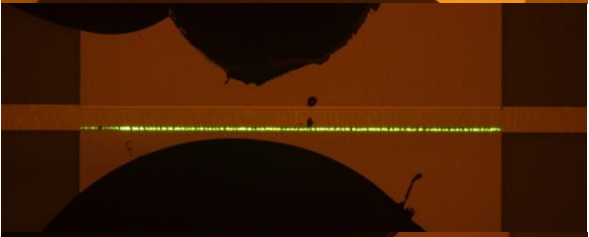
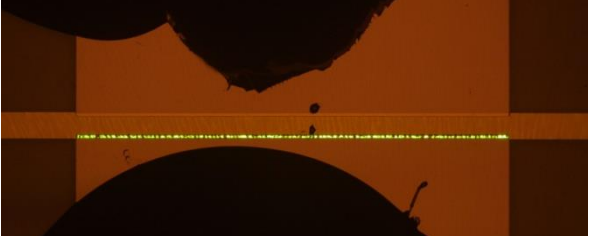


Figure 8.22: Photograph of a transistor device emitting light. Channel dimensions: $L = 50 \mu\text{m}$ and $W = 4000 \mu\text{m}$.

Upon further investigation with a microscope, it became clear that as for the F8BT devices in Section 8.4, this light was not coming from the channel but from the overlap between the aluminium bottom gate and the Au electrode. There was also no light when any voltage was applied to the gate. i.e. this light was seen when V_G was set to 0 V and V_{DS} was swept from 0 to -30 V. Light appeared at around -20 to -25 V and got brighter until -30 V V_{DS} was applied. The light then dimmed and was not visible below around -15 V. A similar effect was seen for a device with dimensions $L = 200 \mu\text{m}$ and $W = 4000 \mu\text{m}$ and relevant microscope images of this device operating under different voltages are summarised in Table 8.6 with a brief description.

Table 8.6: Microscope images and descriptions of light from a device with dissimilar electrodes. Channel dimensions $L = 200 \mu\text{m}$ and $W = 4000 \mu\text{m}$. Note: Black parts are silver paint contacts to the source and drain.

Description	Photograph
a) Light started dimly at around $V_{\text{DS}} = -20 \text{ V}$. Microscope illumination on.	
b) Emitted light increased in brightness. Microscope illumination off.	
c) Relatively uniform bright light at $V_{\text{DS}} = -28 \text{ V}$.	
d) Brighter strip of light moved along left to right between $V_{\text{DS}} = -29$ to 30 V .	
e) As above, but brighter microscope illumination.	
f) V_{DS} sweeping back towards 0 V . Microscope light on.	
g) Light gets dimmer as reaching $V_{\text{DS}} = -20 \text{ V}$. Microscope illumination on.	

Further evidence that these devices were behaving as OLEDs rather than transistors was provided by electrical measurements on a device with channel dimensions of $L = 50 \mu\text{m}$ and $W = 2000 \mu\text{m}$, as shown in Figure 8.23.

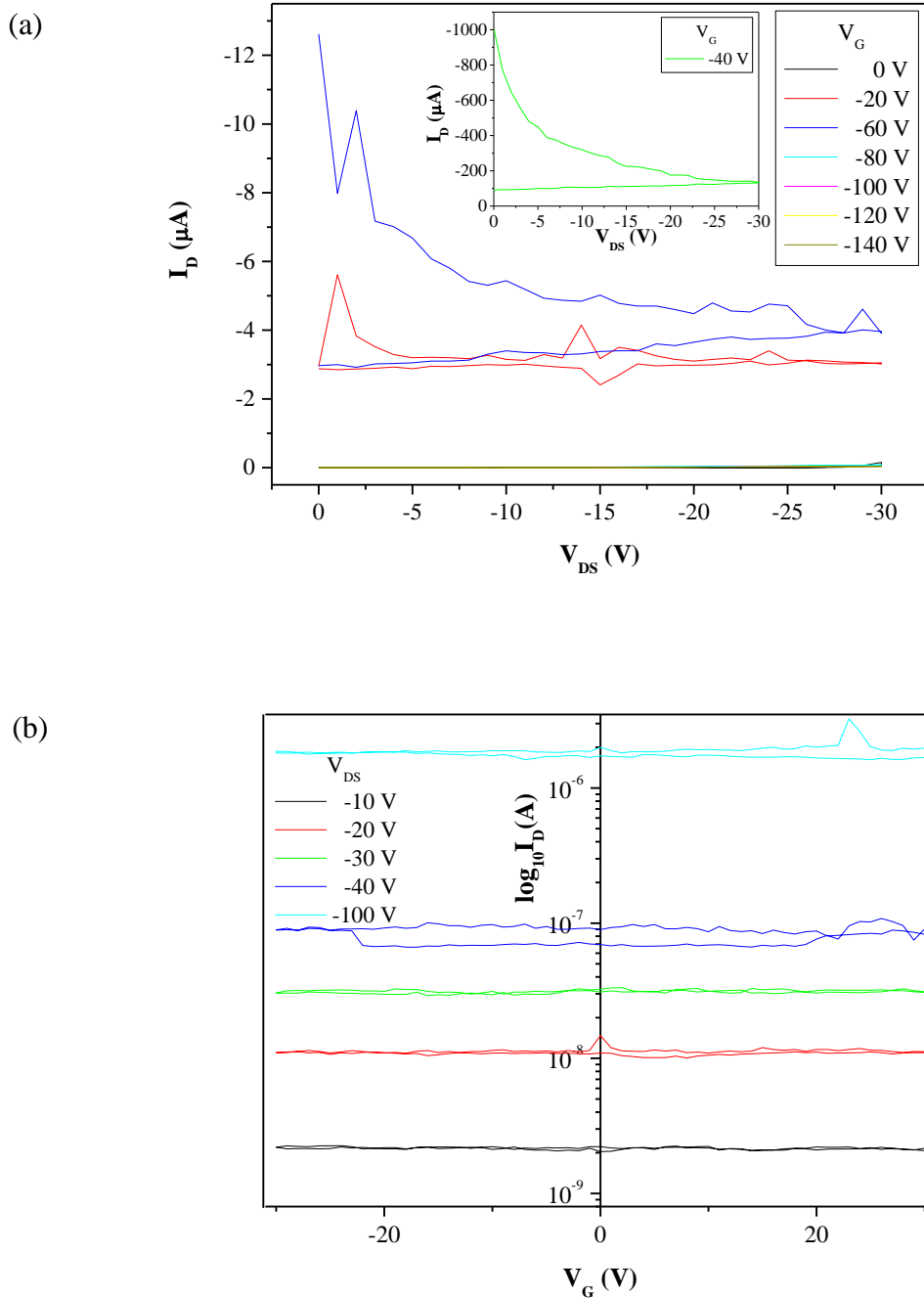


Figure 8.23: (a) Output characteristics for $V_G = 0 \text{ V}$, -20 V and -60 to -100 V applied to F8BT device. $V_G = -40 \text{ V}$ is shown in the inset and gives a much higher I_D . (b) Transfer characteristics of the same transistor device. Device dimensions: $L = 50 \mu\text{m}$ and $W = 2000 \mu\text{m}$.

The transfer characteristics in Figure 8.23(b) were poor, only showing leakage and no dependence on V_G . The output characteristics in Figure 8.23(a) at $V_G = 0$ and -20 V show little change in I_D when sweeping V_{DS} from 0 to -30 V. At $V_G = -40$ V, the behaviour is anomalous and shows evidence of a momentary breakdown with I_D up to -1000 μA , as shown in the inset in Figure 8.23(a). Subsequent measurement at $V_G = -60$ V shows I_D to return to a similar magnitude as seen for $V_G = -20$ V and measurements at higher V_G give I_D similar to that for $V_G = 0$ V.

8.6 Conclusions

Initial experiments highlighted the need for F8BT to be studied in an air and moisture free environment and showed that the best processing technique for preparing spin-coated layers of F8BT involved dissolving the polymer in chloroform at a concentration of 5 mg ml^{-1} and filtering the resulting solution to remove particulates. Xylene, which has been used in the literature,⁴⁻⁶ was found to be unsuitable.

The electroluminescent properties of F8BT were successfully studied by incorporating the material into an out-of-plane OLED device, which emitted green light with CIE (x , y) coordinates (0.38, 0.60). An initial study of F8BT transistors showed promising output and transfer characteristics and some devices exhibited light emission, as would be expected for an OLEFET. However, close inspection of the location of the light emission suggested the devices were in fact behaving as OLEDs rather than transistors.

Further study of F8BT OLEDs identified that altering the temperature at which the F8BT film was annealed improved results. Contrary to a number of publications^{1, 5, 7} it was found that annealing at 30 $^\circ\text{C}$ gave the most stable results whereas a high temperature of 230 $^\circ\text{C}$ gave particularly unstable and unreliable results. AFM measurements revealed that F8BT annealed at low temperatures maintained a crystalline structure whilst films annealed at

230 °C appeared amorphous, suggesting a melting transition or breakdown of the polymer at higher temperatures.

Experiments were also undertaken into F8BT blended with an ionic liquid. The results of this proved that the ionic liquid could be used in an F8BT OLED without any PEDOT:PSS or calcium layers, ideal for further experimentation into preparing an F8BT transistor. Incorporation of F8BT blended with 5% ionic liquid by weight into a transistor structure showed the resulting device emitted light. However, under closer scrutiny the emission was identified to originate from the overlap of the gate and Au electrode i.e. the device was in fact behaving as an OLED rather than a transistor.

The fact that the light always seems to appear through the electrode overlap and never in the channel may mean that there are some significant defects in the device that were not observed in the AFM scans or even in looking at the electrical data, but this seems unlikely. Despite problems with the devices, IL blends showed improved results, so further study in this direction is worthwhile. Other experiments to continue this study might include looking into trying blends with different ionic liquids. It is known that the choice of ionic liquid can enhance the efficiency of OLED emission by a number of orders of magnitude.^{27, 28}

8.7 References

- 1) J. Zaumseil, C. R. McNeill, M. Bird, D. L. Smith, P. P. Ruden, M. Roberts, M. J. McKiernan, R. H. Friend, H. Sirringhaus, *J. Appl. Phys.*, 103, 064517, **2008**.
- 2) H. Kim, M. Shin, Y. Kim, *J. Phys. Chem. C*, 113, 1620-1623, **2009**.
- 3) H. J. Snaith, R. H. Friend, *Synth. Met.*, 147, 105-109, **2004**.

- 4) C. R. McNeill, A. Abrusci, J. Zaumseil, R. Wilson, M. J. McKiernan, J. H. Burroughes, J. J. M. Halls, N. C. Greenham, R. H. Friend, *Appl. Phys. Lett.*, 90, 193506, **2007**.
- 5) R. C. G. Naber, M. Bird, H. Sirringhaus, *Appl. Phys. Lett.*, 93, 023301, **2008**.
- 6) M. C. Gwinner, S. Khodabakhsh, H. Giessen, H. Sirringhaus, *Chem. Mater.*, 21, 4425-4433, **2009**.
- 7) C. L. Donley, J. Zaumseil, J. W. Andreasen, M. M. Nielsen, H. Sirringhaus, R. H. Friend, J.-S. Kim, *J. Am. Chem. Soc.*, 127, 12890-12899, **2005**.
- 8) Y. Kim, M. Shin, H. Kim, *J. Nanoscience and Nanotechnology*, 8, 6247-6252, **2008**.
- 9) R. Steyrlleuthner, S. Bange, D. Neher, *Appl. Phys. Lett.*, 105, 064509, **2009**.
- 10) K. Morii, M. Omoto, M. Ishida, M. Graetzel, *Jap. Soc. Appl. Phys.*, 47, 7366-7368, **2008**.
- 11) A. L. Fisher, K. E. Linton, K. T. Kamtekar, C. Pearson, M. R. Bryce, M. C. Petty, *Chem. Mater.*, 23, 1640-1642, **2011**.
- 12) K. E. Linton, A. L. Fisher, C. Pearson, M. A. Fox, L. O. Pålsson, M. R. Bryce, M. C. Petty, *J. Mater. Chem.*, 22, 11816-11825, **2012**.
- 13) M. C. Rosamond, A. J. Gallant, M. C. Petty, O. Kolosov, D. A. Zeze, *Adv. Mater.*, 23, 5039-5044, **2011**.
- 14) A. Sandström, H. F. Dam, F. C. Krebs, L. Edman, *Nature Commun.*, 3, 1002, **2012**.
- 15) P. Matyba, M. R. Andersson, L. Edman, *Organic Electronics*, 9, 699-710, **2008**.
- 16) P. Matyba, H. Yamaguchi, G. Eda, M. Chhowalla, L. Edman, N. D. Robinson, *ACS Nano*, 4, 637-642, **2010**.

- 17) D. R. Macfarlane, M. Forsyth, P. C. Howlett, J. M. Pringle, J. Sun, G. Annat, W. Neil, E. I. Izgorodina, *Acc., Chem., Res.*, 40, 1165-1173, **2007**.
- 18) A. P. Doherty, C. A. Brooks in *Ionic Liquids as Green Solvents*, ACS Publications, **2003**, Chapter 33.
- 19) C. H. Yang, Q. J. Sun, J. Qiao, Y. F. Li, *J. Phys. Chem. B*, 107, 12981-12988, **2003**.
- 20) S. T. Parker, J. D. Slinker, M. S. Lowry, M. P. Cox, S. Bernhard, G. G. Malliaras, *Chem. Mater.*, 17, 3187-3190, **2005**.
- 21) Y. Shao, G. C. Bazan, A. J. Heeger, *Adv. Mater.*, 19, 365-369, **2007**.
- 22) R. Hagiwara, J. S. Lee, *Electrochemistry*, 75, 23-34, **2007**.
- 23) I. Kenyon in *Electrochemical Organic Displays*, MEng Research and Development Project, **2012**.
- 24) Merck Chemicals, "Merck Livilux PDY-132 (Super Yellow) Data Sheet"
- 25) S. Westenhoff, I. A. Howard, J. M. Hodgkiss, K. R. Kirov, H. A. Bronstein, C. K. Williams, N. C. Greenham, R. H. Friend, *J. Am. Chem. Soc.*, 130, 13653-13658, **2008**.
- 26) Y. Xiong, J.-B. Peng, H.-B. Wu, J. Wang, *Chin. Phys. Lett.*, 26, 097801, **2009**.
- 27) R. Martín, L. Teruel, C. Aprile, J. F. Cabeza, M. Álvaro, H. García, *Tetrahedron*, 64, 6270-6274, **2008**.
- 28) J. P. Chen, J. D. Mackenzie, *Ionic Salt Combinations in Polymer Electroluminescent Inks*, International Patent WO 2011/032010 A1, **2011**.

9 Conclusions & Suggestions for Further Work

9.1 In this Chapter...

This chapter gives a summary and findings of the thesis as well as ideas for further work to develop the research in the future.

9.2 Summary

This thesis has investigated the incorporation of a range of ambipolar materials into OLEDs and transistors. First, a series of analogous carbazole-containing triad molecules were studied. Simple, efficient, deep-blue OLEDs were produced and it was shown how chemical modifications to the molecular structure could enable tuning of the emission colour. Another analogue from the same family of compounds gave green light when incorporated into the OLED structure. White light was also achieved by mixing one of these novel compounds in specific ratios with well-known commercially available yellow emitters and OXD7. Chemically incorporating OXD7 into the molecule itself enabled white light without any mixing.

The second half of this thesis concentrated on the transistor device. Initial studies were carried out on a simple pentacene transistor (and OLED) to provide a proof of concept for the further development of transistors based on three novel materials, compounds **1**, **2** and **8**, synthesised by the Bryce group in the Department of Chemistry at Durham University. The work then moved on to look in depth at the polymer F8BT as a molecule for preparation of light-emitting transistors and incorporation of an ionic liquid to improve charge transport.

9.3 Conclusions

Slight modification to a previously studied donor-acceptor ambipolar compound by addition of a carbazole group allowed for efficient deep blue OLEDs to be produced. These devices produced a deep blue colour with CIE (x, y) coordinates (0.16, 0.08), close to the National Television System Committee standard of CIE (0.14, 0.08). In addition, considering the simple device architecture utilised, and depth of the blue colour, the OLEDs exhibited a very high external quantum efficiency of 4.71%, which is amongst the best for simple blue devices.¹ The efficiency was also found to be dependent on the thin film processing technique utilised, with OLEDs based on thermally evaporated layers of active material giving higher efficiency than those prepared by spin-coating.

Incorporation of further structural analogues of the deep-blue emitting molecule into OLEDs showed how molecular modifications could be used to tune the emission colour. The variation in colour was also found to fit well with the calculated band gap for each molecule, based on DFT calculations. Removal of the fluorene group from the donor-acceptor structure was found to result in very deep blue emission, with CIE coordinates (0.16, 0.05), although the efficiency was observed to drop. Important design rules that have emerged from the study are that the deep blue emission from the molecules originates from the carbazole group and that the presence of a fluorene group adjacent to the carbazole donor separated from the oxadiazole acceptor by a phenylene ring is required to achieve a high device efficiency (EQE > 1%). The relatively small size of the D-A structure combines good processability with a bipolar electronic structure, which allows efficient performance in simple, non-doped OLEDs. These factors coupled with the ability to tune the emission colour makes this new family of materials very attractive for further development.

The dependence of the electroluminescent properties of OLEDs on chemical structure was further highlighted during study into OLEDs based on an analogue to Compound **1** with additional methyl groups. This structural modification to Compound **1** was intended to simplify the chemical synthesis, but was found to have a direct effect on OLED characteristics. The emission colour shifted to green, despite the core D-A triphenylamine-oxidiazole moieties being left intact, emphasising the close link between structure and electroluminescence.

Chemical addition of electron-transporting OXD groups was also considered as one approach to improve the efficiency of the successful deep blue OLED Compound **2**, without the need for incorporation of separate electron transporting materials in the OLED device. Despite blended devices of OXD7 showing improved efficiencies, the chemical attachment of OXD did not improve the efficiency of the OLEDs studied. However, attachment of two OXD groups to the compound did result in a complex, more white emission, possibly as a result of multiple electron-hole recombination routes between the carbazole moiety and OXD groups.

Single-active-layer white OLEDs were successfully produced by blending the deep blue carbazole-based Compound **2**, with the yellow emitting iridium-based phosphorescent dye, PO-01. The emission colour of the blended device shifted from yellow to green and finally to blue, depending on the blend ratio, and a blend of 0.14% PO-01 produced WOLEDs with CIE coordinates (0.30, 0.31), very close to the pure white point of (0.33, 0.33). Blending with the fluorescent yellow polymer Super Yellow was also found to cause a shift in the emission colour from yellow to green but the locus of the data points was observed to miss the pure white point. The efficiency of the PO-01 blended devices was further optimised by the addition of the electron transport compound OXD7 to the blend. The result was a simple white OLED architecture with an external quantum efficiency of

about 2.5%. Although lower than the highest values currently reported in the literature,^{2,3} the simple architecture favours high reproducibility and allows for such WOLEDs to be fabricated at a relatively low cost compared with multilayer device architectures.

White OLEDs were also produced by blending PO-01 with a carbazole analogue with chemically attached OXD groups. However, the efficiency was low at 0.42%. It is suggested that this behaviour is related to the unfavourable stereochemistry of the molecules which produces poor packing in the active layer film.

The ambipolar D-A molecules were further studied by using them in OFET structures, where it was considered that the ambipolar conduction could be used to produce light-emitting transistors. Whilst very useful in OLEDs, transistors incorporating these compounds generally did not show classical transistor behaviour, with output characteristics dominated by leakage or device breakdown. Apparently ambipolar conduction observed in the transfer characteristics for these transistors was attributed to an artefact due to current from the gate contact leaking to the drain.

Transistors based on the successful efficient deep-blue emitting carbazole compound deposited between dissimilar electrodes also gave little current output. Incorporating a layer of pentacene to act as a hole transporter produced transistors with recognisable output and transfer characteristics. However, the behaviour was similar to all-pentacene OFETs and it was considered that the electrical properties of the pentacene dominated the device output characteristics. Transfer characteristics showed a clear hole current but no evidence of an electron current, showing that the ambipolar properties of the carbazole compound did not assist electron conduction in the transistor. Devices based on pentacene and the carbazole compound did however show differences in the value of threshold voltage and the off state of the transistor. Addition of the electron-transporting material, OXD7, also

showed no evidence of enhancing the electron current in these transistors despite its successful use as an electron transport layer in OLEDs.

The electroluminescent properties of the ambipolar polymer F8BT were successfully studied by incorporating the material into an out-of-plane OLED device, which emitted green light with CIE (x , y) coordinates (0.38, 0.60). Important processing parameters were identified throughout the study including the need for F8BT to be studied in an air and moisture free environment. Chloroform was also found to be the best solvent for the preparation of spin-coated films of F8BT, with xylene found to be unsuitable, despite it being reported as the solvent in some literature.⁴⁻⁹ Further contradictions to literature reports were evident regarding the temperature at which F8BT films should be annealed to improve characteristics. Literature suggests the use of a high temperature anneal at 290 °C.^{4, 6, 8} However, in this study films annealed at 230 °C gave unstable electrical results compared to F8BT annealed at 30 °C. AFM scans performed on the films revealed that F8BT annealed at low temperatures maintained a crystalline structure whilst films annealed at 230 °C appeared amorphous, suggesting a melting transition or breakdown of the polymer at higher temperature.

Incorporation of F8BT blended with 5% ionic liquid by weight into a transistor structure showed the resulting device emitted light. However, under closer scrutiny the emission was identified to originate from the overlap of the gate and Au electrode i.e. the device was in fact behaving as an OLED rather than a transistor. Similar behaviour was observed for an F8BT-only transistor where light emission corresponded to visible defects in the insulator. The results of the IL study proved that the ionic liquid could be used in an F8BT OLED without any PEDOT:PSS or calcium layers, ideal for further experimentation into preparing an F8BT transistor.

9.4 Suggestions for Further Work

In completing this study, several additional options for further work have been identified. One area of interest is the effect of both fabrication technique and the thickness of the active layer on device characteristics. First, the effect of spin speed on the layer thickness of the carbazole compound-containing OLEDs could be explored, and the resulting properties such as turn-on voltage and external quantum efficiency measured. Similarly, the effect of the thickness of evaporated films of Compound **2** (and other compounds in the series) on device characteristics could be explored, particularly with respect to improving EQE further.

Annealing is another fabrication step that deserves further study. Since the F8BT annealing study showed how temperature can affect the morphology of the organic layers, a similar approach could be applied to the Compound **2** spin-coated OLEDs. The evaporated devices of all compounds in the series showed crystalline films, whereas the spin-coated films were always amorphous. A different annealing temperature might produce more crystalline spin-coated films and improve device characteristics.

An alternative and direct approach to enhancing EQE in these devices is to experiment with and optimise outcoupling through waveguiding of more light out of the front of each device.

Now that a suitable blue compound (Compound **2**) has been achieved, it is of great interest to research the stability and lifetime of this material and its OLEDs, as lifetime is a key factor for display technology. A starting point may be a study into encapsulation methods (since no devices in this thesis were encapsulated) followed by daily or weekly monitoring of device lifetime. In order to allow for ongoing lifetime tests, a necessary first step would be the assembly of a suitable rig.

A separate area of interest is research into blending. Morphological and solvent studies of the blended-layer WOLEDs and the effects on electro-optical properties should be further explored, especially with respect to steric effects. Also, IL blends with F8BT showed improved results, so further study in this direction is worthwhile. Careful selection of IL can enhance the OLED efficiency by orders of magnitude, as previously discussed, so an exploration into F8BT:IL blends with different ionic liquids could prove valuable as a step closer to producing light-emitting transistors with F8BT.

Finally, given time (approx. one month synthesis time), more of Compound **1** could be produced and incorporated into transistors to allow for a full study of the electrical properties.

9.5 References

- 1) M. Zhu, C. Yang, *Chem. Soc. Rev.*, 42, 4963-4976, **2013**.
- 2) Y.-L. Chang, Z.-H. Lu, *J. Display Technology*, 9, 459-468, **2013**.
- 3) H. Sasabe, J. Kido, *J. Mater. Chem. C*, 1, 1699-1707, **2013**.
- 4) J. Zaumseil, C. R. McNeill, M. Bird, D. L. Smith, P. P. Ruden, M. Roberts, M. J. McKiernan, R. H. Friend, H. Sirringhaus, *J. Appl. Phys.*, 103, 064517, **2008**.
- 5) C. R. McNeill, A. Abrusci, J. Zaumseil, R. Wilson, M. J. McKiernan, J. H. Burroughes, J. J. M. Halls, N. C. Greenham, R. H. Friend, *Appl. Phys. Lett.*, 90, 193506, **2007**.
- 6) R. C. G. Naber, M. Bird, H. Sirringhaus, *Appl. Phys. Lett.*, 93, 023301, **2008**.
- 7) M. C. Gwinner, S. Khodabakhsh, H. Giessen, H. Sirringhaus, *Chem. Mater.*, 21, 4425-4433, **2009**.

- 8) C. L. Donley, J. Zaumseil, J. W. Andreasen, M. M. Nielsen, H. Sirringhaus, R. H. Friend, J.-S. Kim, *J. Am. Chem. Soc.*, 127, 12890-12899, **2005**.
- 9) Y. Kim, M. Shin, H. Kim, *J. Nanoscience and Nanotechnology*, 8, 6247-6252, **2008**.

10 Publications

1) **Deep Blue OLEDs Based on Triphenylamine-oxadiazole-fluorene Triad**

Molecules

A. L. Fisher, C. Pearson, M. C. Petty, K. E. Linton, K. T. Kamtekar, M. R. Bryce

Poster Presentation

International Conference on Organic Electronics ICOE 2010

Paris, France, June **2010**

2) **Efficient Deep-Blue Electroluminescence from an Ambipolar Fluorescent Emitter in a Single-Active-Layer Device**

A. L. Fisher, K. E. Linton, K. T. Kamtekar, C. Pearson, M. R. Bryce, M. C Petty

Chemistry of Materials

Volume 23 Issue 7, Page 1640-1642

Published 12th April **2011**

Impact Factor 8.238

Times Cited (as on 12/10/2013) **37**

3) **Colour tuning of a blue electroluminescence using bipolar carbazole-oxadiazole molecules in single-active-layer organic light-emitting devices (OLEDs)**

K. E. Linton, A. L. Fisher, C. Pearson, M. A. Fox, L. O. Pålsson, M. R. Bryce, M. C.

Petty

Journal of Materials Chemistry

Volume 22 Issue 23, Page 11816-11825

Published 11th May **2012**

Impact Factor 6.101

Times Cited (as on 12/10/2013) **10**

- 4) **Focused ion beam and field-emission microscopy of metallic filaments in memory devices based on thin films of an ambipolar organic compound consisting of oxadiazole, carbazole and fluorene units**

C. Pearson, L. Bowen, M.-W. Lee, A. L. Fisher, K. E. Linton, M. R. Bryce, M. C. Petty

Applied Physics Letters

Volume 102 Issue 21, Article Number 213301

Published 27th May **2013**

Impact Factor 3.794

Times Cited (as on 12/10/2013) 0

Appendix A

Computational Study of the Triad Molecules

Ground state geometry optimisations were carried out on all seven molecules at the B3LYP/6-31G* model chemistry without symmetry constraints. Ethyl groups were used instead of hexyl groups in compounds **1-7** to reduce computational efforts and these model geometries are denoted by the suffix a, i.e. **1a-7a**.

Electronic structure calculations carried out on these geometries **2a-8** show that the HOMOs are located at the carbazolyl groups as expected as shown in the molecular orbitals for **2a** and **7a** (Figure A1).

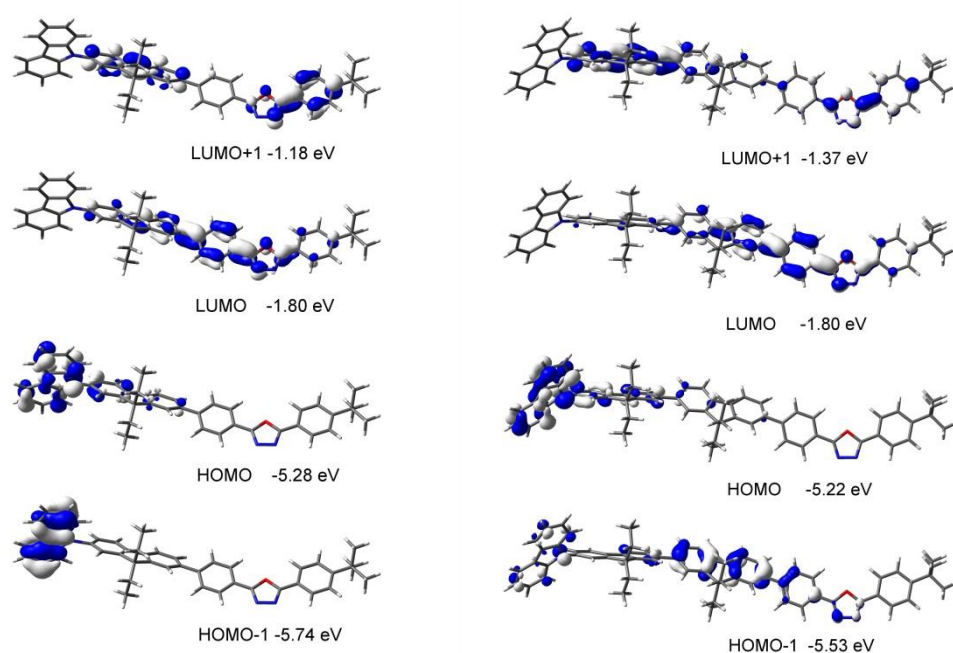


Figure A1: Selected molecular orbitals for **2a** (left) and **7a** (right). Contours drawn at ± 0.04 (e/bohr^3)^{1/2}.

The LUMOs of **3a** and **4a** are located on the heteroaromatic rings. The electron-accepting heteroaromatic linkers in **3** and **4** and the electron-donating OMe and butyl groups at the carbazolyl groups in **5** and **6** lower the HOMO-LUMO gap compared to **2**.

The characters of LUMO and LUMO+1 are the phenylene rings next to the oxadiazole ring for **2a-6a** and **8** rather than the oxadiazole unit itself as viewed in Figure A1 for **2a**. The diaryloxadiazole unit as a whole is a strong π -electron acceptor. The LUMO+1 in **7a** is located on the fluorene unit near the carbazolyl group rather than on the phenylene ring with the butyl group. Thus **7a** has a different orbital make up where the two fluorene units contribute to the LUMO+1 and HOMO-1 of **7a** in Figure A1.

Figure A2 shows the energy levels of triad molecules **1a-8** used in this thesis.

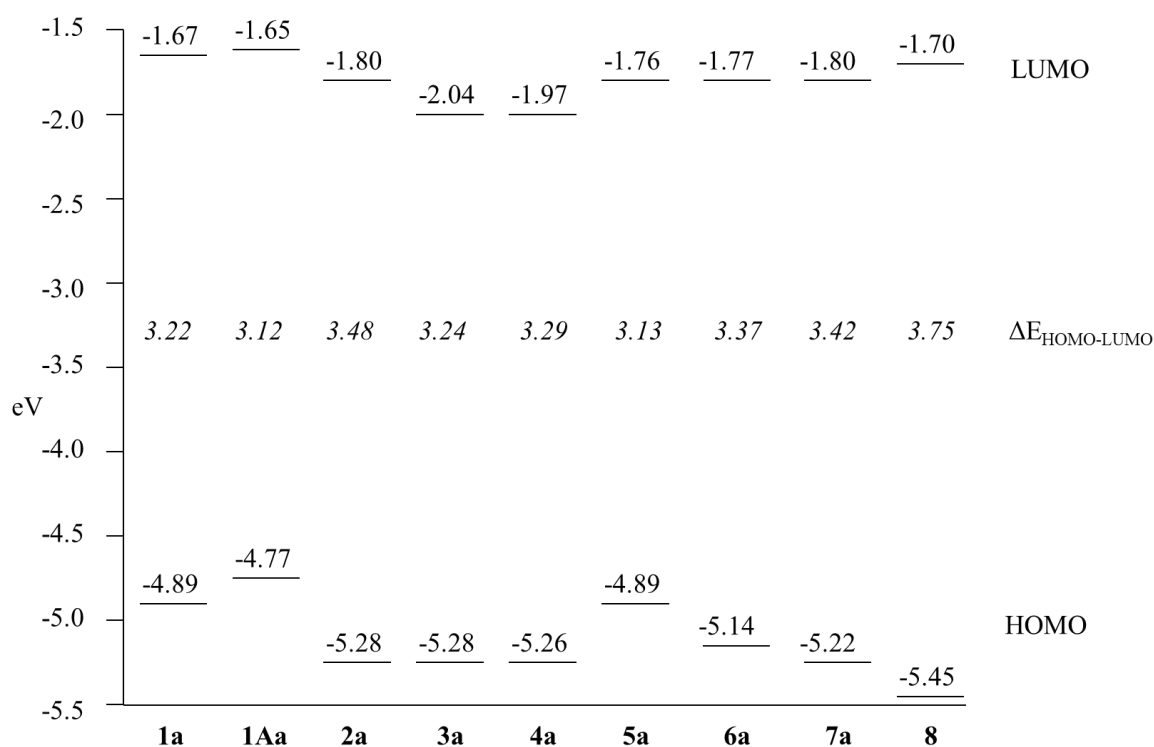


Figure A2: Energy diagram showing HOMO and LUMO of compounds **1a-8**.

The LUMO energy is lowered when a pyridine (**3a**) or thiophene (**4a**) ring replaces the phenylene ring between the fluorene and oxadiazole rings.

The HOMO is lowered when a carbazolyl group (**2a**) is used instead of a diphenylamino group (**1a**). Electron-donating substituents (methoxy **5a** > tBu **6a**) at the carbazolyl groups raise the HOMO energy.

Appendix B

Photoluminescence Measurements

These were carried out by the Department of Chemistry at Durham University.

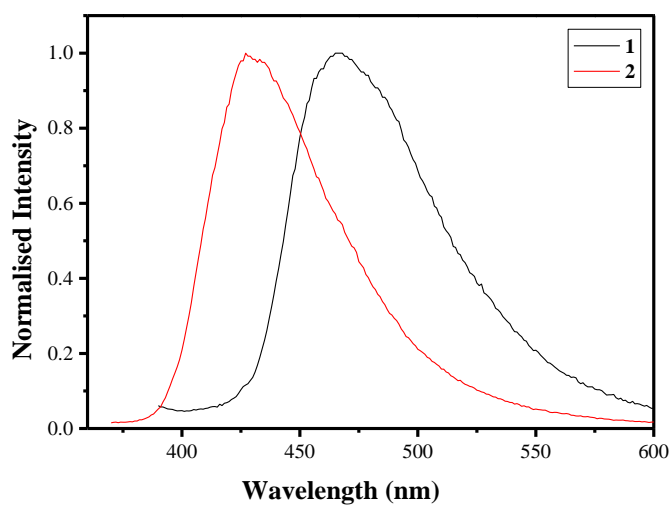


Figure B1: Normalised photoluminescence spectra of compounds **1** and **2** from evaporated thin films.

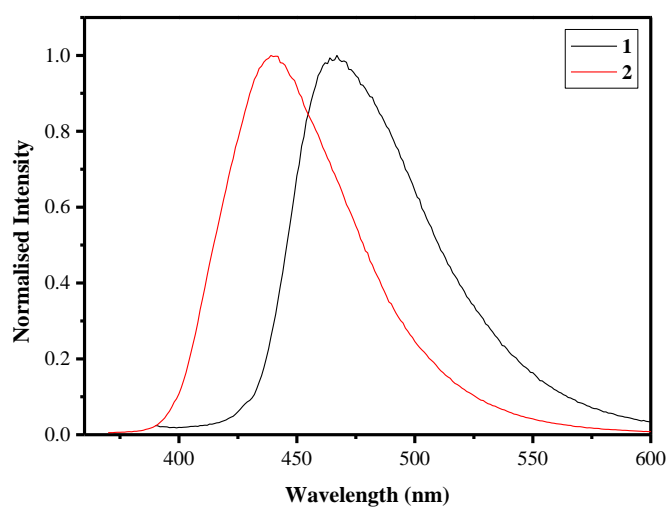


Figure B2: Normalised photoluminescence spectra of compounds **1** and **2** from spin-coated films using DCM as a solvent.

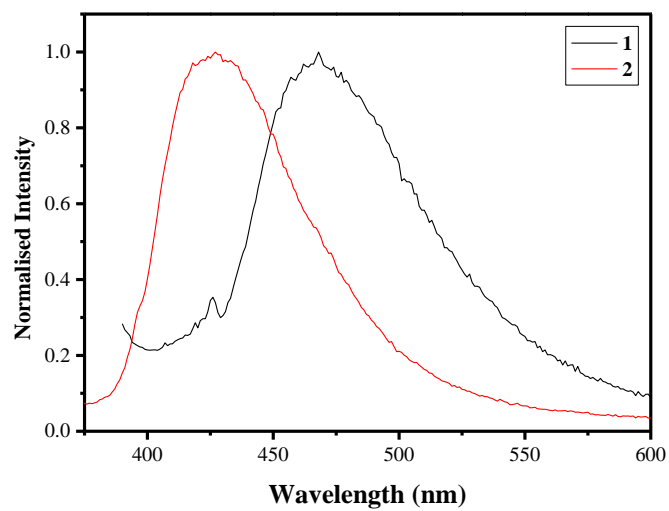


Figure B3: Normalised photoluminescence spectra of compounds **1** and **2** from spin-coated films using toluene as a solvent.

Appendix C

Pentacene OLEDs

Transfer characteristics for pentacene OFETs showed good hole transport capabilities and some evidence of electron transport (Figure 7.2 in the Transistor Development chapter). For this reason, pentacene was incorporated into an OLED to determine whether it would emit light. Two batches of pentacene OLEDs were made, one with larger (Batch 1) and one with smaller (Batch 2) crystals. These larger and smaller crystals were created by changing the rate of evaporation, from 0.05-0.10 nm s⁻¹ for Batch 1 to 1.0-1.5 nm s⁻¹ for Batch 2. As shown by the AFM images in Figure D1, pentacene evaporated at the lower rate showed a dendritic structure with grain size on the order of 1.0-1.5 μm, whilst pentacene evaporated at the higher rate lost the dendritic structure and showed much smaller grains of approximately 100-150 nm.

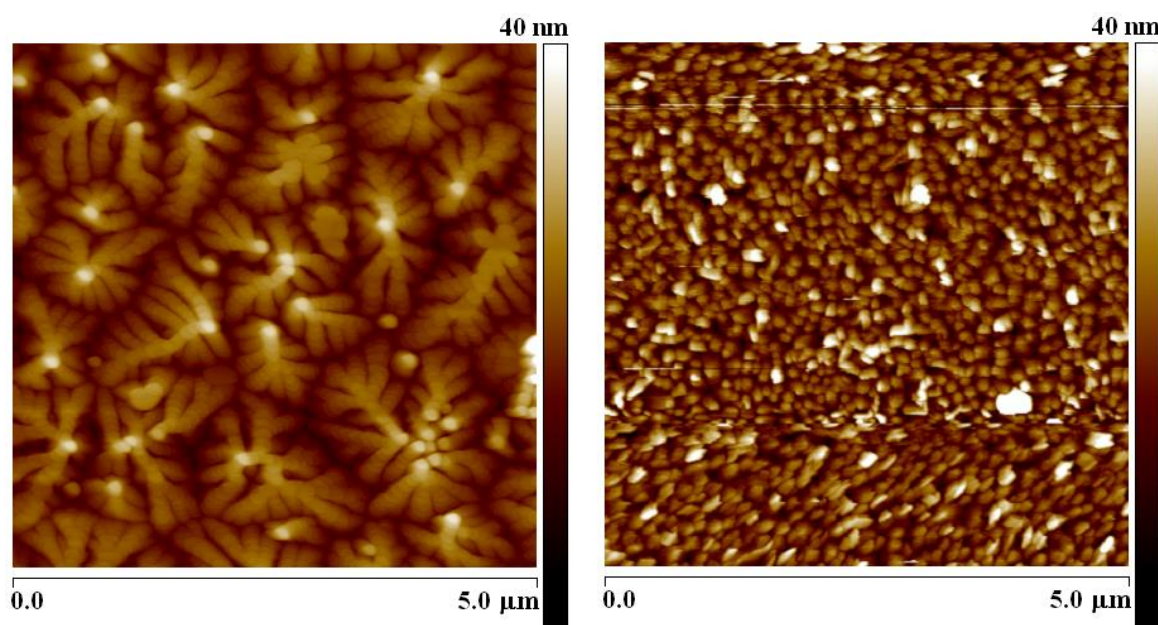


Figure D1: AFM images of pentacene films showing (a) larger Batch 1 crystals evaporated at 0.05-0.10 nm s⁻¹ and (b) smaller Batch 2 crystals evaporated at 1.0-1.5 nm s⁻¹. Images courtesy of Dan Kolb.¹

Current and photocurrent vs bias curves for Batch 1 showed only one functioning device and this result is given in Figure D2. The photocurrent curve for this device shows a turn-on voltage of 3.72 V at a photocurrent of 1 nA. At this voltage, the sample current is 1.13×10^{-3} A. At 5 V, the maximum photocurrent measured was 1.23×10^{-8} A. The fact that the photocurrent was so small indicated that very little light, less than 1 cd m^{-2} , was being emitted, a fact reinforced by the EL spectrum obtained for the same batch (Figure D3(a)). The emission maxima were almost obscured by noise and the colour ambiguous to the naked eye. The EL spectrum was too noisy to show definitive wavelengths for the emission maxima, but after comparison with the EL spectrum obtained for Batch 2, the maxima were estimated to be 610 and 700 nm.

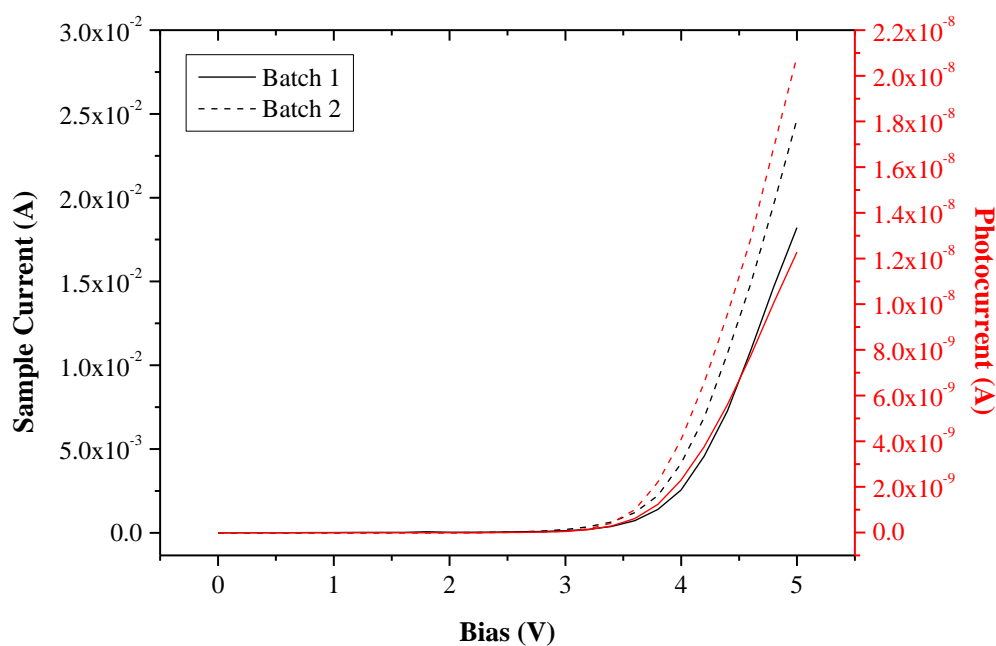


Figure D2: Current and photocurrent vs bias graph for Batch 1 and 2 of devices with structure ITO / PEDOT:PSS / Pentacene / Ca / Al.

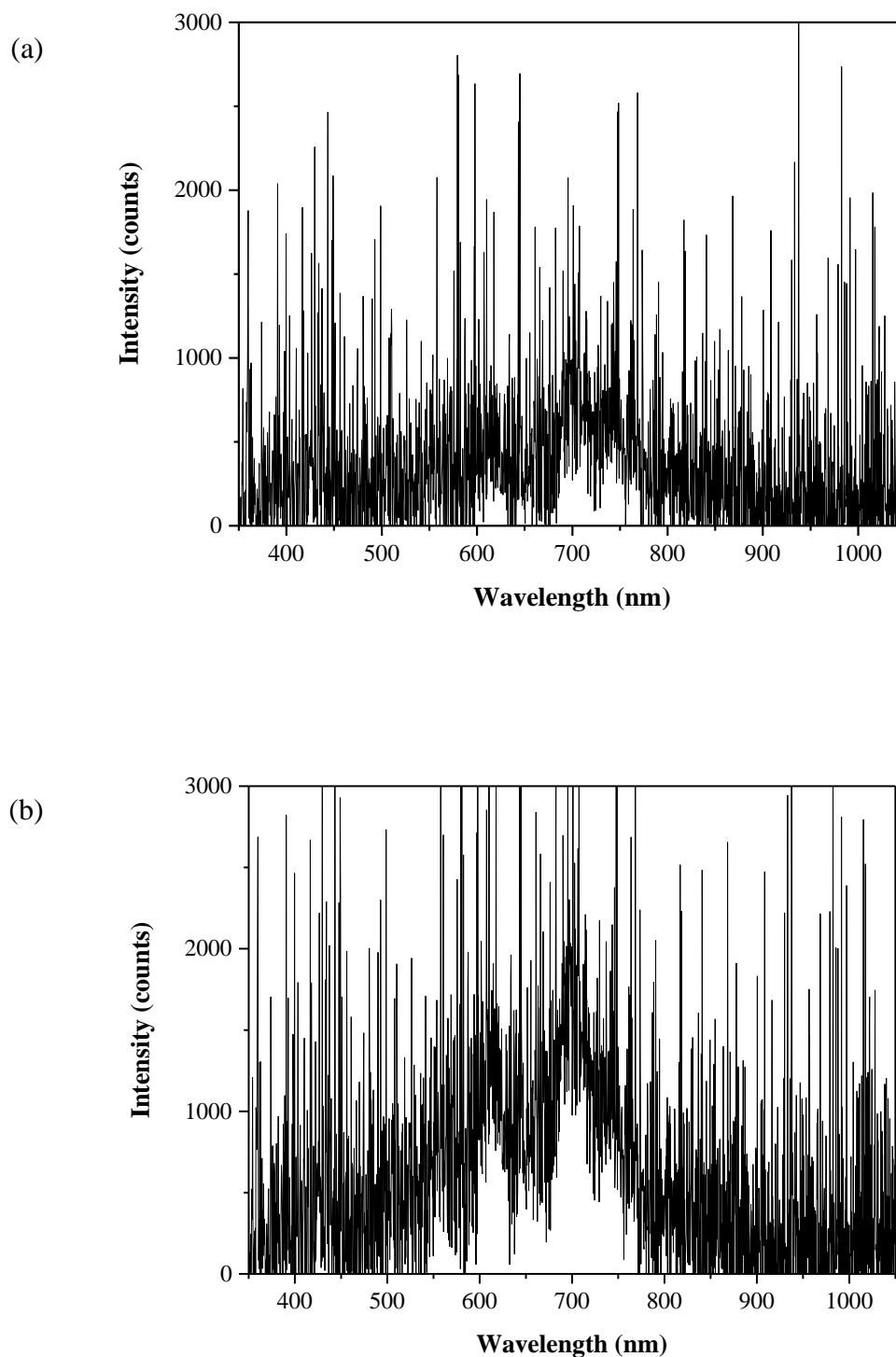


Figure D3: EL spectra for (a) Batch 1 and (b) Batch 2. Measured with current set to 20 mA.

Current and photocurrent vs bias curves for devices in Batch 2 showed more repeatable behaviour and a typical result is included in Figure D2. The turn-on voltage occurred at a slightly lower voltage for this batch at 3.60 V at 1 nA of photocurrent. The photocurrent at

5 V was higher at 2.08×10^{-8} A. As previously mentioned, the EL spectrum obtained for Batch 2 (Figure D3(b)) was slightly clearer, though still noisy and contained two maxima, a smaller peak at 610 and a larger peak at 700 nm. This would imply that pentacene is a red emitter although this could not be distinguished by the naked eye. Red emission would be expected due to the band gap of pentacene being at 1.82 eV.¹ As the light emission was so minute, the results were not used to obtain values of external quantum efficiency or CIE coordinates.

The results for the pentacene OLEDs are not very reproducible and suggest that the devices are not particularly reliable. Also, both batches emitted very little light, resulting in very poor OLEDs. The most likely reason for the poor efficiency is that the pentacene transports insufficient electrons for recombination. Interestingly, although current and photocurrent vs bias characteristics are similar for both batches, the sample current and photocurrent are consistently higher in Batch 2. The EL spectra for Batches 1 and 2 show that Batch 2 gave greater emission when measured, suggesting that smaller crystals of pentacene improve device characteristics and show greater EL.

Overall pentacene gives very poor OLEDs. This result is most likely indicative of the good hole transporting properties of pentacene that make it a good p-type semiconductor but poor emitter. The pentacene OLED was based on just a single organic material. Such a structure makes it very difficult to match both the HOMO and LUMO of the pentacene with the work functions of the anode and cathode, respectively. This serves as a further barrier to equal electron and hole injection and thus to recombination and EL. A major conclusion that may be drawn from this study is that pentacene is unsuitable as an OLEFET material.

References

1. Dan Kolb in *Organic Transistors Based On Pentacene And Dibenzothiophene Derivatives*, PhD Thesis, **2008**, Chapter 5.

Appendix D

25 Wt% F8BT:IL Devices (Batch 3) and Annealing Temperature Study

Based on the promising results for the 5% IL devices in Chapter 8, incorporation of a higher weight percentage of IL was considered. Lee et al¹ compared different blends of IL with Super Yellow and showed that a 25 wt% of IL gave the best overall device characteristics, so this higher percentage was also utilised in this study. Based on the results of the effect of annealing temperature on 5 wt% F8BT:IL devices, the annealing study was also repeated with 25 wt% F8BT:IL with an aim to optimise device characteristics. Devices were also annealed at 230 °C and devices without IL were also produced for comparative purposes. This set of devices is referred to as Batch 3 and the device structures and annealing conditions are summarised in Table E1.

Table E1: Batch 3 substrates, device configuration and annealing temperatures.

Substrate	Device Configuration	Annealing Temperature (°C)
1	ITO / F8BT / Al	30
2	ITO / F8BT / Al	80
3	ITO / F8BT / Al	230
4	ITO / F8BT:IL / Al	30
5	ITO / F8BT:IL / Al	80
6	ITO / F8BT:IL / Al	230

The current and photocurrent vs bias data for F8BT and F8BT:IL devices annealed at different temperatures are given in Figure E1. The F8BT devices annealed at 30 °C and 80 °C show similar IV characteristics both with evidence of resistive effects and turn-on at 6.1

V and 6.9 V, respectively. The device annealed at 230 °C shows current fluctuations at lower voltages and the current rises from the baseline at a lower voltage of 8 V.

The F8BT:IL devices all showed noisy IV behaviour. The devices annealed at 30 °C and 80 °C both showed evidence of diode-like behaviour before apparently breaking down at 4.6 V and 4.8 V, respectively. The F8BT:IL device annealed at 230 °C showed very noisy IV characteristics.

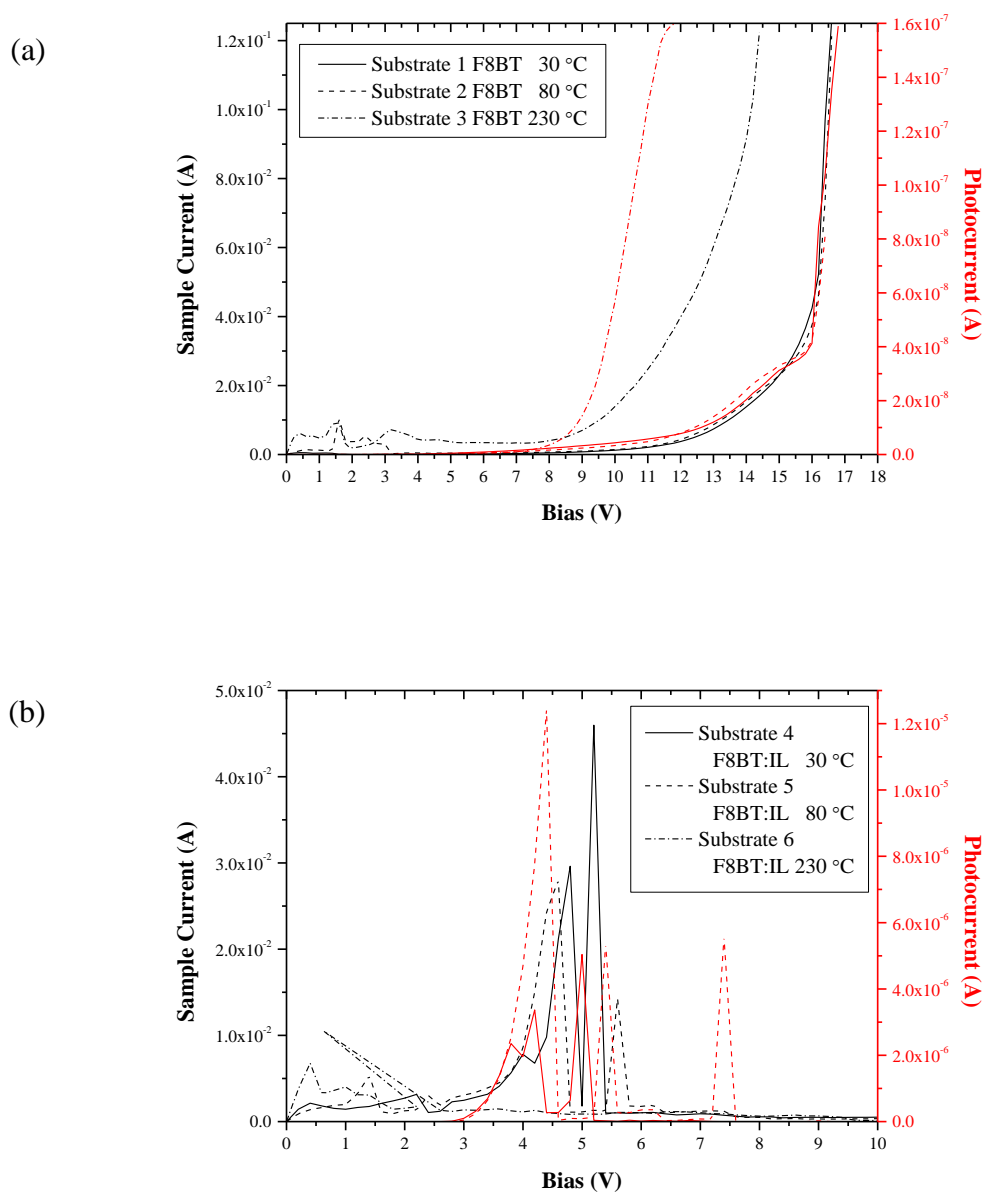


Figure E1: Current and photocurrent vs bias measurements of 25% IL devices from the 6 substrates annealed at different temperatures (a) 1-3 and (b) 4-6.

None of the F8BT devices (Substrates 1-3) produced stable visible light emission and nor did the F8BT:IL devices annealed at 230 °C (Substrate 6). Light emission was observed for F8BT:IL devices annealed at 30 °C and 80 °C (Substrate 4 and 5) and the spectra are given in Figure E2(a) and (b), respectively. The emission from the device annealed at 80 °C is very noisy due to the low level of light produced. The emission spectrum is more obvious for the F8BT:IL device annealed at 30 °C where two peaks at approximately 530 nm and 565 nm are visible. These appear to match the emission maxima observed for the F8BT OLEDs prepared with calcium cathodes reported in Chapter 8 although in this case the 565 nm peak (that coincided with the shoulder for the standard F8BT OLEDs) is slightly more intense than the 530 nm peak, possibly as a result of the low light emission.

The colour of emission for the F8BT:IL devices is plotted on the CIE diagram in Figure E3. The colour is similar, but slightly shifted compared to the 5 wt% F8BT:IL devices shown in Chapter 8.

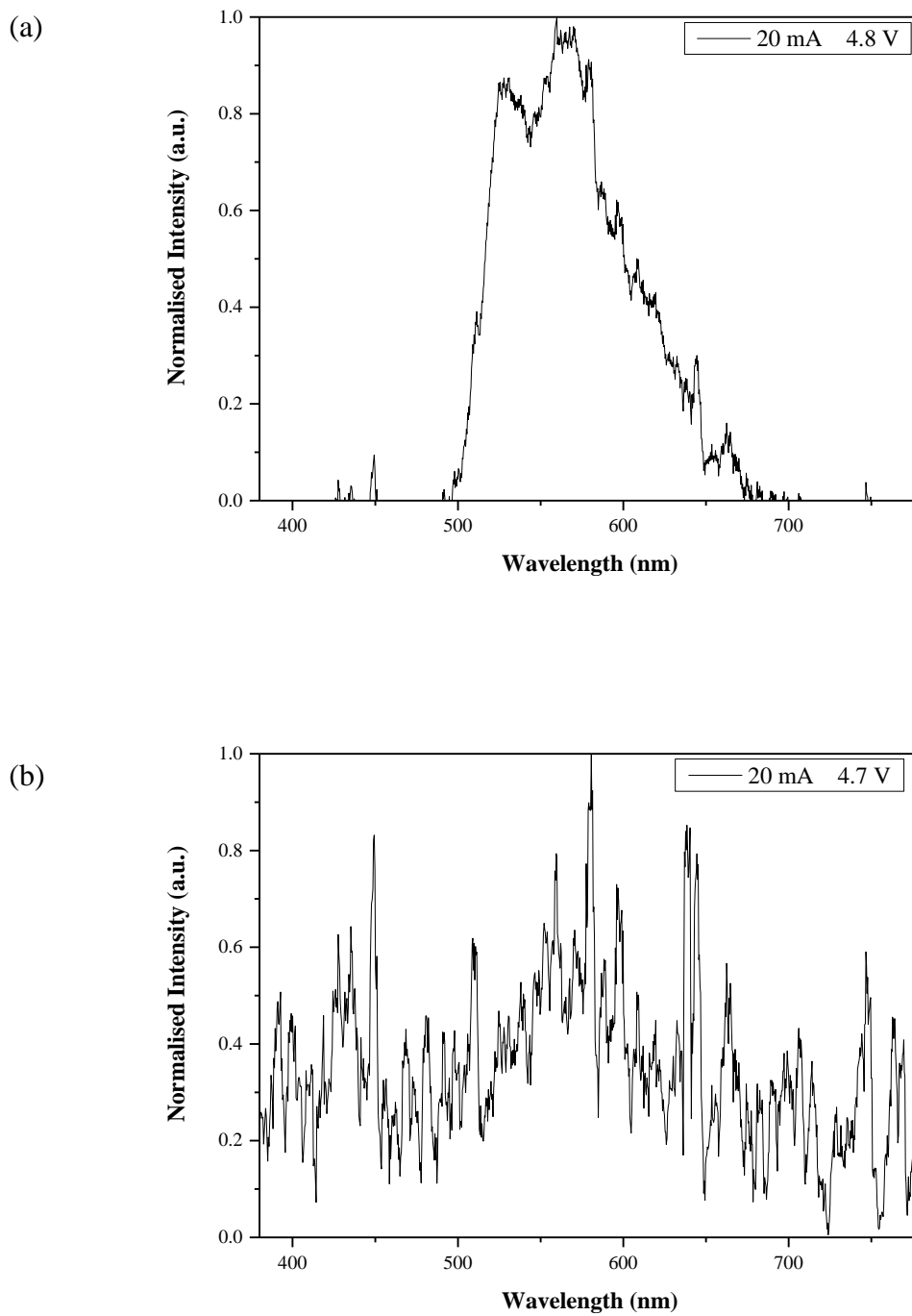


Figure E2: EL graphs of (a) Substrate 4 annealed at 30 °C and (b) Substrate 5 annealed at 80 °C, both measured at 20 mA.

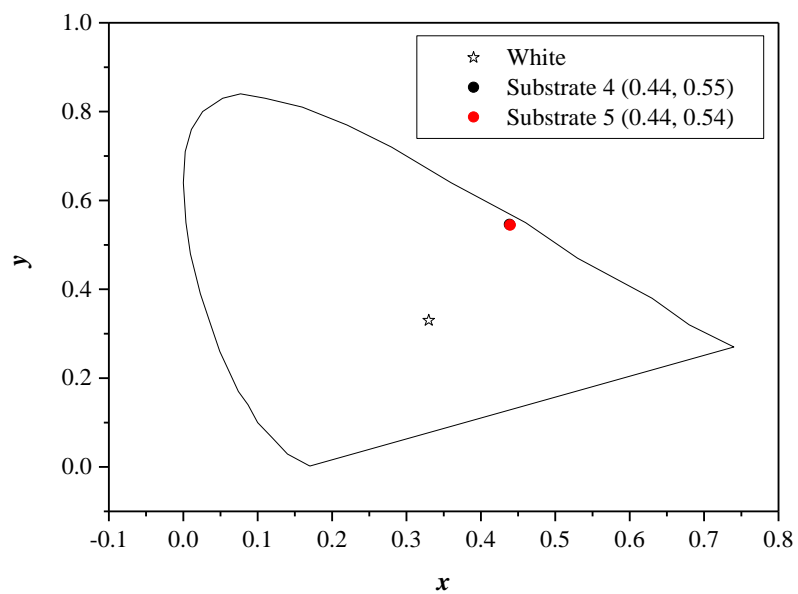
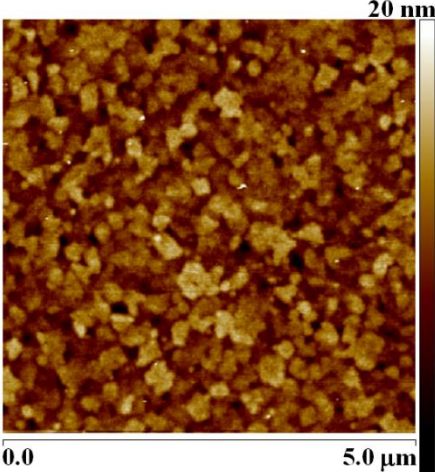
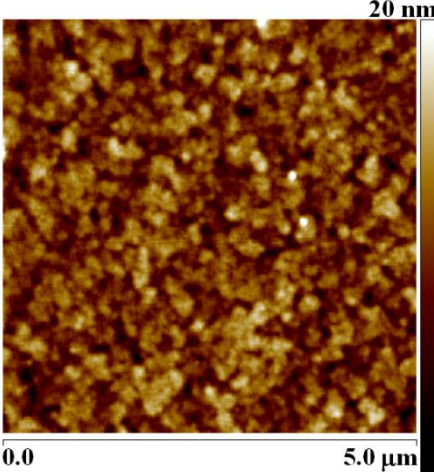
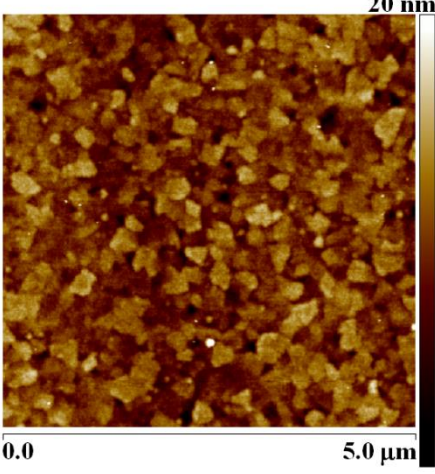
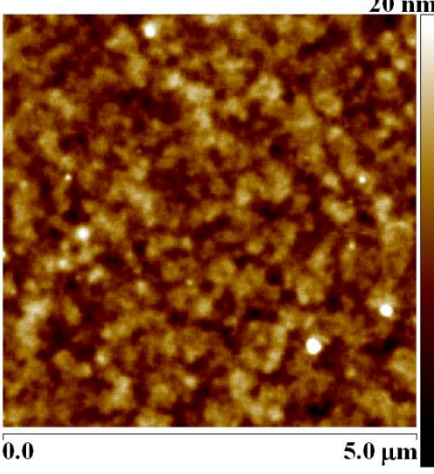
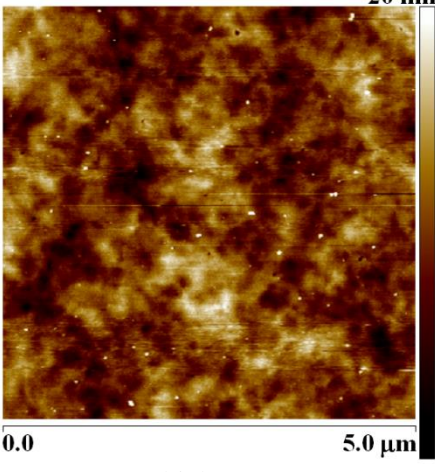
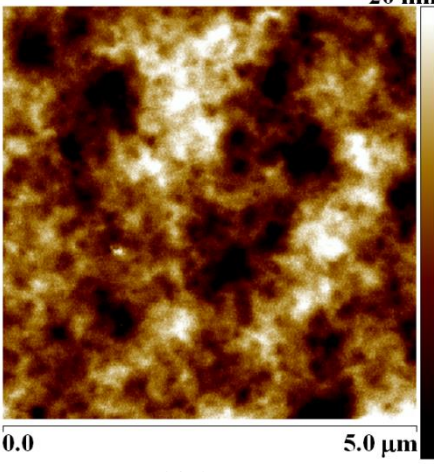


Figure E3: CIE diagram showing coordinates measured at a current of 20 mA on Substrate 4 and 5 mA on Substrate 5 (20 mA measurement could not be obtained).

AFM data of each device are tabulated in Table E2. These AFM images are comparable to the 5% IL study in Chapter 8 where the results are discussed.

Table E2: AFM images of each substrate in Batch 3.

Annealing T (°C)	ITO / F8BT	ITO / F8BT:IL (25 wt%)
30	 <p>Layer Thickness = 76 nm Roughness = 1.98 nm</p>	 <p>Layer Thickness = 55 nm Roughness = 2.14 nm</p>
80	 <p>Layer Thickness = 65 nm Roughness = 1.94 nm</p>	 <p>Layer Thickness = 59 nm Roughness = 2.02 nm</p>
230	 <p>Layer Thickness = 65 nm Roughness = 2.27 nm</p>	 <p>Layer Thickness = 66 nm Roughness = 3.62 nm</p>

References

- 1) H. J. Lee, B. R. Lee, J. S. Park, S. O. Kim, J. Y. Kim, M. H. Song, *Appl. Phys. Lett.*, 98, 253309, **2011**.